
Combining Simulation and Machine Learning for Materials Optimization: Polymer Compatibilization, Disinfection, and Heat Transfer

Kombination von Simulation und *Machine Learning* zur Optimierung von Materialien: Polymerkompatibilisierung, Desinfektion und Wärme-Übertragung

Vom Fachbereich Chemie der Technischen Universität Darmstadt zur Erlangung des Grades Doctor rerum naturalium (Dr. rer. nat.)

Genehmigte Dissertation von M.Sc Tianhang Zhou
Tag der Einreichung: 22.02.2022, Tag der Prüfung: 11.04.2022

1. Gutachten: Prof. Florian Müller-Plathe
 2. Gutachten: Prof. Nico van der Vegt
 3. Gutachten: Prof. Doros Theodorou
- Darmstadt 2022
-



TECHNISCHE
UNIVERSITÄT
DARMSTADT

Eduard-Zintl-Institut für
Anorganische und
Physikalische Chemie

Combining Simulation and Machine Learning for Materials Optimization: Polymer Compatibilization, Disinfection, and Heat Transfer

Kombination von Simulation und *Machine Learning* zur Optimierung von Materialien:
Polymerkompatibilisierung, Desinfektion und Wärme-Übertragung

Accepted doctoral thesis by M.Sc Tianhang Zhou

1. Review: Prof. Florian Müller-Plathe
2. Review: Prof. Nico van der Vegt
3. Review: Prof. Doros Theodorou

Date of submission: 22.02.2022

Date of thesis defense: 11.04.2022

Darmstadt 2022

Bitte zitieren Sie dieses Dokument als:

URN: urn:nbn:de:tuda-tuprints-211319

URL: <https://tuprints.ulb.tu-darmstadt.de/id/eprint/21131>

Dieses Dokument wird bereitgestellt von tuprints,
E-Publishing-Service der TU Darmstadt
<http://tuprints.ulb.tu-darmstadt.de>
tuprints@ulb.tu-darmstadt.de

Die Veröffentlichung steht unter folgender Creative Commons Lizenz:
Namensnennung – Weitergabe unter gleichen Bedingungen 4.0 International
<https://creativecommons.org/licenses/by-sa/4.0/>

Erklärungen laut Promotionsordnung

§8 Abs. 1 lit. c PromO

Ich versichere hiermit, dass die elektronische Version meiner Dissertation mit der schriftlichen Version übereinstimmt.

§8 Abs. 1 lit. d PromO

Ich versichere hiermit, dass zu einem vorherigen Zeitpunkt noch keine Promotion versucht wurde. In diesem Fall sind nähere Angaben über Zeitpunkt, Hochschule, Dissertationsthema und Ergebnis dieses Versuchs mitzuteilen.

§9 Abs. 1 PromO

Ich versichere hiermit, dass die vorliegende Dissertation selbstständig und nur unter Verwendung der angegebenen Quellen verfasst wurde.

§9 Abs. 2 PromO

Die Arbeit hat bisher noch nicht zu Prüfungszwecken gedient.

Darmstadt, 22.02.2022

Tianhangzhou

M.Sc Tianhang Zhou

Acknowledgments

In 2016, I came to TU Darmstadt with a German certificate named “TestDaF”, proving that my German was in C1 level. However, I was confused at that time. Lectures for Master of Science are really different from language courses that teach me how to buy correct things in the supermarket. Thankfully, things took a turn for the better when I began to learn two basic lectures mainly for bachelor students, i.e., Physikalische Chemie II (given by Prof. Dr. Florian Müller-Plathe at that time) and Physikalische Chemie III (given by Prof. Dr. Nico van der Vegt at that time). I learned a lot from their courses. For example, first time I’ve known Schrödingergleichung and Boltzmann-Verteilung in years. But more importantly, I found something very interesting, something that could engage me to keep learning. Looking back, I’m proud that I accomplished my Master studies in Germany, where courses, practicums, and group cooperations form a solid foundation for the future.

I want to thank my thesis advisor (Doktorvater) — Prof. Dr. Florian Müller-Plathe. When I did my master thesis in this group, I gained many basic simulation knowledge (e.g., how to write correct input files and analysis codes). These achievements led me to become complacent. Fortunately, his teachings made me realize what I had overlooked. For example, I learned through him that we shouldn’t use one method without any own justification, but only because it’s popular and many other people use it. In hindsight, his advice at that time was all very basic. However, I can’t imagine what I would have become without his teaching. Also, I want to thank him for his constant advice and tolerance during my Ph.D. studies after 2019. To be honest, I always get lost in the routine science and cannot find the correct way to achieve a good and interesting scientific target. Even now, I don’t feel I’m doing well enough. But I remember his words and guidance. I hope I can understand more from these words in my further academic life and teach something valuable to my students later.

Then I want to give a special thank you to my industry cooperators in Covestro: Dr. Sergii Donets, Dr. José A. Gámez, Dr. Mandy Gieler, Dr. Sven Hobeika, Dr. Jan Meyer, Dr. Marina Reithmeier, Dr. Andreas Seidel. If my Doktorvater let me know what is good science, you let me know what useful science for the industry is. I would like to especially thank the two wonderful coordinators, Mandy and Marina, for your efforts in our cooperation project. Thanks for your patience in waiting for me to realize the difference between science and industry.

I want to express my gratitude to Prof. Dr. Nico van der Vegt for his all interesting lectures, examining my thesis, and providing suggestions in our shared group seminar. Further, I’m grateful to Prof. Dr. Annette Andrieu-Brunsen, Dr. Arash Nikoubashman, for being part of my evaluation committee. Special thanks to Prof. Doros Theodorou for revising my thesis.

Then, I want to express my gratitude to Prof. Dr. Hari Krishna Chilukoti for co-supervising my master thesis and for teaching me how to run simulations with continuous patience. I want to thank Prof. Dr. Hossein Eslami for the many funny jokes we made with each other. I want to extend my thanks to my collaborators and colleagues: Prof. Dr. Michael Böhm, Sree Harsha Bhimineni, Dejian Qiu, Wei Li, Dr. Siantan Bag, Prof. Dr. Guirong Zhang, Prof. Dr. Jiquan Liu, Prof. Dr. Saurav Prasad, Dr. Vikram Reddy Ardham, Dr. Yunfeng Mao, Dr. Shubhadip Das, Dr. Hongyang Huang, Dr. Eunsang Lee, Dr. Hans-Jürgen Bär, Dr. Swaminath

Bharadwaj, Vishal Dadhich, Marvin Bernhardt. Special thanks to Dr. Zhenghao Wu, Dr. Jurek Schneider, Melissa Meinel, Tobias Materzok, Yash Jain, Simon Alberti, and my roommate Maohua Zhang for their company during my Ph.D. journey. Special thanks to my football teammates in “Darmstadtium”: Chen Shen, Yongchao Chen, Mian Dai, Tianshu Jiang, Kun Hu, Prof. Dr. Fei Liang, and Prof. Dr. Hongbin Zhang. Special thanks to Dr. Qing Tan and Dr. Huan Zhao in Düsseldorf. I would also like to thank our wonderful group secretary, Frau Dana Voss, for her kind help in everyday life.

My deepest gratitude goes out to my father, Hongwei Zhou, and my mother, Min Zhou. I arrived in Germany in the autumn of 2015, and it is now the spring of 2022. Without their help and support, I would not have been able to complete my language studies, Master studies, and Ph.D. studies in these years.

I am 28 years old and studies in Germany have taken up a quarter of my life so far. Thanks to all friends in Germany for their love and support. I will remember everything here.

Die vorliegende Dissertation wurde der unter Leitung von Herrn Prof. Dr. Florian Müller-Plathe in der Zeit vom 01. Mai 2019 bis zum 30. April 2022 im Fachbereich Chemie der Technischen Universität Darmstadt durchgeführt.

Teile dieser Arbeit sind veröffentlicht oder eingereicht:

Zhou, T.; Schneider, J.; Wu. Z.; Müller-Plathe, F., The Compatibilization Efficiency of Additives in Homopolymer Blends: a Dissipative Particle Dynamics Study. *Macromolecules*. 2021, 54 (20), 9551-9564.

Zhou, T.; Qiu. D.; Wu. Z.; Albert. S.; Bag S.; Schneider. J.; Müller-Plathe, F., The Compatibilization Efficiency of Graft Copolymers in Incompatible Polymer Blends: Dissipative Particle Dynamics Simulations Combined with Machine Learning, in revision by industry cooperators. (2022)

Zhou, T.; Wu. Z.; Das, S.; Eslami, H.; Müller-Plathe, F., How Ethanolic Disinfectants Disintegrate Coronavirus Model Membranes: A Dissipative-Particle-Dynamics Simulation Study. *Journal of Chemical Theory and Computation*, in revision. (2022)

Zhou, T.; Wu. Z.; Chilukoti, H. K.; Müller-Plathe, F., Sequence-Engineering Polyethylene-Polypropylene Copolymers with High Thermal Conductivity Using a Molecular-Dynamics-Based Genetic Algorithm. *Journal of Chemical Theory and Computation*. 2021, 17 (6), 3772–3782.

Zhou, T.; Chilukoti, H. K.; Wu. Z.; Müller-Plathe, F., Effect of Defects on the Interfacial Thermal Conductance between n-Heneicosane in Solid and Liquid Phases and a Graphene Monolayer. *Journal of Physical Chemistry C*. 2021, 125 (25), 14149–14162.

In dieser Dissertation nicht enthalten, aber im gleichen Zeitraum entstanden sind:

Chilukoti, H. K.; **Zhou, T.**; Ardham, V. R.; Böhm, M. C.; Müller-Plathe, F., Thermal Energy Transport across the Interface between Phase Change Material n-Heneicosane in Solid and Liquid Phases and Few-Layer Graphene. *Journal of Physical Chemistry C*. 2019, 123, 29192–29202.

Eslami, H.; Das, S.; **Zhou, T.**; Müller-Plathe, F., How Alcoholic Disinfectants Affect Coronavirus Model Membranes: Membrane Fluidity, Permeability, and Disintegration. *Journal of Physical Chemistry B* 2020, 124, 10374–10385.

Zusammenfassung

Im letzten halben Jahrhundert wurden erhebliche Fortschritte bei den molekularen Simulationstechniken erzielt, die ein umfassendes Verständnis der Struktur-Eigenschafts-Beziehung weicher Materialien auf verschiedenen Zeit- und Längenskalen ermöglichen. Bislang ist jedoch das optimale Design von Kandidaten für die nächste Generation weicher Materialien aufgrund des enormen chemischen und konfigurativen Raums immer noch anspruchsvoll. Die Techniken des *machine learning* (ML), die eingesetzt werden, um verwertbare Erkenntnisse aus großen, durch Simulationen generierten Daten zu gewinnen, können die Engpässe bei der Optimierung weicher Materialien überwinden. Daher wurde in dieser Arbeit ein Framework entwickelt, der auf der Kommunikation zwischen wechselseitigen Multiskalensimulationen (*atomistic* und *coarse-grained*) und ML zur rationalen Untersuchung weicher Materialien basiert.

Ein Ziel dieser Arbeit ist es, die detaillierten Struktur-Zusammensetzungs-Eigenschafts-Leistungs-Beziehungen weicher Materialien auf Vorwärtsrichtung zu bewerten. Zunächst wird die Kompatibilitätsleistung von Blockcopolymeren (d.h. lineare und Pfropfcopolymere) an der Grenzfläche zwischen zwei inkompatiblen Polymerphasen mit Hilfe von *dissipative-particle-dynamics* (DPD) Simulationen untersucht. Es wird eine phänomenologische analytische Relation entwickelt, um die Abhängigkeit der Kompatibilisierungseffizienz von linearen Blockcopolymeren von der Polymerchemie, der molekularen Architektur und der Anzahl der Copolymermoleküle zu quantifizieren. Pfropfcopolymere weisen jedoch im Vergleich zu linearen Blockcopolymeren größere Unterschiede im Raum der Architekturparameter auf, was den traditionellen empirischen Anpassungsprozess einschränkt. Dementsprechend füttern wir DPD-Ergebnisse mit ML-Modellen und stellen fest, dass die Kombination von DPD und ML in der Lage ist, die Kompatibilisierungseffizienz von Pfropfcopolymeren auf molekularer Ebene genau vorherzusagen. Für ein gegebenes Pfropfcopolymer mit mehreren Deskriptoren (z. B. molekulare Architekturen und chemische Eigenschaften) kann die Kompatibilisierungseffizienz anhand der trainierten ML-Modelle gut vorhergesagt werden. Darüber hinaus bieten ML-Techniken ein Maß für die relative Bedeutung der Deskriptoren, um die Korrelation zwischen Deskriptoren und DPD-Vorhersagen aufzuzeigen. Wir stellen fest, dass die Anzahl der Seitenketten der Pfropfcopolymere allmählich ihre Kompatibilisierungseffizienz dominiert, während die Länge der Seitenketten unwichtig wird, wenn die Mischung stark inkompatibel wird. Dieses Erkenntnis kann den Suchraum in weiteren Simulationen und Experimenten eingrenzen. Darüber hinaus versuchen wir, den Kompatibilisierungsmechanismus der linearen und Pfropfcopolymere zu verstehen, indem wir die Monomerverteilungen, die Anzahl der ungleichen Kontakte zwischen verschiedenen Spezies und die molekularen Konformationen charakterisieren. Insbesondere die Anisotropie der Copolymere, definiert als das Verhältnis ihrer Gyrationselemente in den Richtungen senkrecht und parallel zur Oberfläche, ist sowohl für lineare als auch für Pfropfcopolymere stark mit ihrer Kompatibilisierungseffizienz korreliert.

Wir untersuchen auch die alkoholinduzierten Veränderungen an Coronavirusmembranen unterschiedlicher Zusammensetzung mit DPD-Modellen, d.h. reines Dipalmitoylphosphatidylcholin, Dioleoylphosphatidylcholin und Dimyristoylphosphatidylcholin sowie deren binäre und ternäre Mischmembranen. Die wichtigste Erkenntnis dieser Studie ist, dass eine maximale Ethanolkonzentration von 32 mol % (55 Gew.%) in alkoholischen Desinfektionsmitteln ausreicht, um alle Coronavirus-Modellmembranen, die aus diesen drei Lipiden bestehen, zu zersetzen. Angesichts der großen Unterschiede in der Zusammensetzung und

Struktur gemischter Membranen ist es jedoch schwierig, ihre Übergänge vom intakten zum geschädigten Zustand zu identifizieren. Wir stellen zum Beispiel fest, dass der Übergangspunkt nicht quantitativ auf der Grundlage physikalischer Deskriptoren wie der Fläche pro Lipidmolekül, der Membrandicke und der Orientierungsparameter vorhergesagt werden kann. Außerdem ist die visuelle Prüfung der Membranintegrität in Simulationen mühsam. Die Entwicklung eines einfachen und robusten Werkzeugs zur Charakterisierung der Stabilität von Membranen gegenüber ethanolischen Desinfektionsmitteln kann daher den Optimierungsprozess von Desinfektionsuntersuchungen beschleunigen. Dieses Ziel wird durch das in dieser Studie entwickelte DPD/*deep-neural-network* Framework erreicht, das die Integrität von Lipidmembranen anstelle von menschlicher Beobachter erfasst.

Ein weiteres Ziel dieser Arbeit ist die Entwicklung von Materialien mit optimaler Leistung in Bezug auf die gewünschten Eigenschaften, Zusammensetzungen und Strukturen in umgekehrter Richtung, d. h. inverses Design (Leistung-Eigenschaft-Zusammensetzung-Struktur). Wir setzen einen hybriden Rahmen ein, indem wir einen genetischen Algorithmus und atomistische Molekulardynamiksimulation kombinieren, um Polyethylen-Polypropylen-Copolymere mit hoher Wärmeleitfähigkeit zu entwickeln. Wir stellen fest, dass Polyethylen-Polypropylen-Copolymere mit verschiedenen Sequenzen bei gleichem Monomerverhältnis sehr unterschiedliche Wärmeleitfähigkeiten aufweisen. Dies deutet darauf hin, dass die Monomersequenz einen entscheidenden Einfluss auf den Wärmetransport der Copolymere hat. Eine nicht-periodische und nicht-intuitive optimale Sequenz wird tatsächlich durch diese Hybridmethode identifiziert. Es weist die höchste Wärmeleitfähigkeit im Vergleich zu Homopolymeren und allen regulären Blockcopolymeren, z. B. Diblock, Triblock und Hexablock, auf. Im Vergleich zur Stoffdichte, den Kettenkonformationen und der Dichte der Schwingungszustände hat die Monomersequenz den stärksten Einfluss auf die Geschwindigkeit des Wärmetransports gegenüber inter- und intramolekularen Wechselwirkungen.

Der Erfolg der ML-Methode, die Vorhersagen über Eigenschaften von Materialien in großen Zusammensetzungs- und Konformationsräumen ermöglicht, hängt von der Verfügbarkeit von Trainingsdaten aus Simulationen ab. ML-Methoden wiederum ermöglichen eine robuste *a-posteriori*-Datenanalyse (z. B. Wichtigkeit einzelner Deskriptoren) zur Erforschung von Korrelationen zwischen Deskriptoren und Zieleigenschaften in Simulationen. Dadurch kann der Suchraum von Deskriptoren für weitere Untersuchungen eingegrenzt werden. Zusammenfassend lässt sich sagen, dass die Integration von Multiskalensimulationen mit ML-Algorithmen ein erhebliches Potenzial zur Beschleunigung des Designs weicher Materie bietet. Wir glauben, dass unsere Arbeit effiziente und praktische Ansätze für die Entwicklung eines Hybridrahmens für die Materialoptimierung bietet.

Abstract

In the last half-century, considerable advances have been achieved in molecular simulation techniques aiming at offering a comprehensive understanding of the structure-property relationship of soft materials on several time and length scales. So far, however, the optimal design of candidates for the next-generation soft materials is still a challenging task due to the enormous chemical and configurational space. The machine learning (ML) techniques, which are utilized to extract actionable insights from big data generated from simulations, can overcome the bottlenecks in the tasks of soft materials optimization. Hence, this thesis has developed a framework based on the mutual communication between multiscale simulations (atomistic and coarse-grained) and ML toward rational investigations of soft matter.

One objective of this thesis is to evaluate the detailed structure-composition-property-performance relationships of soft materials in a forward way. We firstly investigate the compatibilizing performance of block copolymers (i.e., linear and graft) on the interface between two incompatible polymer phases by dissipative-particle-dynamics (DPD) simulations. A phenomenological analytical power-law fit is developed to quantify the variation of compatibilization efficiency of linear block copolymers with the polymer chemistries, the molecular architecture, and the number of copolymer molecules. However, graft copolymers have larger diversities in the space of architectural parameters as compared to linear block copolymers, which limits the traditional empirical fitting process. Accordingly, we feed DPD results to ML models and find that the combination of DPD/ML is able to accurately predict the compatibilization efficiency of graft copolymers at the molecular level. For a given graft copolymer with several descriptors (e.g., molecular architectures and chemistries), its compatibilization efficiency can be well predicted from the trained ML models. Moreover, ML techniques provide a descriptor importance measure for the correlation between descriptors and DPD predictions. We find that as the blend changes from weakly incompatible to strongly incompatible, the number of side chains of graft copolymers gradually dominates their compatibilization efficiency while the side chain length becomes unimportant. This finding can narrow the search space in further simulations and experiments. Furthermore, we attempt to understand the compatibilization mechanism of the linear and graft copolymers by characterizing the beads distributions, the number of unlike contacts between different species, and the molecular conformations. Specifically, the relative shape anisotropy of copolymers, defined as the ratio of their gyration tensor elements in directions normal and parallel to the surface, is strongly correlated with their compatibilization efficiency for both linear and graft copolymers.

We also evaluate the alcohol-induced changes on coronavirus membranes of different compositions with DPD models, i.e., pure dipalmitoylphosphatidylcholine, dioleoylphosphatidylcholine, and dimyristoylphosphatidylcholine as well as their binary and ternary mixed membranes. The principal finding of this study is that a maximum ethanol concentration of 32 mol % (55 wt. %) in alcoholic-based disinfectants is sufficient to decompose any coronavirus model membranes composed of these three lipids. However, given the wide variations in compositions and structures of mixed membranes, identifying their transitions from the intact to the disrupted state is challenging. For example, we find that the transition point cannot be quantitatively predicted based on physical descriptors such as the area per lipid molecule, the membrane thickness, and the orientational order parameter. Additionally, the visual inspection of simulation profiles is cumbersome

to characterize the state of these membranes. Developing a simple and robust tool to characterize the stability of membranes against ethanolic disinfectants, can therefore accelerate the optimization process of disinfection investigations. This target is achieved by the developed DPD/deep-neural-network framework in this study, which accesses the integrity of lipid membranes in place of visual inspections.

The other objective of this thesis is to design materials with optimal performance on desired properties, compositions, and structures in the reverse direction, i.e., inverse design (performance-property-composition-structure). We employ a hybrid framework by combining the genetic algorithm and the atomistic molecular dynamics simulation, to design polyethylene-polypropylene copolymers with high thermal conductivity. We find that polyethylene-polypropylene copolymers with various sequences at the same monomer ratio have a broad distribution of thermal conductivities. This indicates that the monomer sequence has a crucial effect on the thermal energy transport of the copolymers. A non-periodic and non-intuitive optimal sequence is indeed identified by this hybrid framework, which gives the highest thermal conductivity compared with both homopolymers and any regular block copolymers, e.g., diblock, triblock, and hexablock. In comparison to bulk density, chain conformations, and vibrational density of states, the monomer sequence has the strongest impact on the efficiency of the thermal energy transport via inter- and intra-molecular interactions.

The success of ML, providing property predictions of materials in both large compositional and conformational spaces, relies on the availability of training data from simulations. In turn, ML methods allow a robust *posteriori* data analysis (e.g., descriptor importance measure) for exploring correlations between descriptors and target properties in simulations, which can narrow the search space of descriptors for further investigations. In short, the computational framework of integrating multiscale simulations with ML algorithms has a significant potential for accelerating the design of soft matter. We believe our work provides efficient and practical approaches to develop the advanced hybrid framework for the materials optimization.

Contents

1	Introduction	1
1.1	A hybrid framework	1
1.2	Compatibilization	4
1.2.1	Background	4
1.2.2	Challenges and Objectives	6
1.3	Disinfection	6
1.3.1	Background	6
1.3.2	Challenges and Objectives	7
1.4	Heat Transfer	10
1.4.1	Background	10
1.4.2	Challenges and Objectives	11
1.5	Structure of this Thesis	12
2	Method	13
2.1	Overview	13
2.2	Molecular Dynamics Simulation	13
2.3	Dissipative-Particle-Dynamics Simulation	14
2.4	Mutual communications between Simulation and Machine Learning	15
2.4.1	Forward Evaluation of the Structure-Property Relationships	15
2.4.2	Inverse Design of Structure by Using Genetic Algorithm	23
3	Results	25
3.1	Optimization of Compatibilization Efficiency of Linear Block Copolymers in Immiscible Homopolymer Blends	25
3.2	Optimization of Compatibilization Efficiency of Graft Copolymers in Immiscible Homopolymer Blends	47
3.3	Optimization of Disinfection Efficiency on Coronavirus Model Membranes	48
3.4	Optimization of Heat Transfer Efficiency of Copolymers from the Perspective of Inverse Design	80
4	Conclusion and Outlook	97
5	Annex: Optimization of Heat Transfer at the Interface	111

1 Introduction

1.1 A hybrid framework

Scientific research can be classified into four paradigms (Figure 1.1): the first paradigm based on purely empirical results (e.g., trial and error), the second paradigm supported by classical theories (e.g., laws of thermodynamics), the third paradigm contingent on computational simulations (e.g., density functional theory (DFT) and molecular dynamics (MD) simulations), and the fourth paradigm driven by big data[1, 2]. Although a comprehensive understanding of structure-property relationships of materials plays a major role in the fourth paradigm, it is impossible to achieve this understanding with a single theory or computational method so far. Multiscale simulation methods, which combine and systematically link several simulation hierarchies, are powerful in addressing phenomena or properties of a given system at several levels of resolution[3]. To be more specific in the field of soft matter science, the relevant multiscale simulations span a wide range of length and time scales, ranging from the sub-atomic (\sim Angstrom and femtosecond) scales to the macroscopic (\sim microns and seconds) scales[3–5]. However, the evolution in this multiscale structural-property characteristics also increases the overall demand for new approaches. The emergence of machine learning (ML) and modern optimization algorithms offers great promise for transcending previous limitations, and forms an advanced framework coupled with multiscale simulations. This hybrid framework is considered to be a promising tool to flourish breakthroughs in soft matter research[6, 7].

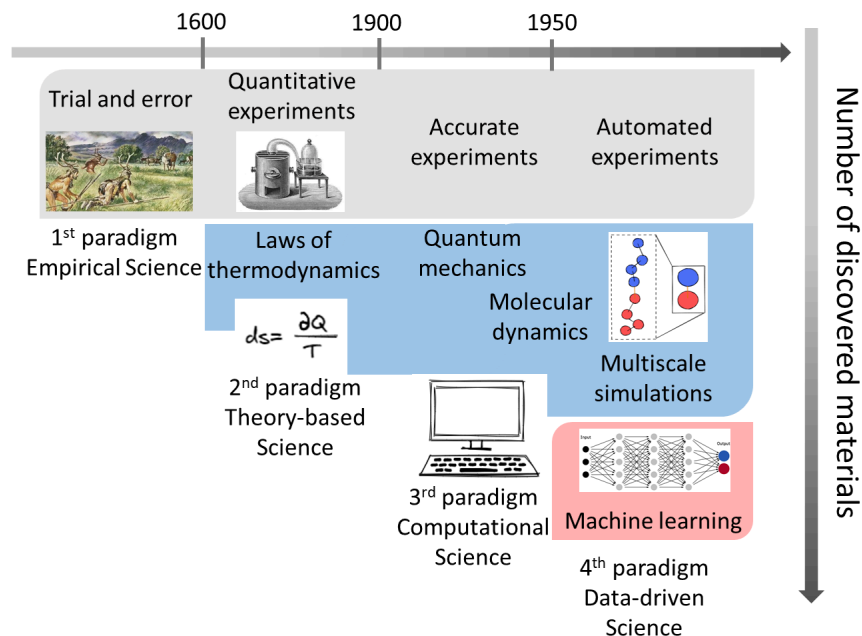


Figure 1.1: The four paradigms of science: empirical, theoretical, computational, and data-driven[1, 2].

In recent years, highly developed quantum chemistry methods could estimate many properties with increasing accuracy, such as band gaps, dielectric constants, refractive indices[8, 9]. However, it is still computationally unfeasible to solve the multi-electron Schrödinger equation for systems with more than thousand atoms sampled in nanoseconds[9]. Accordingly, classical atomistic force-field methods have been developed. In these atomistic force-fields, electronic interactions are usually approximated as simple potential functions from the high-accuracy reference models (e.g., ab initio quantum models) or experiments. However, it is still infeasible and often undesirable to simulate mesoscale systems with these atomistically detailed models[4]. The process of collecting many microscopic degrees of freedom into fewer larger ones is denoted as coarse-graining (CG)[5]. Furthermore, to make simulations at larger spatial-temporal scales (macroscopic) possible, it is appropriate to use continuum mechanics, which assumes that a material is a continuous medium. Then, a polymer can be described by an all-atom model, a united atom model (e.g., grouping carbon with its bonded hydrogen atoms), a bead-spring model with multiple monomers (e.g., dissipative-particle-dynamics (DPD) models[10]) or Kuhn segments per bead, or a single bead or volume element (e.g., continuum models)[11].

A key issue in multiscale simulation is constructing reliable force-fields or high-level CG models considering both the accuracy and the computational cost. For example, an empirical force field can provide a computationally cheap approach to address correct thermodynamics of a simple liquid. Still, it may not be reliable in systems involving chemical reactions, while more accurate methods like ab-initio MD provide reliable force fields, at the expense of a high computational cost[12]. The trade-off between computational cost and accuracy results in the demand for alternative approaches. In 2007, Behler and Parrinello[13] introduced a new kind of neural-network representation of DFT potential-energy surfaces, which is several orders of magnitude faster than DFT but keeps the same accuracy. After that, ML techniques have emerged as an alternative method for constructing effective interaction energies between particles in multiscale simulations[14–17]. The promise of ML is to predict forces and energies with accuracy arbitrarily close to the level of ab-initial methods, but with a much smaller computational cost[17].

Apart from the development of force-fields, two more aspects related to the mutual communication between simulation and ML, have been attracting enormous research attention: 1) evaluating structure-composition-property-performance relationships in a forward way; 2) designing materials with optimal performance on desired properties in the reverse direction, i.e., inverse design[2, 18]. The first aspect is the forward design of materials based on the availability of structure-property relation databases. However, this forward design is limited in the field of synthetic polymers, whose data banks are heterogeneous and often outright unavailable due to a general lack of rapid and parallelizable experimental techniques for measuring polymer properties[7, 19, 20]. One of the main advantages of combining simulations and ML is that a large number of simulation results can be used to form a pre-existing structure-property data set. The ML model is then trained based on this data set to predict properties of many new candidate materials, which can direct the experimental investigation to a very narrow region of the search space[7]. Moreover, identifying some properties (e.g., knotting and phase transition) in polymers and other soft materials is challenging due to the wide variations in microscopic degrees of freedom[21]. Machine learning, which is powerful in recognizing minute changes of a data set, has recently emerged as a powerful tool for recognizing various configurations generated from simulations, and identifying phases[21, 22] and knot types of polymers[23]. The second aspect is the inverse design, a promising approach for establishing an optimal set of structures and compositions of materials with the desired properties[7, 24]. In other words, it can actively search for unknown optimal materials instead of selecting materials with desired properties from multiple materials in the known space[2]. For example, Webb *et al.*[25] have combined coarse-grained polymer modeling, deep neural network model, and model optimization as a data-driven design approach for the chemical design of polymers outside the known range of properties.

Despite great success, a major criticism of ML referred to its “interpretability” still remain. ML algorithms are often treated as black boxes, which not provide us with “physical laws” and that their inner workings are usually outside our understanding[26]. For example, Ghiringhelli et al.[27] have argued that a prediction of new promising materials are doubtful if the scientific connection between descriptors and their prediction is unknown. Although the above controversy persists, there is a growing trend to agree that the interpretability of ML is a multifaceted concept, in which various facets have different priorities and can be addressed separately depending on the dataset and the research goal[26–28]. In the field of soft matter science, the fear that ML models are operating on unphysical principles, can be alleviated by post hoc analysis (e.g., attentive response map, descriptor importance measure)[29–32]. These techniques can reveal the connections between descriptors and target properties, and therefore increase the trust of ML models in our investigations. These discussions are related to bridging the knowledge gap between the two individual communities, i.e., physics-driven simulation and data-driven machine learning. Both communities have profound knowledge about the methods used in their particular fields[16, 33]. Necessary communications and combinations are important to break limits and accelerate the sustainable development of both communities. In this thesis, the key target is to investigate the structure–composition–property–performance relationships of soft materials by combining the multiscale simulations (from atomistic to mesoscale) and ML, both forward and reverse, as shown in Figure 1.2.

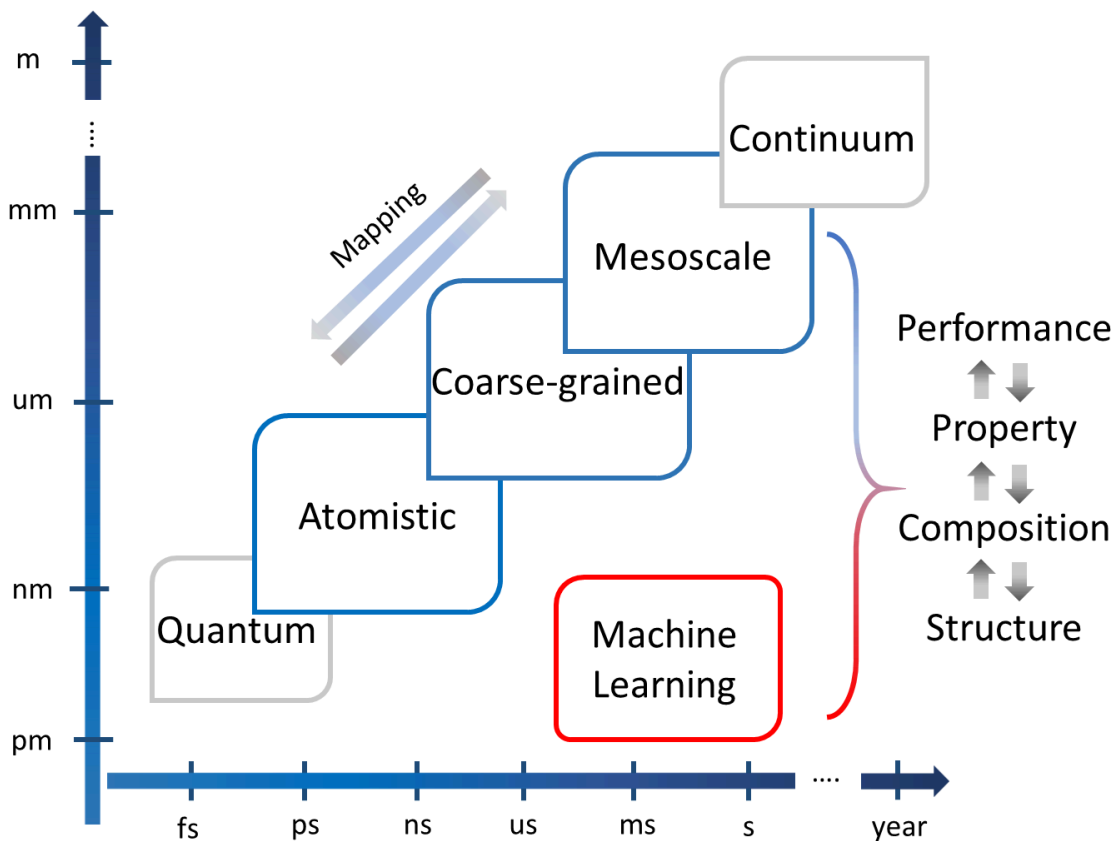


Figure 1.2: Schematic illustration of the key target in this thesis, i.e., forward and inverse evaluations of structure–composition–property–performance relationships of soft materials by combining the multiscale simulations (from atomistic to mesoscale) and machine learning.

1.2 Compatibilization

1.2.1 Background

It is common to mix existing polymers to produce new materials with low cost and specific properties[34–36]. An relationship exists between the miscibility of polymer blends and the Gibbs free energy of mixing $\Delta G_{\text{mix}} = \Delta H_{\text{mix}} - T\Delta S_{\text{mix}}$, where ΔH_{mix} and ΔS_{mix} are the enthalpy and entropy of mixing, respectively. A miscible polymer blend is associated with a negative value of the free energy of mixing ($\Delta G_{\text{mix}} \leq 0$), and within the phase stability condition $(\frac{\partial^2 \Delta G_{\text{mix}}}{\partial \phi_V^2})_{P,T} > 0$, where ϕ_V , T , and P represent the volume fraction, the temperature, and pressure, respectively[37, 38]. Miscible polymer blends are rather an exception than a general rule. Most polymers are immiscible or only partially miscible over certain compositions and temperature ranges resulting from the positive ΔH_{mix} and low magnitude of ΔS_{mix} . It is worth mentioning that ΔS_{mix} decreases as the molecular weight increases, resulting in the phase separation for a high-molecular-weight polymer[38]. The phase separation in polymer blends significantly affects their mechanical, thermal, optical, and physical properties[34, 38–40]. Hence, a major concern in the commercial use of polymer blends is the stabilization of the desired morphology, preventing the break-up of a co-continuous structure into disconnected domains[41–44]. The use of compatibilizers such as suitable block copolymers is a well-established approach in enhancing the performance of the immiscible and partially miscible blends, transforming the coarse morphology of the immiscible blend to fine morphology by reducing the interfacial tension[45–49]. Although the interfacial tension, a value from measurements, is relatively simple, the co-continuous structure is inherently thermodynamically metastable due to an interfacial-tension-driven coarsening phenomenon[38]. An example of this is the study carried out by Kirjava *et al.*, in which the improved stability and morphology of polypropylene/polyamide blends is related to the reduction in interfacial tension after the addition of compatibilizing copolymers. Moreover, the compatibilization efficiency of block copolymers of varying molecular weight and mass concentration in immiscible polymer blends, such as polystyrene/polyisoprene[50], polystyrene/polyethylene[51, 52], and polystyrene/poly (methyl methacrylate) blends[36], has been intensively investigated. A general conclusion from these works is that there exists an optimal molecular weight and mass concentration of copolymers to achieve their best compatibilization efficiency. This can be explained from two perspectives: 1) a part of the block copolymer molecules is trapped into micelles, and further addition of block copolymer yields no improvement above its critical micelle concentration[52]; 2) the existence of an optimal molecular weight is likely due to a trade-off balance between the ability of the block copolymer to diffuse into the interfacial region and its relative effectiveness as a compatibilizer. For example, Galloway *et al.*[52] have found that the middle-molecular-weight block copolymer has an intermediate compatibilization and diffusive efficiency, leading to its best overall performance among all block copolymers.

However, experimental measurements of the interfacial tension are usually time-consuming and cumbersome. Several theoretical models have been developed based on self-consistent field (SCF) theory to quantitatively predict the interfacial tension of incompatible blends as a function of chain lengths, temperature, and Flory-Huggins interaction parameter[53–55]. A simple expression relating γ to the Flory-Huggins interaction parameter χ and chain lengths l_A and l_B as follows:

$$\gamma = \gamma_{\infty} \left[1 - K \left(\frac{1}{\chi l_A} + \frac{1}{\chi l_B} \right) \right] \quad (1.1)$$

$$\gamma_{\infty} = \rho s k_B T \left(\frac{\chi}{6} \right)^{\frac{1}{2}} \quad (1.2)$$

where ρ is the density, K is a constant and s is the statistical segment size with $R_e^2 = n_m s^2$. For the statistical segment size, R_e^2 is the mean-squared end-to-end distance and n_m is the number of beads per chain[53, 56]. The constant value K is selected as $\pi^2/12 \sim 0.8$ and $2 \ln 2 \sim 1.4$ under different approximations from Broseta *et al.*[53] and Ermoshkin and Semenov[56], respectively. It should be noted that Ermoshkin and Semenov derived their model to better reproduce the properties of strongly-incompatible system, and the value of their K is comparable to other work[57] with the same aim. Kim *et al.*[58] found that values of interfacial tension obtained from above SCF models are similar to those of polystyrene/poly (methyl methacrylate) blends measured experimentally from both the Choi[59] and Paliarne models[60]. Investigations based on SCF theory are of great significance as they provide valuable insight into the prediction and mark the first theoretical attempt to assess the broader impact of properties (e.g., chemistry details and chain lengths) of polymer blends on their compatibility. However, most SCF studies are limited by various approximations and a failure to exactly address the property of compatibilized blend. These limitations include that the interplay of thermodynamics and coil structure in the interface is hard to treat correctly in the presence of compatibilizers; fluctuations near the critical point are difficult to account for[61]. For example, Govorun and Erukhimovich[62] proposed a predictive SCF theoretical model on the adsorbed interfacial area per diblock copolymer in homopolymer blends, which is, however, only suitable for the flat interface when the homopolymer chain length is long enough.

Computer simulations can avoid uncontrolled approximations in the system and provide valuable microscopic insights into the interfacial behaviors of the compatibilized blends. Müller *et al.* [61, 63] have reported a series of Mont Carlo simulations regarding several unclear effects (e.g., bond fluctuations) in previous SCF studies, on the segregation behavior of immiscible homopolymer blends. Groot and Warren[10] have established a link between DPD parameters and Flory–Huggins χ parameters for polymeric systems, and found that DPD simulation results match well with the experimental results[64]. Qian *et al.* [65] have performed DPD simulations, and summarized two conclusions for the compatibilization efficiency of symmetric diblock copolymers: a) long diblock copolymers show a better compatibilization efficiency because they can penetrate deeper into the homopolymer region as compared to short diblock copolymers at a constant number of copolymer molecules; b) the effect of volume concentrations on improving the compatibilization efficiency is more prominent for short diblock copolymers. Meenakshisundaram *et al.* [66] have found by MD that regular multiblock copolymers (constant areal concentration) with a different number of blocks exhibit different compatibilization efficiencies. Wang *et al.* [67] have addressed the issues of graft copolymers. They have demonstrated that the compatibilizing efficiency of the graft copolymer first increases, and then decreases with increasing the length of side chain, when the backbone length and number of side chains are fixed. Moreover, these computational methods have been strongly used to investigate the underlying compatibilization mechanisms of copolymers. Recall that the mixing behavior of polymer blends is correlated with the unfavorable ΔH_{mix} and low value of ΔS_{mix} . Regarding the unfavorable ΔH_{mix} , Ryu *et al.* [68] have investigated by MD the number of direct contacts between immiscible homopolymer beads in the presence of graft copolymers. They attribute the reduction in interfacial tension to the reduction of unfavorable contacts between the two immiscible homopolymer species, caused by the interfacial coverage of graft copolymers. In terms of the ΔS_{mix} , previous research findings reported almost consistently point towards the conformation of compatibilizers (e.g., the end-to-end distance, the radius of gyration, and the related stretching anisometry calculated from them)[40, 68–70]. For example, Sun and Guo[69] have demonstrated that the balance between the stretching normal to the interface normal direction and the expansion in the interface plane of copolymers are crucial for understanding the variation of their compatibilization efficiency.

1.2.2 Challenges and Objectives

Although, many experiments, simulations, and theories have been developed to predict the interfacial properties of immiscible homopolymer blends[49, 65, 66, 71–74]. Even the efficiency of most common symmetric diblock copolymers, cannot be predicted by a simple and general quantitative description from the realistic chemical details. As mentioned previously, there is a failure of theory to exactly address the properties of compatibilized blends and experimental measurements usually need long time. Hence, we want to investigate the mechanisms involved in the compatibilization process and provide a promising way to predict the compatibilization efficiency of linear block copolymer additives with different structures in their respective polymer blends:

- **Optimization of Compatibilization Efficiency of Linear Block Copolymers in Immiscible Homopolymer Blends**

Compared with linear block copolymers, graft copolymers have more complex branched molecular structures consisting of backbone and multiple side chains. Despite the success of many previous works[67, 75, 76], there has, to our knowledge, not been a comprehensive simulation-and-theory study looking at the general effect of the diversity in the molecular architecture of graft copolymers on the compatibilization efficiency with different chemical details. These previous works usually investigate the compatibilization efficiency of graft copolymers by keeping one or two of the above descriptors constant. An overall evaluation of the descriptors-efficiency (compatibilization) relationship of graft copolymers demands new approaches. Machine learning methods have proven to be successful in the investigation of material properties with multiple descriptors. Hence, we want to establish a prediction model considering the structure and conformation complexity of graft copolymers on their compatibilization efficiency with the assistance of ML. Moreover, the importance rank of different descriptors, which is extracted as the post hoc interpretability of ML models, can provide guidance for the further investigations:

- **Optimization of Compatibilization Efficiency of Graft Copolymers in Immiscible Homopolymer Blends**

1.3 Disinfection

1.3.1 Background

The nCoV-2019 outbreak has become a global pandemic[77, 78]. Most people worldwide are under some form of lockdown or be suggested to stay-at-home to minimize the sustained spread of the virus. Currently, rapid progress has been achieved in the development of safe and effective coronavirus vaccines and potential SARS-CoV-2 therapies[79–82]. However, a significant portion of the world's population remains unvaccinated. More worse, the new variants of SARS-CoV-2 may spread among vaccinated people. For example, a fast-spreading SARS-CoV-2 variant known as Omicron, has already shown its potential to evade vaccines and cause reinfections[83]. The mutations of SARS-CoV-2 variants are mainly in the Spike-protein, which is a major modulator of infectivity and immune evasion[83]. It is noted that the Spike-protein and other proteins are mechanically anchored by the host-derived lipid bilayer, which gives the virus its distinctive shape and structure, to protect its RNA from the surrounding environment (Figure 1.3 (a))[84–87]. Therefore, washing hands with sanitizer that disrupts the lipid bilayer of virus, remains a significant way to prevent the spread of SARS-CoV-2 (as well as its variants)[88, 89]. In this process, the deactivation of the

virus is mainly controlled by its lipid membrane permeability to alcohol, which can be simplified as Figure 1.3 (b). Among all lipid types, phosphatidylcholines (PCs) are the most important lipid components of living organisms. Specifically, they are the main components of the endoplasmic reticulum Golgi intermediate compartment (ERGIC), where coronaviruses are replicated and assembled[90, 91]. Additionally, the lung, the primary organ affected by the coronavirus, mostly uses dipalmitoylphosphatidylcholine (DPPC), i.e., one of PCs, as the abundant constituent of its surfactants[92]. As well as PCs (~50 %), the ERGIC of a mammalian cell contains smaller amounts of (~15-25 %) phosphatidylethanolamines (PEs) and (~10-15 %) phosphatidylinositols (PIs)[93]. It is worth mentioning that The PCs-, PEs-, and PIs-molecules have different head groups but the same hydrophobic tails[94], which consist of saturated and/or unsaturated acyl chains of various lengths.

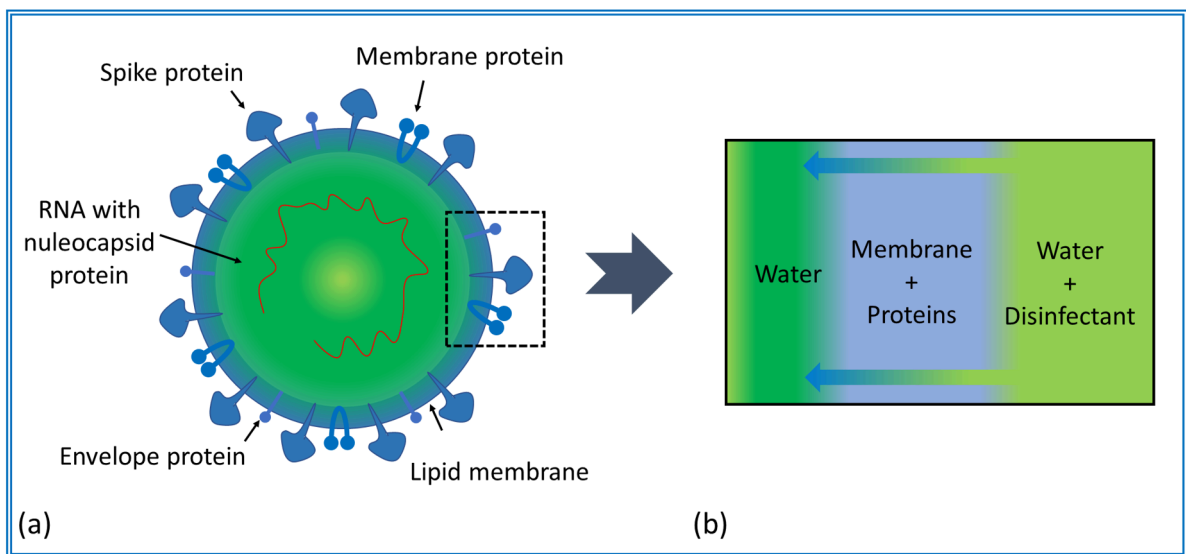


Figure 1.3: (a) Illustration of the structure of coronavirus replotted based on previous literature[84]. (b) Simplified schematic representation of the deactivation effect of disinfectant on the coronavirus model membrane.

1.3.2 Challenges and Objectives

The exact composition of the viral membrane is unknown and presumably changes between individual virus particles. Before proceeding to run simulations, it should be clarified which parameters are more important for the stability of membrane against alcoholic disinfectants. Previous experimental[95–98] reports show that the phase of the membrane, which in turn depends on the hydrocarbon tail length and its degree of saturation, is the main factor determining its stability. Hence, in our first simulation work[99], atomistic MD simulations are performed to investigate the stability of the liquid-crystalline and gel DPPC membranes in the presence of alcoholic disinfectants (n-propanol and ethanol). At a concentration of 10 mol % in the surrounding water, the DPPC membrane (323 K, liquid-crystalline phase) allows almost free passage of the disinfectant molecules. We reliably observe the disintegration of liquid-crystalline membrane at alcohol concentrations above 15 mol %. On the contrast, the gel-phase DPPC bilayer (298 K), is less permeable to alcohol because of the tight packing of lipid molecules. Although the same trend of alcohol weakening effects on the liquid-crystalline phase of the membrane is observed in the gel phase as well, the effect is

less pronounced[99]. Our work demonstrates the importance of the phase of the membrane on its stability against alcoholic disinfectants (Figure 1.4). Moreover, the coronavirus membrane anchors proteins. The presence of these proteins in the structure of the model membrane could possibly influence its stability against damage by ethanol. However, an atomistic study from the other team in our group, which is about the effect of the Envelope-protein on the stability of a mixed lipid bilayer, palmitoylsphingomyelin and palmitoyloleoylphosphatidylcholine, immersed in ethanol-water mixtures, shows that the E-protein has a negligible effect on the partitioning of water and ethanol from aqueous to lipid phase of the membrane (Figure 1.4)[100]. Recall that major lipids PC, PE, and PI have different head groups but share the same hydrophobic tail groups. These hydrophobic tails can be classified as saturated and/or unsaturated acyl chains of various lengths. Hence, the rest parameters that may control the stability of lipid membrane against alcoholic disinfectants, are summarized as the head group type, the tail length, and tail saturation degree of lipids.

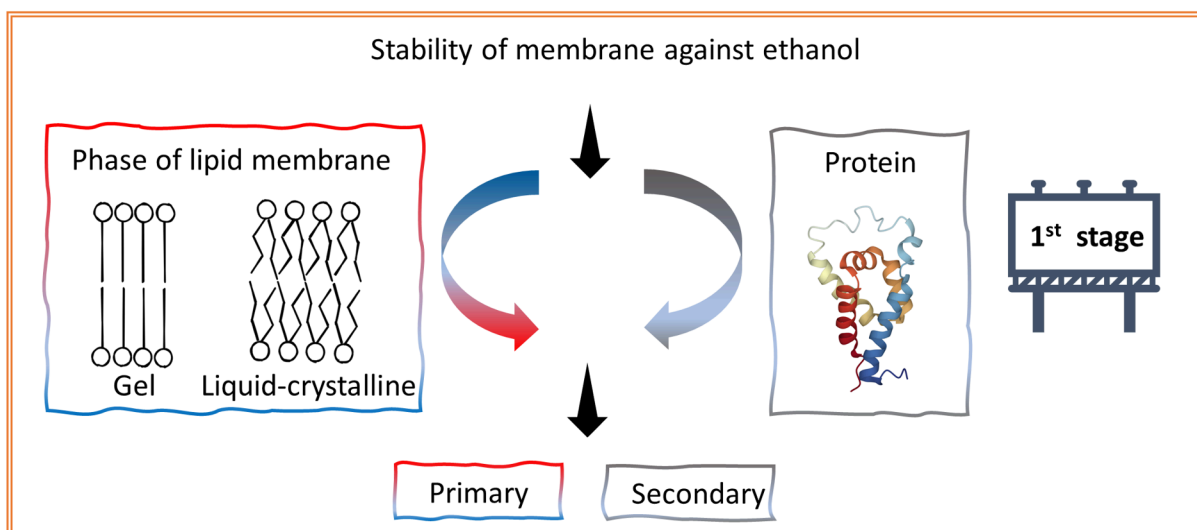


Figure 1.4: Schematic illustration of our first stage work on the stability of coronavirus model membrane against alcoholic disinfectants.

This leads to our second stage work included in this thesis, i.e., evaluating the alcohol-induced changes on coronavirus model membranes with different lipid compositions, as illustrated in Figure 1.5. The first challenge comes as how important these three aforementioned parameters are for the stability of lipid membranes against the damage of ethanol. Our previous atomistic simulation proves the connection between the stability of the membrane and its phase (gel or liquid-crystalline)[99]. Hence, we firstly compare experimental data[101] on the phases (stabilities) of PC-, PE-, and PI-membranes, of different hydrocarbon tail lengths with a different number of unsaturated bonds and would argue that the lipid head group does not have a dominant role in the phase behavior of the membrane. Besides, our previous atomistic simulation results show that the largest free-energy barrier for the passage of small molecules is observed very close to the center of the membrane at all concentrations[99]. Its height depends on the membrane thickness, i.e., the gap that a penetrant needs to cross[99]. It is found experimentally[102] that the thickness of the membrane depends nearly linearly on the length of hydrocarbon tail. In contrast, the type of the head group does not have a noticeable influence on the membrane thickness. Hence, it is the

hydrocarbon tails and their composition, which ultimately controls the membrane stability (Figure 1.5). This argument is also in line with previous atomistic simulations[103, 104] of the stability of membranes of pure palmitoyloleoylphosphatidylcholine (one of PCs) and phosphatidylethanolamine (one of PEs) at high ethanol concentrations. As mentioned previously, PCs are the main components of the ERGIC, where coronaviruses are replicated and assembled. The composition of ERGIC presumably resembles that of the viral coating membrane, since the viral genome does not provide for lipid manufacture. We then reasonably justify simulating mixed-PC membranes as coronavirus model membranes, to investigate their stability against disinfectants. Therefore, we select three PCs with different classes of hydrocarbon chains, namely DPPC (consisting of long saturated hydrocarbon chains), dioleoylphosphatidylcholine (consisting of long unsaturated hydrocarbon chains), and dimyristoylphosphatidylcholin (consisting of short saturated hydrocarbon chains) as the components of mixed lipid bilayers.

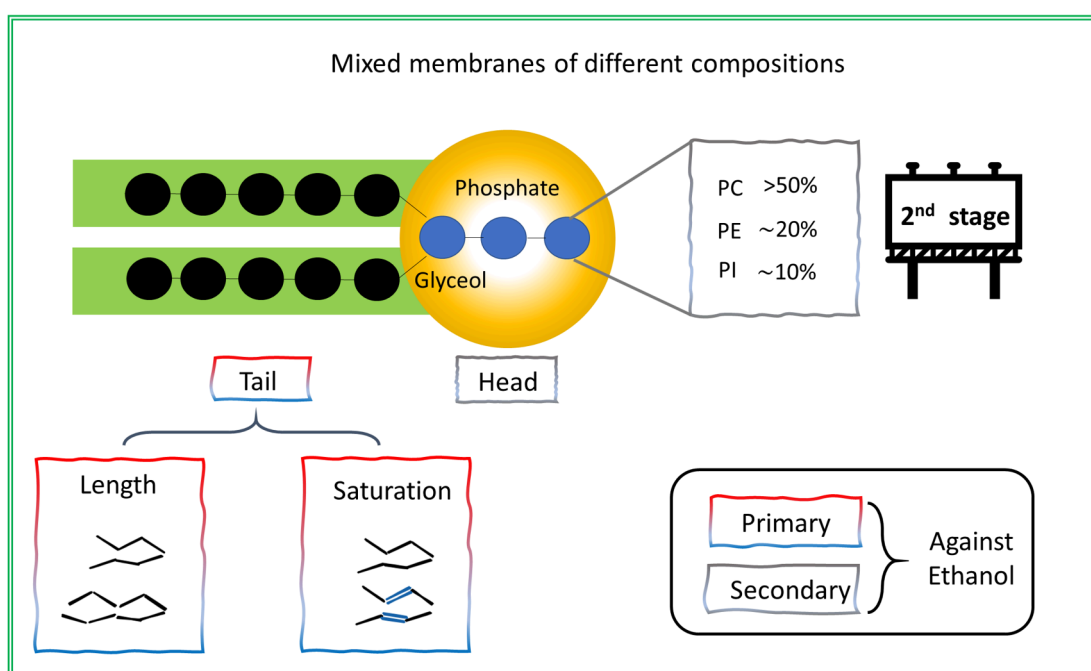


Figure 1.5: Schematic illustration of our second stage work on the stability of coronavirus model membrane against alcoholic disinfectants.

In principle, the widely used all-atomistic molecular dynamics (AA-MD) simulation can exactly provide insight into the links between structures and physical properties of lipid membranes. However, even a pure DPPC membrane of total 64 lipid molecules (surface area ~ 0.7 nm) sampled in 750 ns, needs several weeks on 12 CPU cores in our previous atomistic work[99]. Hence, it remains challenging to investigate the targeted mixed lipid membranes with different compositions by AA-MD simulation. The dissipative-particle-dynamics (DPD) simulation is a cheap coarse-grained method to handle complex systems with length and time scales beyond the molecular scales. DPD models of lipid molecules immersed in *pure* water are well developed in the literature[105, 106]. The remaining unclear point is the choice of proper interaction parameter between ethanol and lipid beads in the DPD simulation. We clarify this point by scanning the interaction parameter over the reasonable region given in the literature[106], against the free energy barrier for the passage of a single ethanol molecule across the membrane, according to our

previous atomistic simulation results[99].

Having defined the compositions of coronavirus membrane and selected the proper simulation method, the third challenge is how can we more robustly characterize the ethanol-induced intact-ruptured transition in these membranes. The ethanol-induced transition is not a sharp transition, which is time-consuming to characterize from plenty of visual inspections of the simulation profiles. There are many recent emphases on developing the framework between simulation and ML for identifying and quantifying phase transitions in soft materials systems[21–23]. Motivated by these studies, we want to investigate the underlying mechanisms of membrane failure in the presence of ethanol and characterize it by applying a hybrid simulation/deep-neural-network framework:

- **Optimization of Disinfection Efficiency on Coronavirus Model Membranes**

1.4 Heat Transfer

1.4.1 Background

The low thermal conductivity of polymeric materials ($0.1 - 0.5 \text{ W m}^{-1} \text{ K}^{-1}$)[107] is one of the major technological barriers for their applications in many fields. For example, the limited heat dissipation due to the low thermal conductivity may cause degradation and reduce the reliability and performance of polymeric products in energy storage and semiconductor fabrications[108, 109].

Over the past two decades, research aimed at enhancing the thermal conductivity of polymeric materials has emphasized the addition of highly conductive fillers, including graphite, carbon nanotubes as well as other inorganics[110, 111]. The thermal conductivity of fillers is much higher than that of polymers. For example, Balandin *et al.*[112] have reported a measurement of the thermal conductivity of suspended single-layer graphene around $5000 \text{ W m}^{-1} \text{ K}^{-1}$, which is one of the highest thermal conductivities of currently known materials. However, the thermal conductivity of composites such as graphene/low-density-polyethylene (LD-PE) composite ($\sim 1.4 \text{ W m}^{-1} \text{ K}^{-1}$)[113] is very low as compared to the filler. There are two possible reasons: 1) fillers used in nanocomposites are influenced by the process and therefore different from those pristine materials prepared for individual characterization of thermal properties. For example, graphene in a composite usually have some defects (e.g., Stone-Wales defect and vacancy defects), which could greatly reduce its effective thermal conductivity[110]; 2) Interfacial thermal resistance between the filler and soft matrix can greatly reduce the benefits from the high thermal-conductivity fillers, resulting in a low thermal conductivity of the composite[110, 111]. These two perspectives have been intensively discussed in our previous works[114, 115] with graphene embedded in a soft matrix, i.e., n-alkanes phase change material. Increasing the amount of filler is a common way to enhance the thermal conductivity of composites. However, large amount of fillers may cause the aggregation of them and also significantly increase the material cost[110].

On the other hand, looking for polymers with high intrinsic thermal conductivity has also attracted great interest. These approaches can be classified as two main classes. First, the intrinsic thermal conductivity can be enhanced by improving the order of chain alignment of polymers or engineering their molecular architectures (e.g., chain length). For example, the thermal conductivity of PE nanofibers can reach as high as $104 \text{ W m}^{-1} \text{ K}^{-1}$ after stretching[116]. The thermal conductivity of ultrahigh-molecular-weight polyethylene (UHMW-PE) has also been reported as $40 \text{ W m}^{-1} \text{ K}^{-1}$ [117]. Second, the spatial arrangement of chains can be tuned via blending different polymers. Kim *et al.*[118] have mixed poly(N-acryloyl

piperidine) (PAP) with poly(acrylic acid) (PAA), and found an optimum composition of PAP to enhance the thermal conductivity of PAA/PAP polymer blends to $\sim 1.7 \text{ W m}^{-1} \text{ K}^{-1}$. Although significant progress has been made in enhancing the intrinsic thermal conductivity of polymers, these methods suffer from several limitations: 1) tuning chain alignment can improve the thermal conductivity in the alignment dimension. However, an isotropic high thermal conductivity material is commonly more desirable[110]; 2) the application of high-molecular-weight polymers is limited due to their high viscosity and poor processability; 3) blending polymers to enhance the thermal conductivity is difficult, because of its complex synthesis conditions[110, 118]. Another limitation for the polymer blending is the possible phase separation, which has been discussed in the Section 1.2.

1.4.2 Challenges and Objectives

Apart from approaches motioned above, Wei and Luo found that the thermal conductivity of PE-polypropylene (PP) diblock copolymers can be changed by their block ratio[119]. This provides an opportunity to produce bulk polymers with a high thermal conductivity. Unfortunately, all reported thermal conductivities of diblock copolymers in their work are below that of the PE homopolymer. Since the monomer sequence has recently been reported to influence multiple material properties of block copolymers such as complex morphology[120], coil-collapse transitions[121], and electrostatic interactions[122, 123], there comes a question: Will a specific monomer sequence of copolymers enable a maximum thermal conductive efficiency?

To answer this question, we first need strategies to efficiently explore huge number of possible sequences. For example, it is 2^N permutations for a copolymer molecule of chain length N which has only two types of monomers. Although several sequence-defined polymers with limited chain length and chemistries have been synthesized[120, 124], it remains a challenge for polymer chemists to synthesize routinely sequence-defined polymers[6]. In contrast, molecular dynamics (MD) simulation is a valuable and powerful tool for these sequence-defined polymers. Advanced machine-learning algorithms are being increasingly interlinked with MD simulation to accelerate material design[25, 125–128]. Recently, Simmons and co-workers proposed a computational framework by integrating the genetic algorithm (GA) with the coarse-grained MD to design polymeric materials with target properties[129, 130].

In more specifics, the thermal conductivity can be calculated in a relatively short simulation time[131, 132]. Thus, it is an ideal test bed for trying out mutual couplings between MD and ML algorithms as compared to other properties. On the other hand, atomistic MD simulation is able to provide more insight into the details of processes such as the thermal energy transport via intramolecular interactions of polymers, which is hard to investigate by coarse-grained methods. Therefore, this section is also a test for combining ML with atomistic MD simulation, whereas all other sections use coarse-grained dissipative-particle-dynamics method. In short, we want to explore whether the inverse-design polymer sequence engineering is a promising approach for tuning the thermal conductivity or not, and to provide an example application of integrating atomistic MD modeling (with chemical details) with GA for computational material design:

- **Optimization of Heat Transfer Efficiency of Copolymers from the Perspective of Inverse Design**

1.5 Structure of this Thesis

The thesis is divided into four chapters. Chapter one conveys backgrounds and motivations of this thesis. Chapter two provides an introduction to the simulation techniques and machine learning algorithms involved in this thesis. Chapter three and Annex show research output including three peer-reviewed papers (Section 3.1, Section 3.4, and Annex) and two manuscripts under review (Section 3.2 and Section 3.3). Finally, a brief summary and conclusion are given in the fourth chapter. Several comments on the hybrid framework between simulations and machine learning methods have been provided then.

2 Method

2.1 Overview

In this chapter, the methods used in this thesis are introduced. The main simulation techniques employed, i.e., molecular dynamics (MD) and dissipative-particle-dynamics (DPD), have been well described in the literature. We refer the reader to several excellent treatises: introduction to MD[133]; review of DPD[134]; comparison between MD and DPD[135]; introduction to coarse-graining[5] and multiscale simulations[3, 4]. Moreover, machine learning (ML) methods have rapidly revolutionized scientific research over the last years. Although there are many excellent reviews on machine learning, it maybe still difficult for people to understand them easily due to the knowledge gap between ML and simulation communities. Here, we try to shed light on ML algorithms by comparing them with several traditional approaches that are usually used in the pure simulation investigations.

2.2 Molecular Dynamics Simulation

The molecular dynamics algorithm, which consists of the numerical solution of the classical equations of motion, could be written as:

$$\mathbf{f}_i = -\frac{\partial U}{\partial r_i} \quad (2.1)$$

$$\dot{\mathbf{r}}_i = \frac{\mathbf{p}_i}{m_i} \quad \text{and} \quad \dot{\mathbf{p}}_i = \mathbf{f}_i \quad (2.2)$$

where the derivative of the potential energy $\partial U/\partial r_i$ calculates the force \mathbf{f}_i acting on the i th atom with mass m_i , and the atomic momentum is \mathbf{p}_i . The step-by-step numerical integration of above equations can be performed with Verlet algorithm[136, 137]. The potential energy U in Eq.2.7 is usually expressed as the sum of the non-bonded and intramolecular potentials as:

$$U = U_{\text{non-bonded}} + U_{\text{intramolecular}} \quad (2.3)$$

The non-bonded interactions between atoms, $U_{\text{non-bonded}}$, is traditionally split into 1-body, 2-body, 3-body, and higher order terms. The 1-body term represents an externally applied potential field or the effect of a wall, which is usually not presented in periodic simulations of bulk systems. The Lennard-Jones potential is the most commonly used form for the 2-body pair interactions between particle i and j :

$$U_{ij} = 4\varepsilon_{ij} \left[\left(\frac{\sigma_{ij}}{r_{ij}} \right)^{12} - \left(\frac{\sigma_{ij}}{r_{ij}} \right)^6 \right] \quad (2.4)$$

where ε_{ij} and σ_{ij} are the Lennard-Jones interaction parameters between the atoms i and j ; r_{ij} is the distance between them. Moreover, three-body (and higher order) interactions are usually neglected. If electrostatic charges are present, the appropriate Coulomb potential U_{Coulomb} is added as:

$$U_{\text{Coulomb}} = \frac{q_i q_j}{4\pi\varepsilon_0 r_{ij}} \quad (2.5)$$

where q_i and q_j are charges of atom i and j , and ε_0 is the vacuum permittivity. For the intramolecular bonded interactions, the simplest molecular model include following terms:

$$U_{\text{intramolecular}} = U_{\text{bond}} + U_{\text{angle}} + U_{\text{torsion}} \quad (2.6)$$

where the bond-potential U_{bonds} controls adjacent pairs of atoms in a molecule; the angle-potential U_{angle} involve three atom coordinates; and the torsion potential U_{torsion} are defined in terms of three connected bonds, hence four atomic coordinates.

2.3 Dissipative-Particle-Dynamics Simulation

Dissipative particle dynamics is a coarse-grained particle-based simulation technique[10]:

1. Unlike the MD simulation, the DPD simulation involves potentials of a form independent of the physical system. Hence, the relation of natural DPD length and time scales to physical units needs to be established, i.e., mapping process[135].
2. Like the MD simulation, the motion of the DPD particles is governed by classical equations of motion. However, these forces on the DPD particles are not solely given by conservative interactions. The force f_i acting on a DPD bead i consists of pairwise contributions of a conservative force \mathbf{F}_{ij}^C , a dissipative force \mathbf{F}_{ij}^D , and a random force \mathbf{F}_{ij}^R as[10, 135]:

$$\mathbf{f}_i = \sum_{ij} (\mathbf{F}_{ij}^C + \mathbf{F}_{ij}^D + \mathbf{F}_{ij}^R) \quad (2.7)$$

The dissipative force $\mathbf{F}_{ij}^D = -\eta w^D(r_{ij})(\mathbf{e}_{ij}\mathbf{v}_{ij})\mathbf{e}_{ij}$ and the random force $\mathbf{F}_{ij}^R = \sigma w^R(r_{ij})\xi_{ij}\Delta t^{-0.5}\mathbf{e}_{ij}$ act together as a thermostat, where η and σ are the friction parameter and the noise amplitude with $\eta = \sigma^2/2k_B T$; $\mathbf{r}_{ij} = \mathbf{r}_i - \mathbf{r}_j$, $r_{ij} = |\mathbf{r}_{ij}|$, and $\mathbf{e}_{ij} = \mathbf{r}_{ij}/r_{ij}$; $w^D(r_{ij})$ and $w^R(r_{ij})$ represent the r -dependent weight function for the dissipative and random forces, respectively; ξ_{ij} is a *Gaussian* random number with zero mean for each interaction pairs of beads at each timestep Δt . It is noted that $w^D(r_{ij}) = [w^R(r_{ij})]^2$ and $\sigma = 3$ are used in the general DPD work. The non-bonded conservative force $\mathbf{F}_{ij}^C = \alpha_{ij}(1 - r_{ij}/r_c)\mathbf{e}_{ij}$ ($r_{ij} < r_c$) is purely repulsive and it is defined by the repulsion parameter α_{ij} . In general, the repulsion parameter between different species A and B, α_{AB} , has been related to their Flory-Huggins parameter χ_{AB} as[10]:

$$\alpha_{AB} = \alpha_{AA} + 3.27\chi_{AB} \quad (2.8)$$

Following Groot and Warren's suggestion for a system with a number density of $3r_c^{-3}$, the non-bonded repulsion of like interactions is expressed as $\alpha_{AA} = \alpha_{BB} = 25 k_B T r_c^{-1}$ (as used in Section 3.1 and 3.2),

where r_c is the cutoff distance of the conservative non-bonded force \mathbf{F}_{ij}^C . In order to match the realistic systems, the parameters used in DPD simulations such as repulsion parameters, the bead volume, and bead mass can be obtained from the mapping process (as shown in Section 3.3).

2.4 Mutual communications between Simulation and Machine Learning

2.4.1 Forward Evaluation of the Structure-Property Relationships

Generally speaking, machine learning can be divided into supervised learning, semi-supervised learning, unsupervised learning, and reinforcement learning[26]. The supervised learning aims to find a function that predict unknown properties from known inputs, which can be further divided into two categories as “classification” and “regression” algorithms. Typical classification algorithms are Gradient Boosting[138] and Random Forest[139] algorithms. We use them to predict the compatibilization efficiency of graft copolymer in immiscible homopolymer blends (Section 3.2). Common regression algorithms are neural networks[140], Gaussian process regression[141], and support vector machines[142]. In this thesis, we use the deep-neural-network to characterize the state of lipid membranes (intact and disrupted) immersed in ethanolic disinfectants (Section 3.3). It is worth mentioning that there are two excellent review on these algorithms[26, 143]. We start with a brief introduction of two important terminologies in ML, namely, data split and optimization of hyperparameters.

Data split: In principle, a ML model can memorize every data point with the given data set, and thus result in unrealistic high accuracy if we use the trained ML model to predict properties of the given data set. In order to evaluate the real prediction accuracy, the trained ML model must be tested on a new data that have not been used for the training process. Hence, we need to split the obtained simulation results at the first step into “training” and “testing” dataset (Figure 2.1 (a)). More exactly, the size of training and testing can be evaluated with the learning curve approach, which has been well implemented on ML packages (e.g., Scikit-learn[144] and PyTorch[145]). Usually, there is a plateau when we plot the learning curve score versus the training data size (Figure 2.1 (a)). However, it should be noted that hyperparameters (see the next paragraph) of applied ML models are not optimized at this step. Hence, It is common practice to split the simulation results into 70% training and 30% testing set in the first step[146]. This split (70% training and 30% testing set) needs to be rechecked by the aforementioned learning curve after the optimization of hyperparameters.

Optimization of hyperparameters: In ML, a hyperparameter is a parameter whose value controls the inner learning (training) and prediction process[147, 148]. Maybe a good example to understand the hyperparameters from the view of simulation is: the timestep or any thermostat parameters (e.g., temperature/pressure damping parameters), which should be carefully and reasonably chosen to obtain correct simulation results, are “hyperparameters” in simulation. In contrast, the temperature and pressure themselves are not “hyperparameters”. Also, the fitting parameters like a and b in a linear regression $y = a \cdot x + b$ are not hyperparameters (linear regression also belongs to ML algorithms[149]). Different ML algorithms require different hyperparameters. Given the optimized hyperparameters, the ML algorithm can build the final prediction model.

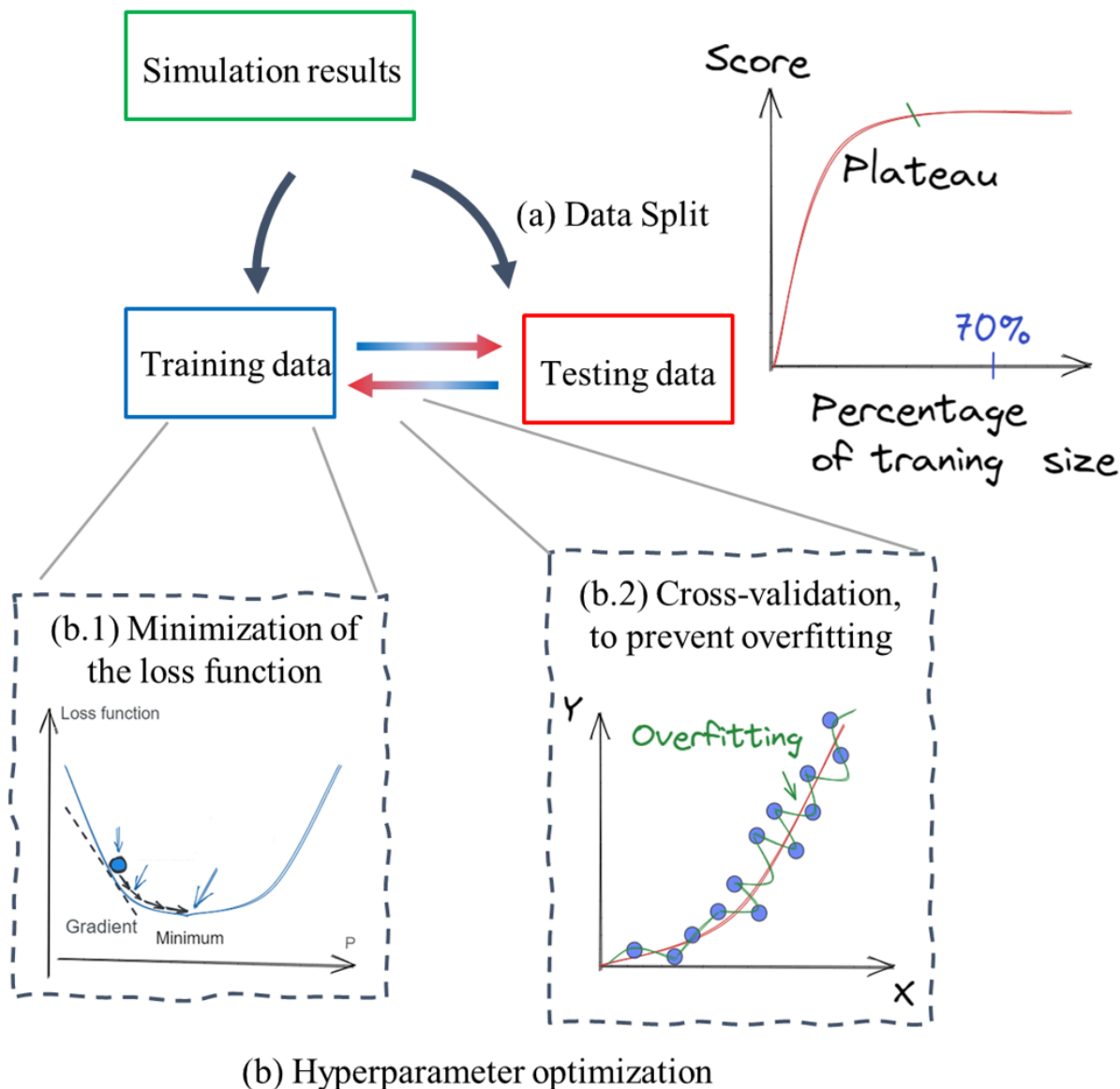


Figure 2.1: Schematic illustration of (a) data split and (b) the optimization of hyperparameters in machine learning.

In this thesis, the optimization of hyperparameters is based on the score of the determination coefficient (R^2) obtained from the cross-validation grid search method (Figure 2.1(b)). As we mentioned previously, the ML model can represent well ‘the given data in principle. A typical overfitted model (the green line) is shown in Figure 2.1 (b.2). It matches too well with the training data and is likely to have a higher inaccuracy on the testing data or any other related data than a regular fitting (the red line). This overfitting phenomenon is prevented by the “cross-validation” process between training data and testing data in the aforementioned

cross-validation grid search optimization process. This method defines a search space, whose dimensions are represented by the targeted hyperparameters and whose scales are determined by the values of these hyperparameters. Consequently, each point in this space is a combination of the hyperparameters with specified values and stands for a model configuration[148]. The search then calculates the scores of R^2 for all the points in the search space and provides the optimum value. The R^2 , which measures the proportion of the variation of one variable that can be predicted by other variables, is mathematically described as follows:

$$R^2 = 1 - \frac{\sum_{i=1}^p (y_i - f_i)^2}{\sum_{i=1}^p (y_i - \bar{y})^2} \quad (2.9)$$

where y_i and f_i represent the “real” results in the data set and the predicted values from ML models, respectively; p is the number of data points in the search space. During this process, the loss function of ML models regarding the training data is minimized to improve the prediction accuracy on training data (Figure 2.1 (b.1)). The loss function is usually defined as the residual between the “real” results and ML predictions. It can be summarized as: (1) the simulation results are first divided into two parts, one as the training set and one as the testing set; (2) the training set is used to train several ML models by minimizing the loss function. (3) each model is evaluated on the testing set by the cross-validation to select the model with the best R^2 . The minimization of the loss function will be discussed in details in the next Section with gradient boosting algorithm.

- **Classification process**

In this section, the gradient boosting (GB) algorithm is used to predict the interfacial tension γ of immiscible homopolymer blends with the addition of graft copolymers. The entire DPD model results contain several predictors: three predictors related to molecular architectures (Figure 2.2 (a)), namely the number of graft side chains (n_s), the length of each graft side chain (l_s) and the backbone (l_b); and the repulsion parameter α_{AB} , which is related to the chemical difference of the two polymers (Figure 2.2 (b)). These descriptors are initially considered as influencing the interfacial tension of systems.

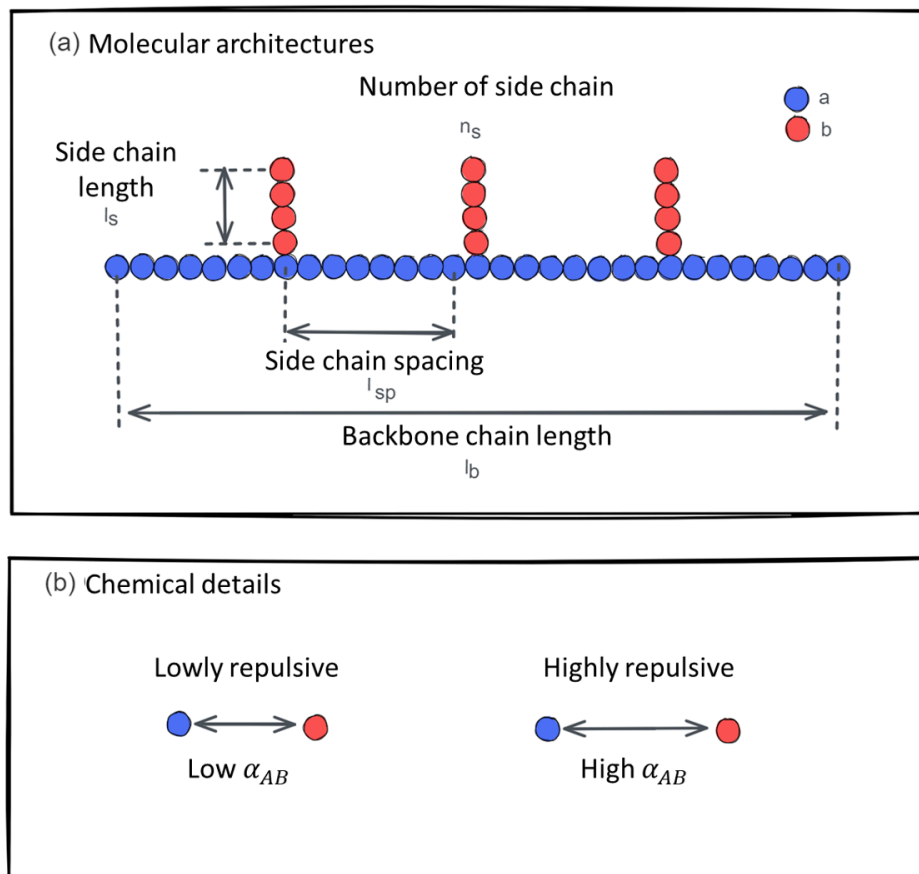


Figure 2.2: (a) Schematic illustration of the molecular architectures for one regular graft copolymer with 31 a type beads in the backbone and 12 b type beads in 3 side chains. The blue and red represent the type a and b beads in the copolymer compatibilizers, respectively. (b) Schematic illustration of the chemical details that is related to the repulsion parameter α_{AB} in dissipative-particle-dynamic simulation. This repulsion parameter α_{AB} is related to the Flory–Huggins χ_{AB} parameters as $\alpha_{AB} = 25 + 3.27\chi_{AB}$ in the general systems.

In an empirical way (Figure 2.3), we first need to assemble these descriptors into a descriptors-ensemble P . Then, we need to find a function to predict the interfacial tension based on P . One example of this approach is the process that we derive manually the power-law function to predict the interfacial tension

of linear block copolymers in Section 3.1. However, this approach is laborious and may not be accurate for graft copolymers, which are complex with more architecture descriptors.

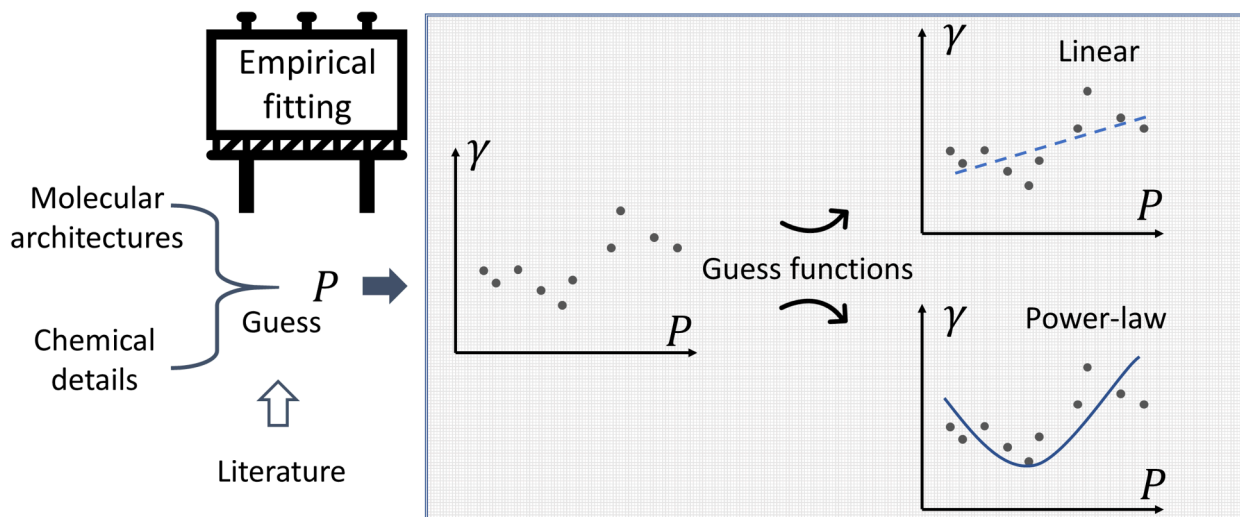


Figure 2.3: Flow chart of an empirical fitting process.

The compatibilization efficiency of graft copolymers can be investigated more robustly by the assistance of ML algorithms. Here, the GB mode, which gives the best prediction accuracy in section 3.2, is illustrated as an example. The GB model builds its estimators sequentially. The estimator is where the ML does one split (classification) progress based on the input data, and “sequentially” means that the n^{th} estimations are built by considering the results of previous estimators (Figure 2.4 (a)). A simple but basic example is like: 1) suppose there is a system with a true value of 10, and the first estimator of GB model predicts 5, the loss (residuals) between true and prediction is then $10 - 5 = 5$; 2) this loss value of 5 is used further as the optimization target for the next estimator, and if the second estimator makes a prediction as 3, the combination of these two estimators predicts $5 + 3 = 8$, and so on. The schematic illustration of the GB model is shown in Figure 2.4 (a). The average of all simulated interfacial tension values is set to be the prediction of the initial estimator as γ_{init} . The loss $\text{Loss}_{\text{init}}$ between this prediction γ_{init} and the actual γ are calculated as $\text{Loss}_{\text{init}} = \gamma - \gamma_{\text{init}}$. The first estimator is then built by separating the descriptors as an ensemble set P (called as “classification” in ML), to minimize the loss $\text{Loss}_1(P)$. As shown in Figure 2.4 (b)), given descriptors could be separated into different ensembles. For example, we can separate the interfacial tension of graft copolymers based on their backbone length in the first estimator, and say that, graft copolymers with more than 31 beads in their backbone have the same interfacial tension value as 0.5 and others have 2. Of course, the predicted interfacial tension value $h_1(P)$ of such classification is not accurate. The GB algorithm compares all $h_1(P)$ from all possible classifications, and chooses the best one that provides the lowest value of $\text{Loss}_1(P)$ in the first estimator. The loss function in the ML model is therefore minimized as shown in Figure 2.4 (c), and can be mathematically described as:

$$\text{Loss}_n(P) = \gamma - (\nu \cdot \text{Loss}_{n-1} + \gamma_{n-1} + h_n(P)) \quad (2.10)$$

$$\gamma_n = \gamma_{n-1} + \text{argmin}_{h_n(P)}(\text{Loss}_n(P)) \quad (2.11)$$

where n represents the current number of the decision tree. The learning rate ν ($\sim 0 - 1$) reduces the contribution of each estimator on the final prediction to prevent overfitting and improve the prediction accuracy. It is worth mentioning that the learning rate ν and the number of descriptors used for the classification process are typical hyperparameters. More details can be found in Section 3.2. Actually, except the classification process, the GB algorithm is roughly similar to the energy minimization process with the gradient descent approach used in the simulation.

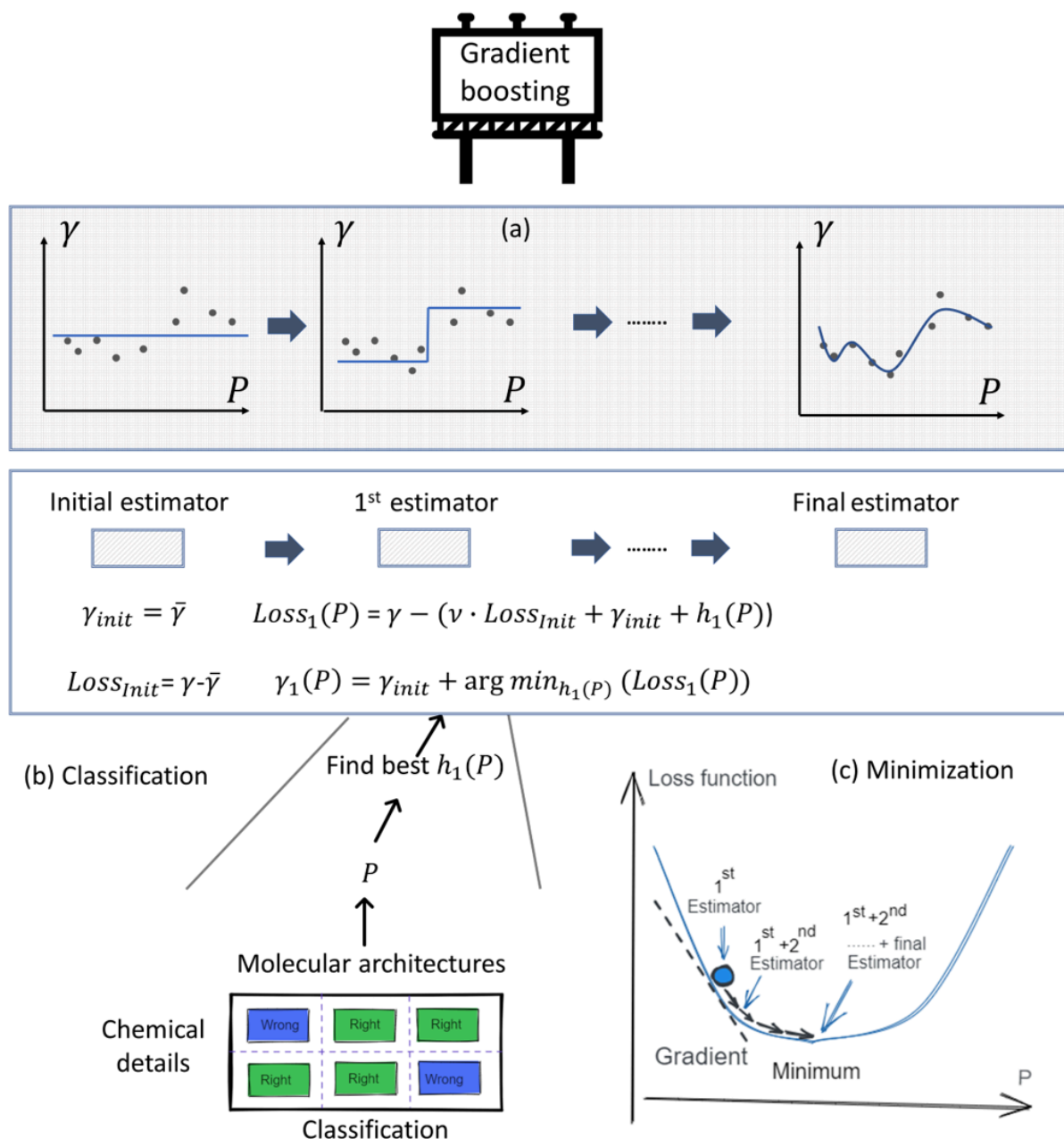


Figure 2.4: Flow chart of (a) the gradient boosting (GB) model, and its (b) classification process and minimization process of the loss function.

- **Regression process**

There are many thermodynamic properties (Figure 2.5 (a)), such as the area per lipid and the orientational order of lipid tails, to describe lipid membranes. However, these parameters are usually calculated by averaging over the simulation time or the number of data points. This simple average process may result in information loss. Moreover, these properties are not necessary to have a one-to-one correlation with the state of the whole lipid membrane since they are “specific” properties. For example, the area per lipid is more related to the behavior of lipid head groups but ignores most contributions from lipid tails. On the other hand, visual inspection of all simulation profiles is not practical due to the time-consuming, especially in the case of large number of simulation systems.

The deep neural network (DNN) can be used to map all particle coordinates, which we collected during the simulation, to state variables, which quantitatively represent the membrane being intact or disrupted (Figure 2.5 (b) and (c)). In the training process, we only use the intact and ruptured states of pure membrane containing one type of lipid molecules to label the trained models. The “label” (intact or disrupted) means how we pre-name the output of trained models depending on different membrane states. Then, we combine these trained models to predict the integrity of all pure and mixed membranes with various ethanol concentrations, and characterize the intact-to-ruptured transition point. As depicted in Figure 2.5 (b), the DNN is a standard feed-forward network composed of fully-connected layers, in which the data flows from the input layer through the hidden layers towards the output layer. Each layer has a certain number of nodes, called neurons, which store information about the importance of the input and associations between the importance of combinations of inputs. The “fully-connected” means that each neuron is connected to all other neurons of the previous and following layers. In all layers, linear operations (regression) are applied to the input data. Recall the GB model, in which we try to minimize the loss function by doing different classifications in each estimator. Similarly, the build of different layers (regression) also aims to get the minimal loss function in the DNN model. The training process is stopped when a reasonably low value of the loss function is reached, and it does not decrease significantly in further runs. To prevent overfitting and to improve generalization error, the dropout technique, which randomly drops out neurons (and their connections) during training, is implemented in our DNN model with a dropout rate of 0.2. This dropout rate indicates that there are 20% neurons that are randomly deactivated in each hidden layer. More details can be found in Section 3.3. Furthermore, the expression “deep” in deep neural network is one example of nomenclature that may confuse simulation experts. Some people call their neural networks with one or two fully connected hidden layer as deep learning. This misrepresents the purpose of deep-learning algorithms that can not be achieved with the number of neural network layers less than three.

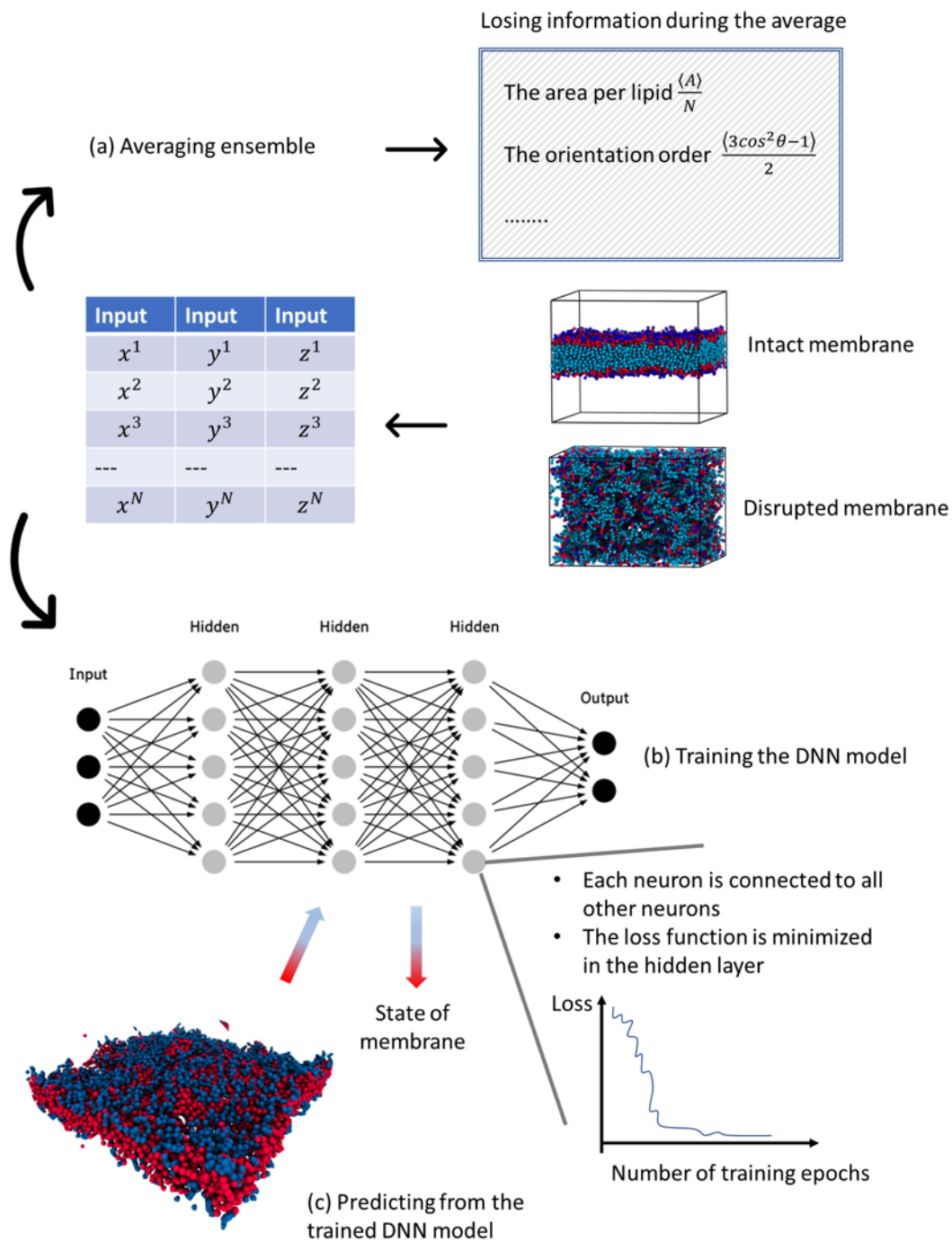


Figure 2.5: (a) Schematic illustration of the traditional thermodynamic properties of lipid membranes. Schematic representation of the (b) training and (c) predicting processes of the state of membrane by using deep-neural-network (DNN). The Cartesian coordinates of lipids are fed as input data to the DNN model. The loss function of DNN model is minimized in the hidden layers.

2.4.2 Inverse Design of Structure by Using Genetic Algorithm

In the previous section, We have discussed the approaches to directly evaluate the structure-property relationship based on the generated data from simulations. It is worth mentioning that the process to “generate data” in simulations can also be optimized. In the traditional way, we can screen all possible candidates to produce the target material with high performance on a desired property. However, this approach consumes plenty of computational resources. The second approach (Figure 2.6) is to initially select a few candidates and then run simulations on them. Based on the first round of simulations, we do the analysis (or inspired from the literature) to select/guess new candidates with possibly higher performance. This approach is more efficient but possibly needs to repeat the manual screening process for many times.

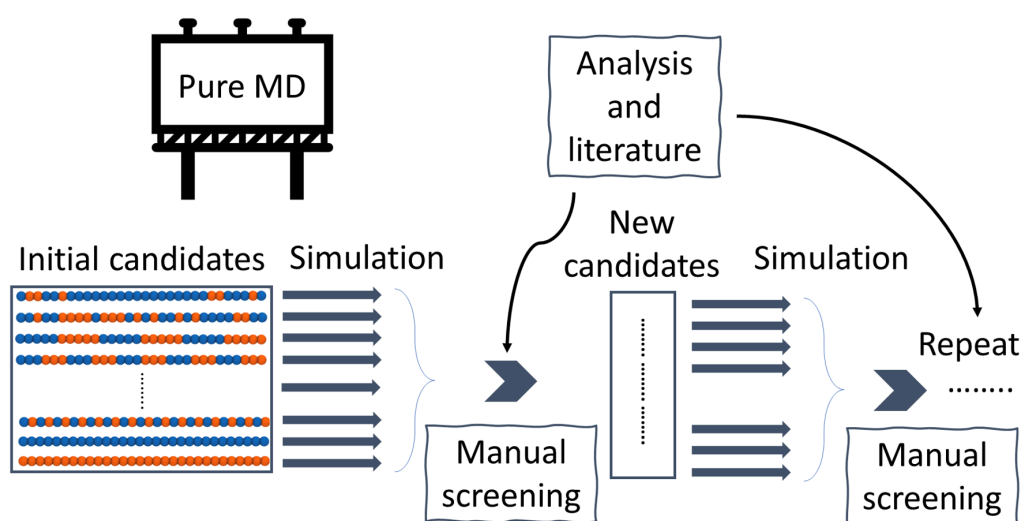


Figure 2.6: Flow chart of the molecular dynamics (MD) simulation with manual screening.

This repeated manual screening process was replaced by the genetic algorithm (GA). The framework between simulation and GA can automatically inversely design the structure of optimal candidate based on our target property, i.e., thermal conductivity. The general idea of GA is to mimic the evolutionary biological selection process to optimize the properties of systems. In this work, the fitness assessment (evaluation of properties) of the GA is conducted via MD simulations. We employ a mapping scheme of polymer sequences to binary genomes in which “0” and “1” represent a polypropylene (PE) monomer and a polyethylene (PP) monomer, respectively, as illustrated in Figure 2.7. An automated protocol performs these fitness evaluations of 30 candidates (MD simulations) simultaneously. After determining the fitness score, a new population with a distribution biased towards higher fitness-score members compared with the previous population is generated by performing three genetic operations, namely, selection, crossover, and mutation (Figure 2.7). Roulette wheel selection is used to select the parents for generating new candidates in the next generation. The crossover operation combines the selected parents to produce new offspring. Since stronger (with high performance) individuals are being selected more often, there is a tendency that the newly generated individuals may become very similar after several generations. The diversity of the population may decline, resulting in the population stagnation. Mutation is a mechanism to inject diversity into the population and to avoid stagnation. These three operations are iterated until the target properties

are achieved, or the maximum number of generations is reached. In more detail, the selected parents are combined via the uniform crossover with a probability of 0.8, in which the child genes are obtained by mixing “father’s” genes with “mother’s” genes at a probability of 0.8. Subsequently, point mutations at a rate of 0.01 per gene are applied to the new candidate in the next generation. For instance, a PP monomer has a probability of 0.01 to be changed into a PE monomer during the point mutation procedure.

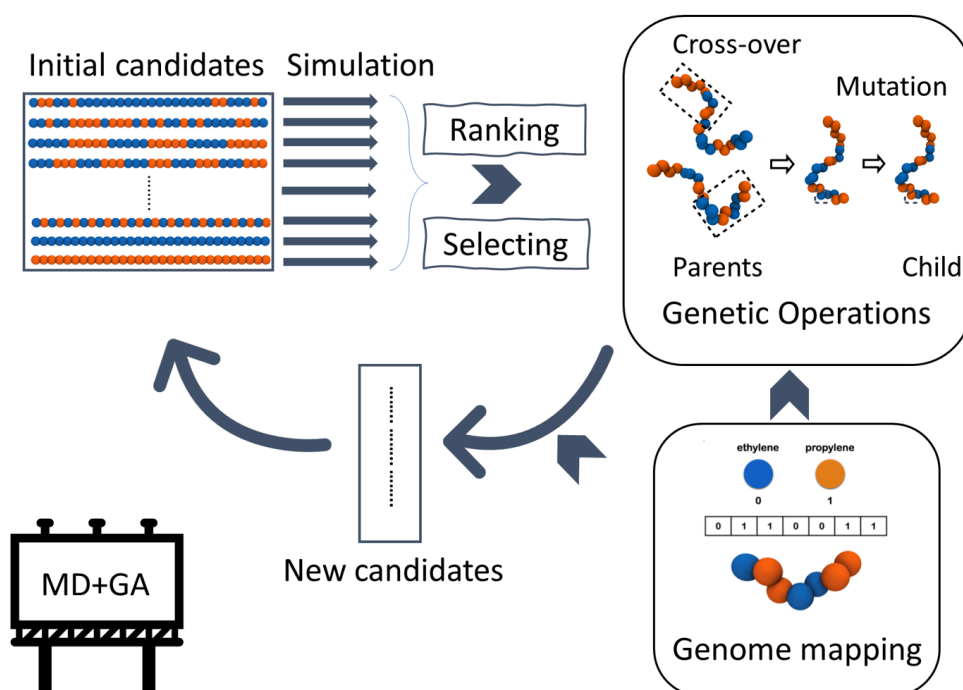


Figure 2.7: Flow chart of the automatic molecular-dynamics-based genetic algorithm (GA) used in this work: Genome mapping; Genetic operations; Evolution processes.

It should be noted that the standard GA, used in artificial intelligence or economics community[150], might reach hundreds to thousands of generations, with each generation composed of a population of tens of individuals (constant through the course of GA). This is too “expensive” for molecular simulation, especially for polymer investigations with chemical details. Accordingly, we use the single candidate elitism[150], in which the candidate with the highest fitness score (highest thermal conductivity k) is cloned to the next generation without any modification. Also, we storage results of all MD simulations in the GA dataset to minimize the number of MD simulations required. The simulation results are reused when a candidate generated from genetic operations is found to repeat from prior generations.

3 Results

3.1 Optimization of Compatibilization Efficiency of Linear Block Copolymers in Immiscible Homopolymer Blends

Reproduced with permission from Zhou et al. [Macromolecules 2021, 54, 20, 9551–9564] Copyright 2021 American Chemical Society.

Compatibilization Efficiency of Additives in Homopolymer Blends: A Dissipative Particle Dynamics Study

Tianhang Zhou, Jurek Schneider, Zhenghao Wu, and Florian Müller-Plathe*

Cite This: *Macromolecules* 2021, 54, 9551–9564

Read Online

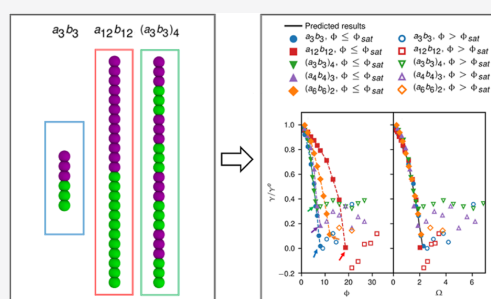
ACCESS |

Metrics & More

Article Recommendations

Supporting Information

ABSTRACT: We study the compatibilizing effect of copolymers of different architectures on the interface between two incompatible polymer phases by dissipative particle dynamics. Three base polymer systems are investigated, namely weakly incompatible (interspecies repulsion parameter of the dissipative particle dynamics interaction α_{AB} : $25 < \alpha_{AB} < 30$), intermediate-incompatible ($30 \leq \alpha_{AB} < 40$), and strongly incompatible systems ($\alpha_{AB} \geq 40$). We find that the compatibilization efficiency of all regular block copolymers in strongly incompatible systems can be predicted by a power-law function, which contains the Flory–Huggins interaction parameter, the areal concentration, and the mean block length of the compatibilizer. Regular multiblock copolymers have better compatibilization performance compared to the symmetric diblock copolymers at the same areal concentration. This is because smaller amounts of the multiblock copolymer are required to saturate a given interfacial area. For asymmetric diblock copolymers in strongly incompatible systems, we find additionally that the length of the shortest block is a more important determinant for the compatibilization efficiency than the ratio of block lengths. Our work reveals the involved mechanisms of the compatibilization process, and it provides a promising route to predict the compatibilization efficiency of differently structured copolymer additives in the respective polymer blends.



INTRODUCTION

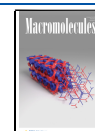
Blending the existing polymers is one process to produce new materials with low cost and specific properties.^{1,2} However, most combinations of homopolymers are immiscible and have high interfacial tension. The most effective way to control the interfacial tension of immiscible blends is by adding compatibilizers.^{3–5} The compatibilization efficiency is defined as the scaled quantity $\frac{\gamma}{\gamma_0} - 1$, where γ_0 is the interfacial tension

of the uncompatibilized homopolymer blend and γ is the interfacial tension of the homopolymer blend in the presence of a compatibilizer. It reaches from 0 (compatibilizer does not reduce the interfacial tension) to -1 (compatibilizer removes the interfacial tension completely). Block copolymers,^{3,6–9} random copolymers,^{10–12} comb/brush copolymers,^{13–16} Janus nanorods,^{17–19} and copolymer-grafted nanoparticles^{20–22} have been investigated as compatibilizers in recent years.

Several models have been developed to quantitatively predict the interfacial tension of monodisperse uncompatibilized homopolymer blends as a function of chain lengths, temperature, and the Flory–Huggins interaction parameter based on self-consistent field (SCF) theory.^{23–25} For the compatibilization efficiency of block copolymers, Noolandi and Hong²⁶ have developed a theoretical model based on SCF theory and demonstrated that at low concentrations the interfacial tension decreases linearly with the concentration of

copolymers. Meenakshisundaram et al.²⁷ have found by molecular dynamics simulations that regular multiblock copolymers with different number of blocks exhibit different compatibilization efficiencies. However, there is still no simple and general quantitative description to predict the compatibilization efficiency of copolymers by considering the realistic chemical details, even for the most common copolymers—symmetric diblock copolymers. On the other hand, Ryu et al.⁶ have investigated the number of direct contacts from unlike beads at the interface in the compatibilized systems. They attributed the reduction of interfacial tension by the addition of compatibilizers to the decreasing number of unfavorable contacts. The ratio between chain extension, parallel and perpendicular to the interface, has also been proven to be significantly correlated with the compatibilization efficiency of copolymers.^{6,10,19,28} However, relationships between the interfacial tension and the above parameters are restricted to selected types of copolymers only, mainly symmetric diblocks.

Received: May 17, 2021
Revised: September 26, 2021
Published: October 8, 2021



It is, therefore, desirable to find one critical parameter, which can be used to universally correlate the variation of interfacial tension with the molecular architecture of many different copolymer additives.

In this work, we employ a relatively cheap computer simulation method, dissipative particle dynamics (DPD),²⁹ which, if carefully parameterized, is able to provide meaningful microscopic and mesoscopic interfacial properties of homopolymer blends in the presence of compatibilizers.^{8,30–32} Moreover, the parameters used in DPD simulations such as repulsion parameters α , the bead volume V_p and bead mass m_i can be obtained from atomistic molecular dynamics (MD) simulations^{30,33,34} or quantum-chemical methods like the conductor-like screening model for real solvents (COSMO-RS),³⁵ which incorporate chemical details. This provides a way to quantify the model and allows realistic modeling.

Here, we first investigate by DPD simulations the interfacial properties of uncompatibilized homopolymer blend systems as references and we study how the chain lengths, chain-length ratio, volume-fraction ratio, and the unlike DPD repulsion parameter α influence their interfacial tensions. Second, we calculate the compatibilization efficiency of symmetric diblock copolymers and regular multiblock copolymers. From these, we derive a phenomenological analytical model. Third, we attempt to understand this theoretical model in terms of density distributions, chain conformations, and unfavorable contact of the homopolymer blend. We lastly investigate unsymmetric diblock copolymers to find the decisive factor, which influences their compatibilization efficiency.

■ SIMULATION DETAILS

Dissipative particle dynamics (DPD) is a coarse-grained particle-based simulation technique.²⁹ The force f_i acting on a DPD bead i consists of pairwise contributions of a conservative force, F_{ij}^C , a dissipative force, F_{ij}^D , and a random force, F_{ij}^R

$$\mathbf{f}_i = \sum_{ij} (\mathbf{F}_{ij}^C + \mathbf{F}_{ij}^D + \mathbf{F}_{ij}^R) \quad (1)$$

The dissipative force $\mathbf{F}_{ij}^D = -\eta w^D(r_{ij})(\mathbf{e}_{ij} \cdot \mathbf{v}_{ij})\mathbf{e}_{ij}$ and the random force $\mathbf{F}_{ij}^R = \sigma w^R(r_{ij})\xi_{ij}\Delta t^{-0.5}\mathbf{e}_{ij}$ act together as a thermostat, where η and σ are the friction parameter and the noise amplitude with $\eta = \sigma^2/2k_B T$; $\mathbf{r}_{ij} = \mathbf{r}_i - \mathbf{r}_j$, $r_{ij} = |\mathbf{r}_{ij}|$, and $\mathbf{e}_{ij} = \mathbf{r}_{ij}/r_{ij}$. $w^D(r_{ij})$ and $w^R(r_{ij})$ represent the r -dependent weight function for the dissipative and random forces, respectively; ξ_{ij} is a Gaussian random number with zero mean for each interaction pairs of beads at each timestep Δt . It is noted that $w^D(r_{ij}) = [w^R(r_{ij})]^2$ and $\sigma = 3$ are used in this work. The nonbonded conservative force $\mathbf{F}_{ij}^C = \alpha_{ij}(1 - r_{ij}/r_c)\mathbf{e}_{ij}(r_{ij} < r_c)$ is purely repulsive and it is defined by the repulsion parameter α_{ij} . The repulsion parameter between different species A and B, α_{AB} , can be related to their Flory–Huggins parameter χ_{AB} as²⁹

$$\alpha_{AB} = \alpha_{AA} + 3.27\chi_{AB} \quad (2)$$

Following Groot and Warren's suggestion for a system with a density of $3r_c^{-3}$, we set the nonbonded repulsion of like interactions to $\alpha_{AA} = \alpha_{BB} = 25k_B T r_c^{-1}$, where r_c is the cutoff distance of the conservative nonbonded force \mathbf{F}_{ij}^C . We use a bead-spring model for the bonded interactions in polymer chains. Bonded interactions along the chains use a harmonic force $\mathbf{F}_{ij}^S = -C\mathbf{r}_{ij}$ on top of the nonbonded interactions. A spring constant of $C = 4.0k_B T r_c^{-2}$ is chosen following previous

DPD studies of copolymers.³⁶ The cutoff distance (r_c), bead mass (m), and energy ($\epsilon = k_B T$) are chosen as reduced units of length, mass, and energy. If necessary, mapping of the cutoff distance (r_c) and bead mass (m) is possible.^{17,30,33} Using them, the reduced time unit is defined as $t = \sqrt{(mr_c/k_B T)}$ with an integration step of $\Delta t = 0.06t$. For convenience, we will use reduced units from here on.

A total of 162 000 beads are simulated in a box with $L_x \times L_y \times L_z = 30 \times 30 \times 60r_c^3$. In the initial configuration of uncompatibilized homopolymer blends, the homopolymers A and B are placed in the two halves of the simulation box, as illustrated in Figure 1a. For the compatibilized system,

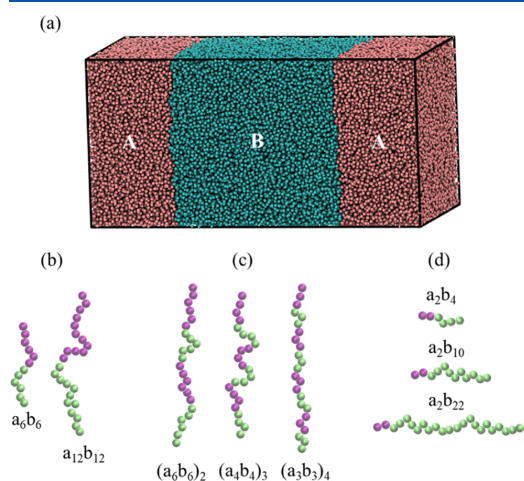


Figure 1. (a) Uncompatibilized system containing A/B blend (the chain length of A and B is 60) with repulsion parameters $\alpha_{AA} = \alpha_{BB} = 25$ and $\alpha_{AB} = 50$. A total of 162 000 beads are simulated in a box with $L_x \times L_y \times L_z = 30 \times 30 \times 60r_c^3$. Pink and cyan represent A and B beads, respectively. Models for the three series of copolymers: (b) symmetric diblock copolymers; (c) regular multiblock copolymers; and (d) unsymmetric diblock copolymers. Purple and green represent type A and B beads in the copolymer compatibilizers and are denoted a and b, respectively.

compatibilizers are added near the two interfaces. This speeds up the interface formation without influencing the interfacial thermodynamic properties.⁶ For clarity, beads of type A and B, which are part of the compatibilizer molecules, are denoted a and b, respectively. The DPD models for 3 series of copolymers are illustrated in Figure 1: symmetric diblock copolymers (Figure 1b), regular multiblock copolymers (Figure 1c), and unsymmetric diblock copolymers (Figure 1d). For example, a_4b_4 denotes a diblock copolymer with four A-type beads and four B-type beads. The evolution of the interfacial tension and mean-squared radius of gyration R_g^2 of systems with simulation time are monitored. The equilibration is considered to have reached when their relative standard deviations are within 5%. Starting from the initial state, at least 1×10^6 steps are required to guarantee equilibration for all systems. The equilibrium is checked by the radius of gyration and surface tension, as illustrated in Supporting Information Figure S1. After equilibrium has been reached, data are collected for another 2×10^6 steps. The trajectory is divided into four blocks to calculate the standard deviation of

properties such as interfacial tension. The interfacial tension γ is derived from the pressure anisotropy^{8,27}

$$\gamma = \left\langle \frac{L_z}{2} \left[P_{zz} - \frac{1}{2} (P_{xx} + P_{yy}) \right] \right\rangle \quad (3)$$

where P_{xx} , P_{yy} , and P_{zz} are the diagonal components of the pressure tensor, and the z direction is the interface normal.

RESULTS AND DISCUSSION

Homopolymer Blends without Compatibilizers. We present first the interfacial tension of uncompatibilized blends of monodisperse homopolymers A and B with equal chain lengths ($l_A = l_B$) and identical volume fractions ($f_A = f_B = 0.5$). The dependence of the interfacial tension γ on the repulsion parameter α_{AB} and chain length is shown in Figure 2. It can be

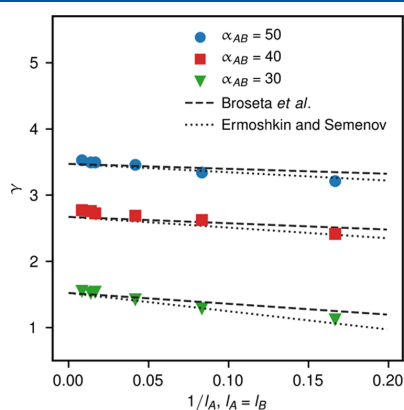


Figure 2. Simulated interfacial tension results from DPD simulations and predicted interfacial tension results versus $1/l_A$ based on eqs 4 and 5 with $K = \frac{\pi^2}{12}$ (Broseta et al.)²³ and $2 \ln 2$ (Ermoshkin and Semenov)⁴⁰ for A/B uncompatibilized homopolymer blends ($l_A = l_B$, $f_A = f_B$). The interfacial statistical segment length s_{int} of the $A_{120}B_{120}$ homopolymer blend (Table 1) has been used. The errors of interfacial tension γ are smaller than the symbols sizes and are not shown here.

seen that γ increases with an increase in α_{AB} from 30 to 50. Qian et al.⁸ have demonstrated that an increase in the repulsion parameter α_{AB} enhances the interfacial tension γ and decreases the number of unlike contacts, which results in a narrower interface thickness. The variation of our bead density distributions with repulsion parameter is consistent with previous works^{8,18} (Supporting Information Figure S2). Additionally, γ increases with the chain length until reaching a plateau γ_{∞} , as shown in Figure 2. This relationship has also been observed in previous experimental³⁷ and theoretical^{38,39} works. In our DPD model, the plateau chain length l_{plateau} is around 8–20 depending on α_{AB} . Based on SCF calculations, a simple expression relating γ to the interaction parameter $\chi = (\alpha_{AB} - 25)/3.27$ and chain lengths l_A and l_B is as follows

$$\gamma = \gamma_{\infty} \left[1 - K \left(\frac{1}{\chi l_A} + \frac{1}{\chi l_B} \right) \right] \quad (4)$$

$$\gamma_{\infty} = \rho s k_B T \left(\frac{\chi}{6} \right)^{1/2} \quad (5)$$

Here, K is a constant value and s is the statistical segment with $R_e^2 = n_m s^2$, where R_e^2 is the mean-squared end-to-end distance and n_m is the number of beads per chain.^{23,40} The constant value K is selected as $\pi^2/12$ and $2 \ln 2$ under different approximations in reference from Broseta et al.²³ and Ermoshkin and Semenov,⁴⁰ respectively. It should be noted that Ermoshkin and Semenov derived their model to better reproduce the properties of the strongly incompatible system, and the value of their K is comparable to the other work⁴¹ with the same aim. Qian et al.⁸ have assumed s as 1 in their DPD simulation and found that the predicted interfacial tension deviated with the calculated interfacial tension. This has also been observed in our work by using $s = 1$, particularly in the strongly incompatible systems (Supporting Information Figure S3). Then, we have calculated the statistical segment length of the homopolymer melt (the repulsion parameter is equal to 25 for each paired bead) and found the value s_{melt} saturated (~ 0.96) for long chains. However, a significant deviation has been observed between the simulated DPD results and predicted results from eqs 4 and 5 using s_{melt} . Since chain extensions are influenced by the interface,^{19,42} we have defined the interfacial statistical segment length s_{int} and bulk statistical segment length s_{bulk} based on the center-of-mass of the chain in the homopolymer blend systems. Homopolymer chains with the center-of-mass ranging from $z_0 - 3$ to $z_0 + 3$ (z_0 is the center of interface) are used to calculate s_{int} while other chains are used to calculate s_{bulk} . The calculated results have been summarized in Table 1. We find that s_{int} is higher than s_{bulk} for

Table 1. Bulk Statistical Segment Length s_{bulk} and Interfacial Statistical Segment Length s_{int} of Homopolymer Blends A_6B_6 , $A_{12}B_{12}$, $A_{24}B_{24}$, $A_{60}B_{60}$, $A_{72}B_{72}$, and $A_{120}B_{120}$ with the Repulsion Parameter $\alpha_{AB} = 30, 40$ and 50

	$\alpha_{AB} = 30$		$\alpha_{AB} = 40$		$\alpha_{AB} = 50$	
	s_{bulk}	s_{int}	s_{bulk}	s_{int}	s_{bulk}	s_{int}
A_6B_6	0.887	0.966	0.888	0.973	0.887	0.985
$A_{12}B_{12}$	0.929	0.982	0.931	0.991	0.933	1.003
$A_{24}B_{24}$	0.942	0.994	0.944	1.009	0.941	1.018
$A_{60}B_{60}$	0.956	1.003	0.960	1.015	0.955	1.024
$A_{72}B_{72}$	0.957	1.004	0.954	1.013	0.959	1.027
$A_{120}B_{120}$	0.966	1.005	0.966	1.015	0.971	1.028

all homopolymer blends and both values increase with the chain length and then saturate. Moreover, the repulsion parameter α_{AB} has a stronger influence on s_{int} than on s_{bulk} . We have applied all statistical segment lengths into eqs 4 and 5 and found that the predicted results based on s_{int} of the long-chain blend $A_{120}B_{120}$ agree well with the DPD simulation results, particularly when K is selected as $2 \ln 2$ in reference from Ermoshkin and Semenov⁴⁰ (Figure 2). This can be explained by the fact that the interfacial tension γ is more strongly correlated with the homopolymer near the interface and the γ_{∞} in eq 5 is obtained from the approximation of the infinite chain length of the homopolymer. We have also investigated the interfacial tension when the two homopolymers have different chain lengths ($l_A \neq l_B$) and volume fractions ($f_A \neq f_B$). Both parameters have a negligible influence on the interfacial tension of uncompatibilized blends (Supporting Information Figure S2). Hence, we have fixed the volume fraction and the chain length of homopolymers A and B as $f_A = f_B$ and $l_A = l_B = l_h$ in the remaining part of this work, where l_h is the chain length of the homopolymer.

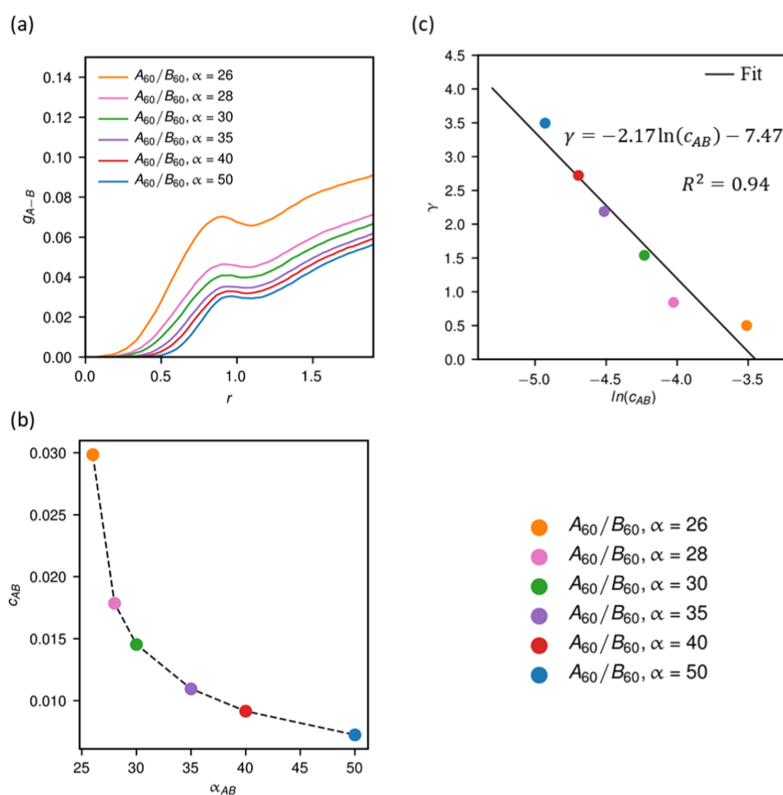


Figure 3. (a) Pair distribution functions $g_{AB}(r)$ and (b) the coordination number c_{AB} between A and B homopolymer beads of the uncompatibilized blends of A_{60}/B_{60} (the chain length of A and B is equal to 60) with the repulsion parameter $\alpha_{AB} = 26, 27, 28, 30, 35, 40,$ and 50 . $g_{AB}(r)$ represents the probability of finding a B-type bead at a distance r away from an A-type bead. c_{AB} is defined as the integral of $g_{AB}(r)$ from 0 to r_c . (c) Correlation between the interfacial tension γ and the coordination number $\ln(c_{AB})$ of uncompatibilized blends of A_{60}/B_{60} with the repulsion parameter $\alpha_{AB} = 26, 27, 28, 30, 35, 40,$ and 50 . The expression is $\gamma = -2.17 \ln(c_{AB}) - 7.47$ with a regression coefficient of $R^2 = 0.94$. The errors of the interfacial tension γ and c_{AB} are smaller than the symbol sizes and are not shown here.

To understand the variation of the interfacial tension, we have evaluated the pair distribution functions $g_{AB}(r)$, which represent the probability of finding a B-type bead at a distance r away from an A-type bead. We show $g_{AB}(r)$ of the uncompatibilized A_{60}/B_{60} systems with different repulsion parameters α_{AB} as in Figure 3a. The magnitude of $g_{AB}(r)$ decreases as α_{AB} increases, indicating a decreasing number of contacts between unlike beads. Moreover, there is a stronger decrease of $g_{AB}(r)$ with α_{AB} between $\alpha_{AB} = 26$ and $\alpha_{AB} = 35$ than between $\alpha_{AB} = 40$ and $\alpha_{AB} = 50$. To more quantitatively examine the number of unfavorable contacts, we have investigated the unlike coordination number c_{AB} with $\alpha_{AB} = 26, 27, 28, 30, 35, 40,$ and 50 in Figure 3b. c_{AB} is defined as the integral over $g_{AB}(r)$ from 0 to r_c as $c_{AB} = \int_0^{r_c} 4\pi r^2 \rho g_{AB}(r) dr$. We find that the value of c_{AB} decreases monotonically with increasing α_{AB} . In terms of the absolute magnitude, the decrease in c_{AB} from $\alpha_{AB} = 26$ to $\alpha_{AB} = 30$ is 0.015, whereas a decrease of 0.07 is measured from $\alpha_{AB} = 30$ to $\alpha_{AB} = 50$, which indicates saturation. On the basis of the decrease of c_{AB} versus α_{AB} , we define three system types: weakly incompatible systems ($25 < \alpha_{AB} < 30$), intermediate-incompatible systems ($30 \leq \alpha_{AB} < 40$), and strongly incompatible systems ($\alpha_{AB} \geq 40$). Moreover, we find that the interfacial tension can be well

fitted by the logarithmic function $\ln(c_{AB})$, as shown in Figure 3c. The resulting expression is $\gamma = -2.17 \ln(c_{AB}) - 7.47$ with a regression coefficient of $R^2 = 0.94$. This implies that both the interfacial tension of uncompatibilized A/B blends and the unlike contacts between A and B beads strongly depends on the strength of the repulsion between unlike polymers α_{AB} .

The homopolymer A/B systems without compatibilizers are taken as a reference for further investigations in this work. The interfacial tension value of this system is used as a reference γ_0 . After adding compatibilizers, the scaled result of $\left(\frac{\gamma}{\gamma_0} - 1\right)$ represents the compatibilizer efficiency for the respective blends system.

Symmetric Diblock Copolymers as Compatibilizers. Symmetric diblock copolymers with two different chain lengths (a_4b_4 and $a_{12}b_{12}$) have been added to reduce the interfacial tension of the uncompatibilized blends for highly incompatible blends ($\alpha_{AB} \geq 40$). Since the copolymer molecules mainly reside in the interfacial region, a volume-based concentration has little meaning. Therefore, we use the concentration of copolymer beads per interface area ϕ , which is defined as follows

$$\phi = \frac{n_c l_c}{I_{cs}} \quad (6)$$

where n_c is the number of chains of the compatibilizer at each interface, l_c is their chain length, and I_{cs} is the cross-sectional interfacial area of the simulation box $L_x \times L_y = 30 \times 30r_c^2$. We first fixed the homopolymer chain length at 60 and the repulsion parameter α_{AB} at 50. The interfacial tensions γ and γ_0 have been calculated from eq 3. The dependence of γ/γ_0 on ϕ is shown in Figure 4a. It decreases with an increase of the

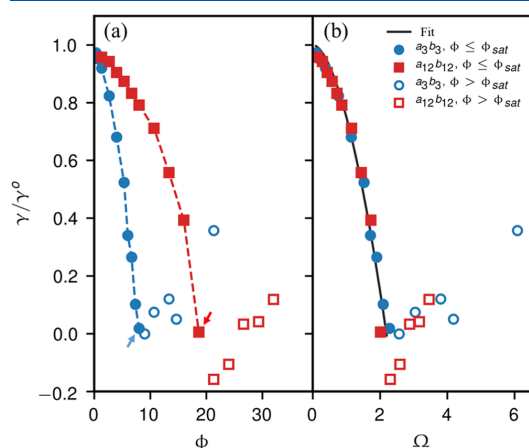


Figure 4. Interfacial-tension reduction γ/γ_0 as a function of (a) areal concentration of diblock compatibilizer ϕ , (b) parameter $\Omega = \phi l_c^{0.7}$ for systems with the addition of a_3b_3 and $a_{12}b_{12}$ with $\alpha_{AB} = 50$ to a blend of A_{60} and B_{60} . The fitting curve is given by eq 8 as a function of Ω . Solid points represent systems at $\phi \leq \phi_{sat}$ and open points are systems at $\phi > \phi_{sat}$.

compatibilizer concentration ϕ . This tendency is more noticeable for short diblock copolymers a_4b_4 than for the longer $a_{12}b_{12}$. We define the areal concentration ϕ where the interfacial tension becomes zero for the first time ($\gamma/\gamma_0 = 0$) as saturation concentration ϕ_{sat} , indicated by colored arrows in Figure 4a. Further addition of compatibilizers beyond the saturation concentration ϕ_{sat} is an inefficient use of compatibilizers. The apparent negative interfacial tension values are a finite-size artifact and do not occur in experiments.²⁷ In this work, we focus on the system with the interfacial tension $\gamma \geq 0$ to understand how to efficiently use compatibilizers. Figure 4a shows that γ/γ_0 is related to both ϕ and l_c . In addition, $\gamma/\gamma_0 = 1$ is given in the case of no compatibilizers. We thus attempt to fit the effects of ϕ and l_c on γ/γ_0 by a power law

$$\frac{\gamma}{\gamma_0} = 1 - K_1 \phi^{K_2} l_c^{K_3} \quad (7)$$

where K_1 , K_2 , and K_3 are assumed to be related to χ in some analogy to eq 4 for uncompatibilized homopolymer blends. To obtain the expressions of K_1 , K_2 , and K_3 , four systems with $\alpha_{AB} = 40, 60, 70$, and 80 have been investigated. The plots of γ/γ_0 of these systems versus ϕ are summarized in Supporting Information Figures S3–S6. From these results, it appears that K_2 and K_3 are not independent but follows $K_3 = K_2 - 0.7$, which can be used to convert the term $(\phi^{K_2} l_c^{K_3})$ into $(\phi l_c^{0.7})^{K_2}$

in eq 7. For convenience, we define a new parameter $\Omega = \phi l_c^{0.7} = \frac{n_c l_c^{0.3}}{I_{cs}}$ and eq 7 becomes a 2-parameter expression

$$\frac{\gamma}{\gamma_0} = 1 - K_1 (\phi l_c^{0.7})^{K_2} = 1 - K_1 \left(\frac{n_c l_c^{0.3}}{I_{cs}} \right)^{K_2} = 1 - K_1 \Omega^{K_2} \quad (8)$$

where $K_1 = -1.05 \times 10^{-2} \chi_{AB} + 0.327$ and $K_2 = 5.43 \times 10^{-2} \chi_{AB} + 1.275$ are obtained from Figure S9 in the Supporting

Information. Then, the value of $\phi_{sat} = \left(\frac{1}{K_1} \right)^{1/K_2} l_c^{0.7}$ is evaluated based on the term $K_1 (\phi_{sat} l_c^{0.7})^{K_2} = 1$ for the symmetric diblock copolymers. Detailed discussions about ϕ_{sat} follow in the next section, which treats diblock and regular multiblock copolymers together. Here, we investigate the connection of the saturated interfacial area per diblock copolymer Σ with the copolymer chain length l_c . Govorun and Erukhimovich⁴³ proposed a theoretical model of Σ based on the SCF method derived from Leibler's model⁴⁴ for the diblock copolymers adsorbed on the flat interface of the homopolymer blend when the homopolymer chain length is long enough

$$\Sigma = \left(\frac{3l_c}{\gamma_0} \right)^{1/3} \left(\frac{\nu}{s} \right)^{2/3} \quad (9)$$

where ν is the monomer volume and is equal to 1/3 in this work. We have calculated the simulated Σ_{sim} statistical segment length s of copolymers, the predicted Σ_{pre} based on the calculated s and Σ_{pre}^* by assuming $s = 1$ from eq 9 in Table 2. We find that Σ_{pre} agrees well with Σ_{sim} with a slight

Table 2. Statistical Segment Length s , the Saturated Area per Copolymer Molecule from Simulation Σ_{sim} , the Predicted Σ_{pre} based on the Obtained s and Σ_{pre}^* by Assuming $s = 1$ from eq 9 for a_3b_3 and $a_{12}b_{12}$ Diblock Copolymers with $\alpha_{AB} = 50$ to a Homopolymer Blend of A_{60} and B_{60}

	s	Σ_{sim}	Σ_{pre}	Σ_{pre}^*
a_3b_3	1.11	0.75	0.77	0.82
$a_{12}b_{12}$	1.20	1.21	1.23	1.31

deviation (~ 1.7 to 2.7%) for systems with the addition of a_3b_3 and $a_{12}b_{12}$ with $\alpha_{AB} = 50$. Moreover, the deviation between Σ_{pre}^* with $s = 1$ and Σ_{sim} is ~ 8.4 to 9.3%, which is also in a reasonable range. This indicates that the predicted model (eq 9) can be used for the rough estimation of the saturated number of the diblock copolymer in the homopolymer blend without running simulation, which has also been discussed in the previous work.⁴⁵

Figure 4 shows that eq 8 holds for both systems with short copolymers as compatibilizers (length $l_c = 6$ and 24) for long ($l_h = 60$) homopolymers. The previous studies^{8,10} have shown, however, that the ratio of compatibilizer and homopolymer chain lengths l_c/l_h can also influence the value of γ/γ_0 . To investigate the influence of l_c/l_h on the consistency between simulation results and predicted results given from eq 8, we have investigated systems of symmetric diblock compatibilizers of three different overall chain lengths ($l_c = 12, 48$, and 96) at $\alpha_{AB} = 50$ with homopolymer chain lengths of 12 and 24, i.e., A_{12}/B_{12} (Figure 5a) and A_{24}/B_{24} (Figure 5b). We observe that simulation results are in line with the predicted results from eq

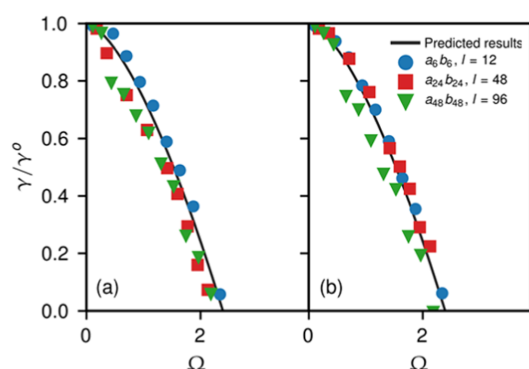


Figure 5. Reduction of interfacial tension between (a) A_{12}/B_{12} blends and (b) A_{24}/B_{24} blends by the addition of diblock compatibilizers of different sizes: a_6b_6 , $a_{24}b_{24}$, $a_{48}b_{48}$. The black curve is the prediction of eq 8 with $\Omega = \phi l_c^{-0.7}$. It should be mentioned that γ_0 in (a) and (b) are different.

8, as long as $l_c/l_h < 1$. If the compatibilizer is much longer than the matrix polymers, there is a slight deviation. Moreover, Berezkin and Kudryavtsev⁴⁶ have investigated the interfacial converge of the symmetric diblock copolymers in the homopolymer blend with $l_c/l_h = 2$ by performing DPD simulations. The saturated value of Ω calculated using their data in the case of $\alpha_{AB} = 50$ is ~ 2.08 to 2.21 , which is lower than the value of 2.29 in this work. This implies a slight deviation between the simulated and predicted results from eq 8 when again $l_c/l_h > 1$. We, therefore, conclude that eq 8 is quite general for describing the reduction of the interfacial tension γ/γ_0 of homopolymer blends by symmetric diblock copolymer compatibilizers.

To understand the underlying relationship between the interfacial tension and the parameters l_c and n_c of diblock copolymers in eq 8, we first considered the bead density distributions. The density distributions of the a-block beads of compatibilizers a_3b_3 and $a_{12}b_{12}$ at areal bead concentrations $\phi = 1.33$ (Figure 6a) and $\phi = 5.33$ (Figure 6b) are illustrated. It

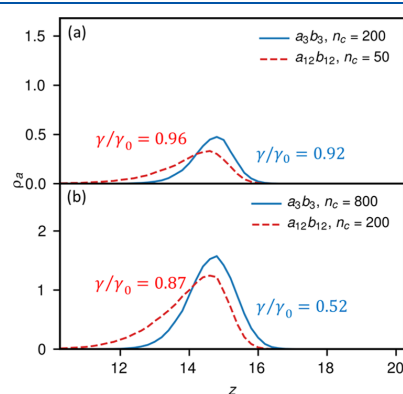


Figure 6. Density distribution of a-block beads (ρ_a) of the compatibilizers in systems with (a) a_3b_3 and $a_{12}b_{12}$ at an areal concentration $\phi = 1.33$; and (b) a_3b_3 and $a_{12}b_{12}$ at an areal concentration $\phi = 5.33$.

is observed that a_3b_3 assembles closer to the interface than the longer $a_{12}b_{12}$ at both concentrations. This results in a higher interfacial tension of a_3b_3 than that of $a_{12}b_{12}$ at the same areal bead concentration ϕ . On the other hand, $a_{12}b_{12}$ can penetrate deeper into the homopolymer region. Hence, the better penetrating ability of $a_{12}b_{12}$ ($\gamma/\gamma_0 = 0.87$, Figure 6b) results in a larger reduction of the interfacial tension γ/γ_0 for the same number of chains $n_c = 200$ compared to a_3b_3 ($\gamma/\gamma_0 = 0.92$, Figure 6a).

These findings are corroborated by eq 8. Because $K_1 > 0$ and $K_2 > 0$, the compatibilizer efficiency of the copolymer $\left(\frac{\gamma}{\gamma_0} - 1\right)$ at a constant areal bead concentration ϕ exhibits a relationship as follows.

$$\frac{\gamma}{\gamma_0} - 1 \sim -l_c^{-0.7} \quad (10)$$

This means that symmetric diblock copolymers with shorter chain lengths l_c have a higher compatibilizer efficiency. By contrast, when keeping the number of compatibilizer molecules n_c constant, the relationship becomes

$$\frac{\gamma}{\gamma_0} - 1 \sim -l_c^{0.3} \quad (11)$$

This indicates that the symmetric diblock copolymers with longer chain length l_c exhibit a higher compatibilizer efficiency. We can summarize this as recognizing that an individual diblock copolymer molecule has a larger compatibilization effect, and depends on the length. When one compares the compatibilization effect for a given, constant amount of compatibilizer material, one finds, however, that many short molecules perform better than a few longer ones. These relationships are related to the efficiency of copolymers in preventing the unlike contacts of the two matrix polymers at the interface. Our observations are consistent with the previous studies for symmetrical diblock copolymers in experimental works^{47,48} and computational work with SCF theory,^{23–25} Monte Carlo,⁴⁹ and DPD methods.⁸ However, we also note that there exist practical maximum and minimum weights for block copolymers. Nam et al.⁴⁷ found that block copolymers with a large molecular weight beyond the micelle weight (M_m) tend to form micelles in the bulk of the homopolymers rather than congregate at the interface for the polystyrene–polyisoprene blend system. Creton and Kramer⁵⁰ reported that block copolymers below the entanglement weight (M_e) cause interface failure when high tensile stress is applied to the polystyrene–poly(2-vinylpyridine) blends. Hence, the critical molecular weights of M_m and M_e should be kept in mind when applying the above conclusion to realistic systems.

Regular Multiblock Copolymers as Compatibilizers.

We will next discuss the compatibilization efficiency of multiblock copolymers for homopolymer blends. We confine the analysis to regular multiblock copolymers, which have alternating blocks of equal lengths of A and B types. They all have a total of 24 beads. In addition to the diblocks $a_{12}b_{12}$ already discussed, we study the tetrablocks $(a_6b_6)_2$, hexablocks $(a_4b_4)_3$, and octablocks $(a_3b_3)_4$. They differ in the number of blocks and block granularity. Thus, it is interesting to find out whether a generalized form of eq 8 is predictive also for these structures. To this end, the dependence of γ/γ_0 on the block length $\left(l_m = \frac{l_c}{n_b}\right)$ has been investigated, where $l_c = 24$ is the

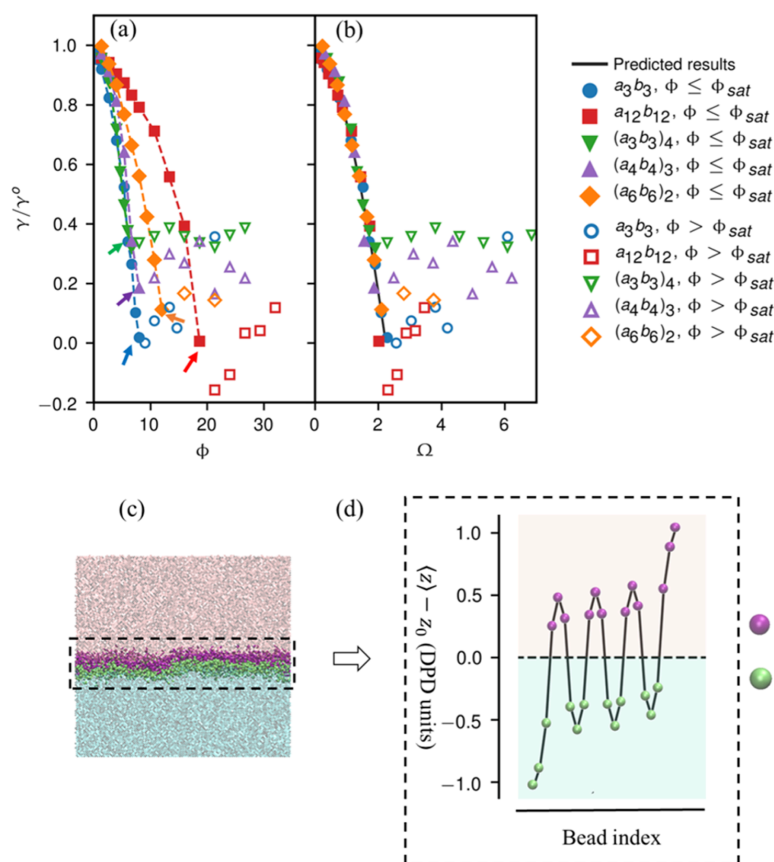


Figure 7. Interfacial tension reduction γ/γ_0 by regular multiblock copolymers as a function of (a) multiblock's areal concentration ϕ and (b) the parameter Ω (see eq 12) for A_{60}/B_{60} polymer blends with $\alpha_{AB} = 50$. The fitting curve is given by eq 12. Solid points represent systems at $\phi \leq \phi_{sat}$ and open points are systems at $\phi > \phi_{sat}$. (c) Snapshot of the interface of an A_{60}/B_{60} blend in the presence of $(a_3b_3)_4$ at $\phi = 5.33$ in a box with $L_x \times L_y \times L_z = 30 \times 30 \times 60r_c^3$. (d) Average distances $\langle (z) - z_0 \rangle$ of the individual beads of the $(a_3b_3)_4$ molecule from the interface position z_0 (dashed line), averaged over all copolymer molecules and all timesteps.

chain length of the copolymer and n_b is the number of blocks in the copolymer molecule. Figure 7a shows γ/γ_0 of all five multiblock systems (including the symmetric diblock copolymers a_3b_3 and $a_{12}b_{12}$) as a function of their areal concentration ϕ for the strongly incompatible ($\alpha_{AB} = 50$) matrix polymers A_{60} and B_{60} in equal amounts. We find that γ/γ_0 of these multiblock systems decreases with increasing concentration until saturation is reached. Below the saturation concentration ϕ_{sat} , γ/γ_0 exhibits a similar decrease for multiblock copolymer compatibilizers as for diblock copolymers. We note that the multiblock copolymers reduce the interfacial tension more efficiently than diblock copolymers $a_{12}b_{12}$ with the same chain length below ϕ_{sat} (Figure 7a). To understand the high compatibilization efficiency of the multiblock copolymers, we have calculated the average distance $\langle (z) - z_0 \rangle$ of each copolymer bead from the average interface position z_0 as a function of their index in the chain. As shown in Figure 8c,d, each bead of $(a_3b_3)_4$ is close to the interface but attempts to reside in the favorable homopolymer domain. As a result, any two neighboring blocks with the same block length 3 behave similarly to the short symmetric diblock a_3b_3 .

Hence, multiblock copolymers with block length l_m could possess similar compatibilization efficiency as the symmetric diblock copolymer with the same block length. With this assumption, the equation of interfacial tension for symmetric multiblock copolymers can be estimated from eq 8 as follows

$$\begin{aligned} \frac{\gamma}{\gamma_0} &= 1 - K_1(\phi l_c^{-0.7})^{K_2} = 1 - K_1[\phi(2l_m)^{-0.7}]^{K_2} \\ &= 1 - K_1\Omega^{K_2} \end{aligned} \quad (12)$$

We show both the results predicted based on eq 12 and the results from DPD simulations in Figure 7b. Simulation results are in line with the predicted results despite a small shift. The shift is observed for multiblock copolymers $(a_3b_3)_4$ and symmetric diblock copolymers a_3b_3 with the same mean block length l_m . $(a_3b_3)_4$ reduces the interfacial tension more efficiently than a_3b_3 when $\phi \leq \phi_{sat}$. It is noted that the length of copolymers should not be much longer than the matrix polymers as the discussions for eq 8 in the previous section. We also observe that copolymers with shorter block lengths (lower l_m) reach saturation ϕ_{sat} earlier but the maximum

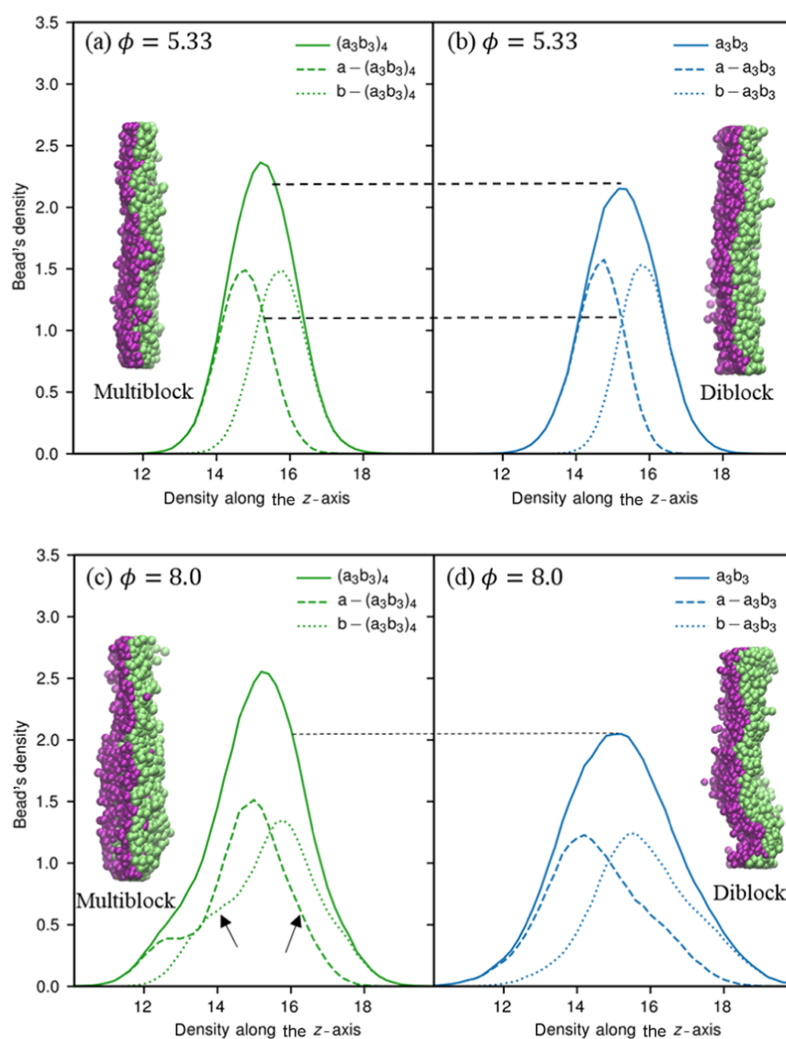


Figure 8. Bead-density distribution of (a) multiblock copolymers $(a_3b_3)_4$ and (b) diblock copolymers a_3b_3 normal to the xy -interface along the z -axis at a low concentration $\phi = 5.33$; dashed line: a-block beads; dotted line: b-block beads; solid line: total. Bead-density distribution of (c) multiblock copolymers $(a_3b_3)_4$ and (d) diblock copolymers a_3b_3 normal to the xy -interface along the z -axis at a low concentration $\phi = 8.0$. Arrows indicate that some beads of $(a_3b_3)_4$ are forced into the energetically unfavorable phases and are surrounded by unlike beads. Inset are snapshots of the copolymer layers in a box with $L_x \times L_y \times L_z = 30 \times 30 \times 60r_c^3$. Purple and green represent the a- and b-block beads in the copolymer compatibilizers, respectively.

overall reduction of γ/γ_0 is smaller compared to $(a_4b_4)_3$ (higher l_m) in Figure 7a.

Moreover, we find that γ/γ_0 of the diblock copolymers a_3b_3 and $a_{12}b_{12}$ is reduced to 0 at ϕ_{sat} whereas γ/γ_0 of $(a_3b_3)_4$ and $(a_4b_4)_3$ with a high number of blocks saturate at a nonzero plateau (Figure 7a). Does the saturation ϕ_{sat} follow the same mechanism for symmetric diblock copolymers and multiblock copolymers? To answer this question, we calculate the bead density distributions along the direction perpendicular to the interface (z -axis) of the diblock copolymer a_3b_3 ($\phi_{\text{sat}} \sim 8$) and regular multiblock copolymer $(a_3b_3)_4$ ($\phi_{\text{sat}} \sim 6.67$), which have the same block unit a_3b_3 , at two concentrations $\phi = 5.33$ and 8 (Figure 8). First, we observe that the peak height of density

distributions of $(a_3b_3)_4$ beads is higher than that of a_3b_3 at both areal concentrations. This indicates that the $(a_3b_3)_4$ copolymer tends to more compactly locate at the interface, resulting in a lower value of ϕ_{sat} . Second, the shapes of the bead distributions of the a- and b-block beads of $(a_3b_3)_4$ are not symmetric about the interface for the higher concentration $\phi = 8$ (Figure 8c). Some beads of $(a_3b_3)_4$ are forced into the energetically unfavorable phases and are surrounded by unlike beads, as indicated by arrows in Figure 8c. Similar behavior has also been observed for the tetrablock copolymer²⁷ and graft copolymer³⁰ at the saturation plateau. In contrast, a- and b-block beads of a_3b_3 distribute equally near the interface by deforming the interface at $\phi = 8$, which can be confirmed from

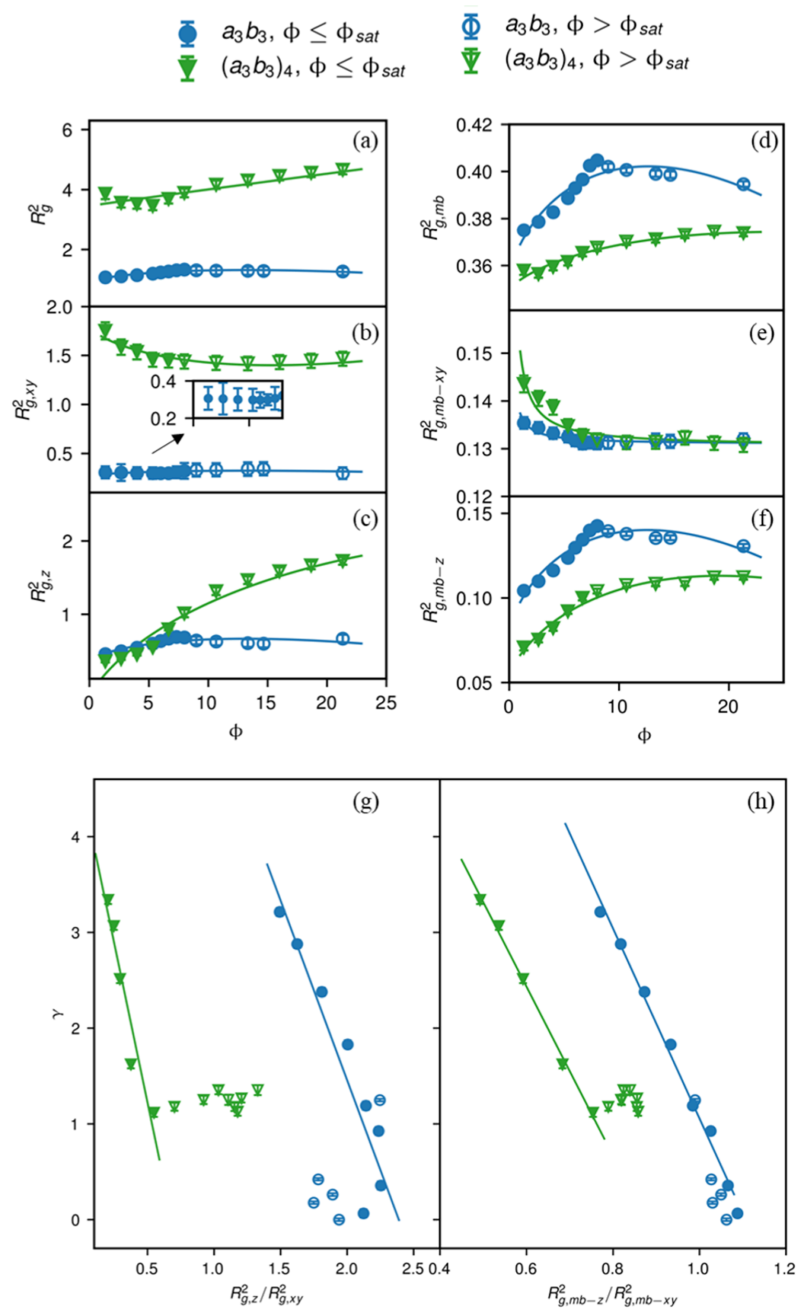


Figure 9. (a) Squared radius of gyration R_g^2 and its components: (b) $R_{g,xy}^2$ parallel to the interface and (c) $R_{g,z}^2$ perpendicular to the interface for copolymers a_3b_3 and $(a_3b_3)_4$ as a function of their areal concentration ϕ . (d) Squared radius of gyration of single blocks $R_{g,mb}^2$ and its components. (e) $R_{g,mb-xy}^2$ parallel to the interface and (f) $R_{g,mb-z}^2$ perpendicular to the interface for copolymers a_3b_3 and $(a_3b_3)_4$ as a function of ϕ . The relationship between interfacial tension and the anisotropy ratios (g) $R_{g,z}^2/R_{g,xy}^2$ and (h) $R_{g,mb-z}^2/R_{g,mb-xy}^2$. Solid symbols represent systems at $\phi \leq \phi_{sat}$ and open points are systems at $\phi > \phi_{sat}$.

the snapshots (Figure 8d). We can further conclude that multiblock copolymers tend to form a second layer but diblock

copolymers prefer to deform the interface when the first layer is almost saturated. The mechanisms involved in the saturation

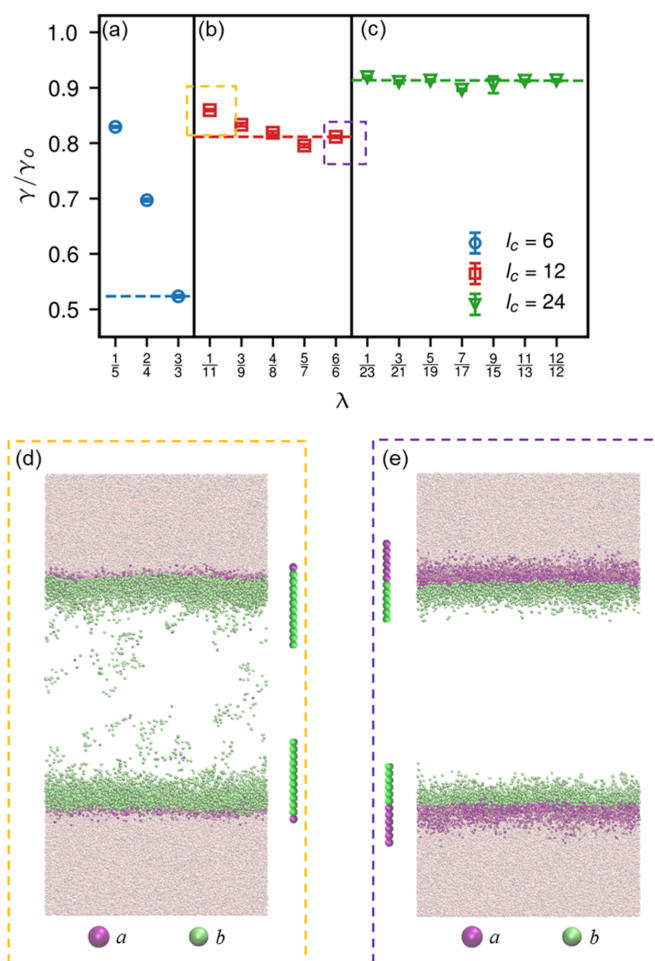


Figure 10. Reduction of the interfacial tension γ/γ_0 as a function of the a-to-b ratio λ for systems containing unsymmetric diblock copolymers of chain length (a) $l_c = 6$, (b) $l_c = 12$, and (c) $l_c = 24$ at an areal concentration of $\phi = 5.33$ in an A_{60}/B_{60} blend with $\alpha_{AB} = 50$. Dashed lines representing γ/γ_0 of symmetric diblock copolymers are a guide to the eye. Snapshots are shown of systems with (d) ab_{11} and (e) a_6b_6 at $\phi = 5.33$ in a box with $L_x \times L_y \times L_z = 30 \times 30 \times 60r_c^3$. The beads of B_{60} are not shown for clarity.

of compatibilization efficiency are, thus, different for symmetric diblock copolymers and multiblock copolymers.

We further investigate the difference between diblock copolymers and multiblock copolymers in their chain conformations, described by the squared radius of gyration R_g^2 as

$$\langle R_g^2 \rangle = \frac{1}{n_c l_c} \sum_{i=1}^{n_c} \sum_{j=1}^{l_c} (r_j^i - r_{cm}^i)^2 \quad (13)$$

where r_j^i is the coordinate of the j th bead in the i th copolymer molecule and r_{cm}^i is the coordinate of the center of mass of the i th copolymer. To monitor the stretching of the copolymer chain along the x , y , and z directions, the three components of the squared radius of gyration $R_{g,x}^2$, $R_{g,y}^2$, and $R_{g,z}^2$ are calculated. $R_{g,xy}^2 = (R_{g,x}^2 + R_{g,y}^2)/2$ is the average of components $R_{g,x}^2$ and $R_{g,y}^2$, which reflects the expansion of the copolymer chains parallel to the interface. The calculated results are summarized in Figure

9. We find that $R_{g,xy}^2$ of the a_3b_3 copolymer is lower than that of the $(a_3b_3)_4$ copolymer at all ϕ (Figure 9b), whereas the values of $R_{g,z}^2$ of a_3b_3 and $(a_3b_3)_4$ overlap with each other below ϕ_{sat} (Figure 9c). Compared with the symmetric diblock copolymer a_3b_3 , the multiblock copolymer $(a_3b_3)_4$ is more expanded parallel to the surface. At the same time, they have comparable chain extensions in the z -direction. Additionally, we note that the initial decrease of R_g^2 of $(a_3b_3)_4$ with ϕ is caused by the decrease of $R_{g,xy}^2$, as in Figure 9b, when $\phi \leq \phi_{sat}$, implying that the conformation of the multiblock copolymers is compressed quickly in the lateral direction, as ϕ increases. It is still unclear how the individual block unit of the $(a_3b_3)_4$ copolymer behaves as compared to the a_3b_3 copolymer. Therefore, we have calculated the $R_{g,mb}^2$ to indicate the block conformation as

$$\langle R_{g,mb}^2 \rangle = \frac{1}{n_b l_m} \sum_{k=1}^{n_b} \sum_{g=1}^{l_m} (r_k^g - r_{cm}^k)^2 \quad (14)$$

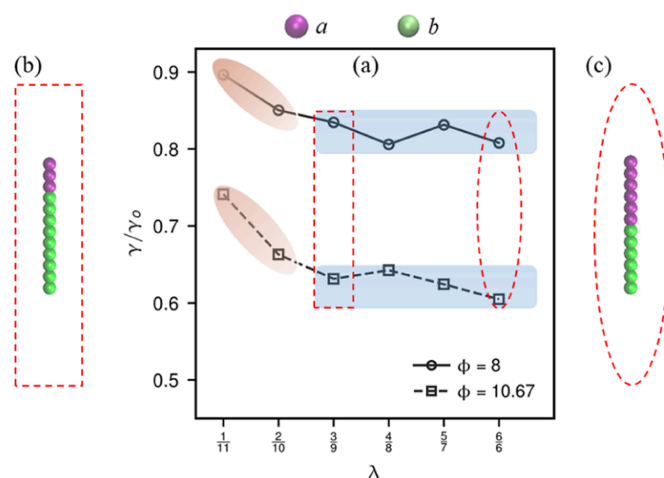


Figure 11. (a) Reduction of the interfacial tension γ/γ_0 as a function of the a-to-b monomer ratio λ for systems containing diblock copolymers with a total of 12 monomers in A_{60}/B_{60} polymer blends with $\alpha_{AB} = 50$ at areal concentrations of $\phi = 8$ and $\phi = 10.67$. (b) and (c) Chain models of a_3b_3 and a_6b_6 , respectively. The regions of initial decay and plateau are highlighted in beige and light-blue, respectively.

where r_{cm}^k is the coordination of g th bead in the k th copolymer block and r_{cm}^k is the coordinate of the center of mass of the k th block of the copolymer chain. We observe that the mean block conformations $R_{g,mb}^2$, $R_{g,mb-xy}^2$, and $R_{g,mb-z}^2$ exhibit similar trends for the copolymers $(a_3b_3)_4$ and a_3b_3 alike, as ϕ increases. However, the single block of $(a_3b_3)_4$ is stretched more parallel to the interface (higher $R_{g,mb-xy}^2$) and more compressed perpendicular to it (lower $R_{g,mb-z}^2$) compared to the a_3b_3 copolymer. This is a consequence of a central block in $(a_3b_3)_4$ being pulled laterally by its neighbors on the chain, and consequently, being hindered to expand as much perpendicularly as the free block in an a_3b_3 . To better understand the competition of stretching of copolymers parallel and perpendicular to the interface, we have plotted the interfacial tension versus the ratios $R_{g,z}^2/R_{g,xy}^2$ and $R_{g,mb-z}^2/R_{g,mb-xy}^2$ in Figure 10g,h, respectively. We observe that the interfacial tension decreases with both anisotropy measures $R_{g,z}^2/R_{g,xy}^2$ and $R_{g,mb-z}^2/R_{g,mb-xy}^2$ for both diblock and multiblock copolymers as long as $\phi \leq \phi_{sat}$. Beyond ϕ_{sat} , however, the anisotropy of a_3b_3 copolymers tends to decrease, whereas that of the $(a_3b_3)_4$ copolymers still increases, albeit at constant interfacial tension. This implies again the different behaviors of the symmetric diblock copolymers and regular multiblock copolymers after reaching saturation. Moreover, it is noted that there is no universal scaling relationship between the interfacial tension and chain conformations as well as the unlike contacts for different copolymer architectures. This can be further confirmed by the unfavorable contact between A and B homopolymers near the interface. In the compatibilized systems, we define the pair distribution functions $g_{AB}(r)$ as the probability of finding a B-type homopolymer bead at a distance r away from an A-type homopolymer bead in the region between $z_0 - 3$ and $z_0 + 3$. It is integrated from 0 to r_c to give the number of unlike neighbors c_{AB} . We find that c_{AB} decreases with the areal concentration, but there is also no simple universal relationship between interfacial tension and the coordination number for compatibilized systems with different copolymers (Supporting Information Figure S10).

Unsymmetric Diblock Copolymers as Compatibilizers

Until now, the discussions were focused on copolymers with equal numbers of a-block and b-block beads (the a-to-b ratio $\lambda = 1$). In practice, however, it is inevitable to also produce unsymmetric diblock copolymers with $\lambda \neq 1$. Thus, to gain insight into the influence of λ on the interfacial properties, we have investigated three unsymmetric diblock copolymers of overall chain lengths $l_c = 6, 12$, and 24 . We denote a chain with one a-block bead and 23 b-block beads, for example as ab_{23} , in the same notation as before. Figure 10a shows the variation of γ/γ_0 with λ for all three chain lengths at $\phi = 5.33$. It is first observed that ab_5 , ab_{11} , and ab_{23} , which contain only a single a-block bead, have the highest γ/γ_0 values. This observation can be understood by considering the partitioning of the copolymer into homopolymer regions. Since the b beads of the copolymer prefer their energetically favorable B-phase region, some copolymer chains with only a small number of a-block beads will be dragged into the B homopolymer phase (Figure 10d). Such a chain is not active in the reduction of interfacial tension. Hence, it can be easily understood that diblock copolymers with low λ perform worse in compatibilization than more symmetric (high λ) diblock copolymers. Therefore, for copolymers of all three chain lengths, γ/γ_0 decreases with increasing λ until it reaches the optimum value of symmetric diblock copolymers. This decrease, however, becomes much weaker as the diblock copolymers become longer. For diblock copolymers with $l_c = 24$, the unsymmetric diblock copolymers exhibit almost the same compatibilization efficiency as the symmetric diblock copolymers, independent of their block length ratio λ (Figure 10c). For diblock copolymers with $l_c = 12$, we find that compatibilization becomes independent of the precise a-to-b ratio for $\lambda > \frac{3}{9}$ in Figure 10b. We may therefore conclude that, for the same performance, one has more leeway in the block-length ratio when the polymers are longer.

To shed some light on the details of this behavior, we report γ/γ_0 of the systems with compatibilizers of $l_c = 12$ and 24 also at higher concentrations $\phi = 8$ and $\phi = 10.67$, as in Figures 11

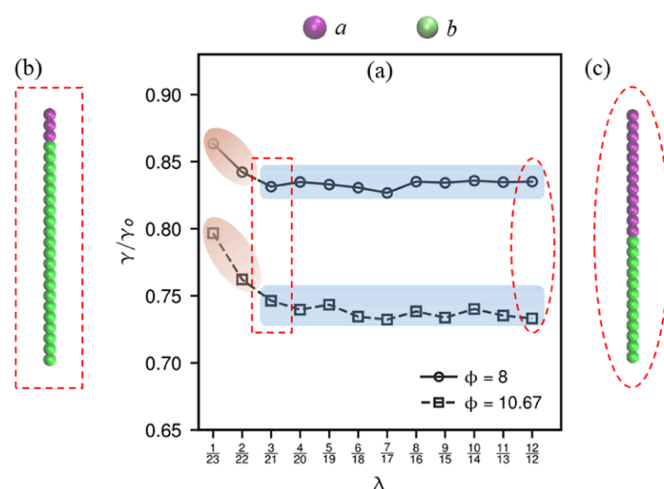


Figure 12. (a) Reduction of the interfacial tension γ/γ_0 as a function of the a-to-b monomer ratio λ for systems containing diblock copolymers with a total of 24 monomers in A_{60}/B_{60} polymer blends with $\alpha_{AB} = 50$ at areal concentrations of $\phi = 8$ and $\phi = 10.67$. (b) and (c) Chain models of a_3b_{21} and $a_{12}b_{12}$, respectively. The regions of initial decay and plateau are highlighted in beige and light-blue, respectively.

and 12. In all cases, γ/γ_0 initially decreases quickly with λ and then reaches a plateau. For copolymers of $l_c = 12$, the plateau begins at around 3/9, for $l_c = 24$ at $\lambda = \frac{3}{21}$. In both cases, the length of the shorter block is equal to 3, i.e., a_3b_9 and a_3b_{21} . This leads to the idea that the length of the shorter block is the decisive factor for the compatibilization efficiency of unsymmetric diblock copolymers. Long unsymmetric diblock copolymers exhibit similar compatibilization efficiency as the symmetric diblock copolymers, once the shortest block has more than 3 monomers. If this condition is met, eq 8 can also be used to estimate the compatibilization efficiency of unsymmetric diblock copolymers. This number 3 is presumably specific to the highly incompatible system treated by the DPD of this work. However, we are led to believe that a lower critical block length exists, which should also be true for other systems.

CONCLUSIONS

In summary, we have compared the compatibilization efficiency of symmetric diblock copolymers, regular multiblock copolymers, and unsymmetric diblock copolymers in immiscible polymer blends. For symmetric diblock copolymers, a power-law fit quantifies the variation of interfacial tension with the number of compatibilizer chains, the chain length, and the DPD interaction parameters. In good agreement with the results from experiments^{47,48} and simulations,^{8,49} the power-law fitting equation indicates that the interfacial tension decreases and that the single long copolymers have better compatibilization efficiency than short homopolymers. The origin of the power-law function (eq 8) can be explained by considering the compensation effect of the chain length and number of chains of copolymers on the compatibilizer efficiency. We then extended eqs 8–12 to indicate all regular copolymers by considering multiblock copolymers as a combination of several chains of symmetric diblock copolymers at the interface. We observed that regular multiblock copolymers can improve the interfacial tension more effectively with an adequate mean block length, as compared to other

compatibilizers if their concentration per interfacial area is kept constant.

We have evaluated the relationships between interfacial tension and several parameters, i.e., the chain conformation of copolymers and the number of unlike contacts. We find that block copolymers, which expand stronger parallel to the interface, also exhibit better compatibilization. The primary molecular concept to explain compatibilization is that the number of unlike contacts between A and B species at the interface is reduced by the addition of compatibilizers. These relationships are also observed for other compatibilizers, such as the graft copolymers^{6,30} and Janus nanorods.¹⁹ Our present study is restricted to linear block copolymers with DPD methods. However, we believe that similar quantitative scaling is also applicable for other compatibilizers with different molecular architectures.

ASSOCIATED CONTENT

Supporting Information

The Supporting Information is available free of charge at <https://pubs.acs.org/doi/10.1021/acs.macromol.1c01076>.

Interfacial tension and structure relaxation process of systems; density profiles of uncompatibilized blend; simulated interfacial tension results and predicted interfacial tension results; interfacial tension as a function of length ratio of uncompatibilized homopolymer blend; interfacial tension as a function of the areal concentration of diblock compatibilizer for systems with different repulsion parameters; two fitting parameters versus Flory–Huggins parameter; correlation between the coordination number and the concentration of compatibilized systems (PDF)

AUTHOR INFORMATION

Corresponding Author

Florian Müller-Plathe – Eduard-Zintl-Institut für Anorganische und Physikalische Chemie, Technische Universität Darmstadt, 64287 Darmstadt, Germany;

orcid.org/0000-0002-9111-7786; Email: f.mueller-plathe@theo.chemie.tu-darmstadt.de

Authors

Tianhang Zhou – Eduard-Zintl-Institut für Anorganische und Physikalische Chemie, Technische Universität Darmstadt, 64287 Darmstadt, Germany; orcid.org/0000-0002-4007-9935

Jurek Schneider – Eduard-Zintl-Institut für Anorganische und Physikalische Chemie, Technische Universität Darmstadt, 64287 Darmstadt, Germany; orcid.org/0000-0002-0286-1678

Zhenghao Wu – Eduard-Zintl-Institut für Anorganische und Physikalische Chemie, Technische Universität Darmstadt, 64287 Darmstadt, Germany; orcid.org/0000-0003-2862-4432

Complete contact information is available at:
<https://pubs.acs.org/10.1021/acs.macromol.1c01076>

Notes

The authors declare no competing financial interest.

ACKNOWLEDGMENTS

The authors would like to thank Covestro AG for funding this work. They also thank Dr. José A. Gámez and Dr. Mandy Gieler for helpful discussions on this research.

REFERENCES

- (1) Cowie, J. M. G. Polymer Alloys and Blends: Thermodynamics and Rheology. *Polym. Int.* **1991**, *25*, 130.
- (2) Ougizawa, T.; Inoue, T. UCST and LCST Behavior in Polymer Blends and Its Thermodynamic Interpretation. *Polym. J.* **1986**, *18*, 521–527.
- (3) Utracki, L. A. Compatibilization of Polymer Blends. *Can. J. Chem. Eng.* **2002**, *80*, 1008–1016.
- (4) Macosko, C. W.; Guégan, P.; Khandpur, A. K.; Nakayama, A.; Marechal, P.; Inoue, T. Compatibilizers for Melt Blending: Premade Block Copolymers. *Macromolecules* **1996**, *29*, 5590–5598.
- (5) Sundararaj, U.; Macosko, C. W. Drop Breakup and Coalescence in Polymer Blends: The Effects of Concentration and Compatibilization. *Macromolecules* **1995**, *28*, 2647–2657.
- (6) Ryu, J. H.; Kim, Y.; Lee, W. B. Inhomogeneity of block copolymers at the interface of an immiscible polymer blend. *Phys. Rev. E* **2018**, *97*, 1–7.
- (7) Ruzette, A.-V.; Leibler, L. Block copolymers in tomorrow's plastics. *Nat. Mater.* **2005**, *4*, 19–31.
- (8) Qian, H.-J.; Lu, Z. Y.; Chen, L. J.; Li, Z. S.; Sun, C. C. Dissipative particle dynamics study on the interfaces in incompatible AB homopolymer blends and with their block copolymers. *J. Chem. Phys.* **2005**, *122*, No. 184907.
- (9) Eastwood, E. A.; Dadmun, M. D. Multiblock Copolymers in the Compatibilization of Polystyrene and Poly(methyl methacrylate) Blends: Role of Polymer Architecture. *Macromolecules* **2002**, *35*, 5069–5077.
- (10) Sun, D.; Guo, H. Monte carlo studies on the interfacial properties and interfacial structures of ternary symmetric blends with gradient copolymers. *J. Phys. Chem. B* **2012**, *116*, 9512–9522.
- (11) Gersappe, D.; Balazs, A. C. Random copolymers as effective compatibilizing agents. *Phys. Rev. E* **1995**, *52*, 5061–5064.
- (12) Dai, C.-A.; Dair, B. J.; Dai, K. H.; Ober, C. K.; Kramer, E. J.; Hui, C.-Y.; Jelinski, L. W. Reinforcement of Polymer Interfaces with Random Copolymers. *Phys. Rev. Lett.* **1994**, *73*, 2472–2475.
- (13) Mah, A. H.; Laws, T.; Li, W.; Mei, H.; Brown, C. C.; Ievlev, A.; Kumar, R.; Verduzco, R.; Stein, G. E. Entropic and Enthalpic Effects in Thin Film Blends of Homopolymers and Bottlebrush Polymers. *Macromolecules* **2019**, *52*, 1526–1535.
- (14) Dong, W.; He, M.; Wang, H.; Ren, F.; Zhang, J.; Zhao, X.; Li, Y. PLLA/ABS Blends Compatibilized by Reactive Comb Polymers: Double Tg Depression and Significantly Improved Toughness. *ACS Sustainable Chem. Eng.* **2015**, *3*, 2542–2550.
- (15) Dong, W.; Wang, H.; He, M.; Ren, F.; Wu, T.; Zheng, Q.; Li, Y. Synthesis of Reactive Comb Polymers and Their Applications as a Highly Efficient Compatibilizer in Immiscible Polymer Blends. *Ind. Eng. Chem. Res.* **2015**, *54*, 2081–2089.
- (16) Gersappe, D.; Harm, P. K.; Irvine, D.; Balazs, A. C. Contrasting the compatibilizing activity of comb and linear copolymers. *Macromolecules* **1994**, *27*, 720–724.
- (17) Li, Q.; Wang, L.; Lin, J.; Zhang, L. Distinctive phase separation dynamics of polymer blends: Roles of Janus nanoparticles. *Phys. Chem. Chem. Phys.* **2019**, *21*, 2651–2658.
- (18) Zhou, Y.; Huang, M.; Lu, T.; Guo, H. Nanorods with Different Surface Properties in Directing the Compatibilization Behavior and the Morphological Transition of Immiscible Polymer Blends in Both Shear and Shear-Free Conditions. *Macromolecules* **2018**, *51*, 3135–3148.
- (19) Zhou, C.; Luo, S. K.; Sun, Y.; Zhou, Y.; Qian, W. Dissipative particle dynamics studies on the interfacial tension of A/B homopolymer blends and the effect of Janus nanorods. *J. Appl. Polym. Sci.* **2016**, *133*, 44098.
- (20) Mural, P. K. S.; Rana, M. S.; Madras, G.; Bose, S. PE/PEO blends compatibilized by PE brush immobilized on MWNTs: improved interfacial and structural properties. *RSC Adv.* **2014**, *4*, 16250–16259.
- (21) Estridge, C. E.; Jayaraman, A. Assembly of diblock copolymer functionalized spherical nanoparticles as a function of copolymer composition. *J. Chem. Phys.* **2014**, *140*, No. 144905.
- (22) Walther, A.; Matussek, K.; Müller, A. H. E. Engineering Nanostructured Polymer Blends with Controlled Nanoparticle Location using Janus Particles. *ACS Nano* **2008**, *2*, 1167–1178.
- (23) Broseta, D.; Fredrickson, G. H.; Helfand, E.; Leibler, L. Molecular weight and polydispersity effects at polymer-polymer interfaces. *Macromolecules* **1990**, *23*, 132–139.
- (24) Helfand, E.; Tagami, Y. Theory of the Interface between Immiscible Polymers. II. *J. Chem. Phys.* **1972**, *56*, 3592–3601.
- (25) Helfand, E.; Tagami, Y. Theory of the interface between immiscible polymers. *J. Polym. Sci., Part B: Polym. Lett.* **1971**, *9*, 741–746.
- (26) Noolandi, J.; Hong, K. M. Interfacial Properties of Immiscible Homopolymer Blends in the Presence of Block Copolymers. *Macromolecules* **1982**, *15*, 482–492.
- (27) Meenakshisundaram, V.; Hung, J. H.; Patra, T. K.; Simmons, D. S. Designing Sequence-Specific Copolymer Compatibilizers Using a Molecular-Dynamics-Simulation-Based Genetic Algorithm. *Macromolecules* **2017**, *50*, 1155–1166.
- (28) Wang, J.; Song, J.; Lu, Y.; Ruan, Y.; An, L. Phase behavior and interfacial properties of diblock copolymer-homopolymer ternary mixtures: Influence of volume fraction of copolymers and interaction energy. *Chin. J. Polym. Sci.* **2017**, *35*, 874–886.
- (29) Groot, R. D.; Warren, P. B. Dissipative particle dynamics: Bridging the gap between atomistic and mesoscopic simulation. *J. Chem. Phys.* **1997**, *107*, 4423–4435.
- (30) Wang, J.; Li, Z.; Gu, X.; Feng, L.; Zhang, C.; Hu, G. A dissipative particle dynamics study on the compatibilizing process of immiscible polymer blends with graft copolymers. *Polymer* **2012**, *53*, 4448–4454.
- (31) Luo, Z.; Jiang, J. Molecular dynamics and dissipative particle dynamics simulations for the miscibility of poly(ethylene oxide)/poly(vinyl chloride) blends. *Polymer* **2010**, *51*, 291–299.
- (32) Maiti, A.; McGrother, S. Bead-bead interaction parameters in dissipative particle dynamics: Relation to bead-size, solubility parameter, and surface tension. *J. Chem. Phys.* **2004**, *120*, 1594–1601.
- (33) Ju, S.-P.; Wang, Y.-C.; Huang, G.-J.; Chang, J.-W. Miscibility of graphene and poly(methyl methacrylate) (PMMA): molecular dynamics and dissipative particle dynamics simulations. *RSC Adv.* **2013**, *3*, 8298–8307.

- (34) Lee, W.-J.; Ju, S. P.; Wang, Y. C.; Chang, J. G. Modeling of polyethylene and poly (L-lactide) polymer blends and diblock copolymer: Chain length and volume fraction effects on structural arrangement. *J. Chem. Phys.* **2007**, *127*, No. 064902.
- (35) Alasiri, H.; Chapman, W. G. Dissipative particle dynamics (DPD) study of the interfacial tension for alkane/water systems by using COSMO-RS to calculate interaction parameters. *J. Mol. Liq.* **2017**, *246*, 131–139.
- (36) Groot, R. D.; Madden, T. J. Dynamic simulation of diblock copolymer microphase separation. *J. Chem. Phys.* **1998**, *108*, 8713–8724.
- (37) Anastasiadis, S. H.; Gancarz, I.; Koberstein, J. T. Interfacial tension of immiscible polymer blends: temperature and molecular weight dependence. *Macromolecules* **1988**, *21*, 2980–2987.
- (38) Wu, D. T.; Fredrickson, G. H.; Carton, J. P.; Ajdari, A.; Leibler, L. Distribution of chain ends at the surface of a polymer melt: Compensation effects and surface tension. *J. Polym. Sci., Part B: Polym. Phys.* **1995**, *33*, 2373–2389.
- (39) Fredrickson, G. H.; Donley, J. P. Influence of broken conformational symmetry on the surface enrichment of polymer blends. *J. Chem. Phys.* **1992**, *97*, 8941–8946.
- (40) Ermoshkin, A. V.; Semenov, A. N. Interfacial tension in binary polymer mixtures. *Macromolecules* **1996**, *29*, 6294–6300.
- (41) Tang, H.; Freed, K. F. Free energy functional expansion for inhomogeneous polymer blends. *J. Chem. Phys.* **1991**, *94*, 1572–1583.
- (42) Jacobs, T. D.; Junge, T.; Pastewka, L. Quantitative characterization of surface topography using spectral analysis. *Surf. Topogr. Metrol. Prop.* **2017**, *5*, No. 013001.
- (43) Govorun, E. N.; Erukhimovich, I. Emulsion stabilization by diblock copolymers: Droplet curvature effect. *Langmuir* **1999**, *15*, 8392–8398.
- (44) Leibler, L. Emulsifying effects of block copolymers in incompatible polymer blends. *Makromol. Chem. Macromol. Symp.* **1988**, *16*, 1–17.
- (45) Erukhimovich, I.; Govorun, E. N.; Litmanovich, A. D. Stabilization of polymer blend structure by diblock copolymers. *Macromol. Theory Simul.* **1998**, *7*, 233–239.
- (46) Berezkin, A. V.; Kudryavtsev, Y. V. Simulation of end-coupling reactions at a polymer-polymer interface: The mechanism of interfacial roughness development. *Macromolecules* **2011**, *44*, 112–121.
- (47) Nam, K. H.; Cho, J. C.; Jo, W. H. Temperature and Molecular Weight Effect of Styrene-Isoprene Diblock Copolymers on the Interfacial Tension between Polystyrene and Polyisoprene. *Polym. J.* **1995**, *27*, 904–910.
- (48) Anastasiadis, S. H.; Gancarz, I.; Koberstein, J. T. Compatibilizing Effect of Block Copolymers Added to the Polymer/Polymer Interface. *Macromolecules* **1989**, *22*, 1449–1453.
- (49) Werner, A.; Schmid, F.; Binder, K.; Müller, M. Diblock copolymers at a homopolymer - Homopolymer interface: A Monte Carlo simulation. *Macromolecules* **1996**, *29*, 8241–8248.
- (50) Creton, C.; Kramer, E. J.; Hadziioannou, G. Critical molecular weight for block copolymer reinforcement of interfaces in a two-phase polymer blend. *Macromolecules* **1991**, *24*, 1846–1853.

Supporting Information: The
compatibilization efficiency of additives in
homopolymer blends: A
dissipative-particle-dynamics study

Tianhang Zhou, Jurek Schneider, Zhenghao Wu, and Florian Müller-Plathe*

*Eduard-Zintl-Institut für Anorganische und Physikalische Chemie, Technische Universität
Darmstadt, Alarich-Weiss-Str. 8, 64287 Darmstadt, Germany*

E-mail: f.mueller-plathe@theo.chemie.tu-darmstadt.de

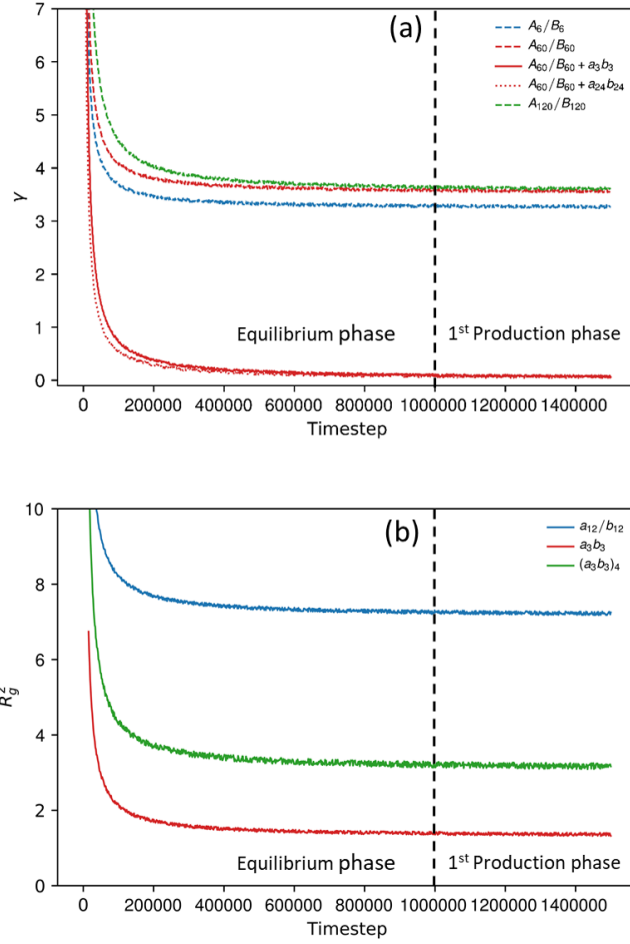


Figure S1: (a) Interfacial tension relaxation process for A_6/B_6 , A_{60}/B_{60} , and A_{120}/B_{120} uncompatibilized polymer blends and compatibilized A_{60}/B_{60} blend with $a_{12}b_{12}$ and a_3b_3 copolymers (around ϕ_{sat}) with $\alpha_{AB} = 50$. (b) Structural relaxation process of ensemble-averaged mean-square radius R_g^2 for the $a_{12}b_{12}$, a_3b_3 , and $(a_3b_3)_4$ copolymers in A_{60}/B_{60} polymer blends around ϕ_{sat} with $\alpha_{AB} = 50$.

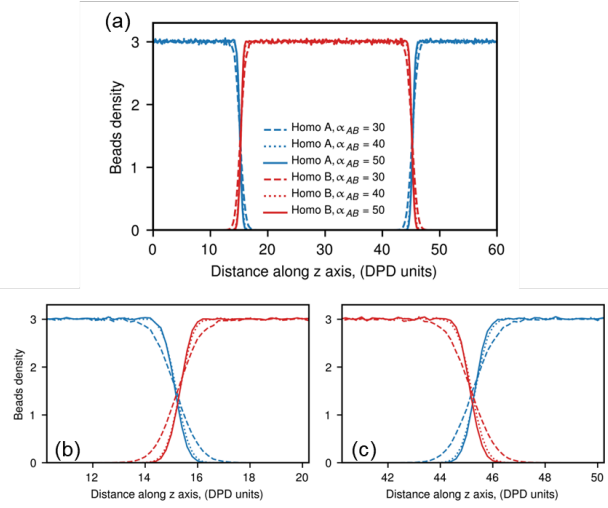


Figure S2: Beads density distributions along z axis of uncompatibilized blend of A_{60}/B_{60} (chain length of A and B equals to 60) with $\alpha_{AB} = 30, 40$ and 50 . (b) and (c) show the enlarged density distribution of the homopolymer A and B beads at the left interface and right interface, respectively.

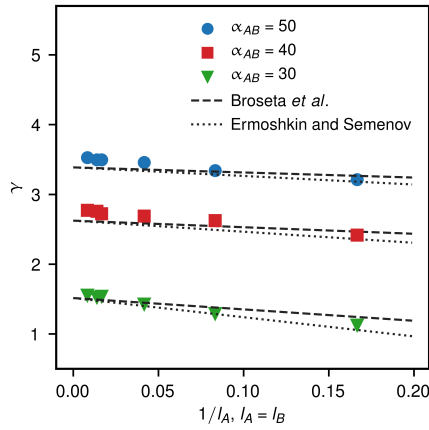


Figure S3: Simulated interfacial tension results from DPD simulations and predicted interfacial tension results versus $1/l_A$ based on Eqs.4 and 5 with $K = \frac{\pi^2}{12}$ (Broseta *et al.*)¹ and $2 \ln 2$ (Ermoshkin and Semenov)² for A/B uncompatibilized homopolymer blends ($l_A = l_B$, $f_A = f_B$). The statistical segment length $s = 1$. The errors of interfacial tension γ are smaller than the symbols sizes and not shown here.

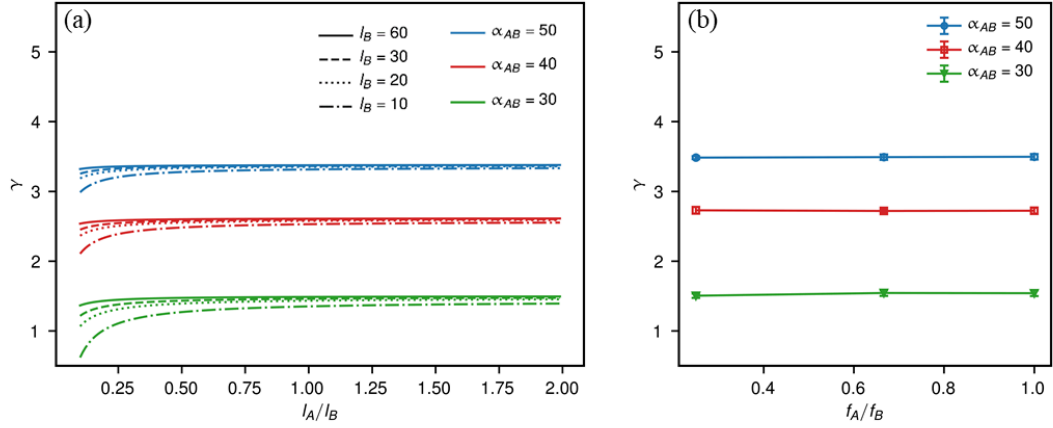


Figure S4: (a) Interfacial tension for $\alpha_{AB} = 30, 40$ and 50 , $f_A = f_B = 0.5$ calculated from Eq.4 versus the ratio of chain length l_A/l_B with chain length $l_B = 10, 20, 30$ and 60 . (b) Interfacial tension for $\alpha_{AB} = 30, 40$ and 50 , $l_A = l_B = 60$ versus the ratio of volume concentration f_A/f_B with $f_A + f_B = 1$.

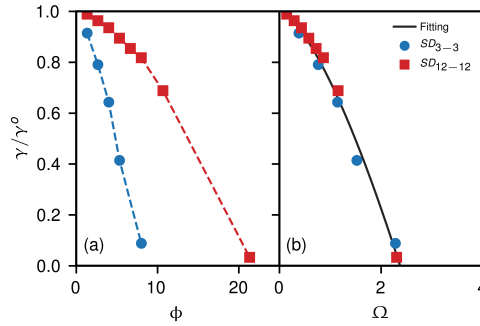


Figure S5: γ/γ_0 as a function of (a) areal concentration of diblock compatibilizer ϕ (b) parameter Ω for systems adding a_4b_4 and $a_{12}b_{12}$ with $\alpha_{AB} = 50$ to a blend of A_{60} and B_{60} . The fitting curve is given by the Eq.8 as a function of Ω . Only systems at $\phi \leq \phi_{\text{sat}}$ are shown.

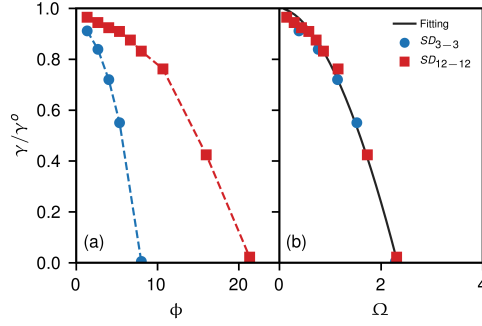


Figure S6: γ/γ_0 as a function of (a) areal concentration of diblock compatibilizer ϕ (b) parameter Ω for systems adding a_4b_4 and $a_{12}b_{12}$ with $\alpha_{AB} = 60$ to a blend of A_{60} and B_{60} . The fitting curve is given by the Eq.8 as a function of Ω . Only systems at $\phi \leq \phi_{\text{sat}}$ are shown.

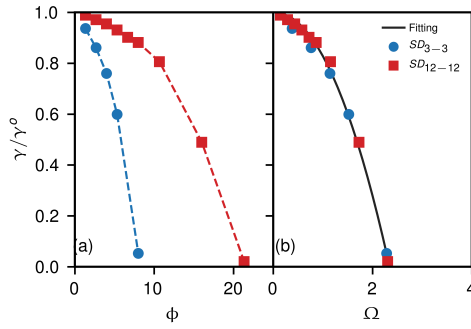


Figure S7: γ/γ_0 as a function of (a) areal concentration of diblock compatibilizer ϕ (b) parameter Ω for systems adding a_4b_4 and $a_{12}b_{12}$ with $\alpha_{AB} = 70$ to a blend of A_{60} and B_{60} . The fitting curve is given by the Eq.8 as a function of Ω . Only systems at $\phi \leq \phi_{\text{sat}}$ are shown.

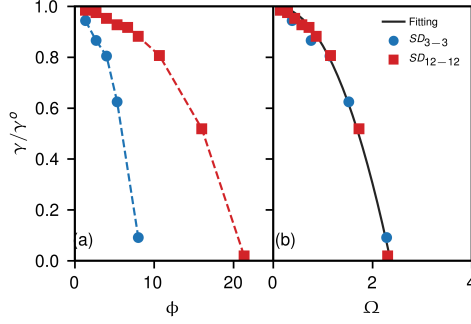


Figure S8: γ/γ_0 as a function of (a) areal concentration of diblock compatibilizer ϕ (b) parameter Ω for systems adding a_4b_4 and $a_{12}b_{12}$ with $\alpha_{AB} = 80$ to a blend of A_{60} and B_{60} . The fitting curve is given by the Eq.8 as a function of Ω . Only systems at $\phi \leq \phi_{\text{sat}}$ are shown.

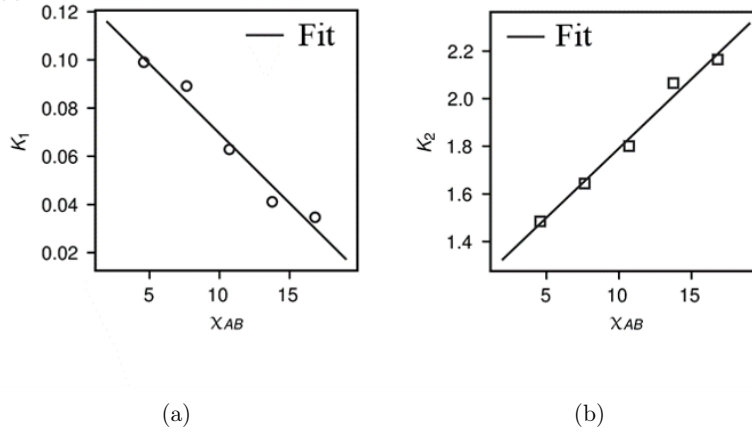


Figure S9: Relationship for parameter (a) K_1 with χ_{AB} as $K_1 = -1.05 \times 10^{-2}\chi_{AB} + 0.327$, $R^2 = 0.98$ and (b) K_2 with χ_{AB} as $K_2 = 5.43 \times 10^{-2}\chi_{AB} + 1.275$, $R^2 = 0.96$. χ_{AB} is the Flory-Huggins parameter between different species A and B.

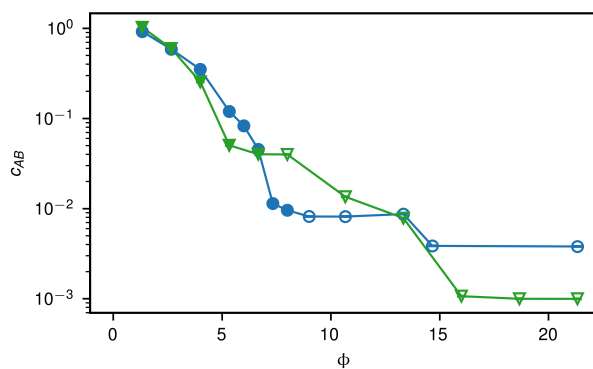


Figure S10: Correlation of the the coordination number c_{AB} and ϕ of compatibilized systems with a_3b_3 and $(a_3b_3)_4$ copolymers. c_{AB} is defined as the integral over $g_{AB}(r)$ from 0 to r_c as $c_{AB} = \int_0^{r_c} 4\pi r^2 \rho g_{AB}(r) dr$. Solid points represent systems at $\phi \leq \phi_{\text{sat}}$ and open points are systems at $\phi > \phi_{\text{sat}}$.

References

- (1) Broseta, D.; Fredrickson, G. H.; Helfand, E.; Leibler, L. Molecular weight and polydispersity effects at polymer-polymer interfaces. *Macromolecules* **1990**, *23*, 132–139.
- (2) Ermoshkin, A. V.; Semenov, A. N. Interfacial tension in binary polymer mixtures. *Macromolecules* **1996**, *29*, 6294–6300.

3.2 Optimization of Compatibilization Efficiency of Graft Copolymers in Immiscible Homopolymer Blends

The Compatibilization Efficiency of Graft Copolymers in Incompatible Polymer Blends: Dissipative Particle Dynamics Simulations Combined with Machine Learning.

Under review by Macromolecules on 21/04/2022

3.3 Optimization of Disinfection Efficiency on Coronavirus Model Membranes

Reproduced with permission from Zhou et al. [J. Chem. Theory Comput. 2022, 18, 4, 2597–2615]
Copyright 2022 American Chemical Society.



How Ethanolic Disinfectants Disintegrate Coronavirus Model Membranes: A Dissipative Particle Dynamics Simulation Study

Tianhang Zhou, Zhenghao Wu, Shubhadip Das, Hossein Eslami,* and Florian Müller-Plathe

Cite This: *J. Chem. Theory Comput.* 2022, 18, 2597–2615

Read Online

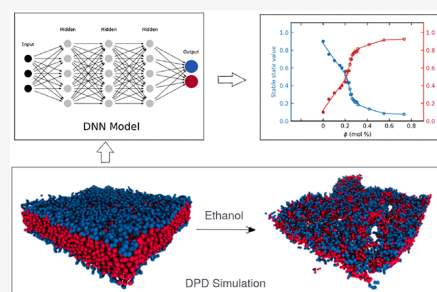
ACCESS |

Metrics & More

Article Recommendations

Supporting Information

ABSTRACT: We have developed dissipative particle dynamics models for pure dipalmitoylphosphatidylcholine (DPPC), dioleoylphosphatidylcholine (DOPC), and dimyristoylphosphatidylcholine (DMPC) as well as their binary and ternary mixed membranes, as coronavirus model membranes. The stabilities of pure and mixed membranes, surrounded by aqueous solutions containing up to 70 mol % ethanol (alcoholic disinfectants), have been investigated at room temperature. We found that aqueous solutions containing 5–10 mol % ethanol already have a significant weakening effect on the pure and mixed membranes. The magnitude of the effect depends on the membrane composition and the ethanol concentration. Ethanol permeabilizes the membrane, causing its lateral swelling and thickness shrinking and reducing the orientational order of the hydrocarbon tail of the bilayer. The free energy barrier for the permeation of ethanol in the bilayers is considerably reduced by the ethanol uptake. The rupture-critical ethanol concentrations causing the membrane failure are 20.7, 27.5, and 31.7 mol % in the aqueous phase surrounding pure DMPC, DOPC, and DPPC membranes, respectively. Characterizing the failure of lipid membranes by a machine-learning neural network framework, we found that all mixed binary and/or ternary membranes disrupt when immersed in an aqueous solution containing a rupture-critical ethanol concentration, ranging from 20.7 to 31.7 mol %, depending on the composition of the membrane; the DPPC-rich membranes are more intact, while the DMPC-rich membranes are least intact. Due to the tight packing of long, saturated hydrocarbon tails in DPPC, increasing the DPPC content of the mixed membrane increases its stability against the disinfectant. At high DPPC concentrations, where the DOPC and DMPC molecules are confined between the DPPC lipids, the ordered hydrocarbon tails of DPPC also induce order in the DOPC and DMPC molecules and, hence, stabilize the membrane more. Our simulations on pure and mixed membranes of a diversity of compositions reveal that a maximum ethanol concentration of 32 mol % (55 wt %) in the alcohol-based disinfectants is enough to disintegrate any membrane composed of these three lipids.



INTRODUCTION

The infectious respiratory coronavirus disease 2019 (COVID-19) caused by the 2019 novel coronavirus (2019-nCoV), also known as SARS-CoV-2 and HCoV-19, has spread throughout the whole world.¹ The outer layer of the coronavirus envelope is composed of the membrane (M), spike (S), and envelope (E) proteins and the host-derived lipid bilayer, which gives the virus its distinctive shape and structure and protects its RNA from the surrounding environment.^{2–5}

Recently, there has been rapid progress in the development of safe and effective vaccines against the coronavirus and development of potential therapies for SARS-CoV-2.^{6–9} However, still a considerable fraction of the world's population is unvaccinated, the new variants of the virus may spread, and there is no established treatment for SARS-CoV-2 infection. Washing one's hands with soap and water or hand sanitizer that contains at least 60–70 wt % alcohol (usually ethanol, n-propanol, isopropyl alcohol, or a mixture of them) is still one important way to prevent the spread of COVID-19 and other corona viruses.^{10,11} Since the viral membrane acts as a barrier to

the penetration of small molecules through it, the deactivation of the virus is primarily controlled by its membrane permeability to alcohol. By using different techniques, investigators have studied the alcohol-induced changes on various lipid bilayer systems.^{11–14} Concentrated alcohol solutions increase the area per lipid molecule, accompanied by a decrease in the bilayer thickness along with disordering and enhanced interdigitation of lipid acyl chains.^{15,16} These changes cause a loss of membrane integrity and make it permeable to the passage of alcohol molecules, water, and other species, a process that eventually leads to membrane rupture.¹⁷ In a recent study, we have reported that the stability of the pure dipalmitoylphosphati-

Received: November 6, 2021

Published: March 14, 2022



dylcholine (DPPC) membrane against alcoholic disinfectants strongly depends on the phase of the membrane.¹⁵ We reliably observed the disintegration of the DPPC membrane in its liquid crystalline phase (323 K), at ethanol concentrations ≈ 15 mol % in the aqueous phase surrounding the membrane, while its gel phase (298 K) remained intact even at higher ethanol concentrations (up to about 20 mol % examined).

Although the exact composition of the viral membrane is unknown and presumably changes between individual virus particles, we know at least that it contains a mixture of lipids that mechanically anchor the S- and E-proteins. Among all lipid types, phosphatidylcholines (PCs) are the most important lipid components of living organisms. Specifically, they are the main components of the endoplasmic reticulum Golgi intermediate compartment (ERGIC), where coronaviruses are replicated and assembled.^{18,19} Additionally, the lung, the primary organ affected by the coronavirus, mostly uses dipalmitoylphosphatidylcholine (DPPC), i.e., one of the PCs, as the abundant constituent of its surfactants.²⁰ As well as PCs ($\sim 50\%$), the ERGIC of a mammalian cell contains smaller amounts of ($\sim 15\text{--}25\%$) phosphatidylethanolamines (PEs) and ($\sim 10\text{--}15\%$) phosphatidylinositols (PIs).²¹ The PCs-, PEs-, and PIs-molecules have different head groups but the same hydrophobic tails,^{21,22} which consist of saturated and/or unsaturated acyl chains of various lengths. Previous experimental^{23–26} and simulation¹⁵ reports show that the phase of the membrane, which in turn depends on the hydrocarbon tail length and its degree of saturation, is the main factor determining its stability. Our results in this work also confirm such a trend for the stabilities of membranes made up of PCs as well of PC mixtures (see the section [Membrane Failure](#)). We have compared experimental data²⁷ on the phases (stabilities) of PC-, PE-, and PI-membranes, of different hydrocarbon tail lengths with a different number of unsaturated bonds, in [Supporting Information](#) Figure S1. Based on these data, we would argue that the lipid headgroup does not have a dominant role in the stability of the membrane. Besides, our previous atomistic simulation results show that the largest free-energy barrier for the passage of small molecules is observed very close to the center of the membrane at both low and high ethanol concentrations.¹⁵ Its height depends on the membrane thickness, i.e., the gap that a penetrant needs to cross.¹⁵ It has been found experimentally²⁸ that the thickness of the membrane depends nearly linearly on the length of hydrocarbon tail. In contrast, the type of the headgroup does not have a noticeable influence on the membrane thickness, which is related to the stability. The headgroup is found to act only as a secondary barrier to membrane penetration, at low ethanol concentrations. Thus, the type of headgroup determines how the first few ethanol molecules partition into the membrane and their accumulation around the headgroup region. At high ethanol concentrations, penetration to the tail region causes a substantial lateral swelling of the membrane, preceding its rupture. Therefore, it is the hydrocarbon tails and their composition, which ultimately controls the membrane stability. This argument is also in line with previous simulations^{29,30} of the stability of membranes of pure palmitoyl-oleoylphosphatidylcholine (POPC, PCs) and phosphatidylethanolamine (POPE, PEs) at high ethanol concentrations. Due to the large number of lipid constituents of ERGIC membranes (whose composition resembles that of the viral coating membrane, since the viral genome does not provide for lipid manufacture), we are forced to only simulate a subset. However, the arguments above allow

us to reasonably justify simulating mixed-PC membranes as coronavirus model membranes, to investigate their stability against disinfectants. Hence, we selected three PCs with different classes of hydrocarbon chains, namely dipalmitoylphosphatidylcholine (DPPC, consisting of long saturated hydrocarbon chains), dioleoylphosphatidylcholine (DOPC, consisting of long unsaturated hydrocarbon chains), and dimyristoylphosphatidylcholine (DMPC, consisting of short saturated hydrocarbon chains) as the components of mixed lipid bilayers. Besides, the coronavirus membrane anchors S-proteins, which fuse with the host cell membrane and facilitate virus entrance to the cell, as well as E- and M-proteins. The presence of these proteins in the structure of the model membrane could possibly influence its stability against damage by ethanol. However, our recent atomistic study on the effect of the E-protein on the stability of a mixed lipid bilayer, palmitoyl-sphingomyelin (PSM) and POPC, immersed in ethanol–water mixtures, has shown that the E-protein has a negligible effect on the partitioning of water and ethanol from the aqueous phase to the lipid phase of the membrane.³¹ In other words, the E-peptide has no appreciable effect on ethanol-induced viral membrane failure in the range of alcohol concentrations studied. Therefore, in this study, we focus our attention on the stability of protein-free DPPC-DMPC-DOPC mixed membranes, as models of the coronavirus membrane, immersed in water–ethanol solutions as disinfectants. It is worth mentioning that the stabilities of pure and mixed membranes, immersed in *pure* water, have been studied by several investigators.^{32,33} However, reports on the stability of mixed membranes, immersed in aqueous solutions containing alcohol, are scarce. This is particularly true at high alcohol concentrations, i.e., common concentrations in alcohol-based disinfectants, in which membrane disintegration becomes an issue of importance.

Atomistic simulations for the compositionally complex lipid mixtures are computationally expensive. Here, we employed a relatively affordable computer simulation method, dissipative particle dynamics (DPD), which, if carefully parametrized, can provide meaningful results. The DPD interaction parameters were chosen from the well developed four-to-one coarse-grained (CG) mapping scheme of the MARTINI-like models,^{34,35} in which four heavy atoms and their attached hydrogen atoms were mapped to one DPD bead. To validate our DPD models, we compared the structural and thermodynamic properties of lipid membranes of different compositions, surrounded by *pure* water, with those available from simulation and experiment. For the ethanol-containing systems, we further examined these properties to capture the effect of ethanol on the membrane stability. In addition to the elucidation of the mechanism of a disinfectant's influence on virus deactivation, we believe that the present study provides insight into numerous other applications such as drug delivery, anesthesia, and cryopreservation, where high concentrations of alcohols are used to modulate functions of biological membranes. Comparing the DPD results with our previous atomistic studies of coronavirus model membranes, we also assess the predictive ability of DPD as a CG model, allowing the achievement of longer time and length scales, which are inaccessible by atomistic simulations.

■ SIMULATION DETAILS

Model. The DPD method has been well described in the literature.³⁶ For its details, we refer the reader to excellent reviews in the literature.^{34,37} Here, we restrict ourselves to a brief explanation of the method. The nonbonded conservative force

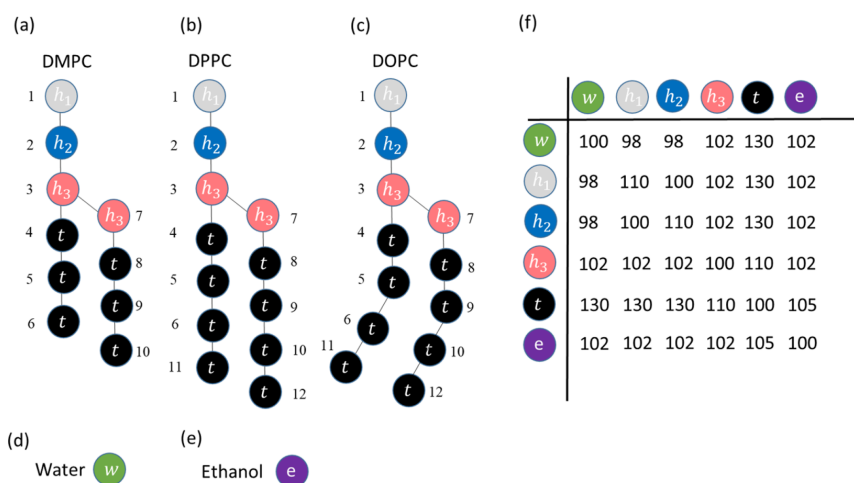


Figure 1. Models of (a) DMPC (dimyristoylphosphatidylcholine), (b) DPPC (dipalmitoylphosphatidylcholine), (c) DOPC (dioleoylphosphatidylcholine), (d) water, and (e) ethanol in this work. Each bead has a mass and volume comparable to four realistic water molecules. (f) The DPD repulsion parameters for all bead–bead interactions.

between two DPD beads i and j , $F_{ij}^C = \alpha_{ij}(1 - r_{ij}/r_c)\mathbf{e}_{ij}(r_{ij} < r_c)$, separated by a distance r_{ij} (\mathbf{e}_{ij} is the corresponding unit vector), is purely repulsive. The repulsion parameter α_{ij} controls the magnitude of repulsion. The cutoff distance (r_c), bead mass (m), and thermal energy per one bead ($k_B T$) are chosen as reduced units of length, mass, and energy in DPD simulation. The reduced time unit is defined accordingly as $t_{\text{DPD}} = r_c \sqrt{m/k_B T}$.

In this work, we have used the DPD model based on the four-to-one mapping scheme of the MARTINI model.^{34,35} For water at a reduced density $\rho = 3$, we map four water molecules into a single DPD bead. The volume of four water molecules is 0.12 nm³. As a cube of volume r_c^3 contains 3 water beads, the cutoff distance corresponds to 0.71 nm. At 298 K, each ethanol molecule has a volume of 0.097 nm³; therefore, the volume of 1.24 ethanol molecules (modeled as a single DPD bead) corresponds to the volume of four water molecules. For the lipid molecules, the volume of the DPD beads (see Figure 1) corresponds to the volume of a single water bead. Setting the DPD repulsion parameter for water, $\alpha_{ww} = 100$, accurately reproduces the compressibility of water at room temperature, $k^{-1} = 16$.^{36,37} The repulsion strength between the similarly charged beads of head groups was increased to compensate for the electrostatic repulsion ($\alpha_{h_1 h_1} = \alpha_{h_2 h_2} = 110$).³⁴ All other repulsion parameters for beads of the same type, α_{ij} , were set to 100. The repulsion parameter for water–ethanol interaction, 102, was taken from the literature.^{34,37} All other repulsion parameters between unlike beads, α_{ij} , were determined from the Flory–Huggins χ -parameter, according to the following expression by Li et al.³⁴

$$\chi = (0.277 \pm 0.002)\Delta\alpha \quad (1)$$

where $\Delta\alpha = \alpha_{ij} - \alpha_{ww}$. The Flory–Huggins χ -parameters between water and hydrocarbons and between the lipid head groups and hydrocarbons have been well discussed in the literature.^{34,37} Li et al.³⁴ reported that these parameters can well describe the compressibility and bending rigidity of the real membranes. In this work, some modifications have been made to

the parameter set reported in the literature.^{34,37} The DPD repulsion parameter α_{et} for the ethanol–tail (hydrocarbon) interaction was tuned, by scanning it over the range 104 to 110 (based on the reports in the literature),^{34,37} against the free energy barrier for the passage of a single ethanol molecule across the membrane, according to our previous atomistic simulation results (see the section [Validation of the Model for Ethanol-Containing Systems](#)).¹⁵ We have summarized the final DPD repulsion parameters for interactions between all bead types in Figure 1(f).

The DPD beads in phospholipids are connected by harmonic bonds

$$U_b(r) = \frac{1}{2}k_b(r - r_0)^2 \quad (2)$$

where U_b is the bond potential, and k_b and r_0 are the spring constant and equilibrium bond length, respectively. The bending angle potential, U_θ , is defined as

$$U_\theta(r) = k_\theta[1 - \cos(\theta - \theta_0)] \quad (3)$$

where k_θ is the force constant, and θ_0 is the equilibrium angle. We have reported the values of k_b , r_0 , k_θ , and θ_0 in Table 1.^{35,38} It should be noted that hydrocarbon chains of DPPC and DOPC are modeled by four connected tail beads, while those of DMPC are modeled as three tail beads. In the case of DOPC, the equilibrium 4–5–6 and 8–9–10 angles are set to 120° to mimic the unsaturated hydrocarbon chains.^{35,38}

In the ethanol-free systems, a total number of 1152 lipid molecules were placed in the center of the xy plane of an xyz periodic box. The dimensions of the simulation box along x and y directions, L_x and L_y , were set according to the known area per lipid molecule for the phospholipids.^{35,38} For the mixed membranes, L_x and L_y were set based on the additivity of the area per lipid for different components. We have tested different initial values of $L_x = L_y$, around the calculated area per lipid, and found that simulations of a constant number, N , of lipid molecules at constant temperature, T , and constant pressure, P , (the NPT ensemble) did not change the lateral dimensions of

Table 1. Equilibrium Bond Lengths and Angles and Their Corresponding Force Constants for DMPC (Dimyristoylphosphatidylcholine), DPPC (Dipalmitoylphosphatidylcholine), and DOPC (Dioleoylphosphatidylcholine)

bond potential			angle potential		
type	r_0 (r_c)	k_b ($k_B T/r_c^2$)	type	θ_0 (deg)	k_θ ($k_B T$)
$h_1 - h_2$	0.47	512	$h_2 - h_3 - t$	180	6
$h_2 - h_3$	0.47	512	$h_2 - h_3 - h_3$	120	6
$h_3 - h_3$	0.31	512	$h_3 - t - t$	180	6
$h_3 - t$	0.59	512	$t - t - t^a$	120, 180	6
$t - t$	0.59	512			

^aExcept for the 4-5-6 and 8-9-10 angles in DOPC, for which the equilibrium $t - t - t$ angle is 120°, the rest of the $t - t - t$ equilibrium angles are 180°.

the simulation box noticeably. The initial box size along the z direction was fixed at $24 r_c$ for all systems. The box size in our simulations was beyond the limit to which finite size effects have been reported to influence the properties studied.³⁹ Three types of systems, namely pure systems (DPPC, DOPC, and DOPC), two-component systems (DPPC-DOPC, DPPC-DMPC, and DMPC-DOPC), and three-component systems (DPPC-DOPC-DMPC), were simulated. In all mixed-membrane systems, the lipids were randomly placed in each leaflet. Therefore, the compositions of both leaflets were the same, but the leaflets were not symmetric (see Figure 2(a)). The compositions of all ethanol-free lipid bilayers simulated in this work are summarized in Figure 2(b). We have simulated the afore-cited lipid bilayers, immersed initially in pure water, in the NPT ensemble to obtain relaxed planar bilayers. To simulate a tensionless membrane, the sizes of the simulation box in the lateral (xy) and normal (z) directions were allowed to change independently, by coupling them to a Berendsen barostat.^{40,41} (the time constants for pressure couplings were $10 t_{\text{dpd}}$). The lateral and normal components of the pressure were fixed at $89 k_B T/r_c^3$, which is the same as that for bulk water at a reduced density of 3. Simulations were done for 5×10^5 steps to achieve equilibrium and for another 5×10^5 steps for data collection.

In the ethanol-containing systems, the number of water and lipid molecules in the system was the same as that of the ethanol-

free systems, but ethanol molecules were added to the aqueous phase to reach the desired concentration of ethanol in water. According to the adopted mapping scheme, the mole fraction of ethanol in the aqueous phase surrounding the membrane is expressed as

$$x_{\text{ethanol}} = \frac{1.24 \cdot n_{\text{ethanol}}}{1.24 \cdot n_{\text{ethanol}} + 4 \cdot n_{\text{water}}} \quad (4)$$

where n_{ethanol} and n_{water} are the number of DPD beads of ethanol and water, respectively. The factors 1.24 and 4 in eq 4 account for the fact that in our mapping one DPD bead represents 1.24 real ethanol molecules but 4 water molecules. Thus, the ethanol mole fraction in this paper corresponds to the experimental mole fraction, not to the mole fraction of DPD beads used. The latter is much closer to the experimental volume fraction, since all DPD beads have the same size. In contrast to the solvent phase, no adjustment is necessary for the mole fractions describing the lipid compositions of the membranes. We have summarized the compositions of systems simulated in this work in Table 2.

Table 2. Compositions of the Water–Ethanol Phase in the Systems Simulated in This Work

mol % of ethanol	wt % of ethanol
0.00	0.00
5.19	12.3
10.3	22.7
13.3	28.1
15.4	31.8
17.1	34.6
20.2	39.4
23.7	44.3
27.5	49.3
31.7	54.4
42.0	64.9
55.4	76.1
73.6	87.7

Based on the mapping scheme adopted in this work,³⁴ the cutoff distance and the time step were 0.71 nm and 1.43 ps ($0.01 t_{\text{dpd}}$), respectively. In order to compare our results with the

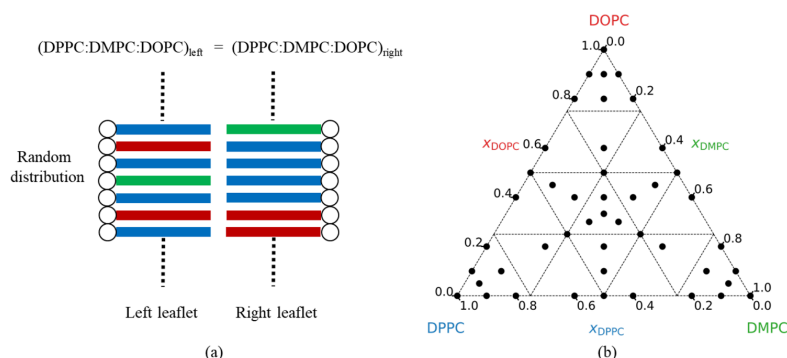


Figure 2. (a) Schematic of the arrangement of lipid chains in each leaflet in a ternary membrane. Blue, green, and red colors represent DPPC (dipalmitoylphosphatidylcholine), DMPC (dimyristoylphosphatidylcholine), and DOPC (dioleoylphosphatidylcholine) lipid molecules, respectively. The compositions of both leaflets are the same, but the membrane is not symmetric. (b) Schematic illustration of systems simulated in this work. The points represent compositions of the systems simulated in this work.

Table 3. Calculated Equilibrium Thermodynamic and Mechanical Properties of Lipid Bilayers, Compared with Previous Simulations and Experiments^a

ratio			this work 298 K				previous simulations			previous experiments		
x_{DPPC}	x_{DMPC}	x_{DOPC}	l_0 (nm)	a_0 (nm ²)	S_0	κ_0 (10 ⁻¹⁹ J)	l_0 (nm)	a_0 (nm ²)	κ_0 (10 ⁻¹⁹ J)	l_0 (nm)	a_0 (nm ²)	κ_0 (10 ⁻¹⁹ J)
1	0	0	4.76	0.576	0.894	12.496	4.71 ^{43a}	0.487 ^{43a}	7.1–8.9 ^{47a}	4.35 ^{15a}	0.50 ^{50a}	
0	1	0	3.52	0.651	0.467	0.471	3.53 ^{51a}	0.597 ^{52a} , 0.606 ^{51a}	0.56 ^{48a}	3.47 ^{53a}	0.616 ^{53a}	
0	0	1	3.89	0.706	0.426	0.557	3.67 ^{44a} , 3.71 ^{46a}	0.724 ^{44a} , 0.674 ^{45a}	0.8–2.2 ^{47a}	3.82 ^{53a}	0.695 ^{53a}	
0.25	0.75	0	3.57	0.647	0.476	0.454					0.74 ^{33b}	
0.5	0.5	0	4.38	0.627	0.556	0.851					0.72 ^{33b}	
0.75	0.25	0	4.53	0.601	0.636	5.24					0.70 ^{33b}	
0.333	0.333	0.333	4.12	0.671	0.516	0.62						

^aRepresents the reference value obtained at 298–303 K. ^bRepresents the reference value obtained at 325 K.

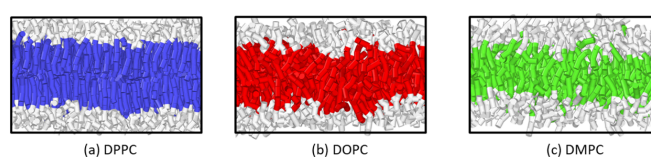


Figure 3. Snapshots of the simulation box, indicating pure (a) DPPC (dipalmitoylphosphatidylcholine), (b) DOPC (dioleoylphosphatidylcholine), and (c) DMPC (dimyristoylphosphatidylcholine) lipid bilayers. Blue, green, and red colors represent the hydrocarbon tails of DPPC, DMPC, and DOPC lipids, respectively.

reports in the literature, we use physical, rather than reduced DPD, units from here on.

Analysis Method. We use four parameters, including the area per lipid molecule, bilayer thickness, orientational order of the hydrocarbon chain, and the bending modulus, to characterize the degree of molecular perturbation caused by the ethanol disinfectant. Specifically, the area per lipid molecule, bilayer thickness, and bending modulus are useful only for the membranes that are still intact, i.e., without obvious holes. The membrane thickness l is defined as the average distance between the choline groups (h_1 in Figure 1) in two leaflets and the area per lipid, a , is defined as

$$a = \frac{L_x \cdot L_y}{N} \quad (5)$$

where N is the number of lipid molecules in each leaflet. The orientational order is defined in terms of the following second-Legendre polynomial

$$S = 0.5(3 \cos^2 \theta - 1) \quad (6)$$

where θ is the angle between a unit vector along the hydrocarbon chain and the bilayer normal unit vector (z axis), and the brackets denote ensemble average. Two hydrocarbon chains of each lipid molecule (Figure 1(a)–(c)) are calculated separately to the connection points (h_3 groups). Goetz et al.⁴² found that the value of bending modulus, κ , deduced from the analysis of the shape fluctuations of the bilayer membranes (in the tensionless state), can be expressed as the following equation

$$\kappa = \frac{K_A l^2}{48} \quad (7)$$

where K_A is the area compressibility. In order to calculate K_A , we measure fluctuations of the interfacial tension, γ . The area per lipid molecule, a , is varied by modifying the lateral size in the NVT ensemble (V being the volume). Then, K_A can be obtained

as the zero-tension limit of the slope of the interfacial tension versus $(a - a_0)/a_0$ as⁴²

$$\gamma = K_A(a - a_0)/a_0 \quad (8)$$

where a_0 is the area per lipid molecule in a tensionless membrane (membrane immersed in the pure water). It should be noted that this procedure for calculation of κ is only suitable for the membranes with negligible spontaneous curvature.³⁴ The interfacial tension γ can be obtained from the pressure anisotropy as

$$\gamma = \left\langle \frac{L_z}{2} \left[P_{zz} - \frac{1}{2}(P_{xx} + P_{yy}) \right] \right\rangle \quad (9)$$

where P_{xx} , P_{yy} , and P_{zz} are the diagonal components of the pressure tensor.

RESULTS AND DISCUSSION

Validation of the Bilayer Models for Ethanol-Free Systems. To validate the lipid bilayer model, immersed in water, we have calculated the area per lipid molecule, a_0 , the membrane thickness, l_0 , the orientation order of hydrocarbon groups, S_0 , and the bending modulus, κ_0 . As summarized in Table 3, our calculated a_0 and l_0 of DPPC, DMPC, and DOPC are in good agreement with experiments^{43–46} at temperatures close to 300 K. Poghosyan and Gharabekyan³³ have investigated the DPPC-DMPC membranes of various compositions at 325 K by performing atomistic simulations. Their observed trend of decreasing a_0 versus x_{DPPC} is compatible with the trend found at 298 K here (see Table 3). For DPPC, closeness of value of S_0 to 1 ($S_0 = 0.894$) indicates that the bilayer is in the gel phase, in which the hydrocarbon chains are in a highly ordered state (Figure 3(a)), while DMPC ($S_0 = 0.467$) and DOPC ($S_0 = 0.426$) bilayers are in the fluid phase, as illustrated in Figure 3(b),(c). The deviations of bending moduli obtained in this work from experimental values of DPPC (~29% to 76%),⁴⁷ DMPC (~-16%),⁴⁸ and DOPC (~-30% to -75%)⁴⁷ can partly be

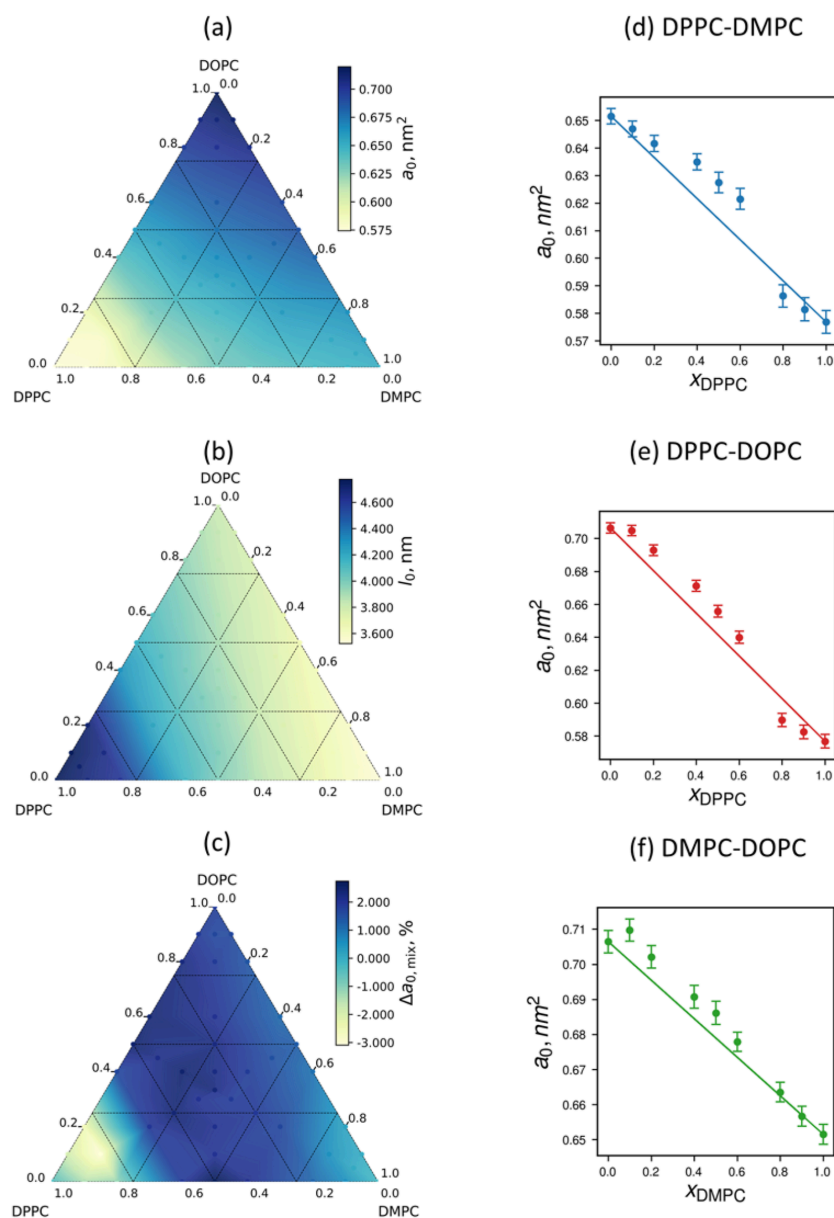


Figure 4. Two-dimensional plots of variation of (a) the area per lipid molecule and (b) the thickness of the bilayer as a function of composition for the ethanol-free systems at 298 K. The color bars represent the area per lipid molecule and the membrane thickness in panels a and b, respectively. (c) $\Delta a_{0,\text{mix}} = a_0 - a_{0,\text{ideal}}$ for mixed membranes. (d–f) Composition-dependence of the area per lipid molecule for DPPC (dipalmitoylphosphatidylcholine)-DMPC (dimyristoylphosphatidylcholine), DPPC-DOPC (dipalmitoylphosphatidylcholine), and DMPC-DOPC binary membranes. The dashed lines indicate the ideal mixing behavior (see eq 10).

due to the softness of DPD beads in our simulations and partly due to experimental uncertainties in measuring the bending modulus. Chaurasia et al.⁴⁹ have compared several methods of evaluating the bilayer bending modulus in simulations and reported that the bending modulus of PC lipid membranes in

the fluid state (325 K) was within the range of $\kappa_0 \sim (0.4–2.1) \times 10^{-19}$ J, which matches well with our calculated results ($\sim(0.4–0.9) \times 10^{-19}$ J) for PC membranes in the liquid phase at 298 K. Because of the lack of experimental data, we cannot compare our calculated bending moduli for mixed membranes with the

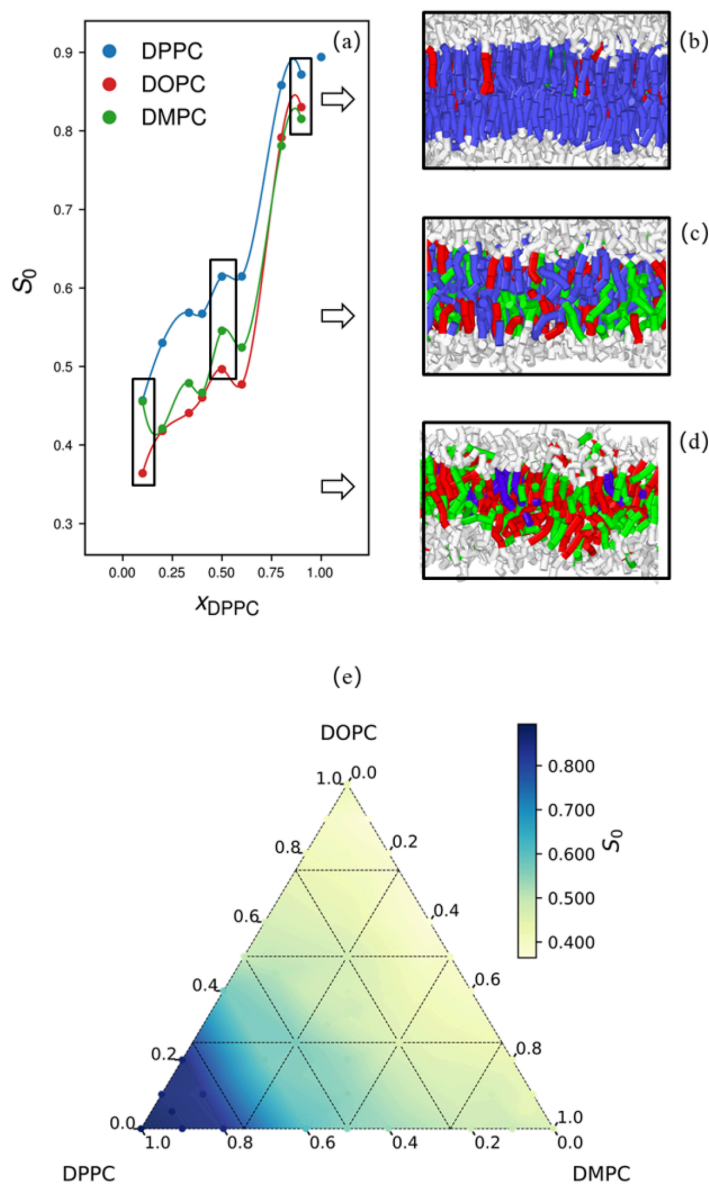


Figure 5. (a) Dependence of the orientational order parameter, S_0 , on the composition for DOPC (dipalmitoylphosphatidylcholine)-DMPC (dimyristoylphosphatidylcholine)-DPPC (dioleoylphosphatidylcholine) ternary bilayers with $x_{\text{DOPC}} = x_{\text{DMPC}}$. (b–d) From top to bottom, snapshots of the simulation box indicating mixed bilayers with $(x_{\text{DPPC}}, x_{\text{DOPC}}, x_{\text{DMPC}}) = (0.1, 0.45, 0.45)$, $(0.5, 0.25, 0.25)$, and $(0.9, 0.05, 0.05)$, respectively. Blue, green, and red colors represent the hydrocarbon tails of DPPC, DMPC, and DOPC lipids, respectively. (e) Dependence of the orientational order of mixed bilayers on the composition for bilayers immersed in pure water at 298 K.

experiment. Based on the agreement of our calculated values of a_0 , l_0 , S_0 , and κ_0 for membranes immersed in pure water, with the corresponding experimental values, we conclude that our DPD models are well parametrized against experimental measurements.

Effect of Composition on the Properties of Membranes in the Absence of Ethanol. Figure 4 depicts the

calculated values of a_0 and l_0 as a function of composition for different membranes.

We found that the area per lipid molecule, a_0 , generally decreases with increasing the mole fraction of DPPC (Figure 4(a)). The trend of the increase in a_0 is $a_0(\text{DOPC-dominated bilayer}) > a_0(\text{DMPC-dominated bilayer}) > a_0(\text{DPPC-dominated bilayer})$. The reverse is true for the bilayer thickness, i.e.,

$l_0(\text{DPPC-dominated bilayer}) > l_0(\text{DOPC-dominated bilayer}) > l_0(\text{DMPC-dominated bilayer})$. We may conclude that in mixed PC membranes, two factors determine the degree of packing of hydrocarbon tails and, hence, the surface area per lipid molecules: the hydrocarbon tail length and its degree of saturation. Membranes consisting of longer hydrocarbon chains (like DPPC) occupy less surface area per lipid molecule than those consisting of shorter hydrocarbon tails (like DMPC). The presence of unsaturated bonds in the hydrocarbon tail acts as a defect for chain packing. Therefore, bilayers containing bends due to unsaturated bonds in their hydrocarbon tails (like DOPC) are less ordered and occupy a larger area per lipid molecule than those with saturated hydrocarbon tails of the same length (like DPPC). There is the same trend for the surface area per lipid molecule in the mixed binary and ternary bilayers. Mixed bilayers composed of DPPC (with its longer saturated hydrocarbon tail) as the major component occupy less surface area per lipid molecule than DMPC-rich (with shorter saturated hydrocarbon tail) bilayers. The maximum surface area per lipid molecule, however, belongs to mixed membranes with DOPC (with a longer unsaturated hydrocarbon tail) as the major component. As the hydrocarbon chain lengths in DOPC and DMPC do not differ considerably, the existence of an unsaturated bond in DOPC plays the dominant role in surface area per lipid molecule and bilayer thickness. We have checked if the parameters a_0 and l_0 for mixed membranes can be expressed as the sum of contributions due to their constituents (ideal mixing), i.e.,

$$a_{0,\text{ideal}} = \sum_i x_i a_{i,0} \quad (10)$$

and

$$l_{0,\text{ideal}} = \sum_i x_i l_{i,0} \quad (11)$$

in Figure 4. In eqs 10 and 11 x_i is the mole fraction of the component i , and subscript "ideal" stands for the ideal mixing. We have quantified the excess area $\Delta a_{0,\text{mix}} = a_0 - a_{0,\text{ideal}}$ in Figure 4(c); the same is done for the excess thickness $\Delta l_{0,\text{mix}} = l_0 - l_{0,\text{ideal}}$ for which the results are reported in Figure S2 of the Supporting Information. The close agreement between calculated and predicted values indicates that in mixed membranes the ideal mixing rule can be regarded as a fairly good approximation for estimation of the area per lipid molecule and the membrane thickness. Shown in Figure 4(d),(e) are the area per lipid molecule of the binary membranes as a function of composition and their deviations from ideality. This near-ideal behavior of mixed membranes is in complete agreement with experimental measurement on DMPC-DSP (distearoylphosphatidylcholine)⁵⁴ and atomistic simulation results on DPPC-DLPC (dilauroylphosphatidylcholine)⁵⁵ membranes.

Another structural parameter to characterize the order of the lipid chain in membranes is the orientational order parameter, S_0 . $S_0 = 1$ would indicate perfect alignment of the hydrocarbon tails with the chain normal, whereas $S_0 = 0$ corresponds to random orientations. The correlation between S_0 and x_{DPPC} for ternary lipid bilayers (in which $x_{\text{DMPC}} = x_{\text{DOPC}}$) is shown as an example in Figure 5(a). We observe that S_0 increases with increasing the mole fraction of DPPC. Snapshots of three ternary lipid bilayers with $x_{\text{DPPC}} = 0.1, 0.5, \text{ and } 0.9$ are shown in Figure 5(b)–(d). At low DPPC mole fractions (Figure 5(b)), the DPPC molecules are disordered by the DMPC and DOPC molecules, resulting in a low value of S_0 . On the other hand, the

better ordered DPPC molecules induce ordering in the DOPC and DMPC molecules at higher DPPC mole fractions (Figure 5(d)). This induced ordering effect is more evident for DMPC than for DOPC molecules. Figure 5(e) shows S_0 as a function of composition for mixed membranes of various compositions. We found that S_0 generally increases with the DPPC content. Additionally, the DMPC-rich membranes are better ordered than DOPC-rich membranes. This can be interpreted in terms of a higher order of hydrocarbon chains in DMPC than those in DOPC (see Table 3).

We have also examined the dependence of the bending modulus κ_0 on the composition of the lipid bilayer in Figure 6.

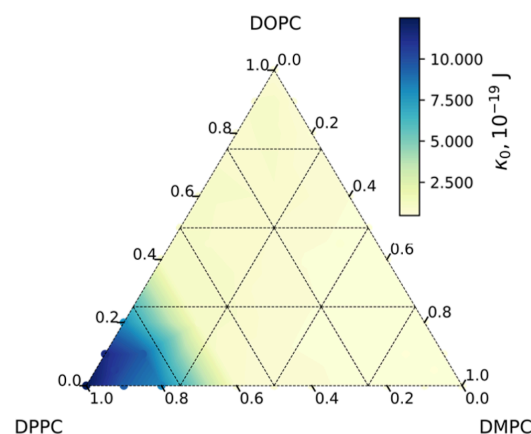


Figure 6. Dependence of the bending modulus of mixed membranes on the composition for membranes immersed in pure water at 298 K.

Our findings indicate that the bending modulus is more sensitive to the composition than the order parameter, the area per lipid molecule, and the membrane thickness. In this case, the DPPC-rich ($x_{\text{DPPC}} > 0.7$) membranes have much higher bending moduli than the others. At the same time, increasing the DPPC mole fraction in binary and/or ternary membranes to a regime with $x_{\text{DPPC}} \sim 0.7$ has only a marginal effect on the bending modulus, and a sharp increase in the bending modulus is seen at $x_{\text{DPPC}} > 0.7$. The bending modulus of lipid membranes with a higher fraction of DPPC ($x_{\text{DPPC}} > 0.8$) is much higher than those with lower DPPC content. Our findings are indicative of the diverse change in the structural properties of lipid bilayers with varying compositions. Examination of the composition-dependence of the bending modulus and its sharp transition at high DPPC mole fractions may raise a question; would it be possible to design a mixed membrane with tunable stability. This is important for the investigation of the effect of ethanol on the stability of membrane, to be discussed.

Validation of the Model for Ethanol-Containing Systems. We have tuned the DPD repulsion parameter for the ethanol-tail interaction against our recent atomistic simulation results⁵⁶ for the partitioning of ethanol between the aqueous and membrane phases for DPPC immersed in aqueous solutions containing ethanol. The experimental gel to liquid crystalline phase transition temperature of DPPC is 315 K.⁵⁷ To characterize the thermodynamic state of our DPPC model, we have shown the temperature-dependence of the order parameter in Figure S2. The sudden change in the order

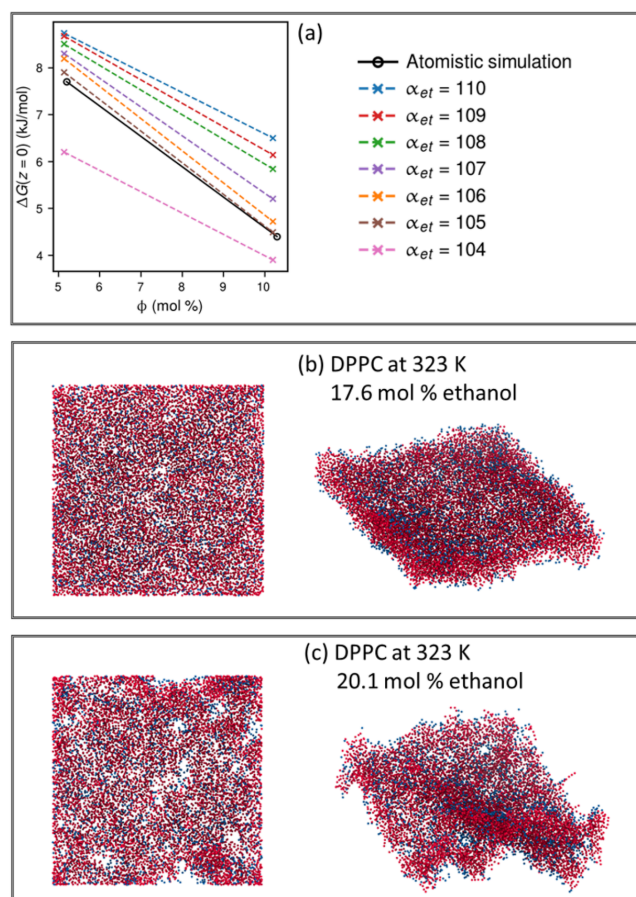


Figure 7. (a) Free energy barrier for the permeation of ethanol in the DPPC (dipalmitoylphosphatidylcholine) lipid bilayer, immersed in an aqueous solution containing ~5 and 10 mol % ethanol, at 323 K. The position $z = 0$ corresponds to the center of the bilayer. The DPD repulsion parameter α_{et} for ethanol-tail (hydrocarbon) beads is varied from 104 to 110 to find the best match between barrier heights calculated from atomistic¹⁵ and DPD simulations. (b) and (c) Snapshots (at 1 μ s) of a DPPC lipid bilayer, surrounded in aqueous solutions containing (b) 17.7 mol % and (c) 20.2 mol % ethanol, at 323 K. The blue and red spheres show head groups and tails, respectively. The water and ethanol molecules are not displayed for clarity.

parameter at $T = 320$ K is indicative of the gel to liquid crystalline phase transition. We performed DPD simulations for DPPC immersed in aqueous solutions containing 5 and 10 mol % ethanol at 323 K. We have calculated the Gibbs free energy (molar) profiles for translocation of ethanol molecules across the membrane from the equilibrium density profiles, i.e.,

$$\Delta G(z) = \mu_i^{\text{ex}}(z) - \mu_i^{\text{ex}}(\text{aqueous}) = -k_B T \ln \left[\frac{\rho_i(z)}{\rho_i(\text{aqueous})} \right] \quad (12)$$

where μ_i^{ex} is the excess chemical potential, i.e., the difference between the chemical potential and that of an ideal gas, ρ is the number density, k_B is the Boltzmann constant, T is the temperature, and $\mu_i^{\text{ex}}(\text{aqueous})$ and $\rho_i(\text{aqueous})$ are the chemical potential and the density in the aqueous phase (surrounding the membrane), respectively. In eq 12, the $\Delta G(z)$ is the molar Gibbs free energy change for transferring a solute molecule i (ethanol) from the bulk aqueous phase to a position z . The free energy profiles for the permeation of ethanol

(calculated by scanning the DPD interaction parameter for ethanol-tail, α_{et} , between 104 and 110) through a DPPC bilayer immersed in an aqueous solution containing 5 and 10 mol % ethanol are shown in Figure 7(a). The repulsion parameter $\alpha_{et} = 105$ best predicts the calculated barrier heights from atomistic simulations. While our previous atomistic simulations show that ethanol introduces a big hole in a DPPC membrane immersed in an aqueous solution containing (17.5 mol %) ethanol, the present DPD simulations predict the DPPC membrane to remain intact at similar ethanol concentrations of 17.7 mol % (up to 1 μ s). To search for the minimum ethanol concentration in the aqueous phase necessary to cause membrane rupture, we have simulated a number of systems in which DPPC is immersed in aqueous solutions containing 17 to 22 mol % ethanol. Our DPD simulations confirm that the membrane undergoes rupture at a slightly higher ethanol concentration (20.2 instead of 17.5 mol %) (see Figure 7). This is a second check for the agreement of our DPD simulation results with atomistic simulation results. Furthermore, in agreement with our atomistic simulation

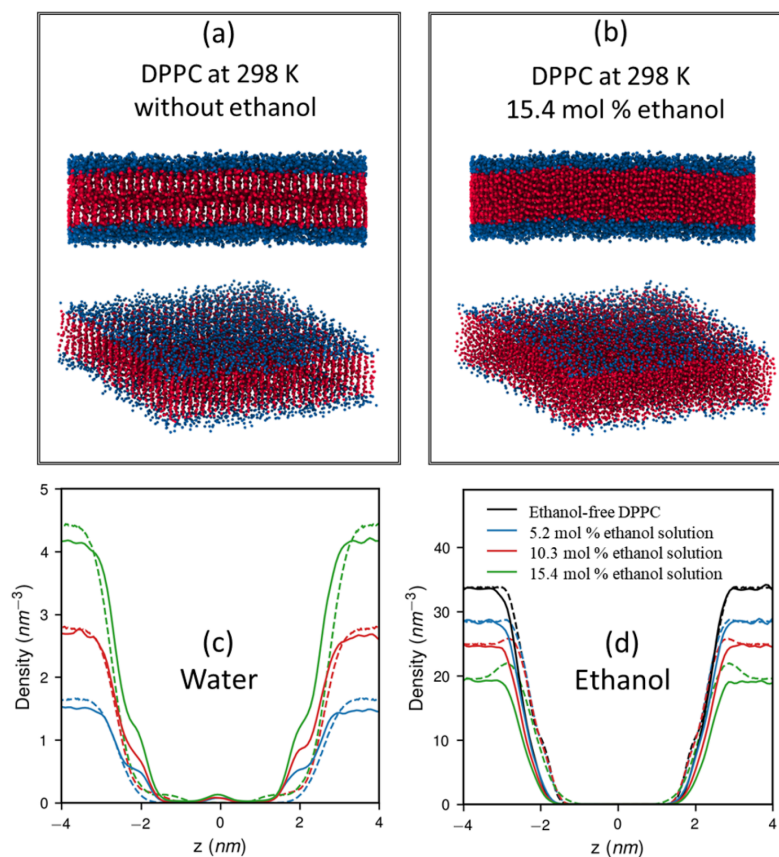


Figure 8. Snapshots (at $1 \mu\text{s}$) of DPPC (dipalmitoylphosphatidylcholine) lipid bilayers, surrounded by (a) pure water and by (b) an aqueous solution containing 15.4 mol % ethanol at 298 K. The blue and red spheres show head groups and tails, respectively. The water and ethanol molecules are not displayed for clarity. Comparison of the number density profiles, calculated from DPD (full curves) and atomistic (dashed curves) simulations, for (c) ethanol and (d) water across the DPPC membrane surrounded by aqueous solutions containing 0, 5, 10, and 15 mol % ethanol at 298 K.

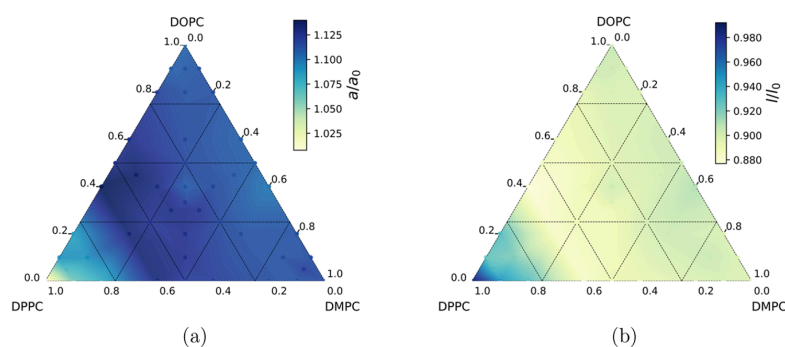


Figure 9. (a) Dependence of the ratio of surface area per lipid molecule for membranes surrounded by an aqueous solution containing 5 mol % ethanol to the corresponding value in the absence of ethanol (a/a_0) on the composition of membrane. (b) The same as (a) for the membrane thickness. a_0 and l_0 are the area per lipid and membrane thickness, respectively, in the ethanol-free systems.

results, we found that the DPPC membrane remains intact at an ethanol concentration of 15.4 mol % at 298 K. This is due to the

fact that the DPPC exists in the more intact gel phase at 298 K. The tight packing of lipid molecules in DPPC is weakened in the

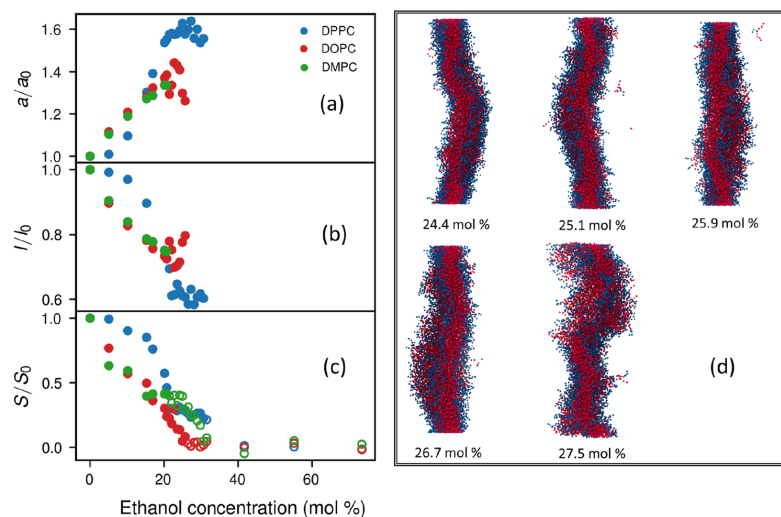


Figure 10. Dependence of (a) area per lipid molecule, (b) membrane thickness, and (c) the orientational order parameter of pure DMPC (dimyristoylphosphatidylcholine), DOPC (dioleoylphosphatidylcholine), and DPPC (dipalmitoylphosphatidylcholine) membranes on the ethanol concentration in the aqueous phase surrounding the membrane. Open (panel c) and filled markers represent the ruptured and intact bilayers, respectively. (d) Snapshots (at 1 μ s) of DOPC lipid bilayers at 298 K, surrounded by aqueous solutions containing 24.4–26.7 mol % ethanol, i.e., close to the rupture-critical ethanol concentration (27.5 mol %) needed for membrane rupture. The blue and red spheres show head groups and the lipid tails, respectively.

presence of 15.4 mol % ethanol (Figure 8(b)), but the membrane remains intact. We show the number density profiles for ethanol and water, partitioned between the aqueous and membrane phases, in Figure 8(c),(d). We observed that increasing the ethanol concentration in the aqueous phase causes accumulation of both ethanol and water molecules near the membrane head groups, and they penetrate further into the region of the hydrocarbon-headgroup interface. This is in complete agreement with the results of our previous atomistic simulations. Because of the fact that the DPD beads are much softer than the atomistic sites, we observe that water and ethanol molecules are exchanged several times between the aqueous phase and the membrane during the time scale of our simulations.

Effect of Ethanol on the Structure of the Lipid Bilayer.

We have summarized the variation of the area per lipid molecule, a , and the membrane thickness, l , for mixed membranes immersed in aqueous solutions containing 5 mol % ethanol and compared them with the corresponding values for ethanol-free water in Figure 9. We found ethanol uptake expands all pure and mixed lipid bilayers laterally (Figure 9(a)) and shrinks them vertically (Figure 9(b)). Among all membranes, the area per lipid and the membrane thickness of DPPC-rich ($x_{\text{DPPC}} > 0.8$) membranes were not significantly affected by the presence of ethanol. The largest changes of the area per lipid molecule and the membrane thickness between membranes immersed in water–ethanol solutions and in ethanol-free solutions are seen for lipid bilayers with $0 < x_{\text{DPPC}} < 0.8$. This indicates that the effect of ethanol on the stability of a membrane depends on its composition. It is worth mentioning that all pure and mixed membranes examined in this work, surrounded by an aqueous solution containing 5 mol % ethanol, are intact (based on a visual inspection of the simulation and density profiles).

Membrane Failure. a. Characterization in Terms of Area Per Lipid, Thickness, and Orientational Order. We have searched for the rupture-critical ethanol concentration in the aqueous phase, needed to cause the rupture of pure DPPC, DMPC, and DOPC membranes, immersed in such a solution. In addition to the ethanol concentrations tabulated in Table 2, we have simulated pure membranes, each immersed in 12 aqueous solutions containing ethanol of varying concentrations from 20 to 32 mol %. Here, the membrane failure was characterized in terms of visual observation of long-lived holes in the membrane. The rupture-critical ethanol concentrations for membrane failure at 298 K are 20.7, 27.5, and 31.7 mol % in the aqueous phase surrounding pure DMPC, DOPC, and DPPC, respectively. In order to establish a link between membrane stability and the parameters (area per lipid molecule a , membrane thickness l , and orientational order of hydrocarbon chains s) discussed above, we have calculated the relative change of each parameter upon transferring the pure membrane (DPPC, DMPC, and DOPC) surrounded by water to an aqueous solution containing ethanol of a given concentration. In Figure 10, we show the ratios of the area per lipid molecule, membrane thickness, and orientational order of the hydrocarbon tail for pure DPPC, DMPC, and DOPC membranes (immersed in aqueous solutions containing ethanol) to the corresponding value in the absence of ethanol. Because of the ambiguity in calculating the area per lipid molecule and membrane thickness for disrupted membranes, we have reported the ratios a/a_0 and l/l_0 only for intact membranes (up to 1 μ s simulation time) in Figure 10(a),(b), but the ratio S/S_0 (Figure 10(c)) was reported for both intact and ruptured membranes. For all three membranes, the a/a_0 increases (by a factor up to ≈ 1.6 for DPPC), and l/l_0 decreases (by a factor ≈ 0.6 for DPPC) with the increasing ethanol concentration in the aqueous phase surrounding the membrane. We have also shown the ratio of

$(a-l)/(a_0l_0)$ as a function of the ethanol concentration (see Supporting Information Figure S4). We found that the membrane volume is less sensitive to the presence of ethanol in the aqueous phase as compared to the surface area and the membrane thickness. Larger fluctuations in the area per lipid molecule and membrane thickness at high ethanol concentrations (which can be regarded as a signature of the stability-failure transition) are the results of frequent opening and closing of holes in the membrane, induced by ethanol. This indicates that ethanol weakens the membrane by fluidizing it, which increases the area per lipid molecule and decreases the membrane thickness, and eventually introduces holes in the membrane, leading to its rupture. The fluidizing effect of ethanol on the membrane obviously decreases the orientational order of the hydrocarbon tail (see Figure 10(d)). Compared to the ratios a/a_0 and l/l_0 , larger deviations are seen for the ratio S/S_0 upon transferring the membrane from pure water to water–ethanol solutions. In this case, the ruptured states can be identified by small values of S/S_0 (close to zero), where $S = 0$ corresponds to the complete random orientation of tails. However, no sharp transition from the intact to the ruptured state, and vice versa, is observed in terms of the orientational order parameter. In other words, we cannot quantitatively predict the location of the phase transition point based on the area per lipid molecule, the membrane thickness, and the orientational order parameter. In order to discriminate between intact and ruptured membranes, we show snapshots (taken at 1 μ s) of the structure of DOPC, immersed in aqueous solutions whose ethanol concentration is close to (but below) the rupture-critical ethanol concentration needed to disrupt the membrane (Figure 10(d)). At the highest ethanol concentrations, the membrane undulates, and even a few lipid molecules are extracted from it. At 26.7 mol % ethanol concentration (just below the phase transition point), the membrane thickness is nonuniform, but it still remains intact (up to 1 μ s). Upon further increase of the ethanol concentration, some parts of the membrane become thin enough to allow free (barrierless) passage of ethanol across the membrane, i.e., a big hole is formed in the membrane.

b. Ethanol Penetration: Partition Coefficient and Permeation Dynamics. The partitioning of ethanol between the lipid membrane and the aqueous phase can be characterized in terms of the partition coefficient

$$K_p = \frac{c_{\text{ethanol}}^{\text{lipid}}}{c_{\text{ethanol}}^{\text{aq}}} \quad (13)$$

where $c_{\text{ethanol}}^{\text{lipid}}$ and $c_{\text{ethanol}}^{\text{aq}}$ are the equilibrium mole concentrations of ethanol in the lipid membrane and in the aqueous phase, respectively. It is noted that $c_{\text{ethanol}}^{\text{aq}}$ is defined as the equilibrium ethanol concentration, which is different from the initial ethanol concentration (before equilibrium). In order to calculate K_p , the number of ethanol molecules in the lipid membrane ($n_{\text{ethanol}}^{\text{lipid}}$) and aqueous phase ($n_{\text{ethanol}}^{\text{aq}}$) and the respective volumes of these two regions (V^{lipid} and V^{aq}) are computed. These parameters, however, cannot be calculated unambiguously, especially at the high ethanol concentrations, where the interface between the regions becomes blurred. Terama et al.⁵⁸ have calculated $c_{\text{ethanol}}^{\text{aq}}$ by assigning the ethanol molecules in the region away from the membrane boundary to the aqueous phase (where the density profiles almost converge to a constant value) and assigning the rest of the ethanol molecules (bounded) to the membrane. These “bounded” ethanol molecules are partly influenced by the membrane, although not completely partitioned into it. Inspired

by a recent work,⁵⁹ we have adopted a method based on the assumption that any deviations in the Gibbs free energy profiles from the corresponding values in the aqueous phase ($\Delta G_{\text{bulk}} \approx 0$) must be due to interactions with the membrane. We have partitioned the simulation along the z direction into a number of bins of width 0.305 nm. The boundary between the lipid membrane and aqueous phases is defined as the layer with $|\Delta G(z) - \Delta G(z)_{\text{bulk}}| = 0.1$ kJ/mol. The results for K_p of three single-lipid membranes in the aqueous phases containing ethanol of varying concentrations from 5 mol % to the concentrations just before rupture are shown in Figure 11.

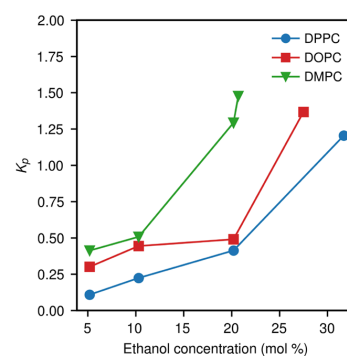


Figure 11. Dependence of the partition coefficient K_p of pure DMPC (dimyristoylphosphatidylcholine), DOPC (dioleoylphosphatidylcholine), and DPPC (dipalmitoylphosphatidylcholine) membranes on the ethanol concentration, in the aqueous phase surrounding the membrane, at 298 K.

The partition coefficients of the pure membranes increase with the increasing ethanol concentration in the aqueous phase surrounding the membrane. This means that the amount of ethanol in the membrane increases disproportionately with the ethanol concentration in the aqueous phase. This is indicative of a synergistic effect. Moreover, the values of the partition coefficients close to the rupture points are nearly the same for the three membranes.

To study the dynamics of the permeation of ethanol through the membrane, we applied an external force to drag two selected ethanol molecules through the membrane (z direction).⁶⁰ We used pure DPPC, DMPC, and DOPC membranes immersed in pure water (where the membrane is stable) and in aqueous solutions containing 20.7, 27.5, and 31.7 mol % ethanol (corresponding to the state point at which the membrane disrupts), respectively. For membranes in pure water, two ethanol molecules were added to the aqueous phase for this purpose. In ethanol-containing systems, two ethanol molecules were selected near the box boundary. Simulations were performed from the equilibrated systems (at 1 μ s). Constant external forces of equal magnitude but opposite directions were imposed on the two ethanol molecules (Figure 12(a)). We tried several drag forces with magnitude ranging from 0.58 to 17.4 pN for all systems. No crossing event has been observed for the DPPC membrane in pure water with an external force up to 5.8 pN within 143 ns. For DOPC and DMPC lipid membranes, however, we have seen at least one crossing event with the same force. For the DPPC membrane, increasing the external force, a full cycle (an ethanol molecule traversing the entire box length along the z direction) was observed at 8.8 pN within 143 ns.

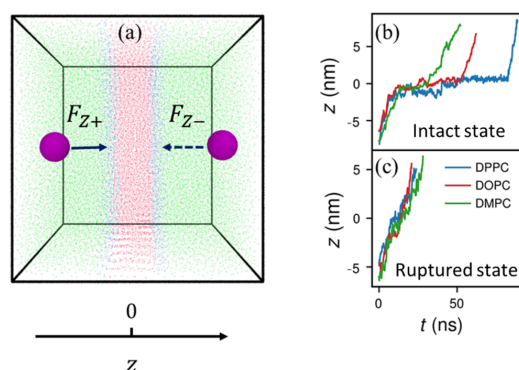


Figure 12. (a) Snapshots (at 1 μ s) of the DPPC (dipalmitoylphosphatidylcholine) lipid bilayer, surrounded by pure water with the addition of two ethanol molecules (purple colored spheres), experiencing external forces along the z axis in different directions at 298 K. The blue and red spheres show head groups and lipid tails, respectively, and the green spheres show water molecules. Tracking the position of ethanol molecules experiencing external forces along the z axis (11.6 pN) in pure DMPC (dimyristoylphosphatidylcholine), DOPC (dioleoylphosphatidylcholine), and DPPC membranes surrounded by (b) pure water and (c) aqueous solutions containing 20.7, 27.5, and 31.7 mol % ethanol, respectively, at 298 K.

Hence, we have fixed the external force at 11.6 pN, to be able to observe enough crossing events and also not so fast crossing the membrane in the high ethanol concentration systems. As shown in Figure 12(b), for membranes immersed in pure water, the crossing period for DPPC is longer than those of DPMC and DOPC, and the limitation of the crossing is due to the time spent in the membrane. At high ethanol concentrations, however, the crossing periods for all three membranes are comparable, and crossing the membrane is as fast as crossing the aqueous phase. In order to quantitatively describe the crossing behavior, we have run 5 independent simulations for each system for a long time (715 ns). The average velocity of ethanol molecules crossing the lipid membrane is defined based on the average time it takes them to cross the membrane. The results have been summarized in Table 4. For all three membranes, the number of crossing events and the crossing rate are similar when the membranes are in the ruptured state.

Table 4. Number of Crossing Events within 715 ns and the Average Velocity of Ethanol Molecules Crossing the Lipid Membrane Experiencing an External Force of 11.6 pN at 298 K^a

system	ethanol (mol %)	n_{cross}	$ v_{\text{cross}} $ (m/s)
DPPC in intact state	0	6	0.06
DMPC in intact state	0	14	0.10
DOPC in intact state	0	10	0.12
DPPC in ruptured state	31.7	17	0.41
DMPC in ruptured state	20.7	19	0.44
DOPC in ruptured state	27.5	18	0.43

^aDMPC (dimyristoylphosphatidylcholine), DOPC (dioleoylphosphatidylcholine), and DPPC (dipalmitoylphosphatidylcholine) membranes surrounded by aqueous solutions containing 20.7, 27.5, and 31.7 mol % are in the ruptured state.

c. Characterization in Terms of Machine-Learned State Variables. We have further implemented a machine-learning framework to characterize the failure of lipid membranes, namely, MembraneNN. The key component of this framework is a deep neural network (DNN), which is a nonlinear model mapping the particle coordinates of a single lipid molecule to state variables representing the order of this lipid molecule in the membrane. As depicted in Figure 13, the DNN is a standard feed-forward network composed of fully connected layers, in which the data flows from the input layer through the hidden layers toward the output layer. Each layer has a certain number of nodes (below), called neurons, which store information about the importance of the input and associations between the importance of combinations of inputs. In all layers, linear operations are applied to the input data d_i^{in} , e.g., $\bar{d}_k = \sum_n w_{ki} d_i^{\text{in}} + b_k$, where w_{ki} and b_k are the weights from layer l to the output layer k and the bias produced at layer k , respectively (Figure 13(b)). Additionally, the rectified linear unit (ReLU) activation function

$$\text{ReLU}(x) = (x)^+ = \max(0, x) \quad (14)$$

where x is the input to a neuron, is applied in intermediate layers to break the linearity: $d_k^{\text{out}} = \text{ReLU}(\bar{d}_k)$.⁶¹ In the output layer, the neurons are activated by a sigmoidal activation function to produce two state variables in the range of 0 to 1. Two state variables λ_1 and λ_2 are introduced to characterize the membrane failure. We only label the data at two extreme states: $\lambda_1 = 1$ and $\lambda_2 = 0$ (representing an intact membrane) and $\lambda_1 = 0$ and $\lambda_2 = 1$ (representing a ruptured membrane); see Figure 14(a). Overfitting is usually a serious problem in DNN models with an increasing number of layers and neurons per layer. To prevent overfitting and to improve the generalization error,⁶² the dropout technique,⁶³ which randomly drops out neurons (and their connections) during training, is implemented in our DNN model with a dropout rate of 0.2. This dropout rate indicates that there are 20% neurons randomly deactivated in each hidden layer. Another important element of the DNN is the loss function. Essentially, the loss function defines properties that the DNN attempts to optimize. Here, we use the mean square error (MSE)

$$\text{MSE}(y, \tilde{y}) = \frac{1}{n} \sum_{i=1}^n (y - \tilde{y})^2 \quad (15)$$

where n is the number of lipid molecules for training, and y and \tilde{y} are the manually labeled target state variables and state variables predicted by the DNN (λ_1 and λ_2) for a single lipid molecule, respectively.

The DNN model is built and trained using PyTorch⁶⁴ (version 1.8.1). Hyperparameters, whose values are used to control the learning process such as the number of layers and neurons in each layer, are usually difficult to determine.⁶⁵ In our framework, we use a grid search to determine these parameters in order to achieve efficiency and accuracy of our DNN. In the production run, we choose the network architecture: 1 input layer, 3 hidden layers, and 1 output layer with neurons in each layer 30-90-90-90-2. The ADAM (adaptive moment estimation) optimizer⁶⁶ with a learning rate of 0.001 is employed to train the DNN model. During training, data are iteratively fed into the network until a termination criterion is reached. Here, we stop the training when a reasonably low value of the loss function is reached, and it does not decrease significantly in further runs.

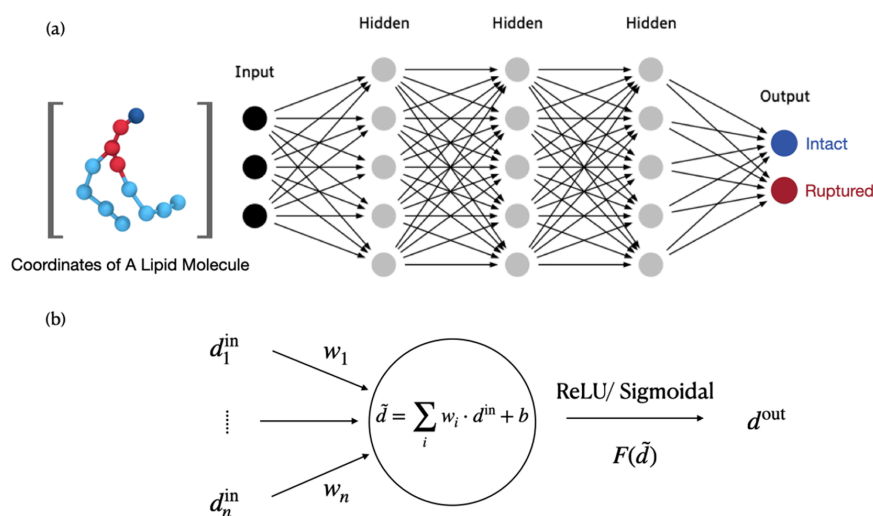


Figure 13. (a) Schematic figure of the deep neural network model. The Cartesian coordinates of all particles in a single lipid molecule are fed as input data to the network. The network has an output layer with two values, λ_1 and λ_2 , that represent the intact and ruptured states of a single lipid molecule, respectively. (b) Schematic figure for a single neuron.

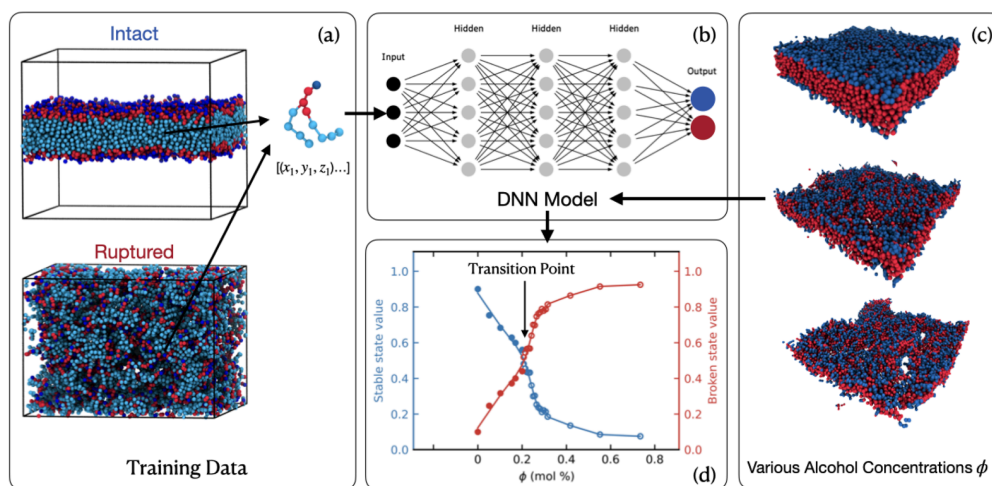


Figure 14. Flowchart of the MembraneNN framework to characterize the failure of lipid membranes (MembraneNN) in this work. (a) Example of training data: snapshots of the intact and ruptured DMPC (dimyristoylphosphatidylcholine) lipid membranes (h_1 head groups with blue color, h_2 and h_3 head groups with red color, and lipid tails with cyan color). (b) Architecture of the DNN model. (c) Snapshots of DMPC lipid membranes in pure water and in aqueous solutions containing 23.7 and 27.5 mol % ethanol (from top to bottom). The blue and red colors in the snapshots show head and tail lipid groups, respectively. (d) Variation of state variables λ_1 and λ_2 for a DMPC bilayer, immersed in aqueous solutions containing various concentrations of ethanol at 298 K. Open and filled markers represent the ruptured and intact bilayers, respectively, as determined by the visual inspection.

The workflow of MembraneNN is summarized here (Figure 14): The first step is to prepare the data for training and prediction. It is basically the trajectories of lipid molecules generated from the coarse-grained simulations of lipid membranes with various ethanol concentrations. At each ethanol concentration, particle coordinates of lipid molecules from 40 trajectory frames at equilibrium are collected, which means we have totally $n_{\text{mole}} \approx 40 \times 1000 \approx 4 \times 10^4$ samples for

developing the DNN model for each type of lipid molecule. It is noted that we move the center-of-mass position of the lipid molecule to the Cartesian origin in order to make the coordinates of a single lipid molecule translation-invariant for training. As aforementioned, we only label the lipid molecules (DPPC, DOPC, and DMPC) at the intact and ruptured states to be ($\lambda_1 = 1, \lambda_2 = 0$) and ($\lambda_1 = 0, \lambda_2 = 1$), respectively. These labeled data are used separately to develop the DNN models

Table 5. Rupture-Critical Ethanol Concentration in the Aqueous Phase, Surrounding Lipid Membranes^a

x_{DPPC}	x_{DMPC}	ethanol (mol %)	x_{DPPC}	x_{DMPC}	ethanol (mol %)	x_{DPPC}	x_{DMPC}	ethanol (mol %)
0.0	1.0	20.7	0.3	0.4	25.6	0.1	0.1	28.2
0.1	0.9	20.8	0.0	0.2	25.9	0.2	0.0	28.3
0.0	0.9	20.9	0.1	0.45	26.0	0.45	0.1	28.8
0.0	0.8	21.5	0.0	0.1	26.1	0.3	0.0	28.9
0.05	0.9	22.1	0.45	0.45	26.2	0.4	0.0	28.9
0.2	0.8	22.5	0.4	0.2	26.8	0.6	0.2	29.2
0.1	0.8	22.5	0.3	0.3	27.0	0.5	0.0	29.4
0.0	0.6	23.0	0.4	0.4	27.1	0.8	0.0	29.6
0.0	0.4	23.4	0.333	0.333	27.4	0.8	0.2	29.8
0.0	0.5	23.6	0.0	0.0	27.5	0.9	0.1	30.2
0.4	0.6	24.1	0.25	0.25	27.5	0.8	0.1	30.4
0.5	0.5	24.4	0.4	0.3	27.6	0.9	0.0	31.0
0.2	0.6	24.6	0.1	0.0	28.0	0.9	0.05	31.1
0.2	0.4	24.8	0.5	0.25	28.0	1.0	0.0	31.6
0.6	0.4	25.2	0.2	0.2	28.0			
0.25	0.5	25.3	0.05	0.05	28.2			

^a x_{DPPC} and x_{DMPC} indicate the mole fractions of DPPC (dipalmitoylphosphatidylcholine) and DMPC (dimyristoylphosphatidylcholine) in the membrane, and the mole fraction of DOPC (dioleoylphosphatidylcholine) can be derived as $x_{\text{DOPC}} = 1 - x_{\text{DPPC}} - x_{\text{DMPC}}$.

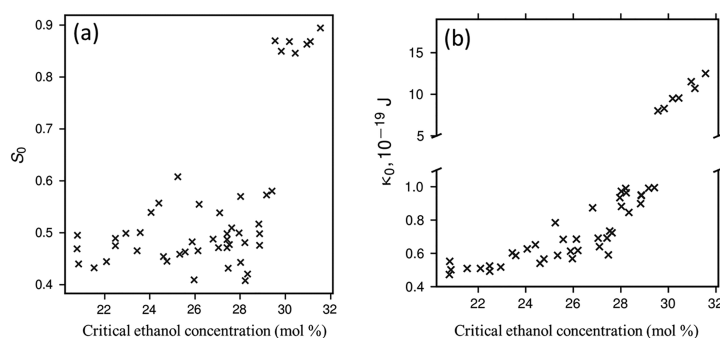


Figure 15. Correlation between (a) the orientational order parameter and (b) the bending modulus of membranes, immersed in *pure* water, and the rupture-critical ethanol concentration (in the aqueous phase surrounding the membrane) at which the membrane disrupts.

with 70% for training and 30% for testing, resulting in one DNN model per lipid type. We use the trained models to predict state variables (λ_1 and λ_2) for lipid molecules at various ethanol concentrations (an example is shown in Figure 14(d)). The integrity of the entire membrane is then defined as the averaged state variables of all lipid molecules in the membrane at a given alcohol concentration. We observe noticeable distributions of the predicted state variables λ_1 and λ_2 of lipid molecules in an intact membrane (see examples in Figure S6), although we manually labeled all lipid molecules of an intact membrane to be $\lambda_1 = 1$ and $\lambda_2 = 0$.

We employ the MembraneNN framework to predict the integrity of all pure and mixed membranes. The intact-to-ruptured transition point is determined via the procedure described in the section Machine Learning Model of the Supporting Information. The results are summarized in Table 5. The rupture-critical ethanol concentration in the aqueous phase surrounding the mixed membranes, composed of DMPC, DOPC, and DPPC, varies between ≈ 20 mol % ethanol (for DMPC dominated membranes) and ≈ 31 mol % ethanol (for DPPC dominated membranes). It is lowest for pure DMPC (the least robust membrane) and highest for pure DPPC (the most resilient membrane).

We have checked whether there exists a correlation between the characteristics of mixed membranes immersed in *pure* water (always intact) and their stabilities against ethanol. In Figure 15, we correlate the orientational order parameter for the hydrocarbon tails and the bending modulus of mixed membranes, immersed in water, with the rupture-critical ethanol concentration in the aqueous phase, at which the membrane disrupts. A general trend for stabilities in the presence of ethanol is seen; a higher ethanol concentration in the aqueous phase is needed to disrupt a more ordered (higher S_0) and stiffer (higher κ_0) mixed membrane. The DPPC-rich membranes ($x_{\text{DPPC}} > 0.8$), however, do not follow the trend of stability of the other mixed membranes; the values of both S_0 and κ_0 are much larger than the corresponding values for membranes with $x_{\text{DPPC}} < 0.8$. On the other hand, an unusually high ethanol concentration in the aqueous phase is needed to disrupt the DPPC-rich membranes. The reason is that at $T = 298$ K, where we did our simulations, the DPPC exists in the gel phase, but the DMPC and DOPC are always in the fluid phase. This is in agreement with the reported gel–liquid crystalline phase transition temperature of DPPC (315 K),⁵⁷ DMPC (297.25 K),⁵⁷ and DOPC (256.65 K).⁵⁷ Therefore, the hydrocarbon tails of the DPPC are much better ordered than those of DOPC and DMPC, and hence, the DPPC

has a much higher bending modulus than the DMPC and DPOC. However, when the surrounding solution contains ethanol, it penetrates into the membrane and fluidizes it. Upon increasing the ethanol concentration in the aqueous phase to ≈ 30 mol %, even the DPPC-rich membranes become weak enough (as a result of ethanol penetration) to rupture.

CONCLUSIONS

We have developed DPD models of three lipids, DPPC (dipalmitoylphosphatidylcholine), DOPC (dioleoylphosphatidylcholine), and DMPC (dimyristoylphosphatidylcholine), and their neat, binary, and ternary mixed membranes as models of the SARS-CoV-2 membrane, immersed in water and in water–ethanol solutions (disinfectants) up to concentrations where the membranes undergo rupture. It is worth noting that the composition of the SARS-CoV-2 membrane is not known; however, it is presumably composed of different phospholipids stolen from its host, which anchor several membrane proteins. Since our previous atomistic simulations³¹ revealed that the E-peptide does not offer noticeable protection against the ethanol-induced failure of the viral membrane, we have simulated mixed membranes composed of DPPC, DMPC, and DOPC, as models of the SARS-CoV-2 membrane without membrane proteins. The molecular mechanisms of ethanol-induced weakening and the impact of ethanol concentration on the deactivation (membrane rupture) of SARS-CoV-2 have been investigated in detail. We have found that two factors influence the membrane stability: the lipid composition of the membrane and the concentration of ethanol in the aqueous disinfectant solution surrounding it. We looked at different properties, including the area per lipid molecule, bilayer thickness, orientational order of the lipid tails, bending modulus, and ethanol permeability, and their dependence on membrane composition and ethanol concentration.

Our DPD models for pure membranes were validated by comparing their areas per lipid molecule and thicknesses against experimental data and reported atomistic simulation results in the literature. Based on the agreement of the calculated properties for neat bilayers in *pure* water with experimental and previous atomistic simulation reports, we conjecture that at 298 K (where we did our DPD simulations) the DPPC exists in the gel phase, but the DMPC and DOPC exist in the fluid phase. For mixed DPPC-PMPC-DOPC bilayers in *pure* water, we found that structural properties depend on the length and the degree of saturation of the hydrocarbon tail of the components. Mixed bilayers composed of DPPC (with longer saturated hydrocarbon tails) as the major constituent occupy less surface area per lipid molecule than DMPC-rich (with shorter saturated hydrocarbon tails) bilayers. However, the maximum surface area per lipid molecule belongs to mixed bilayers dominated by DOPC (with unsaturated bonds in the hydrocarbon tail). Expectedly, the bilayer thickness depends inversely on the surface area per lipid molecule, i.e., the DPPC-rich mixed membranes are thicker than the DOPC- or DMPC-rich bilayers. In the absence of ethanol, the variation of the surface area per lipid a_0 and the bilayer thickness l_0 is about 20% between more fluidic (DMPC and DOPC) and gel-like (DPPC) membranes. Therefore, a_0 and l_0 cannot be usefully employed to predict the stabilities of mixed bilayers of different compositions. The orientational order of the hydrocarbon tail S_0 is, however, a more sensitive parameter in this respect; it varies by a factor of 2 from DMPC/DOPC to DPPC. Interestingly, an even sharper composition-dependent change is seen for the bending modulus

κ_0 . It varies by a factor of ≈ 26 from DMPC/DOPC to DPPC. Another noticeable point is that while the values of a_0 and l_0 for mixed membranes nearly follow an ideal mixing rule, the values of S_0 and κ_0 do not. In terms of the bending modulus, a marked region of stability is seen for DPPC-rich ($x_{\text{DPPC}} > 0.8$) membranes.

In complete agreement with our previous atomistic simulations,¹⁵ we found that aqueous solutions containing 5–10 mol % ethanol have a significant weakening effect on the neat and mixed membranes. With increasing ethanol concentration in the disinfectant solution, the ethanol uptake of the membrane increases disproportionately: There is a synergistic effect, as the ethanol already in the membrane fluidizes it and facilitates the absorption of even more ethanol. The dissolution of ethanol in the membrane causes lateral membrane swelling and the shrinkage of its thickness. Obviously, the ethanol uptake reduces the orientational order of the hydrocarbon tails of the lipids. However, we cannot quantitatively predict the location of the phase transition point based on the area per lipid molecule, the membrane thickness, or the orientational order parameter. Hence, we have further developed a machine-learning framework to access the integrity of lipid membranes in place of visual inspections. We found that the rupture-critical ethanol concentrations needed to induce damage in the mixed membranes vary between that for pure DMPC (the least robust membrane) to that for pure DPPC (the most robust membrane). At 30 mol % ethanol concentration, only DPPC-rich membranes ($x_{\text{DPPC}} > 0.8$) remain intact. This stabilizing effect of DPPC can be correlated with a larger bending modulus for membranes in *pure* water. The tight packing of DPPC molecules, which forms a gel phase when pure, makes the bilayer less permeable to ethanol. It also induces orientational order among the DOPC and DMPC lipids at high DPPC concentrations. Membrane failure can not only be identified by human or machine inspection of its structure. Also the relative transmembrane permeation rates of ethanol, calculated by the nonequilibrium molecular dynamics, show a sudden increase when the membrane develops holes, jumping by as much as a factor of ≈ 7 for DPPC and a smaller factor of ≈ 4 for DMPC and DOPC.

The least robust membrane studied in this work is pure DMPC, which is punctured already by a disinfectant solution containing ≈ 20 mol % (corresponding to ≈ 40 wt %) ethanol. On the other hand, as the DPPC exists in the gel phase at room temperature, it forms one of the most resilient membranes of the coronavirus. Even such a robust membrane, however, fails in aqueous disinfectant solutions containing more than ≈ 32 mol % (corresponding to ≈ 55 wt %) ethanol. Therefore, an ethanol concentration below ≈ 20 mol % in the disinfectants is hardly efficient in the deactivation of the coronavirus. On the other hand, an ethanol concentration above ≈ 32 mol % in the disinfectants will make the viral membrane dysfunctional, regardless of which of the lipids studied here dominates in the membrane.

ASSOCIATED CONTENT

Supporting Information

The Supporting Information is available free of charge at <https://pubs.acs.org/doi/10.1021/acs.jctc.1c01120>.

Dependence of phase of membrane on hydrocarbon tail length and its degree of saturation; composition-dependence of membrane thickness of lipid mixing; phase

transition of DPPC membrane with increasing temperature; dependence of volume of lipid membrane on ethanol concentration; tables of hyperparameters of deep neural network (DNN) and training and predicting data set of DNN; loss function and probability density distribution during training DNN; and machine-learned state variables (PDF)

AUTHOR INFORMATION

Corresponding Author

Hossein Eslami – Eduard-Zintl-Institut für Anorganische und Physikalische Chemie, Technische Universität Darmstadt, 64287 Darmstadt, Germany; College of Sciences, Persian Gulf University, Boushehr 75168, Iran; orcid.org/0000-0002-1990-0469; Email: h.eslami@theo.chemie.tu-darmstadt.de

Authors

Tianhang Zhou – Eduard-Zintl-Institut für Anorganische und Physikalische Chemie, Technische Universität Darmstadt, 64287 Darmstadt, Germany; orcid.org/0000-0002-4007-9935

Zhenghao Wu – Eduard-Zintl-Institut für Anorganische und Physikalische Chemie, Technische Universität Darmstadt, 64287 Darmstadt, Germany; orcid.org/0000-0003-2862-4432

Shubhadip Das – Eduard-Zintl-Institut für Anorganische und Physikalische Chemie, Technische Universität Darmstadt, 64287 Darmstadt, Germany; orcid.org/0000-0003-4432-7657

Florian Müller-Plathe – Eduard-Zintl-Institut für Anorganische und Physikalische Chemie, Technische Universität Darmstadt, 64287 Darmstadt, Germany; orcid.org/0000-0002-9111-7786

Complete contact information is available at: <https://pubs.acs.org/10.1021/acs.jctc.1c01120>

Notes

The authors declare no competing financial interest.

ACKNOWLEDGMENTS

Z.W. and H.E. acknowledge financial support from the Deutsche Forschungsgemeinschaft via the SFB-TRR 146 “Multiscale Simulation Methods for Soft Matter Systems”, Project A8.

REFERENCES

- (1) Dong, E.; Du, H.; Gardner, L. An interactive web-based dashboard to track COVID-19 in real time. *Lancet Infect. Dis.* **2020**, *20*, 533–534.
- (2) Seah, I.; Su, X.; Lingam, G. Revisiting the dangers of the coronavirus in the ophthalmology practice. *Eye* **2020**, *34*, 1155–1157.
- (3) Schoeman, D.; Fielding, B. C. Coronavirus envelope protein: current knowledge. *Virol. J.* **2019**, *16*, 69.
- (4) Sun, S.; Karki, C.; Aguilera, J.; Lopez Hernandez, A. E.; Sun, J.; Li, L. Computational Study on the Function of Palmitoylation on the Envelope Protein in SARS-CoV-2. *J. Chem. Theory Comput.* **2021**, *17*, 6483–6490.
- (5) Choi, Y. K.; Cao, Y.; Frank, M.; Woo, H.; Park, S. J.; Yeom, M. S.; Croll, T. I.; Seok, C.; Im, W. Structure, Dynamics, Receptor Binding, and Antibody Binding of the Fully Glycosylated Full-Length SARS-CoV-2 Spike Protein in a Viral Membrane. *J. Chem. Theory Comput.* **2021**, *17*, 2479–2487.
- (6) Deshmukh, M. G.; Ippolito, J. A.; Zhang, C. H.; Stone, E. A.; Reilly, R. A.; Miller, S. J.; Jorgensen, W. L.; Anderson, K. S. Structure-guided design of a perampanel-derived pharmacophore targeting the SARS-CoV-2 main protease. *Structure* **2021**, *29*, 823–833.e5.
- (7) Zhang, C. H.; Spasov, K. A.; Reilly, R. A.; Hollander, K.; Stone, E. A.; Ippolito, J. A.; Liosi, M. E.; Deshmukh, M. G.; Tirado-Rives, J.; Zhang, S.; Liang, Z.; Miller, S. J.; Isaacs, F.; Lindenbach, B. D.; Anderson, K. S.; Jorgensen, W. L. Optimization of Triarylpyridinone Inhibitors of the Main Protease of SARS-CoV-2 to Low-Nanomolar Antiviral Potency. *ACS Med. Chem. Lett.* **2021**, *12*, 1325–1332.
- (8) Zhang, C. H.; Stone, E. A.; Deshmukh, M.; Ippolito, J. A.; Ghahremanpour, M. M.; Tirado-Rives, J.; Spasov, K. A.; Zhang, S.; Takeo, Y.; Kudalkar, S. N.; Liang, Z.; Isaacs, F.; Lindenbach, B.; Miller, S. J.; Anderson, K. S.; Jorgensen, W. L. Potent Noncovalent Inhibitors of the Main Protease of SARS-CoV-2 from Molecular Sculpting of the Drug Perampanel Guided by Free Energy Perturbation Calculations. *ACS Cent. Sci.* **2021**, *7*, 467–475.
- (9) Ghahremanpour, M. M.; Tirado-Rives, J.; Deshmukh, M.; Ippolito, J. A.; Zhang, C. H.; Cabeza de Vaca, I.; Liosi, M. E.; Anderson, K. S.; Jorgensen, W. L. Identification of 14 Known Drugs as Inhibitors of the Main Protease of SARS-CoV-2. *ACS Med. Chem. Lett.* **2020**, *11*, 2526–2533.
- (10) Kampf, G.; Todt, D.; Pfaender, S.; Steinmann, E. Persistence of coronaviruses on inanimate surfaces and their inactivation with biocidal agents. *J. Hosp. Infect.* **2020**, *104*, 246–251.
- (11) Ly, H. V.; Longo, M. L. The Influence of Short-Chain Alcohols on Interfacial Tension, Mechanical Properties, Area/Molecule, and Permeability of Fluid Lipid Bilayers. *Biophys. J.* **2004**, *87*, 1013–1033.
- (12) Wang, Y.; Dea, P. Interaction of 1-Propanol and 2-Propanol with Dipalmitoylphosphatidylcholine Bilayer: A Calorimetric Study. *J. Chem. Eng. Data* **2009**, *54*, 1447–1451.
- (13) Manca, M. L.; Castangia, I.; Matricardi, P.; Lampis, S.; Fernández-Busquets, X.; Fadda, A. M.; Manconi, M. Molecular arrangements and interconnected bilayer formation induced by alcohol or polyalcohol in phospholipid vesicles. *Colloids Surf., B* **2014**, *117*, 360–367.
- (14) Zhang, M.; Peyear, T.; Patmanidis, I.; Greathouse, D. V.; Marrink, S. J.; Andersen, O. S.; Ingólfsson, H. I. Fluorinated Alcohols’ Effects on Lipid Bilayer Properties. *Biophys. J.* **2018**, *115*, 679–689.
- (15) Eslami, H.; Das, S.; Zhou, T.; Müller-Plathe, F. How Alcoholic Disinfectants Affect Coronavirus Model Membranes: Membrane Fluidity, Permeability, and Disintegration. *J. Phys. Chem. B* **2020**, *124*, 10374–10385.
- (16) Henderson, C. M.; Block, D. E. Examining the role of membrane lipid composition in determining the ethanol tolerance of *Saccharomyces cerevisiae*. *Appl. Environ. Microbiol.* **2014**, *80*, 2966–2972.
- (17) Patra, M.; Salonen, E.; Terama, E.; Vattulainen, I.; Faller, R.; Lee, B. W.; Holopainen, J.; Karttunen, M. Under the influence of alcohol: The effect of ethanol and methanol on lipid bilayers. *Biophys. J.* **2006**, *90*, 1121–1135.
- (18) Fung, T. S.; Liu, D. X. Human Coronavirus: Host-Pathogen Interaction. *Annu. Rev. Microbiol.* **2019**, *73*, 529–557.
- (19) Stertz, S.; Reichelt, M.; Spiegel, M.; Kuri, T.; Martínez-Sobrido, L.; García-Sastre, A.; Weber, F.; Kochs, G. The intracellular sites of early replication and budding of SARS-coronavirus. *Virology* **2007**, *361*, 304–315.
- (20) Holm, B. A.; Wang, Z.; Egan, E. A.; Notter, R. H. Content of Dipalmitoyl Phosphatidylcholine in Lung Surfactant: Ramifications for Surface Activity. *Pediatr. Res.* **1996**, *39*, 805–811.
- (21) Vance, J. E. Phospholipid Synthesis and Transport in Mammalian Cells. *Traffic* **2015**, *16*, 1.
- (22) Drescher, S.; van Hoogevest, P. The phospholipid research center: Current research in phospholipids and their use in drug delivery. *Pharmaceutics* **2020**, *12*, 1235.
- (23) Khatari, Z.; Brotons, G.; Akkawi, M.; Arbely, E.; Arkin, I. T.; Salditt, T. SARS Coronavirus E protein in phospholipid bilayers: An X-ray study. *Biophys. J.* **2006**, *90*, 2038–2050.
- (24) Guillén, J.; Pérez-Berná, A. J.; Moreno, M. R.; Villalain, J. A second SARS-CoV S2 glycoprotein internal membrane-active peptide. Biophysical characterization and membrane interaction. *Biochemistry* **2008**, *47*, 8214–8224.

- (25) Keough, K. M.; Davis, P. J. Gel to Liquid-Crystalline Phase Transitions in Water Dispersions of Saturated Mixed-Acid Phosphatidylcholines. *Biochemistry* **1979**, *18*, 1453–1459.
- (26) Svetlovics, J. A.; Wheaton, S. A.; Almeida, P. F. Phase separation and fluctuations in mixtures of a saturated and an unsaturated phospholipid. *Biophys. J.* **2012**, *102*, 2526–2535.
- (27) Koynova, R.; Tenchov, B. Lipids: Phase Transitions. *Wiley Encyclopedia of Chemical Biology*; 2008; DOI: 10.1002/9780470048672.webc287.
- (28) Kučerka, N.; Heberle, F. A.; Pan, J.; Katsaras, J. Structural significance of lipid diversity as studied by small angle neutron and X-ray scattering. *Membranes* **2015**, *5*, 454.
- (29) Konas, R. M.; Daristotle, J. L.; Harbor, N. B.; Klauda, J. B. Biophysical Changes of Lipid Membranes in the Presence of Ethanol at Varying Concentrations. *J. Phys. Chem. B* **2015**, *119*, 13134–13141.
- (30) Gurtovenko, A. A.; Anwar, J. Interaction of ethanol with biological membranes: The formation of non-bilayer structures within the membrane interior and their significance. *J. Phys. Chem. B* **2009**, *113*, 1983–1992.
- (31) Das, S.; Meinel, M. K.; Wu, Z.; Müller-Plathe, F. The role of the envelope protein in the stability of a coronavirus model membrane against an ethanolic disinfectant. *J. Chem. Phys.* **2021**, *154*, 245101.
- (32) Brown, M. F.; Thurmond, R. L.; Dodd, S. W.; Otten, D.; Beyer, K. Elastic Deformation of Membrane Bilayers Probed by Deuterium NMR Relaxation. *J. Am. Chem. Soc.* **2002**, *124*, 8471–8484.
- (33) Poghosyan, A. H.; Gharabekyan, H. H.; Shahinyan, A. A. Molecular dynamics simulations of DMPC/DPPC mixed bilayers. *Int. J. Mod. Phys. C* **2007**, *18*, 73–89.
- (34) Li, X.; Gao, L.; Fang, W. Dissipative particle dynamics simulations for phospholipid membranes based on a four-to-one coarse-grained mapping scheme. *PLoS One* **2016**, *11*, e0154568.
- (35) Wan, M.; Gao, L.; Fang, W. Implicit-solvent dissipative particle dynamics force field based on a four-to-one coarse-grained mapping scheme. *PLoS One* **2018**, *13*, e0198049.
- (36) Groot, R. D.; Warren, P. B. Dissipative particle dynamics: Bridging the gap between atomistic and mesoscopic simulation. *J. Chem. Phys.* **1997**, *107*, 4423–4435.
- (37) Groot, R. D.; Rabone, K. L. Mesoscopic simulation of cell membrane damage, morphology change and rupture by nonionic surfactants. *Biophys. J.* **2001**, *81*, 725–736.
- (38) Li, W.; Zhang, M.; Zhang, J.; Han, Y. Self-assembly of cetyl trimethylammonium bromide in ethanol-water mixtures. *Front. Chem. China* **2006**, *1*, 438–442.
- (39) Gao, L.; Shillcock, J.; Lipowsky, R. Improved dissipative particle dynamics simulations of lipid bilayers. *J. Chem. Phys.* **2007**, *126*, 015101.
- (40) Berendsen, H. J. C.; Postma, J. P. M.; van Gunsteren, W. F.; DiNola, A.; Haak, J. R. Molecular dynamics with coupling to an external bath. *J. Chem. Phys.* **1984**, *81*, 3684–3690.
- (41) Lin, Y.; Pan, D.; Li, J.; Zhang, L.; Shao, X. Application of Berendsen barostat in dissipative particle dynamics for nonequilibrium dynamic simulation. *J. Chem. Phys.* **2017**, *146*, 124108.
- (42) Goetz, R.; Gompper, G.; Lipowsky, R. Mobility and Elasticity of Self-Assembled Membranes. *Phys. Rev. Lett.* **1999**, *82*, 221–224.
- (43) Rand, R. P.; Parsegian, V. A. Hydration forces between phospholipid bilayers. *Biochim. Biophys. Acta - Rev. Biomembr.* **1989**, *988*, 351–376.
- (44) Pan, J.; Tristram-Nagle, S.; Kučerka, N.; Nagle, J. F. Temperature Dependence of Structure, Bending Rigidity, and Bilayer Interactions of Dioleoylphosphatidylcholine Bilayers. *Biophys. J.* **2008**, *94*, 117–124.
- (45) Kucerka, N.; Nagle, J. F.; Sachs, J. N.; Feller, S. E.; Pencic, J.; Jackson, A.; Katsaras, J. Lipid bilayer structure determined by the simultaneous analysis of neutron and X-ray scattering data. *Biophys. J.* **2008**, *95*, 2356–2367.
- (46) Liu, Y.; Nagle, J. F. Diffuse scattering provides material parameters and electron density profiles of biomembranes. *Phys. Rev. E* **2004**, *69*, 40901.
- (47) Lee, C. W.; Chiang, Y. L.; Liu, J. T.; Chen, Y. X.; Lee, C. H.; Chen, Y. L.; Hwang, I. S. Emerging Roles of Air Gases in Lipid Bilayers. *Small* **2018**, *14*, 1802133.
- (48) Steltenkamp, S.; Müller, M. M.; Deserno, M.; Hennesthal, C.; Steinem, C.; Janshoff, A. Mechanical Properties of Pore-Spanning Lipid Bilayers Probed by Atomic Force Microscopy. *Biophys. J.* **2006**, *91*, 217–226.
- (49) Chaurasia, A. K.; Rukangu, A. M.; Philen, M. K.; Seidel, G. D.; Freeman, E. C. Evaluation of bending modulus of lipid bilayers using undulation and orientation analysis. *Phys. Rev. E* **2018**, *97*, 032421.
- (50) Schubert, T.; Schneck, E.; Tanaka, M. First order melting transitions of highly ordered dipalmitoyl phosphatidylcholine gel phase membranes in molecular dynamics simulations with atomistic detail. *J. Chem. Phys.* **2011**, *135*, 055105.
- (51) Kučerka, N.; Liu, Y.; Chu, N.; Petrache, H. I.; Tristram-Nagle, S.; Nagle, J. F. Structure of Fully Hydrated Fluid Phase DMPC and DLPC Lipid Bilayers Using X-Ray Scattering from Oriented Multilamellar Arrays and from Unilamellar Vesicles. *Biophys. J.* **2005**, *88*, 2626–2637.
- (52) Petrache, H. I.; Tristram-Nagle, S.; Nagle, J. F. Fluid phase structure of EPC and DMPC bilayers. *Chem. Phys. Lipids* **1998**, *95*, 83–94.
- (53) Orsi, M.; Michel, J.; Essex, J. W. Coarse-grain modelling of DMPC and DOPC lipid bilayers. *J. Phys.: Condens. Matter* **2010**, *22*, 155106.
- (54) Sankaram, M. B.; Thompson, T. E. Deuterium Magnetic Resonance Study of Phase Equilibria and Membrane Thickness in Binary Phospholipid Mixed Bilayers. *Biochemistry* **1992**, *31*, 8258–8268.
- (55) de Joannis, J.; Jiang, Y.; Yin, F.; Kindt, J. T. Equilibrium distributions of dipalmitoyl phosphatidylcholine and dilauroyl phosphatidylcholine in a mixed lipid bilayer: Atomistic semigrand canonical ensemble simulations. *J. Phys. Chem. B* **2006**, *110*, 25875–25882.
- (56) Eslami, H.; Gharibi, A.; Müller-Plathe, F. Mechanisms of Nucleation and Solid–Solid-Phase Transitions in Triblock Janus Assemblies. *J. Chem. Theory Comput.* **2021**, *17*, 1742–1754.
- (57) Attwood, S. J.; Choi, Y.; Leonenko, Z. Preparation of DOPC and DPPC supported planar lipid bilayers for atomic force microscopy and atomic force spectroscopy. *Int. J. Mol. Sci.* **2013**, *14*, 3514–3539.
- (58) Terama, E.; Ollila, O. H.; Salonen, E.; Rowat, A. C.; Trandum, C.; Westh, P.; Patra, M.; Karttunen, M.; Vattulainen, I. Influence of ethanol on lipid membranes: From lateral pressure profiles to dynamics and partitioning. *J. Phys. Chem. B* **2008**, *112*, 4131–4139.
- (59) Potter, T. D.; Barrett, E. L.; Miller, M. A. Automated Coarse-Grained Mapping Algorithm for the Martini Force Field and Benchmarks for Membrane–Water Partitioning. *J. Chem. Theory Comput.* **2021**, *17*, 5777–5791.
- (60) Müller, T. J.; Müller-Plathe, F. A comparison of sulfur mustard and heptane penetrating a dipalmitoylphosphatidylcholine bilayer membrane. *J. Hazard. Mater.* **2009**, *168*, 13–24.
- (61) Glorot, X.; Bordes, A.; Bengio, Y. Deep Sparse Rectifier Neural Networks. *JMLR Workshop and Conference Proceedings* **2011**, 315–323.
- (62) Mohri, M.; Rostamizadeh, A.; Talwalkar, A. *Foundations of machine learning*; Adaptive computation and machine learning series; MIT Press: Cambridge, MA, 2012.
- (63) Hinton, G. E.; Srivastava, N.; Krizhevsky, A.; Sutskever, I.; Salakhutdinov, R. R. *Improving neural networks by preventing co-adaptation of feature detectors*. 2012, arXiv:1207.0580. [arXiv e-prints. https://arxiv.org/abs/1207.0580](https://arxiv.org/abs/1207.0580) (accessed 2022-03-11).
- (64) Paszke, A.; Gross, S.; Massa, F.; Lerer, A.; Bradbury, J.; Chanan, G.; Killeen, T.; Lin, Z.; Gimeshain, N.; Antiga, L.; Desmaison, A.; Kopf, A.; Yang, E.; DeVito, Z.; Raison, M.; Tejani, A.; Chilamkurthy, S.; Steiner, B.; Fang, L.; Bai, J.; Chintala, S. In *Advances in Neural Information Processing Systems 32*; Wallach, H., Larochelle, H., Beygelzimer, A., d'Alché-Buc, F., Fox, E., Garnett, R., Eds.; Curran Associates, Inc.: 2019; pp 8024–8035.
- (65) LeCun, Y.; Bengio, Y.; Hinton, G. Deep learning. *Nature* **2015**, *521*, 436–444.

(66) Kingma, D. P.; Ba, J. *Adam: A Method for Stochastic Optimization*. 2017, arXiv:1412.6980. *arXiv e-prints*. <https://arxiv.org/abs/1412.6980> (accessed 2022-03-11).

(67) Lewis, R. N.; Zhang, Y. P.; McElhaney, R. N. Calorimetric and spectroscopic studies of the phase behavior and organization of lipid bilayer model membranes composed of binary mixtures of dimyristoylphosphatidylcholine and dimyristoylphosphatidylglycerol. *Biochim. Biophys. Acta - Biomembr.* **2005**, *1668*, 203–214.

Supporting Information: How Ethanolic Disinfectants Disintegrate Coronavirus Model Membranes: A Dissipative-Particle-Dynamics Simulation Study

Tianhang Zhou,[†] Zhenghao Wu,[†] Shubhadip Das,[†] Hossein Eslami,^{*,†,‡} and
Florian Müller-Plathe [†]

[†]*Eduard-Zintl-Institut für Anorganische und Physikalische Chemie, Technische Universität
Darmstadt, Alarich-Weiss-Str. 8, 64287 Darmstadt, Germany*

[‡]*College of Sciences, Persian Gulf University, Boushehr 75168, Iran*

E-mail: h.eslami@theo.chemie.tu-darmstadt.de

Dependence of the Phase of the Membrane on the Hydrocarbon Tail Length and its Degree of Saturation

Figure S1 shows that the phase of the membrane depends on the hydrocarbon tail length and its degree of saturation. In other words, the type of the head group does not have a noticeable influence on the phase of the membrane.

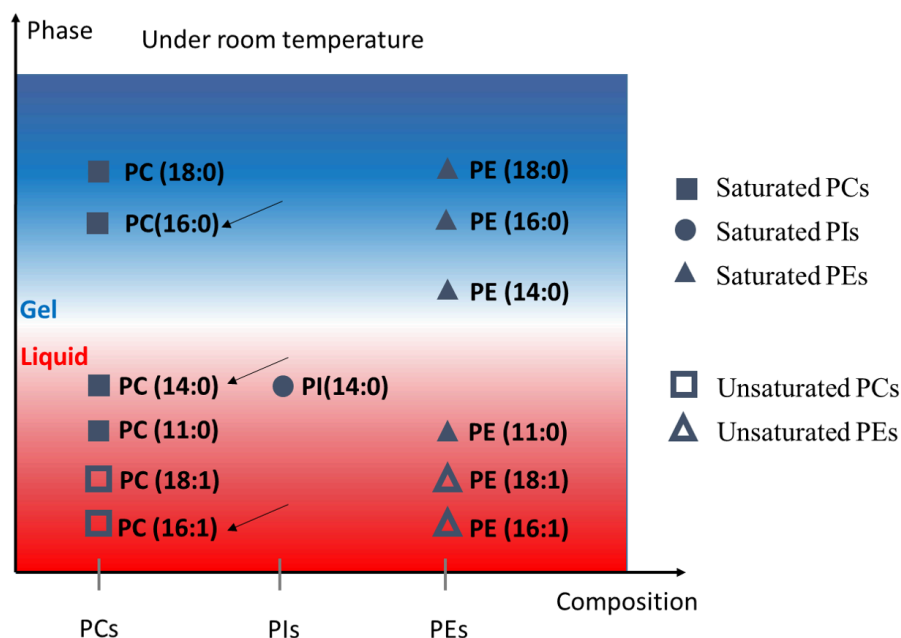


Figure S1: Dependence of the phase of the phosphatidylcholines (PCs)-, phosphatidylethanolamines (PEs)-, and phosphatidylinositols (PIs)-membranes on the hydrocarbon tail length and its degree of saturation at room temperature. The data are taken from the literature.¹ The numbers in parenthesis are the length of the hydrocarbon tail and the number of unsaturated bonds in the hydrocarbon tail of the lipid molecule. For example, the dimyristoylphosphatidylcholin (DMPC), which is studied in this work, contains hydrocarbon tails of length 14 and has no unsaturated bonds, is shown as PC (14:0). To our knowledge, there is only one reported value in the literature on PI membranes. The arrows indicate the three PCs studied in this work, namely, DMPC, dioleoylphosphatidylcholine (DOPC), and dipalmitoylphosphatidylcholine (DPPC). Solid and open symbols represent saturated and unsaturated lipids, respectively.

Mixing of lipids

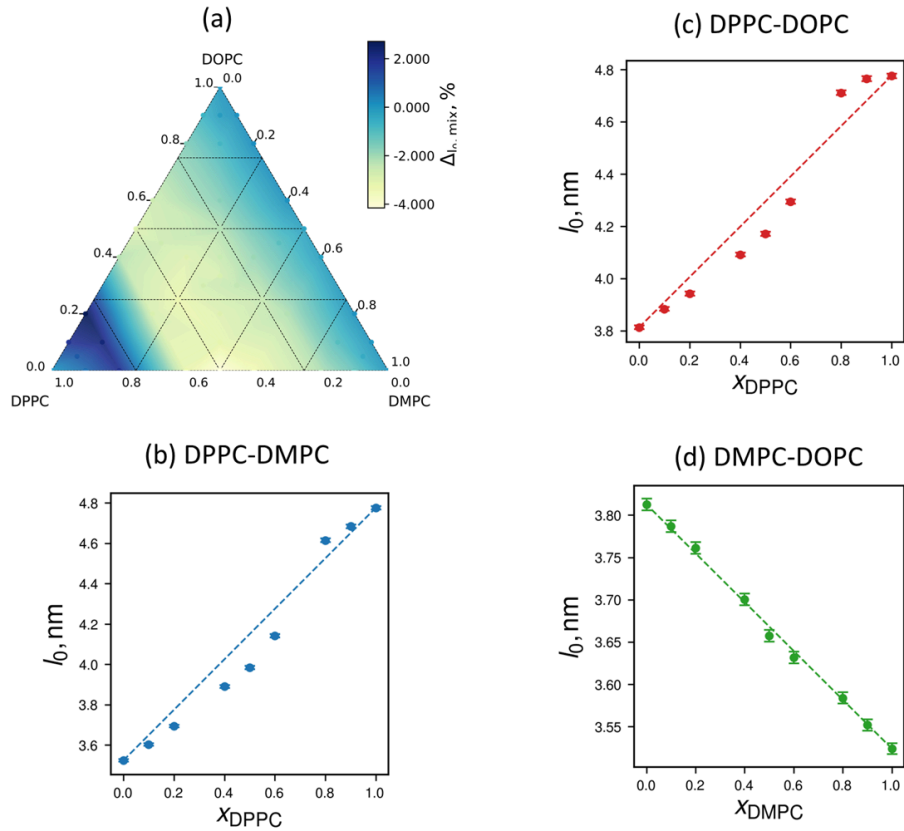


Figure S2: (a) $\Delta l_{0,\text{mix}} = l_0 - l_{0,\text{ideal}}$ for mixed membranes. (b-c) Composition-dependence of the membrane thickness for DPPC (dipalmitoylphosphatidylcholine) -DMPC (dimyristoylphosphatidylcholine), DPPC-DOPC (dipalmitoylphosphatidylcholine), and DMPC-DOPC binary membranes. The dashed lines indicate ideal mixing behavior (see Eq. (11) the main text).

Phase transition of DPPC membrane with increasing temperature

As shown in Figure S3, DPPC lipid membrane shows a clear gel to the liquid crystalline phase transitions at 320 K. This is also confirmed by the orientational order parameter $S_0 = 0.512$, which is closed to those of DOPC ($S_0 = 0.426$) and DMPC ($S_0 = 0.467$).

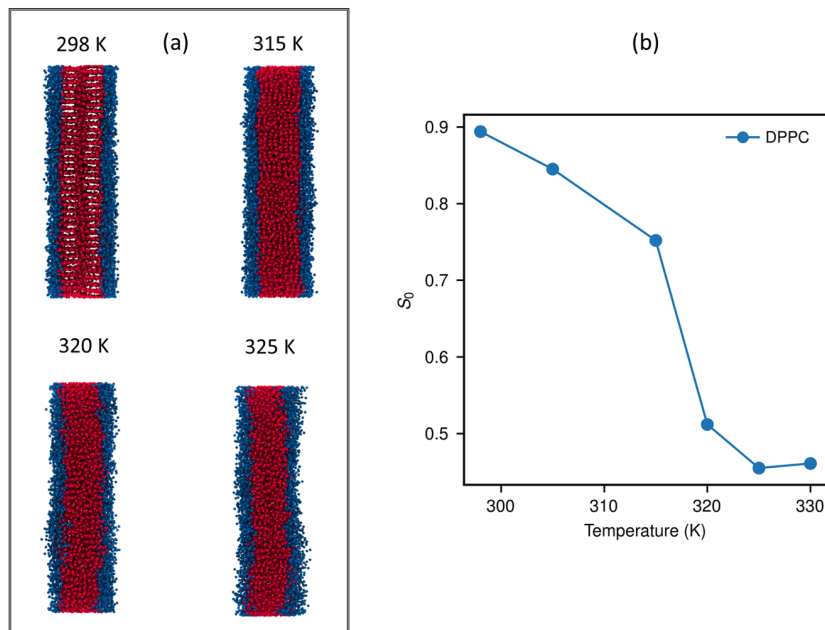


Figure S3: (a) Snapshots of DPPC (dipalmitoylphosphatidylcholine) lipid bilayers surrounded by *pure* water at different temperatures. The blue and red spheres show head groups and the lipid tails, respectively. (b) Temperature-dependence of the orientational order parameter for DPPC immersed in *pure* water.

Machine learning model

Table S1: Hyperparameters of DNN

Hyperparameters	Values
Batch size	100
Learning rate	0.001
Number of NN layers	5
Dropout rate	0.2
Activate function	ReLU

Training and predicting of DNN

The training and testing datasets for developing DNN models in our MembraneNN framework are summarized in the table below:

Table S2: The training and testing datasets for developing DNN models

Composition	Alcohol Concentration	Training datasets	Testing datasets
DPPC	0 mol %	2.8×10^4 molecules	1.2×10^4 molecules
	70 mol %	2.8×10^4 molecules	1.2×10^4 molecules
DMPC	0 mol %	2.8×10^4 molecules	1.2×10^4 molecules
	70 mol %	2.8×10^4 molecules	1.2×10^4 molecules
DOPC	0 mol %	2.8×10^4 molecules	1.2×10^4 molecules
	70 mol %	2.8×10^4 molecules	1.2×10^4 molecules

The trained DNN models using these pure membranes are used to predict state variables for mixed membranes of various compositions.

Loss function during training DNN

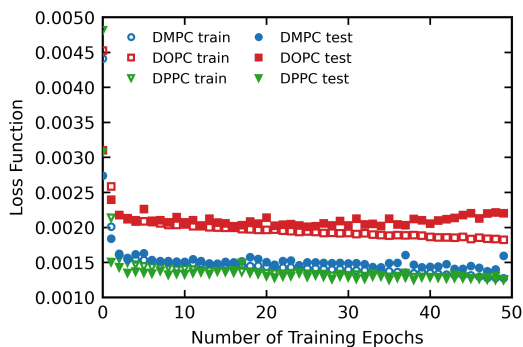


Figure S5: Loss functions of respective DNN models for DMPC (dimyristoylphosphatidylcholine, blue color), DOPC (dioleoylphosphatidylcholine, red color) and DPPC (dipalmitoylphosphatidylcholine, green color) lipid molecules. The hollow and filled symbols are training and test loss values.

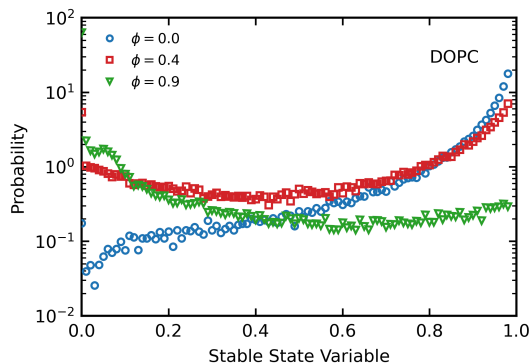


Figure S6: Probability density distribution of machine learned intact state variables for DOPC (dioleoylphosphatidylcholine) lipid molecules at alcohol concentrations $\phi = 0.0$ (blue), $\phi = 0.4$ (red) and $\phi = 0.9$ (green).

The intact λ_1 and ruptured λ_2 state values of the DMPC single membrane are shown in Figure S7. The crossing point (~ 20.7 mol % ethanol) of the two curves fitted through λ_1 and λ_2 points, represents the stability-rupture transition in DMPC (see Figure S7). For the DOPC and DPPC, the transition points are at ~ 27.5 and 31.6 mol % ethanol (see Figures S8 and S9), respectively. However, a close look at the transition regimes shown in Figure

S7-S9, show that unlike the common phase transitions such as liquid-vapor² or solid-liquid^{3,4} transitions, the intact-ruptured transition in membranes is not a sharp transition. From the intact region to the ruptured state, the two parameters (λ_1 and λ_2) vary gradually. An estimation of linear variations of λ_1 and λ_2 over the intact region and extrapolation to the crossing point, represents well the transition points; 19.4, 28.1, and 30.3 mol %, for DMPC, DOPC, and DPPC, respectively, which are very close to the transition points found as the crossing points of λ_1 and λ_2 curves. This means that using the concentrations from Table 2 in the manuscript and subsequent extrapolation to the crossing point is enough to find the stability-rupture transition quite accurately.

Machine-learned state variables

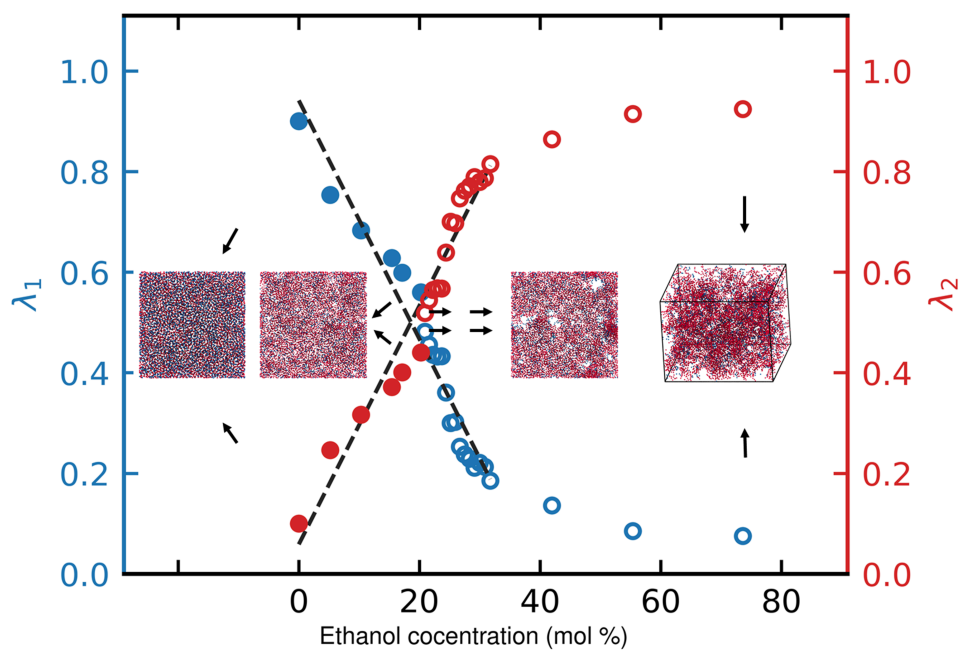


Figure S7: Variation of state variables λ_1 and λ_2 for a DMPC (dimyristoylphosphatidylcholine) bilayer, immersed in aqueous solutions containing various concentrations of ethanol at 298 K. Open and filled markers represent the ruptured and intact bilayers, respectively. Snapshots corresponding to $(\lambda_1, \lambda_2) = (0.9, 0.1)$, $(0.56, 0.44)$, $(0.48, 0.52)$, and $(0.08, 0.92)$ are shown in the figure. The blue and red colors in the snapshots show head and tail lipid groups, respectively.

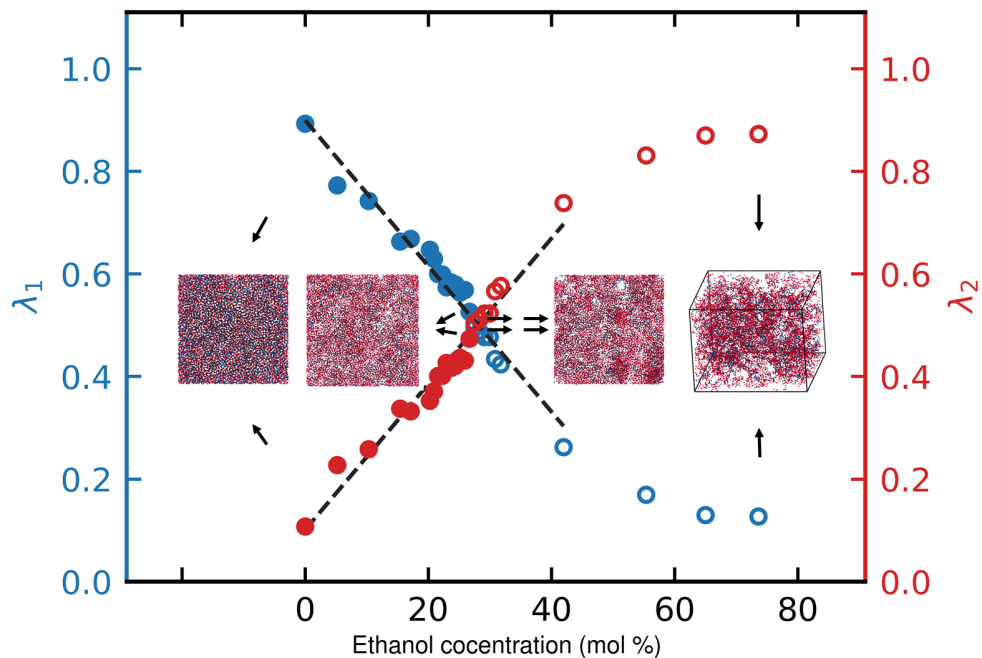


Figure S8: Variation of parameters λ_1 and λ_2 for DOPC (dioleoylphosphatidylcholine) bilayer, immersed in aqueous solutions containing ethanol, with ethanol concentration at 298 K. Open and filled markers represent the disrupted and intact bilayers, respectively. Snapshots of simulation box corresponding to $(\lambda_1, \lambda_2) = (0.89, 0.11)$, $(0.49, 0.51)$, $(0.48, 0.52)$, and $(0.13, 0.87)$ are shown in the figure. The blue and red colors in the snapshots show head and tail lipid groups, respectively.

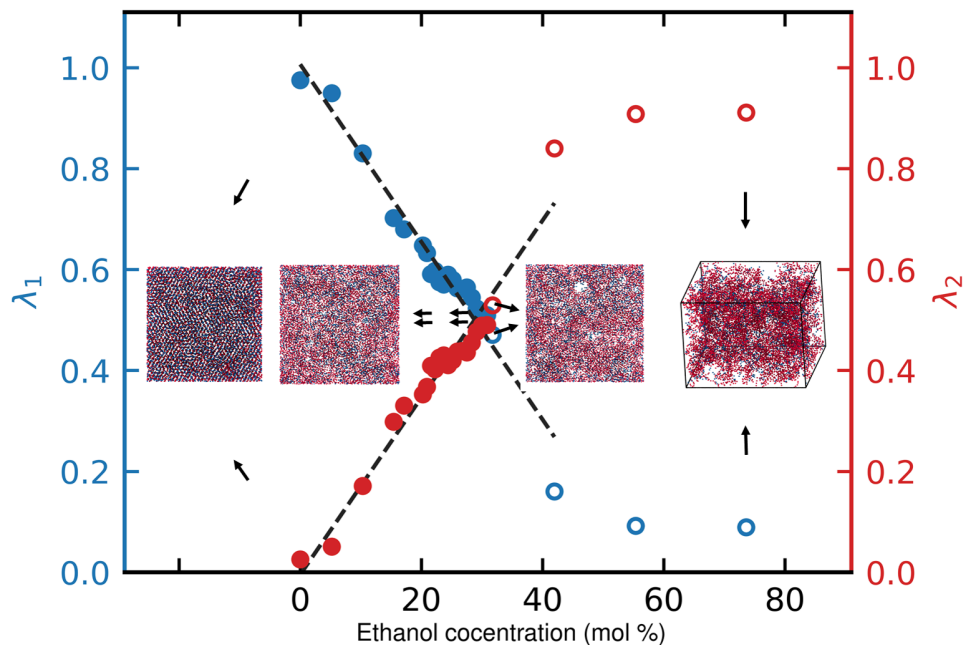


Figure S9: Variation of parameters λ_1 and λ_2 for DPPC (dipalmitoylphosphatidylcholine) bilayer, immersed in aqueous solutions containing ethanol, with ethanol concentration at 298 K. Open and filled markers represent the disrupted and intact bilayers, respectively. Snapshots of simulation box corresponding to $(\lambda_1, \lambda_2)=(0.98, 0.02)$, $(0.51, 0.49)$, $(0.47, 0.53)$, and $(0.09, 0.91)$ are shown in the figure. The blue and red colors in the snapshots show head and tail lipid groups, respectively.

References

- (1) Koynova, R.; Tenchov, B. Lipids: Phase Transitions. *Wiley Encycl. Chem. Biol.* **2008**,
- (2) Eslami, H.; Müller-Plathe, F. Molecular dynamics simulation in the grand canonical ensemble. *J. Comput. Chem.* **2007**, *28*, 1763–1773.
- (3) Eslami, H.; Khani, M.; Müller-Plathe, F. Gaussian Charge Distributions for Incorporation of Electrostatic Interactions in Dissipative Particle Dynamics: Application to Self-Assembly of Surfactants. *J. Chem. Theory Comput.* **2019**, *15*, 4197–4207.

-
- (4) Eslami, H.; Gharibi, A.; Müller-Plathe, F. Mechanisms of Nucleation and Solid–Solid-Phase Transitions in Triblock Janus Assemblies. *J. Chem. Theory Comput.* **2021**, *17*, 1742–1754.

3.4 Optimization of Heat Transfer Efficiency of Copolymers from the Perspective of Inverse Design

Reproduced with permission from Zhou et al. [J. Chem. Theory Comput. 2021, 17, 6, 3772–3782]
Copyright 2021 American Chemical Society.

Sequence-Engineering Polyethylene–Polypropylene Copolymers with High Thermal Conductivity Using a Molecular-Dynamics-Based Genetic Algorithm

Tianhang Zhou,[§] Zhenghao Wu,^{*,§} Hari Krishna Chilukoti, and Florian Müller-Plathe

Cite This: *J. Chem. Theory Comput.* 2021, 17, 3772–3782

Read Online

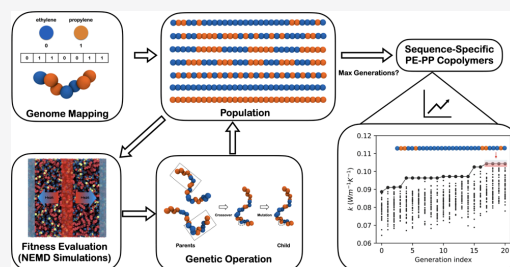
ACCESS |

Metrics & More

Article Recommendations

Supporting Information

ABSTRACT: Polymer sequence engineering is emerging as a potential tool to modulate material properties. Here, we employ a combination of a genetic algorithm (GA) and atomistic molecular dynamics (MD) simulation to design polyethylene–polypropylene (PE–PP) copolymers with the aim of identifying a specific sequence with high thermal conductivity. PE–PP copolymers with various sequences at the same monomer ratio are found to have a broad distribution of thermal conductivities. This indicates that the monomer sequence has a crucial effect on thermal energy transport of the copolymers. A non-periodic and non-intuitive optimal sequence is indeed identified by the GA, which gives the highest thermal conductivity compared with any regular block copolymers, for example, diblock, triblock, and hexablock. In comparison to the bulk density, chain conformations, and vibrational density of states, the monomer sequence has the strongest impact on the efficiency of thermal energy transport via inter- and intra-molecular interactions. Our work highlights polymer sequence engineering as a promising approach for tuning the thermal conductivity of copolymers, and it provides an example application of integrating atomistic MD modeling with the GA for computational material design.



INTRODUCTION

The rapid development of modern industries in energy storage and semiconductor fabrications demands advanced functional materials. Block and random copolymers have emerged as promising candidates because of their rich advantages, including high ionic conductivity, convenient microdomain tunability, and facile processability.^{1–8} However, the low intrinsic thermal conductivity of polymeric materials limits the heat dissipation during the operation. Consequently, the generated heat may cause degradation and reduce the reliability and performance of copolymeric products. Hence, much effort has been directed toward understanding and controlling the heat exchange in copolymeric materials.^{9–12}

It is well known that alignment of polymer chains is one way to enhance the thermal conductivity of pure polymeric materials.^{13–16} For instance, ultra-drawn polyethylene nanofibers have a thermal conductivity of $104 \text{ W m}^{-1} \text{ K}^{-1}$, which is 3 orders higher than in the amorphous state.¹⁵ The spatial arrangement of chains can be achieved via blending different polymers. This approach has also been proved to increase the thermal conductivity of polymeric materials.^{17,18} These studies indicate that the thermal conductivity of polymeric materials has an intimate relationship with the chain conformation. The microscopic conformations in block copolymers can be tuned by changing either the fraction or the sequence of monomers,

providing an opportunity to achieve a high thermal conductivity in bulk polymers. For example, Wei and Luo found that the thermal conductivity of polyethylene–polypropylene (PE–PP) diblock copolymers can be tuned by the block ratio.¹⁹ Moreover, the monomer sequence has recently been reported to influence multiple material properties of block copolymers such as complex morphology,²⁰ coil–collapse transitions,²¹ and electrostatic interactions.^{22,23} Will a specific monomer sequence of copolymers enable a maximum thermal-conductive efficiency?

To answer this question, we first need strategies to efficiently explore a huge number of possible sequences. For example, it is 2^N permutations for a copolymer liquid of chain length N which has only two types of monomers. Although several sequence-defined polymers with limited chain length and chemistries have been synthesized,^{20,24,25} it remains a challenge for polymer chemists to synthesize routinely sequence-defined polymers.²⁶ In contrast, molecular dynamics (MD) simulation

Received: February 5, 2021

Published: May 5, 2021



has been a valuable and powerful tool for studying various properties of polymeric materials such as rheology,²⁷ dynamics,^{28,29} and thermal energy transport.^{30–32} Advanced machine-learning algorithms are being increasingly interlinked with MD simulation to accelerate material design.^{33–37} Recently, Simmons and co-workers proposed a computational framework by integrating the genetic algorithm (GA) with the coarse-grained MD simulations to design polymeric materials with target properties.^{38–40} Compared with the growing prevalence of machine-learning material design frameworks, which train models with the existing experimental or simulation data and predict material properties interpolatively, the use of MD simulation for fitness assessment in the GA allows us to design target materials with properties well outside the known materials. More recently, Patra et al. demonstrated an optimization workflow connecting a Monte Carlo tree search with MD simulations for inverse copolymer design in a scalable and efficient way.⁴¹

In this work, we employ a combinational strategy, which combines GA and atomistic MD simulations, to study the sequence effect on the thermal conductivity of an example system, a united-atom model of PE–PP copolymers. Here, the atactic form of polypropylene chains is chosen. We conduct non-equilibrium MD (NEMD) simulations to evaluate thermal conductivities for a total of ~600 different sequences of PE–PP copolymers generated automatically by the GA algorithm. This evolutionary algorithm successfully finds a non-periodic and non-intuitive optimal sequence of PE–PP copolymers with high thermal conductivity, which is better than any of the PE and PP homopolymers and regular block copolymers, for example, diblock, triblock, and hexablock. The conventional statistical parameters to describe copolymers such as the mean block length and monomer fraction are found to be insufficient in predicting the thermal conductivity of PE–PP copolymers. The correlations between thermal conductivity and chain conformations of copolymers have been investigated. To gain an insight into vibrational modes that are modified or initiated by the varying sequence and their influence on the thermal energy transfer of PE–PP copolymers, the vibrational density-of-states (VDOS) at the monomer level has also been analyzed.

METHODOLOGY

GA. The general idea of GA is to mimic the evolutionary biological selection process with the aim of optimizing the system's properties. In standard GA, the initial population of individuals is randomly selected.⁴² Each individual in the population is then evaluated according to some problem-specific fitness function. After determining the fitness score, a new population with a distribution biased toward higher-fitness-score members compared with the previous population is generated by performing three genetic operations: selection, crossover, and mutation. Figure 1 illustrates the implementation of GA operations in this work. First, the candidates with higher-fitness scores are selected as parents to produce new offspring (copolymer sequences). In practice, to simulate the survival of the fittest, the candidates with higher-fitness scores are selected with higher probabilities than those with lower-fitness scores via fitness-proportional selection such as roulette wheel selection. Second, the crossover operation combines the selected parents to produce new offspring. Since stronger (fitter) individuals are being selected more often, there is a tendency that the newly generated individuals may become

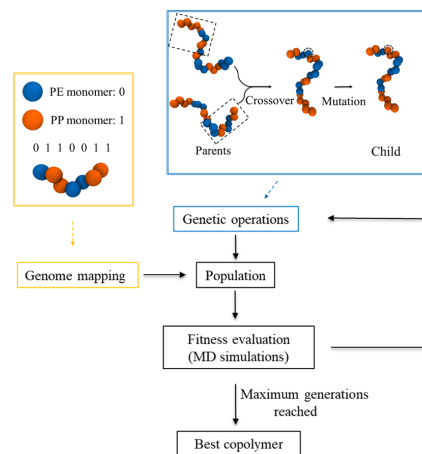


Figure 1. Flow chart of the molecular-dynamics-based GA used in this work: genome mapping; genetic operations; and evolution processes.

very similar after several generations, and the diversity of the population may decline. This could lead to population stagnation. Mutation is a mechanism employed to inject diversity into the population to avoid stagnation. These three operations are iterated until the target properties are achieved or the maximum number of generations is reached. In this work, the fitness assessment of the GA is conducted via MD simulations. We employ a mapping scheme of polymer sequences to binary genomes in which “0” and “1” represent a PE monomer and a PP monomer, respectively, as illustrated in Figure 1. Each copolymer chain contains 30 monomers, with each possible candidate mapped to a 30-gene binary genome. The optimization of GA is initiated with a population of 30 randomly generated monomer sequences. The fitness score of a single candidate is represented by the thermal conductivity of the sequence-specific PE–PP copolymer melt measured by NEMD simulations. These fitness evaluations of 30 candidates (MD simulations) are performed simultaneously via an automated protocol.

This automated protocol yields the computed thermal conductivity k of a batch of PE–PP copolymer sequences. The raw fitness score of each sequence is then defined as $z = k$. To maintain consistent selection pressure, a linear scaling $f(z) = az + b$, where a and b are constants, is performed to normalize the fitness scores f to span the interval from 0 to 1 within each generation.⁴² Our GA utilizes the single candidate elitism,⁴² in which the candidate with the highest-fitness score (highest thermal conductivity k) is cloned to the next generation without any modification. At the same time, other members of the successor generation are generated by the standard GA: after each generation, roulette wheel selection is used to select the parents for generating new candidates in the next generation. The selected parents are combined via the uniform crossover with a probability of 0.8, in which the child genes are obtained by mixing “father’s” genes with “mother’s” genes at a probability of 0.8. Subsequently, point mutations at a rate of 0.01 per gene are applied to a new candidate in the next generation. For instance, a PP monomer has a probability of 0.01 to be changed into a PE monomer during the point mutation procedure.

In GAs such as this where the target of optimization is a physical property measured through simulation, the speed-determining step is frequently the fitness evaluation. In MD-GA of this work, approximately 8 h of MD simulation on 40 CPUs is required to determine the fitness score (thermal conductivity) of each copolymer sequence within reasonable uncertainty bounds ($\pm\sim 5.0\%$). A regular optimization using the GA might reach hundreds to thousands of generations, with each generation composed of a population of tens of individuals (constant through the course of GA). Differently, the results of all MD simulations are stored by the GA such that the prediction is reused when a particular copolymer sequence is found to repeat from prior generations in order to minimize the number of MD simulations required in this work. The thermal conductivity of the rediscovered copolymer sequence is recalled from the database of prior generations rather than running fresh MD simulations. The population size of each generation is therefore variable in our GA, similar to the prior work of Simmons et al.³⁸ The copolymer sequences rediscovered in each generation are accumulated, which effectively increases the population size. The population size as a function of generations is shown in Figure 2.

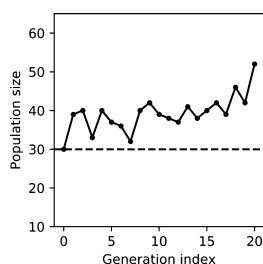


Figure 2. Actual population size (solid line) and the number of new fitness evaluations (MD simulations) (dashed line) as a function of generation index in the molecular-dynamics-based GA.

MD Simulations. The optimized potential for liquid simulations-united atom force field is employed to describe the interactions between PE and PP monomers (as summarized in Table S1).⁴³ Compared with the all-atom model, previous studies showed that the united-atom model reproduces thermal transport properties of polymeric fluids more accurately.⁴⁴ The chains of PE and PP homopolymers and examples of regular and irregular PE-PP copolymers are shown in Figure 3a–f, where hydrogen atoms are adsorbed by carbon atoms. The number of repeat units in the polymer chains is chosen to be 30 in all systems studied in this work. The initial configuration of copolymers with chains of the same monomer sequences is generated by Moltemplate.⁴⁵ The total number of united atoms in the system is kept to be ~ 18000 , resulting in a cubic simulation box with the side length of ~ 80 Å. An example snapshot of the diblock copolymer $PE_{15}PP_{15}$ system is shown in Figure 3g. All simulations are carried out using the large-scale molecular/atom parallel simulator package under periodic boundary conditions.⁴⁶ Initially, systems are equilibrated in the *NPT* ensemble at $T = 600$ K and $P = 1$ bar for 6 ns using the Nosé–Hoover thermostat and barostat with the coupling times of 0.2 and 2.0 ps, respectively. A timestep of 2 fs is used in all simulations during equilibration. At this temperature, PE and PP chains are relatively flexible, and the

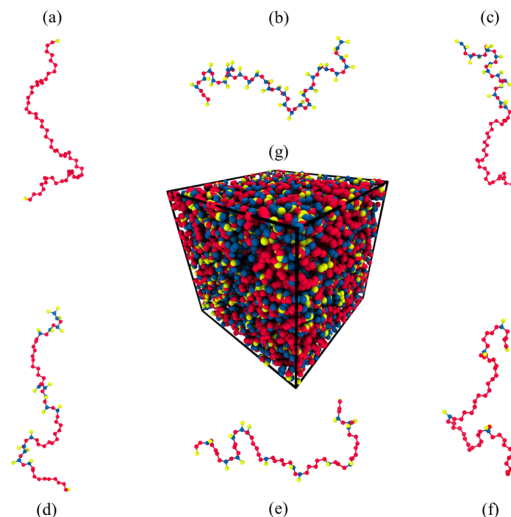


Figure 3. Schematics of polymer chain models with 30 monomers of the (a) PE (polyethylene) homopolymer, (b) PP (polypropylene) homopolymer, (c) regular diblock ($PE_{15}PP_{15}$) copolymer, (d) regular decablock ($(PE_3PP_3)_5$) copolymer, and (e,f) irregular copolymers obtained from molecular-dynamics-based GA with PE contents (e) 53.3% and (f) 80%. (g) Snapshot of a regular diblock copolymer $PE_{15}PP_{15}$ system at 600 K and 1 bar. The CH_3 , CH_2 , and CH united atoms are shown in yellow, red, and blue colors, respectively.

structure relaxation is sufficiently achieved within the given equilibration time. The relaxation process of radius of gyration for an example copolymer system is shown in Figure S1 of Supporting Information.

After equilibration, a non-equilibrium simulation follows to calculate the thermal conductivity of the copolymers with a timestep of 0.5 fs. Figure 4 shows a schematic of the NEMD simulation method. Specifically, a constant energy per time is added into and subtracted from the “hot” (heat source) and “cold” (heat sink) regions. The heat source of thickness 10 Å is positioned in the center and two heat sinks, each with thickness of 5 Å, are set at two edges of the periodic simulation box. The velocity rescaling method is used to maintain the desired temperature of the heat source and sink. The thermal conductivity of each copolymer sequence is calculated by Fourier’s law: $k = -J/(dT/dz)$, where J is the heat flux at the steady state and dT/dz is the temperature gradient. 20 Å-wide regions, which are used for calculating the temperature gradient, are located in between the hot and cold regions. The NEMD calculations performed at a constant volume using the box dimension averaged over the last half period from the equilibration step. One example of the temperature profile at the steady state is shown in Figure 4b. The data collection run of NEMD simulations is divided into three blocks, from each of which a thermal conductivity value is computed. The thermal conductivity of each copolymer sequence is averaged over these values with their standard deviation taken as error bars. More details about the simulation details can be found in the Supporting Information.

Spectral Analysis. In order to better understand the mechanisms of thermal energy transport in bulk copolymer

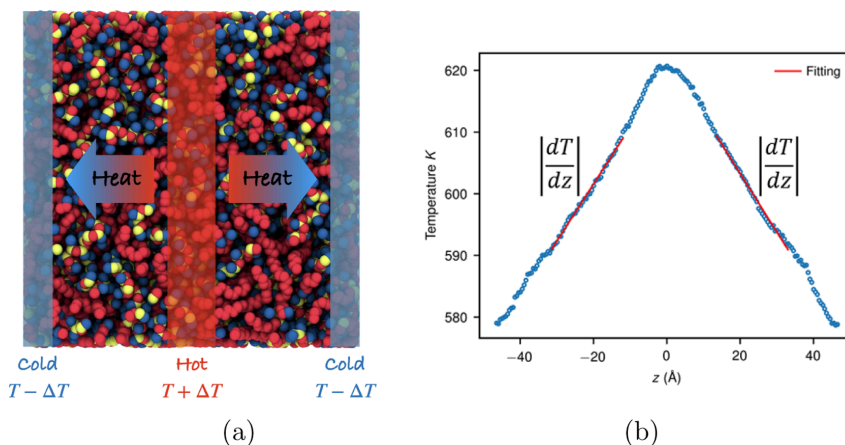


Figure 4. (a) Snapshot of a regular diblock copolymer PE₁₅PP₁₅ system under NEMD simulations. Regions of heat addition and subtraction are labeled as “hot” and “cold”, respectively. (b) An example of the steady-state temperature profile along the direction of heat transfer (z) in the NEMD simulation. The temperature gradient is calculated from the average of two absolute values.

systems, the VDOS $D(\omega)$ has been analyzed, which is defined as

$$D(\omega) = \frac{1}{k_B T} \sum_i m_i \int_{-\infty}^{+\infty} d\tau \epsilon^{i\omega\tau} \langle v_i(\tau) \cdot v_i(0) \rangle \quad (1)$$

where τ is the time and ω is the frequency. In this work, m_i and v_i are the average mass and velocity at the center of mass of monomers i , respectively. The Fourier transform of the velocity auto-correlation function is proportional to the VDOS.⁴⁷ In order to analyze the thermal conductivity results, we calculate the VDOS of all monomers in the polymer chain. The velocities are collected every 20 MD steps (40 fs) for 1.0 ps time blocks. A Gaussian convolution with a width of 1.6 THz was applied to smooth the spikes in the VDOS.³²

RESULTS AND DISCUSSION

We start by evaluating the performance of the MD–GA strategy on designing high-thermal-conductive PE–PP copolymers. As shown in Figure 5, the highest thermal conductivity of the copolymer at each generation increases during the evolution of MD–GA. GA optimization is terminated at the 20th generation, partially, because of the time constraint since the MD simulation of the PE–PP united-atom model is relatively expensive; more importantly, the improvement of the highest thermal conductivity is found to be stagnant with additional generations. We find that the thermal conductivity of the optimal sequence obtained at the 20th generation is enhanced about 7 and 45% compared with PE and PP homopolymers, respectively. This indicates that our MD–GA workflow is indeed able to identify the optimal sequence of PE–PP block copolymers with high thermal conductivity. An optimal sequence with $k = 0.104 \text{ W m}^{-1} \text{ K}^{-1}$ is also shown in the inset of Figure 5. It is noted that this sequence is evidently non-periodic and non-intuitive. Specifically, this GA-optimized sequence has a long block of PE located in the center and small fractions of PP monomers near the ends of the chain. These arrangements of blocks in this specific sequence balance the thermal energy transfer via bonded and non-bonded interactions, which enables it to reach a maximum efficiency.

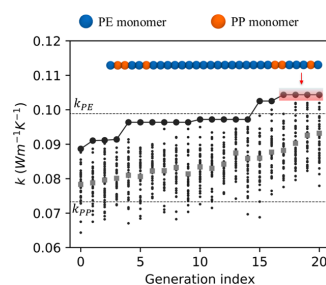


Figure 5. Thermal conductivity of all copolymer sequences obtained from the MD–GA strategy (black points) vs the generation index at $T = 600 \text{ K}$ and $P = 1 \text{ bar}$. The best copolymer candidates for each generation are denoted with large black points. Blue and orange beads represent PE and PP monomers, respectively. Light and dark dashed lines are the thermal conductivity of PE and PP homopolymers. The gray-squared symbols represent the mean fitness of the thermal conductivity for various copolymer sequences at each generation.

The underlying physical origin of this sequence specificity in thermal energy transfer in PE–PP copolymers is discussed in detail in the following sections.

It has long been believed that the mean block length of copolymers is a meaningful descriptor and predictor for their properties. In order to understand the sequence specificity, we first focus on the correlation between the mean block length of all MD–GA generated copolymer sequences and their calculated thermal conductivities. The mean block length l_b is defined as the arithmetic mean of the length of all PE and PP blocks: $l_b = N/N_b$, where N and N_b are the total number of monomers and the number of blocks, respectively. Figure 6 depicts the thermal conductivity as a function of mean block length l_b of all sequences. Notably, the MD–GA strategy generates copolymer sequences covering many different mean block lengths l_b ranging from ~ 1.5 to ~ 6 . The thermal conductivity generally increases when the mean block length is within the regime of $1 < l_b \leq 2.8$, and when $l_b > 2.8$, the mean block length seems not to affect the thermal conductivity

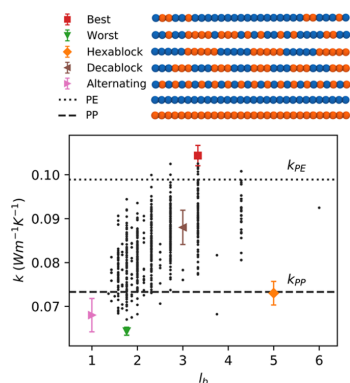


Figure 6. Thermal conductivity of all copolymer sequences obtained from the MD–GA strategy (black points) vs mean block length (l_b). The best, worst, hexablock, decablock, and alternating copolymers are highlighted in red, green, orange, brown, and pink color symbols, respectively. All systems are at $T = 600$ K and $P = 1$ bar. Blue and orange beads represent PE and PP monomers, respectively.

significantly. Furthermore, the variation of the thermal conductivity is approximately 10–40% in copolymers with the same l_b . This broad distribution of thermal conductivity therefore indicates that the mean block length alone is not a good prediction for the thermal conductivity of PE–PP copolymers. Additionally, we find that the optimal sequence identified by the MD–GA strategy outperforms all regular block copolymers, namely, hexablock ((PE₃PP₃)₃), decablock ((PE₃PP₃)₅), and alternating ((PE₁PP₁)₁₅) copolymers, by at least ~15% on the thermal conductivity.

Another statistical parameter to describe block copolymers is the monomer fraction. Therefore, we analyze the inter-correlations between the monomer fraction, the mean block length, and the thermal conductivity of all copolymer sequences. Figure 7 shows the thermal conductivity of all copolymer sequences as a function of the mean block length l_b and the PE monomer fraction λ , where λ is defined as the ratio

between the number of PE monomers and the total number of monomers equal to 30 for a single copolymer chain. The dark blue points in Figure 7 correspond to the regime of PE–PP copolymers with high thermal conductivity; the lighter color represents the lower thermal conductivity. We observe that the thermal conductivity of PE–PP copolymers is enhanced with the increase of both the mean block length and the PE monomer fraction, while it reaches a high value in the vicinity of $l_b \approx 4$ and $\lambda \approx 0.8$, as shown in Figure 7a. However, a great number of light color points are also found in PE–PP copolymers with almost all mean block lengths and PE monomer fractions in the three-dimensional plots, as shown in Figure 7b. This indicates the uniqueness of the optimal sequence, and it again demonstrates the effect of the monomer sequence on the thermal energy transport of PE–PP copolymers. The thermal conductivities presented above, upon which the analyses are based, are measured at $T = 600$ K because the polymer structure can be equilibrated faster at high temperatures. The thermal conductivities of several typical regular, random, and optimal copolymer sequences calculated at $T = 300$ K are shown in Figure S3. The general trend of the thermal transport behavior of PE–PP copolymers as a function of the mean block length l_b or ethylene monomer fraction λ is essentially the same at room temperature as that at high temperatures. Most importantly, the optimal sequence is still found to outperform any other copolymer sequences at room temperature.

Previous studies suggest that thermal conductivity of polymeric materials is closely correlated with chain conformations (e.g., radius of gyration).^{18,19,48–50} For example, Luo and co-workers have extensively shown that an amorphous polymer with more extended chains has a higher thermal conductivity.¹⁸ We measure chain extensions in terms of radius of gyration R_g to examine its possible relation with the monomer sequence effect on copolymer thermal energy transport. Figure 8a describes the correlation between the thermal conductivity of copolymers with varying sequences and the ensemble averaged mean-square radius of gyration $\langle R^2 \rangle$. Specifically, PE–PP copolymers with the same $\langle R^2 \rangle$ have diverse thermal conductivities, variation of which is approximately 25%. A linear fit is found to reasonably describe the

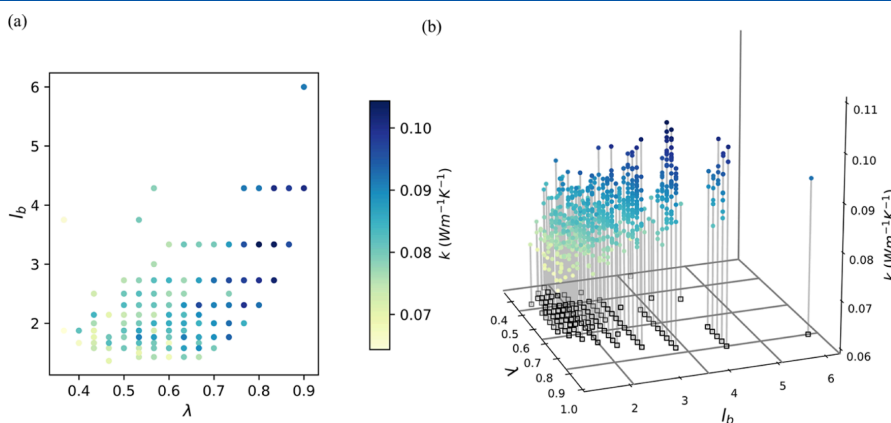


Figure 7. (a) Two-dimensional and (b) three-dimensional plots of the variation of thermal conductivities of copolymers from the MD–GA strategy as a function of the PE monomer fraction λ and the mean block length l_b at $T = 600$ K and $P = 1$ bar.

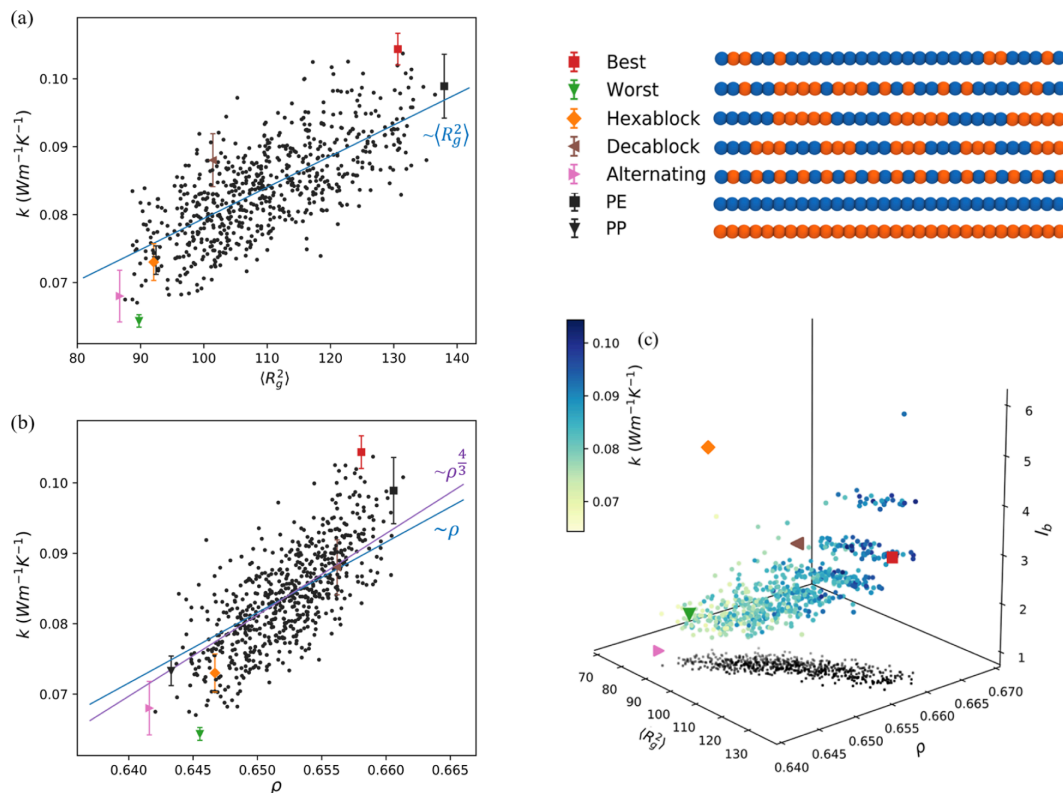


Figure 8. (a) Thermal conductivity of each copolymer obtained from MD-based GA (black points) vs mean-square radius ($\langle R_g^2 \rangle$). The solid blue line is the fit of average thermal conductivity of all copolymers $\sim \langle R_g^2 \rangle$. (b) Thermal conductivity of each copolymer obtained from MD-based GA (black points) vs the mass density (ρ). The solid blue line is the fit of average thermal conductivity of all copolymers $\sim \rho$. The solid purple line is the fit of average thermal conductivity of all copolymers $\sim \rho^{4/3}$. (c) Thermal conductivities of copolymers (color-coded) as a function of $\langle R_g^2 \rangle$, ρ , and the mean block length l_b . All systems are at $T = 600$ K and $P = 1$ bar.

relation between the thermal conductivity of various copolymer sequences and their $\langle R_g^2 \rangle$. Furthermore, it is evidently observed that a copolymer sequence with a high thermal conductivity possesses a large $\langle R_g^2 \rangle$. However, the exact relation between the monomer sequence and the chain conformations in copolymers is still not comprehensively understood,³⁵ and it is out of the scope of this work.

We also consider the connection of material properties such as the bulk density⁴⁸ with the effect of monomer sequence observed in thermal transport behaviors of PE–PP copolymers. As a first approximation, Hands et al.⁵¹ proposed an empirical prediction for the thermal conductivity of polymer liquids above the glass-transition temperature: $k \approx \rho^{4/3}$. This relation has been found to reasonably predict the thermal conductivity of numerous polymer chemistries.^{50,52} Figure 8b depicts the thermal conductivity of various copolymer sequences as a function of their densities. As in the discussion about chain conformations mentioned above, we also use a linear equation to fit the relation between the bulk density and thermal conductivity of PE–PP copolymers with various sequences. Compared with the Hands model, the linear equation performs similarly in describing their relation. Moreover, we find that copolymers with high thermal

conductivity are found in the regime of higher bulk densities. The intimate relation between the bulk density and the thermal conductivity is generally valid in PE–PP copolymers, albeit with variations of $\sim 25\%$ in thermal conductivity among copolymers of the same bulk density. Additionally, we analyze the correlation between the radius of gyration, the bulk density, the mean block length, and the thermal conductivity of all copolymer sequences, as shown in Figure 8c. Specifically, the bulk density and squared radius of gyration are observed to be roughly in a linear correlation. The dark blue points, which represent the copolymers with high thermal conductivities, tend to cluster at the region of large density and radius of gyration, regardless of the mean block length. The long tails of light blue points at various mean block lengths once more underline the monomer specificity of the thermal energy transfer in PE–PP copolymers.

We further investigate the efficiency of thermal energy transfer via bonded and non-bonded interaction by calculating the VDOS. Milkus et al. used the VDOS to characterize the variation of thermal conductivities due to chain stiffness and chain lengths in polymer liquids.⁵³ They found that, in principle, the low-frequency VDOS corresponds to inter- and intra-chain non-bonded interactions and the high-frequency

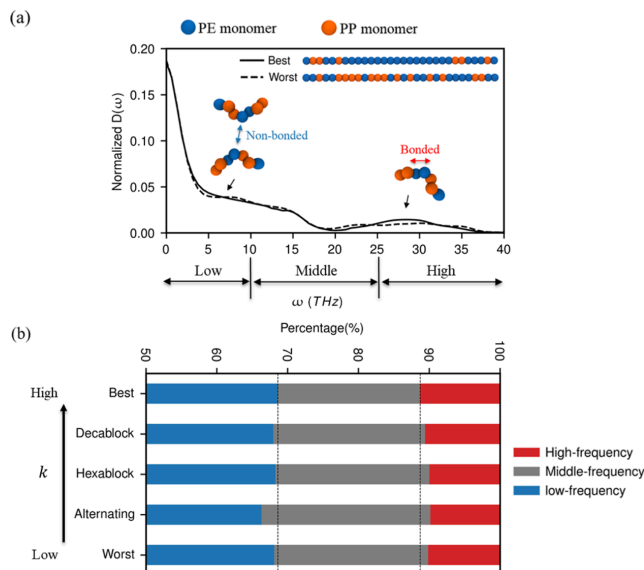


Figure 9. (a) Normalized VDOS of monomers of the best and worst copolymers at $T = 600$ K and $P = 1$ bar. $D(\omega)$ is calculated from the center of mass and the average velocity of monomers. The schematic illustration shows the best and worst copolymer chains. (b) Percentage of contributions from each frequency regions for the best, worst, hexablock, decablock, and alternating copolymers.

VDOS corresponds to bonded interactions. Recently, the VDOS has also been used to investigate the variation of the thermal conductivity of polymeric systems under external strain fields.⁵⁴ Here, the monomer VDOS profiles $D(\omega)$ of the best and the worst copolymers (Figure 9a) have been calculated from eq 1, where the average mass and velocity at the center of mass of monomers have been used. The VDOS is normalized so that the integral area of $D(\omega)$ is unity. We separate VDOS into three frequency regions: low- (0–10 THz), middle- (10–25 THz), and high- (>25 THz) frequency regions (Figure 9a). We notice that the VDOSs of two sequence-specific copolymers are very similar except for small derivations in low- and high-frequency regions. We calculated the ratio of the respective regions in order to analyze the contributions from the different frequency regions more quantitatively via

$$\int_{\omega_{i,s}}^{\omega_{i,e}} D(\omega) d\omega \times 100\% \quad (2)$$

where $\omega_{i,s}$ and $\omega_{i,e}$ are the lower and upper frequencies of the i th frequency region, respectively. Figure 9b shows the percentage of contributions for five types of copolymers including both regular block and sequence-specific copolymers. The contributions of the low- and high-frequency vibrations in the optimal sequence with a high thermal conductivity are evidently larger compared with those for other copolymer sequences. This implies that the copolymer with optimal sequence exhibits high efficiencies of thermal energy transfer via both bonded and non-bonded interactions. It is noted that the middle-frequency VDOSs are vibrational modes that are expected to be associated with the angular interaction.⁵³ The exact examination of the effect of the angular interaction on the thermal energy transfer needs detailed spectral analysis, which is not the focus of this study.

The detailed VDOS analysis illustrates the different efficiencies of thermal energy transfer through bonded and non-bonded interactions in PE–PP copolymers. We further analyze the intermolecular distance to elucidate the mechanism of thermal energy transfer through non-bonded interactions in PE–PP copolymers with various monomer sequences. For instance, the smaller intermolecular distance usually leads to larger non-bonded interactions, enabling it to contribute more to the thermal energy transfer. Indeed, a prior work of Wei and Luo revealed that the replacement of PP monomers by PE monomers results in increasing efficiency of the thermal energy transfer through non-bonded interactions in PE–PP diblock copolymer melts.¹⁹ To this end, we examine the intermolecular radial distribution function $g(r)$ to understand different efficiencies of thermal energy transfer routes, particularly, non-bonded interactions in the sequence-specific copolymers. The intermolecular radial distribution function $g(r)$ is defined as the probability of finding a monomer (center of mass) in different polymer chains at a distance r from a given monomer. As seen in Figure 10a, we find that the distance between chains in the copolymer with the optimal sequence is evidently smaller than any other typical copolymer sequences, implying a higher efficiency of thermal energy transfer via non-bonded interactions. Additionally, the smaller intermolecular distance of the decablock copolymer compared with that of hexablock copolymer, as shown in Figure 10a, supports that the former outperforms the latter in terms of thermal conductivity, although they have the same 1:1 ratio of PE and PP monomers. Furthermore, we investigate the coordination number c_{inter} which is defined as the integral over $g(r)$ from 0 to the position r_p of the first peak of $g(r)$ as

$$c_{\text{inter}} = \int_0^{r_p} 4\pi r^2 \rho_m g(r) dr \quad (3)$$

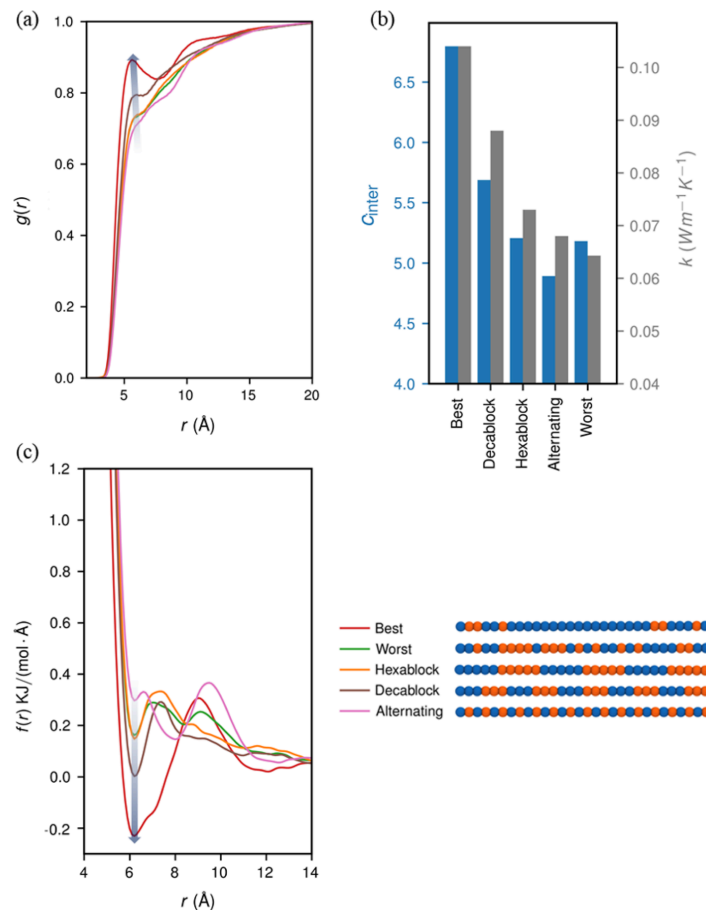


Figure 10. (a) Intermolecular radial distribution functions $g(r)$, (b) correlation between the coordination number c_{inter} and the thermal conductivity k , and (c) non-bonded force $f(r)$ for the best, worst, hexablock, decablock, and alternating copolymers. The intermolecular radial distribution function $g(r)$ is defined as the probability of finding a monomer (center of mass) in different polymer chains at a distance r from a given monomer. The coordination number c_{inter} is defined as the integral $g(r)$ from 0 to the position r_p of the first peak of $g(r)$. The non-bonded force $f(r)$ is derived from the gradient of the potential of mean force (PMF).

where ρ_m is the number density of monomers. This coordination number c_{inter} is usually used to quantitatively characterize the number of contacts between molecules. As seen in Figure 10b, we find that this quantity is closely correlated with the thermal conductivity of various copolymer sequences. Specifically, the optimal sequence with a high thermal conductivity has the highest c_{inter} in comparison with several typical regular block copolymers. The PMF $U_{\text{PMF}}(r)$ can be computed via Boltzmann inversion of the radial distribution functions^{55,56}

$$U_{\text{PMF}}(r) = k_{\text{B}}T \ln g(r) \quad (4)$$

where k_{B} is the Boltzmann constant. Even though it is not the exact solution (only exact in infinitely dilute systems), the PMF can serve to roughly measure the magnitude of non-bonded interactions. The non-bonded forces $f(r)$ are thus able to be derived from the gradient of the PMFs: $f(r) = -dU_{\text{PMF}}(r)/dr$. As seen in Figure 10c, the magnitude of the

non-bonded forces $f(r)$ is obviously more attractive in the optimal sequence than in any other copolymer sequence, consistent with its smaller intermolecular distance seen in Figure 10a.

CONCLUSIONS

We employ a computational framework of a MD-based GA to design PE–PP copolymers with high thermal conductivity. The integration of atomistic MD simulation (united-atom models) as fitness evaluation with the GA is reported, to our knowledge, for the first time. Our results demonstrate that the actual monomer sequence substantially affects the thermal energy transfer in PE–PP copolymers. This is strongly confirmed by the wide distribution of thermal conductivities observed in PE–PP copolymers with either the same overall monomer composition or the same mean block length. The traditional descriptor of block copolymers, namely, mean block

length, is thus a poor predictor for the thermal conductivity of PE–PP copolymers. An irregular optimal sequence identified after 20 MD–GA generations outperforms any other copolymer sequences on thermal energy transfer. This optimal sequence is found at the PE monomer fraction $\lambda \approx 0.8$ and mean block length $l_b \approx 4$ through analyzing the correlation between them and the thermal conductivity of all copolymer sequences. It contains a segment of pure polyethylene (17 monomers) in the center, followed by two 6 and 7 monomer-long segments which contain ethylene and propylene in equal proportions and random order. We note in particular that the thermal conductivity of the optimized sequence is higher than that of pure PE homopolymer. To understand the underlying physical origins of the sequence specificity, the radii of gyration of all copolymer sequences are measured. The thermal conductivity of PE–PP copolymers follows the radius of gyration, which means that it is more likely to find a high thermal conductivity for a PE–PP copolymer with a more extended chain (larger $\langle R_g^2 \rangle$). The correlation between the thermal conductivity and the bulk density of PE–PP copolymers is similar to that of the radius of gyration. However, a broad distribution of thermal conductivities is still observed for copolymers with both similar $\langle R^2 \rangle$ and bulk density.

The emerging physical picture is that the monomer sequence (relative positions of these monomers) plays a significant role in the heat transfer of PE–PP copolymers, although there is a trade-off between the monomer composition and the mean block length. Additionally, we perform a detailed analysis of the VDOS to examine the efficiencies of thermal energy transfer through different molecular interactions, for example, bonded and non-bonded interactions. It identifies three modes of thermal energy transfer in polymer liquids: (i) high-frequency mode of bond interactions, (ii) low-frequency mode of non-bonded interactions, and (iii) intermediate-frequency mode of many-body interactions such as angular interactions. Compared with several typical block copolymers, the high thermal conductivity of the optimal sequence is attributed to the optimized thermal energy transfer via both (i) bonded and (ii) non-bonded interactions. Additionally, we find that the higher efficiency of thermal energy transfer through non-bonded interactions can be explained by the shorter intermolecular distance, characterized by the intermolecular radial distribution functions. The enhancement of the thermal conductivity of the sequence-specific PE–PP copolymer is not high in comparison with the better homopolymer PE ($\approx 8\%$). It is interesting though that admixture of a small fraction of the worse-conducting PP can further improve the better-conducting PE. Furthermore, the genetic-algorithm-cum-molecular-dynamics method is able to capture the subtle improvements. Gratifyingly, it seems possible for the monomer sequence effect on thermal energy transport to be turned toward practical applications using novel monomer chemistries, for example, conjugated⁵⁷ and reactive groups,⁵⁸ identified during the recent development of polymeric materials with high thermal conductivity. Overall, our work demonstrates that polymer sequence engineering is a promising approach to modulate the thermal conductivity of PE–PP copolymers, and we believe that the computational framework of integrating atomistic MD simulation with the GA has a significant potential for accelerating the design of copolymeric materials.

■ ASSOCIATED CONTENT

SI Supporting Information

The Supporting Information is available free of charge at <https://pubs.acs.org/doi/10.1021/acs.jctc.1c00134>.

Force fields of the united model of polyethylene and polypropylene melts; structure relaxation process of an example hexablock copolymer system; details of NEMD simulations; and thermal conductivity of several typical copolymer sequences at $T = 300$ K (PDF)

■ AUTHOR INFORMATION

Corresponding Author

Zhenghao Wu – *Eduard-Zintl-Institut für Anorganische und Physikalische Chemie, Technische Universität Darmstadt, 64287 Darmstadt, Germany*; orcid.org/0000-0003-2862-4432; Email: z.wu@theo.chemie.tu-darmstadt.de

Authors

Tianhang Zhou – *Eduard-Zintl-Institut für Anorganische und Physikalische Chemie, Technische Universität Darmstadt, 64287 Darmstadt, Germany*

Hari Krishna Chilukoti – *Department of Mechanical Engineering, National Institute of Technology Warangal, Warangal 506004, Telangana, India*; *Eduard-Zintl-Institut für Anorganische und Physikalische Chemie, Technische Universität Darmstadt, 64287 Darmstadt, Germany*; orcid.org/0000-0002-7882-0805

Florian Müller-Plathe – *Eduard-Zintl-Institut für Anorganische und Physikalische Chemie, Technische Universität Darmstadt, 64287 Darmstadt, Germany*; orcid.org/0000-0002-9111-7786

Complete contact information is available at: <https://pubs.acs.org/doi/10.1021/acs.jctc.1c00134>

Author Contributions

[§]T.Z. and Z.W. contributed equally to this work.

Notes

The authors declare no competing financial interest.

■ ACKNOWLEDGMENTS

Z.W. gratefully acknowledges the financial support through the Deutsche Forschungsgemeinschaft via the SFB-TRR 146 “Multiscale Simulation Methods for Soft Matter Systems”, Project A8.

■ REFERENCES

- (1) Majewski, P. W.; Gopinadhan, M.; Jang, W.-S.; Lutkenhaus, J. L.; Osuji, C. O. Anisotropic Ionic Conductivity in Block Copolymer Membranes by Magnetic Field Alignment. *J. Am. Chem. Soc.* **2010**, *132*, 17516–17522.
- (2) Weber, R. L.; Ye, Y.; Schmitt, A. L.; Banik, S. M.; Elabd, Y. A.; Mahanthappa, M. K. Effect of Nanoscale Morphology on the Conductivity of Polymerized Ionic Liquid Block Copolymers. *Macromolecules* **2011**, *44*, 5727–5735.
- (3) Zhang, S.; Lee, K. H.; Frisbie, C. D.; Lodge, T. P. Ionic Conductivity, Capacitance, and Viscoelastic Properties of Block Copolymer-Based Ion Gels. *Macromolecules* **2011**, *44*, 940–949.
- (4) Guan, T.; Qian, S.; Guo, Y.; Cheng, F.; Zhang, W.; Chen, J. Star Brush Block Copolymer Electrolytes with High Ambient-Temperature Ionic Conductivity for Quasi-Solid-State Lithium Batteries. *ACS Mater. Lett.* **2019**, *1*, 606–612.
- (5) Morris, M. A.; Sung, S. H.; Ketkar, P. M.; Dura, J. A.; Nieuwendaal, R. C.; Epps, T. H. Enhanced Conductivity via

Homopolymer-Rich Pathways in Block Polymer-Blended Electrolytes. *Macromolecules* **2019**, *52*, 9682–9692.

(6) Xie, S.; Meyer, D. J.; Wang, E.; Bates, F. S.; Lodge, T. P. Structure and Properties of Bicontinuous Microemulsions from Salt-Doped Ternary Polymer Blends. *Macromolecules* **2019**, *52*, 9693–9702.

(7) Seo, Y.; Shen, K.-H.; Brown, J. R.; Hall, L. M. Role of Solvation on Diffusion of Ions in Diblock Copolymers: Understanding the Molecular Weight Effect through Modeling. *J. Am. Chem. Soc.* **2019**, *141*, 18455–18466.

(8) Ma, B.; Nguyen, T. D.; Olvera de la Cruz, M. Control of Ionic Mobility via Charge Size Asymmetry in Random Ionomers. *Nano Lett.* **2020**, *20*, 43–49.

(9) Han, Z.; Fina, A. Thermal conductivity of carbon nanotubes and their polymer nanocomposites: A review. *Prog. Polym. Sci.* **2011**, *36*, 914–944.

(10) Yan, X.; Gu, J.; Zheng, G.; Guo, J.; Galaska, A. M.; Yu, J.; Khan, M. A.; Sun, L.; Young, D. P.; Zhang, Q.; Wei, S.; Guo, Z. Lowly loaded carbon nanotubes induced high electrical conductivity and giant magnetoresistance in ethylene/1-octene copolymers. *Polymer* **2016**, *103*, 315–327.

(11) Ghahramani, N.; Seyed Esfahani, S. A.; Mehranpour, M.; Nazoockdast, H. The effect of filler localization on morphology and thermal conductivity of the polyamide/cyclic olefin copolymer blends filled with boron nitride. *J. Mater. Sci.* **2018**, *53*, 16146–16159.

(12) Gao, A.; Zhao, F.; Wang, F.; Zhang, G.; Zhao, S.; Cui, J.; Yan, Y. Highly conductive and light-weight acrylonitrile-butadiene-styrene copolymer/reduced graphene nanocomposites with segregated conductive structure. *Composites, Part A* **2019**, *122*, 1–7.

(13) Choy, C. L.; Luk, W. H.; Chen, F. C. Thermal conductivity of highly oriented polyethylene. *Polymer* **1978**, *19*, 155–162.

(14) Choy, C. L.; Wong, Y. W.; Yang, G. W.; Kanamoto, T. Elastic modulus and thermal conductivity of ultradrawn polyethylene. *J. Polym. Sci., Part B: Polym. Phys.* **1999**, *37*, 3359–3367.

(15) Shen, S.; Henry, A.; Tong, J.; Zheng, R.; Chen, G. Polyethylene nanofibres with very high thermal conductivities. *Nat. Nanotechnol.* **2010**, *5*, 251–255.

(16) Loomis, J.; Ghasemi, H.; Huang, X.; Thoppey, N.; Wang, J.; Tong, J. K.; Xu, Y.; Li, X.; Lin, C.-T.; Chen, G. Continuous fabrication platform for highly aligned polymer films. *Technology* **2014**, *02*, 189–199.

(17) Kim, G.-H.; Lee, D.; Shanker, A.; Shao, L.; Kwon, M. S.; Gidley, D.; Kim, J.; Pipe, K. P. High thermal conductivity in amorphous polymer blends by engineered interchain interactions. *Nat. Mater.* **2015**, *14*, 295–300.

(18) Wei, X.; Zhang, T.; Luo, T. Chain conformation-dependent thermal conductivity of amorphous polymer blends: the impact of inter- and intra-chain interactions. *Phys. Chem. Chem. Phys.* **2016**, *18*, 32146–32154.

(19) Wei, X.; Luo, T. The effect of the block ratio on the thermal conductivity of amorphous polyethylene-polypropylene (PE-PP) diblock copolymers. *Phys. Chem. Chem. Phys.* **2018**, *20*, 20534–20539.

(20) Patterson, A. L.; Danielsen, S. P. O.; Yu, B.; Davidson, E. C.; Fredrickson, G. H.; Segalman, R. A. Sequence Effects on Block Copolymer Self-Assembly through Tuning Chain Conformation and Segregation Strength Utilizing Sequence-Defined Polypeptoids. *Macromolecules* **2019**, *52*, 1277–1286.

(21) Murnen, H. K.; Khokhlov, A. R.; Khalatur, P. G.; Segalman, R. A.; Zuckermann, R. N. Impact of Hydrophobic Sequence Patterning on the Coil-to-Globule Transition of Protein-like Polymers. *Macromolecules* **2012**, *45*, 5229–5236.

(22) Chang, L.-W.; Lytle, T. K.; Radhakrishna, M.; Madinya, J. J.; Vélez, J.; Sing, C. E.; Perry, S. L. Sequence and entropy-based control of complex coacervates. *Nat. Commun.* **2017**, *8*, 1273.

(23) Lytle, T. K.; Chang, L.-W.; Markiewicz, N.; Perry, S. L.; Sing, C. E. Designing Electrostatic Interactions via Polyelectrolyte Monomer Sequence. *ACS Cent. Sci.* **2019**, *5*, 709.

(24) Lutz, J.-F. Defining the Field of Sequence-Controlled Polymers. *Macromol. Rapid Commun.* **2017**, *38*, 1700582.

(25) Rosales, A. M.; Segalman, R. A.; Zuckermann, R. N. Polypeptoids: a model system to study the effect of monomer sequence on polymer properties and self-assembly. *Soft Matter* **2013**, *9*, 8400.

(26) Perry, S. L.; Sing, C. E. 100th Anniversary of Macromolecular Science Viewpoint: Opportunities in the Physics of Sequence-Defined Polymers. *ACS Macro Lett.* **2020**, *9*, 216–225.

(27) Everaers, R. Rheology and Microscopic Topology of Entangled Polymeric Liquids. *Science* **2004**, *303*, 823–826.

(28) Kremer, K.; Grest, G. S. Dynamics of entangled linear polymer melts: A molecular-dynamics simulation. *J. Chem. Phys.* **1990**, *92*, 5057–5086.

(29) Wu, Z.; Milano, G.; Müller-Plathe, F. Combination of Hybrid Particle-Field Molecular Dynamics and Slip-Springs for the Efficient Simulation of Coarse-Grained Polymer Models: Static and Dynamic Properties of Polystyrene Melts. *J. Chem. Theory Comput.* **2021**, *17*, 474–487.

(30) Müller-Plathe, F. A simple nonequilibrium molecular dynamics method for calculating the thermal conductivity. *J. Chem. Phys.* **1997**, *106*, 6082–6085.

(31) Cahill, D. G.; Ford, W. K.; Goodson, K. E.; Mahan, G. D.; Majumdar, A.; Maris, H. J.; Merlin, R.; Phillpot, S. R. Nanoscale thermal transport. *J. Appl. Phys.* **2003**, *93*, 793–818.

(32) Chilukoti, H. K.; Zhou, T.; Ardham, V. R.; Böhm, M. C.; Müller-Plathe, F. Thermal Energy Transport across the Interface between Phase Change Material-Heneicosane in Solid and Liquid Phases and Few-Layer Graphene. *J. Phys. Chem. C* **2019**, *123*, 29192–29202.

(33) Jackson, N. E.; Bowen, A. S.; Antony, L. W.; Webb, M. A.; Vishwanath, V.; de Pablo, J. J. Electronic structure at coarse-grained resolutions from supervised machine learning. *Sci. Adv.* **2019**, *5*, No. eaav1190.

(34) Jackson, N. E.; Webb, M. A.; de Pablo, J. J. Recent advances in machine learning towards multiscale soft materials design. *Curr. Opin. Chem. Eng.* **2019**, *23*, 106–114.

(35) Webb, M. A.; Jackson, N. E.; Gil, P. S.; de Pablo, J. J. Targeted sequence design within the coarse-grained polymer genome. *Sci. Adv.* **2020**, *6*, No. eabc6216.

(36) Upadhyay, R.; Kosuri, S.; Tamasi, M.; Meyer, T. A.; Atta, S.; Webb, M. A.; Gormley, A. J. Automation and data-driven design of polymer therapeutics. *Adv. Drug Deliv. Rev.* **2021**, *171*, 1–28.

(37) Deringer, V. L.; Bernstein, N.; Csányi, G.; Ben Mahmoud, C.; Ceriotti, M.; Wilson, M.; Drabold, D. A.; Elliott, S. R. Origins of structural and electronic transitions in disordered silicon. *Nature* **2021**, *589*, 59–64.

(38) Meenakshisundaram, V.; Hung, J.-H.; Patra, T. K.; Simmons, D. S. Designing Sequence-Specific Copolymer Compatibilizers Using a Molecular-Dynamics-Simulation-Based Genetic Algorithm. *Macromolecules* **2017**, *50*, 1155–1166.

(39) Patra, T. K.; Meenakshisundaram, V.; Hung, J.-H.; Simmons, D. S. Neural-Network-Biased Genetic Algorithms for Materials Design: Evolutionary Algorithms That Learn. *ACS Comb. Sci.* **2017**, *19*, 96–107.

(40) Meenakshisundaram, V.; Hung, J.-H.; Simmons, D. S. Design rules for glass formation from model molecules designed by a neural-network-biased genetic algorithm. *Soft Matter* **2019**, *15*, 7795–7808.

(41) Patra, T. K.; Loeffler, T. D.; Sankaranarayanan, S. K. R. S. Accelerating copolymer inverse design using monte carlo tree search. *Nanoscale* **2020**, *12*, 23653.

(42) Mitchell, M. *An Introduction to Genetic Algorithms*; Complex adaptive systems, 1996.

(43) Jorgensen, W. L.; Madura, J. D.; Swenson, C. J. Optimized intermolecular potential functions for liquid hydrocarbons. *J. Am. Chem. Soc.* **1984**, *106*, 6638–6646.

(44) Zhang, M.; Lussetti, E.; de Souza, L. E. S.; Müller-Plathe, F. Thermal Conductivities of Molecular Liquids by Reverse Nonequilibrium Molecular Dynamics. *J. Phys. Chem. B* **2005**, *109*, 15060–15067.

- (45) Jewett, A. I.; Zhuang, Z.; Shea, J.-E. Moltemplate a Coarse-Grained Model Assembly Tool. *Biophys. J.* **2013**, *104*, 169a.
- (46) Plimpton, S. Fast Parallel Algorithms for Short-Range Molecular Dynamics. *J. Comput. Phys.* **1995**, *117*, 1–19.
- (47) Allen, M. P.; Tildesley, D. J. *Computer Simulation of Liquids*; Oxford science publications, 2009.
- (48) Lussetti, E.; Terao, T.; Müller-Plathe, F. Nonequilibrium Molecular Dynamics Calculation of the Thermal Conductivity of Amorphous Polyamide-6,6. *J. Phys. Chem. B* **2007**, *111*, 11516–11523.
- (49) Shanker, A.; Li, C.; Kim, G.-H.; Gidley, D.; Pipe, K. P.; Kim, J. High thermal conductivity in electrostatically engineered amorphous polymers. *Sci. Adv.* **2017**, *3*, No. e1700342.
- (50) Wei, X.; Luo, T. Chain length effect on thermal transport in amorphous polymers and a structure-thermal conductivity relation. *Phys. Chem. Chem. Phys.* **2019**, *21*, 15523–15530.
- (51) Hands, D.; Lane, K.; Sheldon, R. P. Thermal conductivities of amorphous polymers. *J. Polym. Sci., Part C: Polym. Symp.* **1973**, *42*, 717–726.
- (52) Agari, Y.; Ueda, A.; Omura, Y.; Nagai, S. Thermal diffusivity and conductivity of PMMA/PC blends. *Polymer* **1997**, *38*, 801–807.
- (53) Milkus, R.; Ness, C.; Palyulin, V. V.; Weber, J.; Lapkin, A.; Zaccaro, A. Interpretation of the Vibrational Spectra of Glassy Polymers Using Coarse-Grained Simulations. *Macromolecules* **2018**, *51*, 1559–1572.
- (54) Donovan, B. F.; Warzoha, R. J.; Cosby, T.; Giri, A.; Wilson, A. A.; Borgdorff, A. J.; Vu, N. T.; Patterson, E. A.; Gorzkowski, E. P. Strained Polymer Thermal Conductivity Enhancement Counteracted by Additional Off-Axis Strain. *Macromolecules* **2020**, *53*, 11089–11097.
- (55) Soper, A. K. Empirical potential Monte Carlo simulation of fluid structure. *Chem. Phys.* **1996**, *202*, 295–306.
- (56) Reith, D.; Pütz, M.; Müller-Plathe, F. Deriving effective mesoscale potentials from atomistic simulations: Mesoscale Potentials from Atomistic Simulations. *J. Comput. Chem.* **2003**, *24*, 1624–1636.
- (57) Xu, Y.; Wang, X.; Zhou, J.; Song, B.; Jiang, Z.; Lee, E. M. Y.; Huberman, S.; Gleason, K. K.; Chen, G. Molecular engineered conjugated polymer with high thermal conductivity. *Sci. Adv.* **2018**, *4*, No. eaar3031.
- (58) Chen, A.; Wu, Y.; Zhou, S.; Xu, W.; Jiang, W.; Lv, Y.; Guo, W.; Chi, K.; Sun, Q.; Fu, T.; Xie, T.; Zhu, Y.; Liang, X.-g. High thermal conductivity polymer chains with reactive groups: a step towards true application. *Mater. Adv.* **2020**, *1*, 1996–2002.

Sequence-Engineering Polyethylene-Polypropylene Copolymers with High Thermal Conductivity Using a Molecular-Dynamics-Based Genetic Algorithm

Tianhang Zhou,^{†,¶} Zhenghao Wu,^{†,¶} Hari Krishna Chilukoti,^{‡,†} and Florian
Müller-Plathe^{*,†}

[†]*Eduard-Zintl-Institut für Anorganische und Physikalische Chemie, Technische Universität
Darmstadt, Alarich-Weiss-Str. 8, 64287 Darmstadt, Germany*

[‡]*Department of Mechanical Engineering, National Institute of Technology Warangal,
Warangal 506004, Telangana, India*

[¶]*Contributed equally to this work*

E-mail: z.wu@theo.chemie.tu-darmstadt.de

Force Fields

The OPLS force field is adopted to describe the interactions for polyethylene and polypropylene homopolymers and copolymers, which includes bond, angle, dihedral, and non-bonded interactions, as shown in Table S1

Table S1: OPLS-UA force field for Polyethylene and Polypropylene

Bond Interactions $U_{\text{bond}}(r) = K_b(r - r_b)^2$				
Interaction Type	K_b [kcal/mol/Å ²]	r_b [Å]		
All bonds	260.0	1.526		
Angle Interactions $U_{\text{angle}}(\theta) = K_\theta(\theta - \theta_0)^2$				
Interaction Type	K_θ [kcal/mol/rad ²]	θ_0 [rad]		
CH ₃ – CH – CH ₃	63.0	1.946		
CH ₂ – CH – CH ₃	63.0	1.962		
CH ₂ – CH ₂ – CH ₂	63.0	1.962		
CH ₂ – CH – CH ₂	63.0	1.962		
CH ₂ – CH ₂ – CH ₃	63.0	1.962		
CH – CH ₂ – CH	63.0	1.962		
Dihedral Interactions $U_{\text{dihedral}}(\theta) = \frac{1}{2} \sum_{i=1}^4 K_i [1 + \cos(i\phi)]$				
Interaction Type	K_1 [kcal/mol]	K_2 [kcal/mol]	K_3 [kcal/mol]	K_4 [kcal/mol]
CH ₂ – CH ₂ – CH ₂ – CH ₂	-3.40	1.25	-2.50	0.00
CH ₂ – CH ₂ – CH ₂ – CH ₃	-3.40	1.25	-2.50	0.00
CH – CH ₂ – CH ₂ – CH ₂	-3.40	1.25	-2.50	0.00
CH ₂ – CH – CH ₂ – CH ₂	-3.40	1.25	-2.50	0.00
CH – CH ₂ – CH – CH ₂	-2.50	1.25	3.10	0.00
CH – CH ₂ – CH – CH ₃	-2.50	1.25	3.10	0.00
CH ₃ – CH ₂ – CH – CH ₃	-2.50	1.25	3.10	0.00
Pair Interaction $U_{\text{LJ}}(r) = 4\epsilon[(\frac{\sigma}{r})^{12} - (\frac{\sigma}{r})^6]$ $r < r_C$				
Interaction Type	ϵ [kcal/mol]	σ [Å]	r_c [Å]	
CH – CH	0.080	3.85	10	
CH ₂ – CH ₂	0.118	3.905	10	
CH ₃ – CH ₃	0.175	3.905	10	

Equilibrium simulation

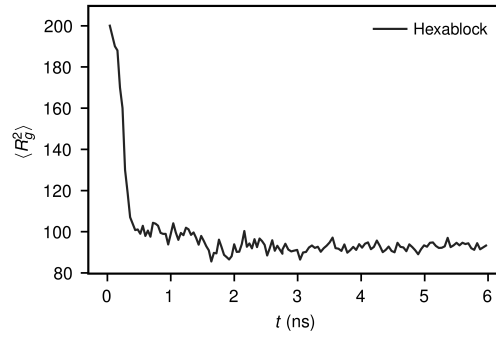


Figure S1: Structural relaxation process of ensemble-averaged mean-square radius $\langle R_g^2 \rangle$ for the system of hexablock copolymers.

NEMD simulation details

We conduct non-equilibrium simulation follows the equilibration step to calculate the thermal conductivity of the copolymers with a timestep of 0.5 fs. The cumulative energy of homopolymer polypropylene (PP) from the third calculation chunk (2 ns) in NEMD simulation heat is shown in S2. It is observed that the system reaches the steady state. The heat flux J is then calculated as $J = (d(E/2)/dt)$.

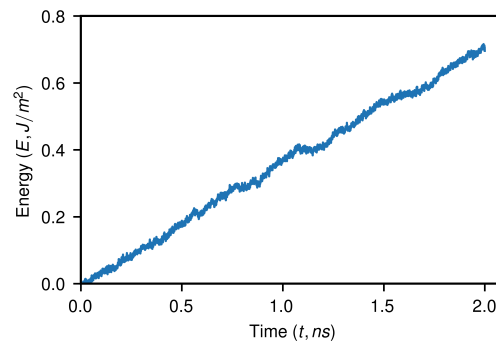
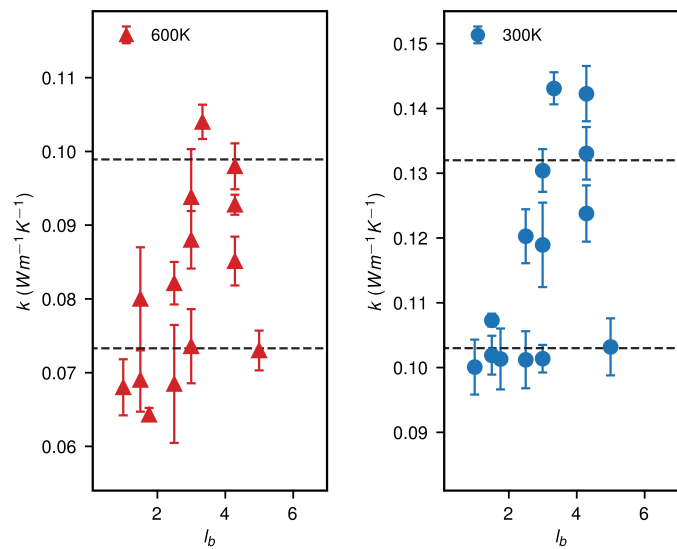


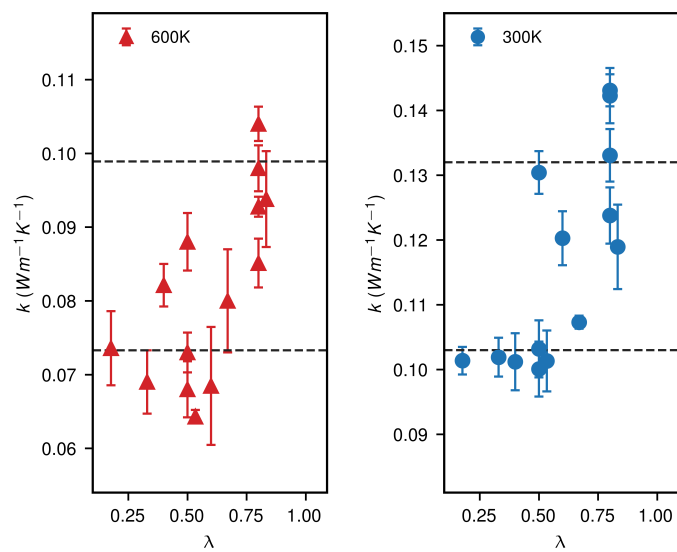
Figure S2: The cumulative energy of homopolymer polypropylene (PP) from the NEMD simulation in melt state.

Comparison between amorphous and melts

The thermal conductivity of eleven copolymers (typical regular, random as well as the optimal copolymer sequences) at room temperature ($T = 300$ K) are examined and shown in Figure S2. We find that the magnitude of thermal conductivity is different but the trend is same at 300 K and 600 K: The general trend of the thermal transport behavior of PE-PP copolymers as a function of mean block length l_b or ethylene monomer fraction λ at room temperature is essentially the same as that at high temperature.



(a)



(b)

Figure S3: (a) The thermal conductivity of several typical regular, random as well as the optimal copolymer sequences versus mean block length (l_b). (b) The thermal conductivity of several typical regular, random as well as the optimal copolymer sequences versus ethylene monomer fraction (λ). Red and blue points represent systems in 300 K and 600 K, respectively.

4 Conclusion and Outlook

In this thesis, we first investigate the compatibilization efficiency of linear block copolymers (Section 3.1) and graft copolymers (Section 3.2) in immiscible homopolymer blends by performing dissipative-particle-dynamics (DPD) simulation. Compatibilizers play critical roles in polymer blending that is an essential technology in the polymer processing industry. Our studies strengthen the idea that the compatibilization efficiency of copolymers can be predicted based on their molecular architectures and chemical details. Then, the global pandemic coronavirus outbreak significantly affects most humans' life all over the world. We investigate the ethanol concentration in alcoholic-based disinfectants sufficient to decompose coronavirus model membranes (Section 3.3). I believe this work can help people optimize the efficiency of alcoholic disinfectants, which satisfies the requirement of killing viruses. These works are based on the straightforward machine-learning (ML) assisted evaluation of the detailed structure-composition-property-performance relationships. The fourth work (section 3.4) arises from a simple question related to the thermal transfer efficiency: is it possible to establish a framework to optimize the thermal conductivity in an automatic and efficient manner? This question is answered by following the "inverse design" idea, and an optimum copolymer candidate with high thermal conductivity is obtained from the framework combining the molecular dynamics (MD) simulation and genetic algorithm (GA).

In Section 3.1, the compatibilization efficiency of symmetric diblock copolymers, unsymmetric diblock copolymers, and regular multiblock copolymers is investigated in immiscible homopolymer blends with different chemistries (the DPD repulsion parameter $\alpha_{AB} = 28, 35, \text{ and } 50$). For symmetric diblock copolymers, a power-law fit is used to quantify the variation of their compatibilization efficiency as a function of the number of compatibilizer chains, the chain length, and the DPD repulsion parameters. This power-law fitting equation has been validated with both experiments[49, 151] and simulations[65, 152]. The useful findings can be further summarized as:

1. Low-molecular-weight symmetric diblock copolymers are better compatibilisers for a given cost, while copolymers with higher weight are more appropriate to use with a constant number of copolymer molecules.
2. Unsymmetric diblock copolymers exhibit similar compatibilization efficiency as symmetric diblock copolymers, once their shortest blocks are beyond a certain number of monomers. In this work, the critical ratio of the shortest block is $\sim 14\% - 33\%$ for different unsymmetric copolymers.
3. Regular multiblock copolymers show the highest compatibilization efficiency with an adequate mean block length, as compared to other linear block copolymers.

In Section 3.2, we extend the target compatibilizers from linear block copolymers to graft copolymers, which have more descriptors of their molecular architecture. An increase of the compatibilization efficiency of graft copolymers with an increase in the areal concentration is evident. However, the diverse distribution of the compatibilization efficiency at the same areal concentration indicates that the molecular structure has a crucial effect on the interfacial properties of graft copolymers. Although many previous works[67, 153, 154] have investigated the compatibilization efficiency of graft copolymers in specific systems by keeping

one or two architecture descriptors constant, it remains unclear how they influence the compatibilization efficiency with the varying chemistries. Our work finds that:

4. As the blend changes from weakly incompatible to strongly incompatible, the number of side chains of graft copolymers gradually dominates their compatibilization efficiency while the side chain length becomes unimportant.
5. The side chain positions strongly influence the compatibilization efficiency of graft copolymers. Mid-grafted copolymers (side chains distributed near the centre of the backbone) provide a high compatibilization efficiency.

Establishing a predictive model, like the power-law fit for linear block copolymers, becomes much more challenging now due to the structural complexity of the graft copolymers. Hence, the ML method is introduced. The gradient boosting (GB) method provides the best accuracy. The post hoc descriptor importance analysis shows that the number of grafted side chains more strongly correlates with the compatibilization efficiency of graft copolymers than the backbone length and side chain length. Moreover, the relative shape anisometry of copolymers, defined as the ratio of their gyration tensor elements in directions normal and parallel to the interface, is strongly correlated with their compatibilization efficiency for all copolymers in this thesis. When transferring above conclusions to realistic systems, it should be noted that there exist practical maximum and minimum weights for block copolymers. For example, Nam *et al.* [151] found that block copolymers with a high molecular weight beyond the micelle weight (M_m) tend to form micelles in the bulk of the homopolymers rather than congregate at the interface for the polystyrene-polyisoprene blend system. Creton and Kramer [155] reported that block copolymers below the entanglement weight (M_e) cause interface failure when high tensile stress is applied to the polystyrene/poly(2-vinylpyridine) blends. On the other hand, the optimum copolymer candidate with the best compatibilization efficiency so far is evaluated only based on the interfacial tension. However, several experiments [36, 50–52] have proven that the dynamical properties of copolymers, i.e., how fast and how much of them can reach the interface during mixing, also influence their overall compatibilization performance. These dynamical issues of compatibilizers will be addressed in our future work.

In section 3.3, the ethanol-induced weakening effect on a coronavirus model membrane is addressed in detail. DPD models of three lipids, dipalmitoylphosphatidylcholine, dioleoylphosphatidylcholine, and dimyristoylphosphatidylcholine, and their neat, binary and ternary mixed membranes are investigated by immersing them in water and in water-ethanol solutions (disinfectants) up to concentrations where the membranes undergo rupture. The main findings could be summarized as:

1. An ethanol concentration above ≈ 32 mol % in the disinfectants, will make the viral membrane dysfunctional, regardless of which of the lipids studied here dominates in the membrane.
2. An ethanol concentration below ≈ 20 mol % in the disinfectants, is hardly efficient in the deactivation of coronavirus model membranes.

We observe that the dissolution of ethanol in the membrane causes lateral membrane swelling and the shrinkage of its thickness. The ethanol uptake also reduces the orientational order of the hydrocarbon tails of the lipids. However, we cannot quantitatively predict the location of the transition point from the intact to the disrupted states of the membrane, based on the area per lipid molecule, the membrane thickness, or the orientational order parameter of lipid tails. Hence, we further develop a machine-learning framework to assess the integrity of lipid membranes in place of visual inspections. More importantly, this framework shows a promising potential to be a simple and robust tool suitable for biological membranes to characterize their states.

In section 3.4, We employ a computational framework of a MD-based genetic algorithm to design polyethylene–polypropylene (PE-PP) copolymers with high thermal conductivity. The integration of atomistic MD simulation (united-atom models) as fitness evaluation with the genetic algorithm is reported, to our knowledge, for the first time. An irregular optimal sequence identified after 20 MD-GA generations outperforms any other copolymer sequences on thermal energy transfer. There are two main findings:

1. The actual monomer sequence substantially affects the thermal energy transfer in PE-PP copolymers.
2. The thermal conductivity of the optimized PE-PP copolymer is higher than that of both PE and PP homopolymers.

The enhancement of the thermal conductivity of the optimized sequence-specific PE-PP copolymer is not so high in comparison with the better of the homopolymers, PE ($\approx 8\%$). It is interesting, though that admixture of a small fraction of the worse-conducting PP can further improve the thermal transfer efficiency of better-conducting PE. The emerging physical picture is that the monomer sequence (relative positions of these monomers) plays a significant role in the heat transfer of PE-PP copolymers, although there is a trade-off between the monomer composition and the mean block length. Additionally, we perform a detailed analysis of the vibrational density of states to examine the efficiencies of thermal energy transfer through different molecular interactions, e.g., bonded and non-bonded interactions. It identifies three modes of thermal energy transfer in polymer liquids: (a) high-frequency mode of bond interactions, (b) low-frequency mode of non-bonded interactions, and (c) intermediate-frequency mode of many-body interactions such as angular interactions. Compared with several typical block copolymers, the high thermal conductivity of the optimal sequence is attributed to the optimized thermal energy transfer via both (a) bonded and (b) non-bonded interactions.

The examples studied allow some comments on the combination between machine learning and simulation. Compared to the traditional technique for establishing an empirical predictive model (Section 3.1), ML is often more robust when the underlying mechanisms that link the input and the output are unclear or difficult to characterize (Section 3.2 and 3.3). However, this advantage also corresponds to one of the major criticisms of ML algorithms, namely being black boxes. To achieve some interpretability and visualization of ML models, a post hoc analysis and human deep thinking on the role of physical descriptors are necessary. Furthermore, basic principles of different ML algorithms need to be clarified before using them. For example, it is inappropriate to use neural networks only with two layers for characterizing a complex structure-property relationship. The continuous quantities like phase transitions are also almost impossible to be investigated by decision-tree-based ML algorithms (e.g., Random Forest). It has to be noted that there seems to be a recent competition for the integration of ML into simulations and experiments. In my opinion, this competition is a good phenomenon that can accelerate the development of new materials. Nevertheless, it is valid only when we try to extract physical information from ML models and understand their fundamental principles. In short, we need to keep in mind that machine learning is a powerful tool that should be used appropriately based on our scientific target, rather than “I use machine learning because so many people use”. I hope this thesis can give some inspirations to the new Master/Ph.D. students in their brand-new scientific research.

Bibliography

- (1) Agrawal, A.; Choudhary, A. Perspective: Materials informatics and big data: Realization of the “fourth paradigm” of science in materials science. *APL Materials* **2016**, *4*, 053208.
- (2) Long, T. Accelerating the discovery of crystalline materials with desired intrinsic properties by machine learning, en, Ph.D. Thesis, Darmstadt: Technische Universität, 2022.
- (3) Peter, C.; Kremer, K. Multiscale simulation of soft matter systems. *Faraday Discuss.* **2010**, *18*.
- (4) Peter, C.; Kremer, K. Multiscale simulation of soft matter systems – from the atomistic to the coarse-grained level and back. *Soft Matter* **2009**, *5*, 4357.
- (5) Müller-Plathe, F. Coarse-Graining in Polymer Simulation: From the Atomistic to the Mesoscopic Scale and Back. *ChemPhysChem* **2002**, *3*, 754–769.
- (6) Perry, S. L.; Sing, C. E. 100th Anniversary of Macromolecular Science Viewpoint: Opportunities in the Physics of Sequence-Defined Polymers. *ACS Macro Lett.* **2020**, 216–225.
- (7) Patra, T. K. Data-Driven Methods for Accelerating Polymer Design. *ACS Polym. Au* **2022**, *2*, 8–26.
- (8) Schleder, G. R.; Padilha, A. C. M.; Acosta, C. M.; Costa, M.; Fazio, A. From DFT to machine learning: recent approaches to materials science—a review. *J. Phys. Mater.* **2019**, *2*, 032001.
- (9) Friesner, R. A. Ab initio quantum chemistry: Methodology and applications. *Proceedings of the National Academy of Sciences* **2005**, *102*, 6648–6653.
- (10) Groot, R. D.; Warren, P. B. Dissipative particle dynamics: Bridging the gap between atomistic and mesoscopic simulation. *J. Chem. Phys.* **1997**, *107*, 4423–4435.
- (11) Schneider, J. Development and Application of Multiscale Methods for Simulating Polymer Properties, en, Ph.D. Thesis, Darmstadt: Technische Universität Darmstadt, 2021.
- (12) Li, L. Development of Machine Learning Algorithms in Density Functional Theory, en, Ph.D. Thesis, UC Irvine, 2016.
- (13) Behler, J.; Parrinello, M. Generalized Neural-Network Representation of High-Dimensional Potential-Energy Surfaces. *Phys. Rev. Lett.* **2007**, *98*, 146401.
- (14) Zhang, L.; Han, J.; Wang, H.; Car, R.; E, W. Deep Potential Molecular Dynamics: A Scalable Model with the Accuracy of Quantum Mechanics. *Phys. Rev. Lett.* **2018**, *120*, 143001.
- (15) Behler, J. Neural network potential-energy surfaces in chemistry: a tool for large-scale simulations. *Phys. Chem. Chem. Phys.* **2011**, *13*, 17930.
- (16) Noé, F.; Tkatchenko, A.; Müller, K.-R.; Clementi, C. Machine Learning for Molecular Simulation. *Annu. Rev. Phys. Chem.* **2020**, *71*, 361–390.
- (17) Friederich, P.; Häse, F.; Proppe, J.; Aspuru-Guzik, A. Machine-learned potentials for next-generation matter simulations. *Nat. Mater.* **2021**, *20*, 750–761.
- (18) Olson, G. B. Computational Design of Hierarchically Structured Materials. *Science* **1997**, *277*, 1237–1242.

-
- (19) Le, T.; Epa, V. C.; Burden, F. R.; Winkler, D. A. Quantitative Structure–Property Relationship Modeling of Diverse Materials Properties. *Chem. Rev.* **2012**, *112*, 2889–2919.
- (20) Bereau, T.; Andrienko, D.; Kremer, K. Research Update: Computational materials discovery in soft matter. *APL Materials* **2016**, *4*, 053101.
- (21) Bhattacharya, D.; Patra, T. K. dPOLY: Deep Learning of Polymer Phases and Phase Transition. *Macromolecules* **2021**, *54*, 3065–3074.
- (22) Wei, Q.; Melko, R. G.; Chen, J. Z. Y. Identifying polymer states by machine learning. *Phys. Rev. E* **2017**, *95*, 32504.
- (23) Vandans, O.; Yang, K.; Wu, Z.; Dai, L. Identifying knot types of polymer conformations by machine learning. *Phys. Rev. E* **2020**, *101*, 22502.
- (24) Sattari, K.; Xie, Y.; Lin, J. Data-driven algorithms for inverse design of polymers. *Soft Matter* **2021**, *17*, 7607–7622.
- (25) Webb, M. A.; Jackson, N. E.; Gil, P. S.; de Pablo, J. J. Targeted sequence design within the coarse-grained polymer genome. *Sci. Adv.* **2020**, *6*.
- (26) Schmidt, J.; Marques, M. R. G.; Botti, S.; Marques, M. A. L. Recent advances and applications of machine learning in solid-state materials science. *npj Comput Mater* **2019**, *5*, 83.
- (27) Ghiringhelli, L. M.; Vybiral, J.; Levchenko, S. V.; Draxl, C.; Scheffler, M. Big Data of Materials Science: Critical Role of the Descriptor. *Phys. Rev. Lett.* **2015**, *114*, 105503.
- (28) Johnson, S. R. The Trouble with QSAR (or How I Learned To Stop Worrying and Embrace Fallacy). *J. Chem. Inf. Model.* **2008**, *48*, 25–26.
- (29) Mikulskis, P.; Alexander, M. R.; Winkler, D. A. Toward Interpretable Machine Learning Models for Materials Discovery. *Advanced Intelligent Systems* **2019**, *1*, 1900045.
- (30) Tamasi, M.; Patel, R.; Borca, C.; Kosuri, S.; Mugnier, H.; Upadhya, R.; Murthy, N. S.; Webb, M.; Gormley, A. Machine Learning on a Robotic Platform for the Design of Polymer-Protein Hybrids. *ChemRxiv* **2022**.
- (31) Rong, Y.; Padron, A. V.; Hagerty, K. J.; Nelson, N.; Chi, S.; Keyhani, N. O.; Katz, J.; Datta, S. P. A.; Gomes, C.; McLamore, E. S. Post hoc support vector machine learning for impedimetric biosensors based on weak protein–ligand interactions. *Analyst* **2018**, *143*, 2066–2075.
- (32) Lee, F. L.; Park, J.; Goyal, S.; Qaroush, Y.; Wang, S.; Yoon, H.; Rammohan, A.; Shim, Y. Comparison of Machine Learning Methods towards Developing Interpretable Polyamide Property Prediction. *Polymers (Basel)* **2021**, *13*, 3653.
- (33) Von Rueden, L.; Mayer, S.; Sifa, R.; Bauckhage, C.; Garcke, J. In *Advances in Intelligent Data Analysis XVIII*, ed. by Berthold, M. R.; Feelders, A.; Krempel, G., Springer International Publishing: Cham, 2020, pp 548–560.
- (34) Utracki, L. A.; Walsh, D. J.; Weiss, R. A. In *Multiphase Polymers: Blends and Ionomers*; ACS Symposium Series 395, Vol. 395, Section: 1, 1989, pp 1–35.
- (35) Fairley, G. R.; Prud'homme, R. E. In *Multiphase Polymers: Blends and Ionomers*; ACS Symposium Series 395, Vol. 395, Section: 8, 1989, pp 211–228.
- (36) Macosko, C. W.; Guégan, P.; Khandpur, A. K.; Nakayama, A.; Marechal, P.; Inoue, T. Compatibilizers for Melt Blending: Premade Block Copolymers. *Macromolecules* **1996**, *29*, 5590–5598.
- (37) Manias, E.; Utracki, L. A. In *Polymer Blends Handbook*, Utracki, L. A., Wilkie, C. A., Eds.; Springer Netherlands: Dordrecht, 2014, pp 171–289.

-
- (38) Utracki, L. A.; Mukhopadhyay, P.; Gupta, R. K. In *Polymer Blends Handbook*, Utracki, L. A., Wilkie, C. A., Eds.; Springer Netherlands: Dordrecht, 2014, pp 3–170.
- (39) Allard, J. Effect of compatibilization on the phase separation of polymer blends. **2018**.
- (40) Li, Q.; Wang, L.; Lin, J.; Zhang, L. Distinctive phase separation dynamics of polymer blends: Roles of Janus nanoparticles. *Phys. Chem. Chem. Phys.* **2019**, *21*, 2651–2658.
- (41) Fayt, R.; Jérôme, R.; Teyssié, P. In *Multiphase Polymers: Blends and Ionomers*; ACS Symposium Series 395, Vol. 395, Section: 2, 1989, pp 38–66.
- (42) Koning, C.; Van Duin, M.; Pagnouille, C.; Jerome, R. Strategies for compatibilization of polymer blends. *Prog. Polym. Sci.* **1998**, *23*, 707–757.
- (43) Forteln, I.; Josef, J. The Effects of Copolymer Compatibilizers on the Phase Structure Evolution in Polymer Blends — A Review. **2021**.
- (44) Pandav, G.; Ganesan, V. Efficacy of different block copolymers in facilitating microemulsion phases in polymer blend systems. *Macromolecules* **2013**, *46*, 8334–8344.
- (45) Tomić, N. Z.; Marinković, A. D., *Compatibilization of polymer blends by the addition of graft copolymers*, 2019.
- (46) Utracki, L. A. Compatibilization of Polymer Blends. *Can. J. Chem. Eng.* **2002**, *80*, 1008–1016.
- (47) Milner, S. T. How do copolymer compatibilizers really work? *MRS Bull.* **1997**, *22*, 38–42.
- (48) Lyatskaya, Y.; Balazs, A. C. Using copolymer mixtures to compatibilize immiscible homopolymer blends. *Macromolecules* **1996**, *29*, 7581–7587.
- (49) Anastasiadis, S. H.; Gancarz, I.; Koberstein, J. T. Compatibilizing Effect of Block Copolymers Added to the Polymer/Polymer Interface. *Macromolecules* **1989**, *22*, 1449–1453.
- (50) Retsos, H.; Margiolaki, I.; Messaritaki, A.; Anastasiadis, S. H. Interfacial tension in binary polymer blends in the presence of block copolymers: Effects of additive MW. *Macromolecules* **2001**, *34*, 5295–5305.
- (51) Lyu, S.; Jones, T. D.; Bates, F. S.; Macosko, C. W. Role of Block Copolymers on Suppression of Droplet Coalescence. *Macromolecules* **2002**, *35*, 7845–7855.
- (52) Galloway, J. A.; Jeon, H. K.; Bell, J. R.; Macosko, C. W. Block copolymer compatibilization of cocontinuous polymer blends. *Polymer* **2005**, *46*, 183–191.
- (53) Broseta, D.; Fredrickson, G. H.; Helfand, E.; Leibler, L. Molecular weight and polydispersity effects at polymer-polymer interfaces. *Macromolecules* **1990**, *23*, 132–139.
- (54) Helfand, E.; Tagami, Y. Theory of the interface between immiscible polymers. *J. Polym. Sci. Part B Polym. Lett.* **1971**, *9*, 741–746.
- (55) Helfand, E.; Tagami, Y. Theory of the Interface between Immiscible Polymers. II. *J. Chem. Phys.* **1972**, *56*, 3592–3601.
- (56) Ermoshkin, A. V.; Semenov, A. N. Interfacial tension in binary polymer mixtures. *Macromolecules* **1996**, *29*, 6294–6300.
- (57) Tang, H.; Freed, K. F. Free energy functional expansion for inhomogeneous polymer blends. *J. Chem. Phys.* **1991**, *94*, 1572–1583.
- (58) Sung, Y. T.; Seo, W. J.; Kim, Y. H.; Lee, H. S.; Kim, W. N. Evaluation of interfacial tension for poly(methyl methacrylate) and polystyrene by rheological measurements and interaction parameter of the two polymers. *Korea Aust. Rheol. J.* **2004**, *16*, 135–140.

-
- (59) Choi, S. J.; Schowalter, W. R. Rheological properties of nondilute suspensions of deformable particles. *The Physics of Fluids* **1975**, *18*, 420–427.
- (60) Paliarne, J. F. Linear rheology of viscoelastic emulsions with interfacial tension. *Rheol Acta* **1990**, *29*, 204–214.
- (61) Müller, M.; Binder, K.; Oed, W. Structural and thermodynamic properties of interfaces between coexisting phases in polymer blends: A Monte Carlo simulation. *J. Chem. Soc. Faraday Trans.* **1995**, *91*, 2369–2379.
- (62) Govorun, E. N.; Erukhimovich, I. Emulsion stabilization by diblock copolymers: Droplet curvature effect. *Langmuir* **1999**, *15*, 8392–8398.
- (63) Müller, M.; Schick, M. Bulk and interfacial thermodynamics of a symmetric, ternary homopolymer-copolymer mixture: A Monte Carlo study. *J. Chem. Phys.* **1996**, *105*, 8885–8901.
- (64) Anastasiadis, S. H.; Gancarz, I.; Koberstein, J. T. Interfacial tension of immiscible polymer blends: temperature and molecular weight dependence. *Macromolecules* **1988**, *21*, 2980–2987.
- (65) Qian, H. J.; Lu, Z. Y.; Chen, L. J.; Li, Z. S.; Sun, C. C. Dissipative particle dynamics study on the interfaces in incompatible AB homopolymer blends and with their block copolymers. *J. Chem. Phys.* **2005**, *122*.
- (66) Meenakshisundaram, V.; Hung, J. H.; Patra, T. K.; Simmons, D. S. Designing Sequence-Specific Copolymer Compatibilizers Using a Molecular-Dynamics-Simulation-Based Genetic Algorithm. *Macromolecules* **2017**, *50*, 1155–1166.
- (67) Wang, J. J.; Li, Z. Z.; Gu, X. P.; Feng, L. F.; Zhang, C. L.; Hu, G. H. A dissipative particle dynamics study on the compatibilizing process of immiscible polymer blends with graft copolymers. *Polymer (Guildf)*. **2012**, *53*, 4448–4454.
- (68) Ryu, J. H.; Kim, Y.; Lee, W. B. Inhomogeneity of block copolymers at the interface of an immiscible polymer blend. *Phys. Rev. E* **2018**, *97*, 1–7.
- (69) Sun, D.; Guo, H. Monte carlo studies on the interfacial properties and interfacial structures of ternary symmetric blends with gradient copolymers. *J. Phys. Chem. B* **2012**, *116*, 9512–9522.
- (70) Zhou, C.; Luo, S. K.; Sun, Y.; Zhou, Y.; Qian, W. Dissipative particle dynamics studies on the interfacial tension of A/B homopolymer blends and the effect of Janus nanorods. *J. Appl. Polym. Sci.* **2016**, *133*, 1–7.
- (71) Noolandi, J.; Hong, K. M. Interfacial Properties of Immiscible Homopolymer Blends in the Presence of Block Copolymers. *Macromolecules* **1982**, *15*, 482–492.
- (72) Leibler, L. Emulsifying effects of block copolymers in incompatible polymer blends. *Makromol. Chemie. Macromol. Symp.* **1988**, *16*, 1–17.
- (73) Matsen, M. W. Architectural effect on the surface tension of an aba triblock copolymer melt. *Macromolecules* **2010**, *43*, 1671–1674.
- (74) Sun, D.; Guo, H. Influence of compositional gradient on the phase behavior of ternary symmetric homopolymer-copolymer blends: A Monte Carlo study. *Polymer (Guildf)*. **2011**, *52*, 5922–5932.
- (75) Lohse, D. J.; Datta, S.; Kresge, E. N. Graft Copolymer Compatibilizers for Blends of Polypropylene and Ethylene-Propylene Copolymers. *Macromolecules* **1991**, *24*, 561–566.
- (76) Braun, D.; Fischer, M.; Hellmann, G. P. Block-graft copolymers as compatibilizers in polymer blends. *Polymer (Guildf)*. **1996**, *37*, 3871–3877.

-
- (77) Dong, E.; Du, H.; Gardner, L. An interactive web-based dashboard to track COVID-19 in real time. *Lancet Infect. Dis.* **2020**, *20*, 533–534.
- (78) Artika, I. M.; Dewantari, A. K.; Wiyatno, A. Molecular biology of coronaviruses: current knowledge. *Heliyon* **2020**, *6*.
- (79) Deshmukh, M. G.; Ippolito, J. A.; Zhang, C. H.; Stone, E. A.; Reilly, R. A.; Miller, S. J.; Jorgensen, W. L.; Anderson, K. S. Structure-guided design of a perampanel-derived pharmacophore targeting the SARS-CoV-2 main protease. *Structure* **2021**, *29*, 823–833.
- (80) Zhang, C.-H. et al. Optimization of Triarylpyridinone Inhibitors of the Main Protease of SARS-CoV-2 to Low-Nanomolar Antiviral Potency. *ACS Med. Chem. Lett.* **2021**, *12*, 1325–1332.
- (81) Zhang, C. H. et al. Potent Noncovalent Inhibitors of the Main Protease of SARS-CoV-2 from Molecular Sculpting of the Drug Perampanel Guided by Free Energy Perturbation Calculations. *ACS Central Science* **2021**, *7*, 467–475.
- (82) Ghahremanpour, M. M.; Tirado-Rives, J.; Deshmukh, M.; Ippolito, J. A.; Zhang, C. H.; Cabeza De Vaca, I.; Liosi, M. E.; Anderson, K. S.; Jorgensen, W. L. Identification of 14 Known Drugs as Inhibitors of the Main Protease of SARS-CoV-2. *ACS Medicinal Chemistry Letters* **2020**, *11*, 2526–2533.
- (83) Callaway, E.; Ledford, H. How bad is Omicron? What scientists know so far. *Nature* **2021**, *600*, 197–199.
- (84) Seah, I.; Su, X.; Lingam, G. Revisiting the dangers of the coronavirus in the ophthalmology practice. *Eye* **2020**, *34*, 1155–1157.
- (85) Schoeman, D.; Fielding, B. C. Coronavirus envelope protein: current knowledge. *Viol. J.* **2019**, *16*, 69.
- (86) Sun, S.; Karki, C.; Aguilera, J.; Lopez Hernandez, A. E.; Sun, J.; Li, L. Computational Study on the Function of Palmitoylation on the Envelope Protein in SARS-CoV-2. *J. Chem. Theory Comput.* **2021**, *17*, 6483–6490.
- (87) Choi, Y. K.; Cao, Y.; Frank, M.; Woo, H.; Park, S. J.; Yeom, M. S.; Croll, T. I.; Seok, C.; Im, W. Structure, Dynamics, Receptor Binding, and Antibody Binding of the Fully Glycosylated Full-Length SARS-CoV-2 Spike Protein in a Viral Membrane. *J. Chem. Theory Comput.* **2021**, *17*, 2479–2487.
- (88) Kampf, G.; Todt, D.; Pfaender, S.; Steinmann, E. Persistence of coronaviruses on inanimate surfaces and their inactivation with biocidal agents. *J. Hosp. Infect.* **2020**, *104*, 246–251.
- (89) Ly, H. V.; Longo, M. L. The Influence of Short-Chain Alcohols on Interfacial Tension, Mechanical Properties, Area/Molecule, and Permeability of Fluid Lipid Bilayers. *Biophys. J.* **2004**, *87*, 1013–1033.
- (90) Fung, T. S.; Liu, D. X. Human Coronavirus: Host-Pathogen Interaction. *Annu. Rev. Microbiol.* **2019**, *73*, 529–557.
- (91) Stertz, S.; Reichelt, M.; Spiegel, M.; Kuri, T.; Martínez-Sobrido, L.; García-Sastre, A.; Weber, F.; Kochs, G. The intracellular sites of early replication and budding of SARS-coronavirus. *Virology* **2007**, *361*, 304–315.
- (92) Holm, B. A.; Wang, Z.; Egan, E. A.; Notter, R. H. Content of Dipalmitoyl Phosphatidylcholine in Lung Surfactant: Ramifications for Surface Activity. *Pediatr. Res.* **1996**, *39*, 805–811.
- (93) Vance, J. E. Phospholipid Synthesis and Transport in Mammalian Cells. *Traffic* **2015**, *16*, 1–18.

-
- (94) Drescher, S.; van Hoogevest, P. The Phospholipid Research Center: Current Research in Phospholipids and Their Use in Drug Delivery. *Pharmaceutics* **2020**, *12*, 1235.
- (95) Khattari, Z.; Brotons, G.; Akkawi, M.; Arbely, E.; Arkin, I. T.; Salditt, T. SARS Coronavirus E protein in phospholipid bilayers: An X-ray study. *Biophys. J.* **2006**, *90*, 2038–2050.
- (96) Guillén, J.; Pérez-Berná, A. J.; Moreno, M. R.; Villalaín, J. A second SARS-CoV S2 glycoprotein internal membrane-active peptide. Biophysical characterization and membrane interaction. *Biochemistry* **2008**, *47*, 8214–8224.
- (97) Keough, K. M.; Davis, P. J. Gel to Liquid-Crystalline Phase Transitions in Water Dispersions of Saturated Mixed-Acid Phosphatidylcholines. *Biochemistry* **1979**, *18*, 1453–1459.
- (98) Svetlovics, J. A.; Wheaten, S. A.; Almeida, P. F. Phase separation and fluctuations in mixtures of a saturated and an unsaturated phospholipid. *Biophys. J.* **2012**, *102*, 2526–2535.
- (99) Eslami, H.; Das, S.; Zhou, T.; Müller-Plathe, F. How Alcoholic Disinfectants Affect Coronavirus Model Membranes: Membrane Fluidity, Permeability, and Disintegration. *J. Phys. Chem. B* **2020**, *124*, 10374–10385.
- (100) Das, S.; Meinel, M. K.; Wu, Z.; Müller-Plathe, F. The role of the envelope protein in the stability of a coronavirus model membrane against an ethanolic disinfectant. *J. Chem. Phys.* **2021**, *154*, 245101.
- (101) Koynova, R.; Tenchov, B. Lipids: Phase Transitions. *Wiley Encycl. Chem. Biol.* **2008**.
- (102) Kučerka, N.; Heberle, F. A.; Pan, J.; Katsaras, J. Structural significance of lipid diversity as studied by small angle neutron and X-ray scattering, ISSN: 20770375 Issue: 3 Pages: 454–472 Publication Title: Membranes (Basel). Volume: 5, 2015.
- (103) Konas, R. M.; Daristotle, J. L.; Harbor, N. B.; Klauda, J. B. Biophysical Changes of Lipid Membranes in the Presence of Ethanol at Varying Concentrations. *J. Phys. Chem. B* **2015**, *119*, 13134–13141.
- (104) Gurtovenko, A. A.; Anwar, J. Interaction of ethanol with biological membranes: The formation of non-bilayer structures within the membrane interior and their significance. *J. Phys. Chem. B* **2009**, *113*, 1983–1992.
- (105) Groot, R. D.; Rabone, K. L. Mesoscopic simulation of cell membrane damage, morphology change and rupture by nonionic surfactants. *Biophys. J.* **2001**, *81*, Publisher: Elsevier, 725–736.
- (106) Li, X.; Gao, L.; Fang, W. Dissipative particle dynamics simulations for phospholipid membranes based on a four-to-one coarse-grained mapping scheme. *PLoS One* **2016**, *11*, 26–28.
- (107) Chae, H. G.; Kumar, S. Making Strong Fibers. *Science* **2008**.
- (108) Yan, X.; Gu, J.; Zheng, G.; Guo, J.; Galaska, A. M.; Yu, J.; Khan, M. A.; Sun, L.; Young, D. P.; Zhang, Q.; Wei, S.; Guo, Z. Lowly loaded carbon nanotubes induced high electrical conductivity and giant magnetoresistance in ethylene/1-octene copolymers. *Polymer (Guildf)*. **2016**, *103*, 315–327.
- (109) Ghahramani, N.; Seyed Esfahani, S. A.; Mehranpour, M.; Nazockdast, H. The effect of filler localization on morphology and thermal conductivity of the polyamide/cyclic olefin copolymer blends filled with boron nitride. *J. Mater. Sci.* **2018**, *53*, 16146–16159.
- (110) Huang, C.; Qian, X.; Yang, R. Thermal conductivity of polymers and polymer nanocomposites. *Mater. Sci. Eng. R Reports* **2018**, *132*, 1–22.
- (111) Li, A.; Zhang, C.; Zhang, Y.-F. Thermal Conductivity of Graphene-Polymer Composites: Mechanisms, Properties, and Applications. *Polymers* **2017**, *9*, 437.

-
- (112) Balandin, A. A.; Ghosh, S.; Bao, W.; Calizo, I.; Teweldebrhan, D.; Miao, F.; Lau, C. N. Superior Thermal Conductivity of Single-Layer Graphene. *Nano Lett.* **2008**, *8*.
- (113) Gaska, K.; Kádár, R.; Xu, X.; Gubanski, S.; Müller, C.; Pandit, S.; Mokkaapati, V. R. S. S.; Mijakovic, I.; Rybak, A.; Siwek, A.; Svensson, M. Highly structured graphene polyethylene nanocomposites. *AIP Conference Proceedings* **2019**, *2065*, 030061.
- (114) Zhou, T.; Chilukoti, H. K.; Wu, Z.; Müller-Plathe, F. Effect of Defects on the Interfacial Thermal Conductance between n-Heneicosane in Solid and Liquid Phases and a Graphene Monolayer. *J. Phys. Chem. C* **2021**, *125*, 14149–14162.
- (115) Chilukoti, H. K.; Zhou, T.; Ardhham, V. R.; Böhm, M. C.; Müller-Plathe, F. Thermal Energy Transport across the Interface between Phase Change Material n-Heneicosane in Solid and Liquid Phases and Few-Layer Graphene. *J. Phys. Chem. C* **2019**, *123*, 29192–29202.
- (116) Shen, S.; Henry, A.; Tong, J.; Zheng, R.; Chen, G. Polyethylene nanofibres with very high thermal conductivities. *Nat. Nanotechnol.* **2010**, *5*, 251–255.
- (117) Choy, C. L.; Wong, Y. W.; Yang, G. W.; Kanamoto, T. Elastic modulus and thermal conductivity of ultradrawn polyethylene. *J. Polym. Sci. Part B Polym. Phys.* **1999**, *37*, 3359–3367.
- (118) Kim, G.-H.; Lee, D.; Shanker, A.; Shao, L.; Kwon, M. S.; Gidley, D.; Kim, J.; Pipe, K. P. High thermal conductivity in amorphous polymer blends by engineered interchain interactions. *Nat. Mater.* **2015**, *14*, 295–300.
- (119) Wei, X.; Luo, T. The effect of the block ratio on the thermal conductivity of amorphous polyethylene-polypropylene (PE-PP) diblock copolymers. *Phys. Chem. Chem. Phys.* **2018**, *20*, 20534–20539.
- (120) Patterson, A. L.; Danielsen, S. P.; Yu, B.; Davidson, E. C.; Fredrickson, G. H.; Segalman, R. A. Sequence Effects on Block Copolymer Self-Assembly through Tuning Chain Conformation and Segregation Strength Utilizing Sequence-Defined Polypeptoids. *Macromolecules* **2019**, *52*, 1277–1286.
- (121) Murnen, H. K.; Khokhlov, A. R.; Khalatur, P. G.; Segalman, R. A.; Zuckermann, R. N. Impact of hydrophobic sequence patterning on the coil-to-globule transition of protein-like polymers. *Macromolecules* **2012**, *45*, 5229–5236.
- (122) Chang, L. W.; Lytle, T. K.; Radhakrishna, M.; Madinya, J. J.; Vélez, J.; Sing, C. E.; Perry, S. L. Sequence and entropy-based control of complex coacervates. *Nat. Commun.* **2017**, *8*, 1–7.
- (123) Lytle, T. K.; Chang, L. W.; Markiewicz, N.; Perry, S. L.; Sing, C. E. Designing Electrostatic Interactions via Polyelectrolyte Monomer Sequence. *ACS Cent. Sci.* **2019**, *5*, 709–718.
- (124) Rosales, A. M.; Segalman, R. A.; Zuckermann, R. N. Polypeptoids: A model system to study the effect of monomer sequence on polymer properties and self-assembly. *Soft Matter* **2013**, *9*, 8400–8414.
- (125) Jackson, N. E.; Bowen, A. S.; Antony, L. W.; Webb, M. A.; Vishwanath, V.; de Pablo, J. J. Electronic structure at coarse-grained resolutions from supervised machine learning. *Sci. Adv.* **2019**, *5*, eaav1190.
- (126) Jackson, N. E.; Webb, M. A.; de Pablo, J. J. Recent advances in machine learning towards multiscale soft materials design. *Current Opinion in Chemical Engineering* **2019**, *23*, 106–114.
- (127) Upadhyaya, R.; Kosuri, S.; Tamasi, M.; Meyer, T. A.; Atta, S.; Webb, M. A.; Gormley, A. J. Automation and data-driven design of polymer therapeutics. *Advanced Drug Delivery Reviews* **2021**, *171*, 1–28.
- (128) Deringer, V. L.; Bernstein, N.; Csányi, G.; Ben Mahmoud, C.; Ceriotti, M.; Wilson, M.; Drabold, D. A.; Elliott, S. R. Origins of structural and electronic transitions in disordered silicon. *Nature* **2021**, *589*, 59–64.

-
- (129) Patra, T. K.; Meenakshisundaram, V.; Hung, J.-H.; Simmons, D. S. Neural-Network-Biased Genetic Algorithms for Materials Design: Evolutionary Algorithms That Learn. *ACS Comb. Sci.* **2017**, *19*, 96–107.
- (130) Meenakshisundaram, V.; Hung, J.-H.; Simmons, D. S. Design rules for glass formation from model molecules designed by a neural-network-biased genetic algorithm. *Soft Matter* **2019**, *15*, 7795–7808.
- (131) Müller-Plathe, F. A simple nonequilibrium molecular dynamics method for calculating the thermal conductivity. *The Journal of Chemical Physics* **1997**, *106*, 6082–6085.
- (132) Cahill, D. G.; Ford, W. K.; Goodson, K. E.; Mahan, G. D.; Majumdar, A.; Maris, H. J.; Merlin, R.; Phillpot, S. R. Nanoscale thermal transport. *Journal of Applied Physics* **2003**, *93*, 793–818.
- (133) Allen, M. P., *Introduction to Molecular Dynamics Simulation*, Number: FZJ-2014-02193; John von Neumann Institute for Computing: 2004.
- (134) Español, P.; Warren, P. B. Perspective: Dissipative particle dynamics. *J. Chem. Phys.* **2017**, *146*.
- (135) Keaveny, E. E.; Pivkin, I. V.; Maxey, M.; Em Karniadakis, G. A comparative study between dissipative particle dynamics and molecular dynamics for simple- and complex-geometry flows. *J. Chem. Phys.* **2005**, *123*, 104107.
- (136) Swope, W. C.; Andersen, H. C.; Berens, P. H.; Wilson, K. R. A computer simulation method for the calculation of equilibrium constants for the formation of physical clusters of molecules: Application to small water clusters. *J. Chem. Phys.* **1982**, *76*, 637–649.
- (137) VERLET, L. Computer "Experiments" on Classical Fluids. II. Equilibrium Correlation Functions. *Phys. Rev.* **1968**, *165*, Publisher: American Physical Society, 201–214.
- (138) Safavian, S.; Landgrebe, D. A survey of decision tree classifier methodology. *IEEE Transactions on Systems, Man, and Cybernetics* **1991**, *21*, 660–674.
- (139) Svetnik, V.; Liaw, A.; Tong, C.; Culberson, J. C.; Sheridan, R. P.; Feuston, B. P. Random Forest: A Classification and Regression Tool for Compound Classification and QSAR Modeling. *J. Chem. Inf. Comput. Sci.* **2003**, *43*, 1947–1958.
- (140) Abraham, A. In *Handbook of Measuring System Design*; John Wiley & Sons, Ltd: 2005.
- (141) Williams, C.; Rasmussen, C. In *Advances in Neural Information Processing Systems 8*, Touretzky, D., Mozer, M., Hasselmo, M., Eds., Copyright of the Massachusetts Institute of Technology Press (MIT Press); *Advances in Neural Information Processing Systems 8* ; Conference date: 01-01-1996 Through 01-01-1996; MIT: 1996.
- (142) Basak, D.; Pal, S.; Ch, D.; Patranabis, R. In *Neural Information Processing Letters and Reviews*, 2007, pp 203–224.
- (143) Zhou, T.; Song, Z.; Sundmacher, K. Big Data Creates New Opportunities for Materials Research: A Review on Methods and Applications of Machine Learning for Materials Design. *Engineering* **2019**, *5*, 1017–1026.
- (144) Pedregosa, F. et al. Scikit-learn: Machine Learning in Python. *Journal of Machine Learning Research* **2011**, *12*, 2825–2830.
- (145) Paszke, A.; Gross, S.; Chintala, S.; Chanan, G.; Yang, E.; DeVito, Z.; Lin, Z.; Desmaison, A.; Antiga, L.; Lerer, A. Automatic differentiation in PyTorch. **2017**.
- (146) Xu, Y.; Goodacre, R. On Splitting Training and Validation Set: A Comparative Study of Cross-Validation, Bootstrap and Systematic Sampling for Estimating the Generalization Performance of Supervised Learning. *J. Anal. Test.* **2018**, *2*, 249–262.

-
- (147) Claesen, M.; De Moor, B. Hyperparameter Search in Machine Learning. *arXiv:1502.02127 [cs, stat]* **2015**, arXiv: 1502.02127.
- (148) Bergstra, J.; Yamins, D.; Cox, D. D. In *Proceedings of the 12th Python in Science Conference*, ed. by van der Walt, S.; Millman, J.; Huff, K., 2013, pp 13–19.
- (149) Maulud, D.; Abdulazeez, A. M. A Review on Linear Regression Comprehensive in Machine Learning. *Journal of Applied Science and Technology Trends* **2020**, *1*, Number: 4, 140–147.
- (150) Mitchell, M., *An introduction to genetic algorithms*; Complex adaptive systems; MIT Press: Cambridge, Mass, 1996.
- (151) Nam, K. H.; Cho, J. C.; Jo, W. H. Temperature and Molecular Weight Effect of Styrene–Isoprene Diblock Copolymers on the Interfacial Tension between Polystyrene and Polyisoprene. *Polym. J.* **1995**, *27*, 904–910.
- (152) Werner, A.; Schmid, F.; Binder, K.; Müller, M. Diblock copolymers at a homopolymer - Homopolymer interface: A Monte Carlo simulation. *Macromolecules* **1996**, *29*, 8241–8248.
- (153) Vp, S.; Mohanty, S.; Nayak, S. K. Effect of poly (lactic acid)-graft-glycidyl methacrylate as a compatibilizer on properties of poly (lactic acid)/banana fiber biocomposites. *Polym. Adv. Technol.* **2016**, *27*, 515–524.
- (154) Zhang, C. L.; Feng, L. F.; Gu, X. P.; Hoppe, S.; Hu, G. H. Efficiency of graft copolymers as compatibilizers for immiscible polymer blends. *Polymer (Guildf)*. **2007**, *48*, 5940–5949.
- (155) Creton, C.; Kramer, E. J.; Hadziioannou, G. Critical molecular weight for block copolymer reinforcement of interfaces in a two-phase polymer blend. *Macromolecules* **1991**, *24*, 1846–1853.

5 Annex: Optimization of Heat Transfer at the Interface

Reproduced with permission from Zhou et al. [J. Phys. Chem. C 2021, 125, 25, 14149–14162] Copyright 2021 American Chemical Society. As the supporting document for the heat transfer.

Effect of Defects on the Interfacial Thermal Conductance between *n*-Heneicosane in Solid and Liquid Phases and a Graphene Monolayer

Tianhang Zhou,* Hari Krishna Chilukoti,* Zhenghao Wu, and Florian Müller-Plathe



Cite This: *J. Phys. Chem. C* 2021, 125, 14149–14162



Read Online

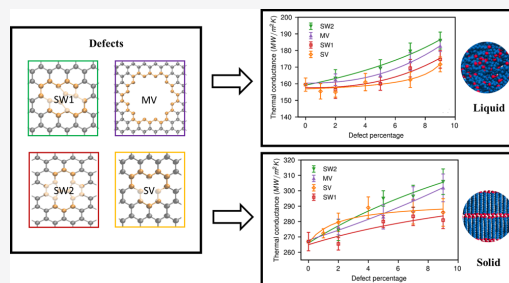
ACCESS |

Metrics & More

Article Recommendations

Supporting Information

ABSTRACT: The molecular level mechanism of heat transport across the interface between solid and liquid *n*-heneicosane and monolayer graphene with three types of defects (single-vacancy, multivacancy (MV), and Stone–Wales (SW) (SW1 and SW2 cases are considered based on the orientation of the defects)) has been studied using nonequilibrium molecular dynamics simulations. The influence of the alignment of an ideal crystal structure (heneicosane molecules positioned perpendicular and parallel to the graphene basal plane) and two heating modes (in the “heat-matrix” mode, heat enters the defective graphene sheet from one side of its basal plane and leaves from the other side, and in the “heat-graphene” mode, the heat is entering from the heated graphene layer to the cooled heneicosane from both sides of the basal plane) on the thermal conductance has been examined. With an increase in the defect percentage (up to 9.0%), the thermal conductance is found to be increasing for all types of defects under both heating modes. It is observed that both MV and SW2 defects in graphene result in the largest enhancement in the conductance under the heat-matrix mode, whereas the SW1 defect yields maximum improvement under the heat-graphene mode. Spectral analysis indicates that the vibrational modes of all frequencies are important for the interfacial heat transfer.



1. INTRODUCTION

Due to their high energy density and isothermal operation, latent heat thermal energy storage units are popular to store excess thermal energy. Solid–liquid phase change materials (PCMs) find applications in the storage of solar energy which is discontinuous in nature,¹ passive cooling of electric devices,² and waste heat recovery systems.³ Because of their high latent heat, good thermal and chemical stability, insignificant or no super cooling, nontoxicity, low vapor pressure, and low cost, organic PCMs are promising candidates for energy storage applications.^{4,5} The rate at which the thermal energy is stored and released is directly proportional to the PCMs’ thermal conductivity. So, materials having high thermal conductivity in both liquid and solid phases are desirable for PCMs. However, organic PCMs, inherently, have a low thermal conductivity. Therefore, a lot of effort has been directed toward increasing the thermal conductivity of PCMs.

To improve the thermal conductivity of a base material in either the solid or liquid state, a common approach is to add materials with high thermal conductivity as fillers. In the recent past, due to their high thermal conductivity, carbon-based nanoadditives, e.g., graphene and carbon nanotubes, have been used as fillers, and they have demonstrated good performance in enhancing the thermal conductivity of the nanocomposite.^{6–10}

One of the important parameters that will significantly influence the overall thermal conductivity of the nanocomposite is the thermal boundary resistance between the host matrix and the nanofillers. Furthermore, this is also a vital input variable in the effective medium theory.¹¹ Experimental investigation of molecular level heat transfer characteristics across the interfaces is challenging. Molecular dynamics (MD) simulation is one of the computer simulation techniques that is well suited to study the mechanism of nanoscale interfacial heat transfer as well as for evaluating the magnitude of thermal conductance.^{12–31} In our recent article,²³ we observed that the thermal conductance at the interface between edge-on ideal crystal and single-layer graphene is two times higher than that for the interface between liquid heneicosane and graphene.

The graphene sheets are synthesized using techniques like chemical vapor deposition (CVD), epitaxial growth,³⁰ micro-mechanical cleavage, electrochemical exfoliation, unzipping

Received: May 28, 2021

Revised: June 3, 2021

Published: June 16, 2021



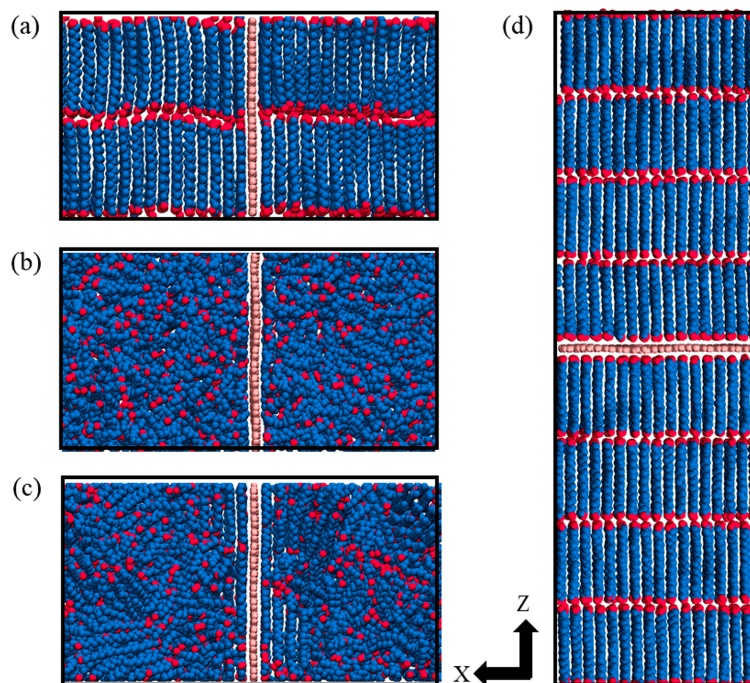


Figure 1. Snapshots of the 9.0% SV defective single-layer graphene–heneicosane computational system with different phases and structures of heneicosane: (a) parallel-aligned crystal system, (b) liquid system, (c) disordered solid system, and (d) perpendicular-aligned crystal system. The CH_3 and CH_2 units of a heneicosane molecule are shown in red and blue, respectively. The graphene layer is illustrated in pink.

carbon nanotubes, and so forth.³² It is known that defects are inevitable during the production process. Furthermore, to tailor the properties of graphene, defects can be artificially generated using ion/electron beam irradiation and purification.³² Various types of defects such as vacancy,³³ Stone–Wales,³⁴ line,³⁵ doping,³⁶ and adatoms³⁷ may occur in graphene. Molecular dynamics studies suggest that defects considerably reduce the thermal conductivity of graphene.^{32,38–40} At the same time, it is important to know how these defects influence the heat transfer at the interface between the graphene and matrix because this is considered to be an important parameter governing the overall thermal conductivity of the nanocomposite. Recently, a few researchers have investigated the influence of vacancy defects on the thermal conductance between defective graphene and a soft matrix. For example, Liu et al.²⁸ examined the sensitivity of two modes of heating and vacancy defects on the thermal conductance at the liquid octane–graphene interface. Li et al.¹⁴ examined heat transfer across defective graphene (with single-vacancy (SV), double-vacancy, Stone–Wales (SW), and multivacancy (MV) defects)—epoxy interfaces under the heat-matrix mode and found that SW and MV defects improve interfacial heat transfer. However, it is not yet understood how the interfacial thermal conductance will be influenced when the graphene has defects and the alkane is in the solid state. Previous works suggested that the introduction of defects into the graphene sheet results in enhanced overlap between the vibrational density of states (VDOS) of embedded graphene and liquid matrix, which is attributed to the improved interfacial thermal conductance.^{28,41,42} Nevertheless, it is still unclear that

how changes in the VDOS of graphene can be traced to the defective regions or atoms in graphene. More studies are desired to understand the physical mechanism of interfacial heat transfer involving defective graphene in order to provide guidelines for improving the overall thermal performance of nanocomposites in different phases.

In this article, we have performed nonequilibrium molecular dynamics simulations (NEMD) to examine the heat transfer characteristics through the interface between heneicosane ($\text{C}_{21}\text{H}_{44}$) in both solid and liquid phases and monolayer defective graphene. The effects of three types of randomly dispersed defects, viz., SV, MV, and SW, in graphene and two modes of heating on the interfacial thermal conductance have been investigated. To gain insight into which vibrational modes are modified or initiated by defects and how they might influence the thermal energy transfer across the interface, the vibrational density-of-states and the spectral distribution of the interfacial heat flux have been analyzed.

2. MOLECULAR MODEL AND SIMULATION DETAILS

Schematics of the constructed simulation systems are illustrated in Figure 1. Heneicosane ($\text{C}_{21}\text{H}_{44}$) is selected as an *n*-alkane since it is frequently used as a phase change material at room temperature (melting point 313.55 K⁴³). A past study from our group showed that for the study of thermal transport properties of alkanes the united atom model gives better results over the all-atom model.⁴⁴ Therefore, heneicosane molecules are described using a united atom model where CH_3 and CH_2 groups are considered as single interaction sites. The molecular interaction

between heneicosane atoms is modeled with the NERD potential⁴⁵ (Table S1, Supporting Information). An all-atom model is used to represent graphene, and the interactions among carbon atoms are considered using the optimized Tersoff potential⁴⁶ (Table S2, Supporting Information). More information about these two potentials and the interaction parameters between graphene and heneicosane atoms is given in the Supporting Information part I.

Similar to our previous work,²³ to examine the influence of the solid structure of heneicosane on the interfacial thermal conductance, we construct three types of systems. These are named as “parallel-aligned system”, “perpendicular-aligned system”, and “disordered-solid system”. Heneicosane molecules are aligned parallel to the graphene basal plane in the parallel-aligned system (cf. Figure 1a). On the other hand, heneicosane molecules are oriented perpendicular to the graphene basal plane in the perpendicular-aligned system (cf. Figure 1d). The thermal transport in *n*-alkanes in the solid state is examined by considering an ideal-crystal model in an earlier work, where all molecules are in favor of a particular direction.²¹ The lengths of the simulation systems are summarized in the Supporting Information part II. We use the LAMMPS package to perform all simulations.⁴⁷ The LJ interactions beyond a cutoff radius of 1.4 nm are neglected. During equilibration, periodic boundary conditions are implemented in all three directions, and a time step of 1 fs is used.

Schematics of three types of defects examined in this work are illustrated in Figure 2. A missing single carbon atom in the

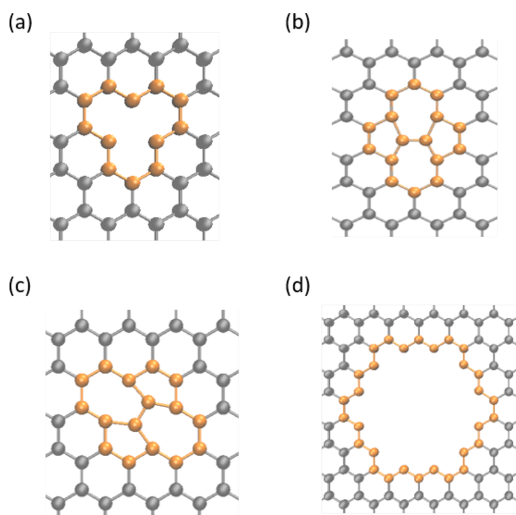


Figure 2. Schematic illustration of different types of defects in a monolayer graphene: (a) SV, (b) SW1, (c) SW2, and (d) MV.

graphene lattice results in a single-vacancy (SV). The SV defect is easily constructed in the graphene sheet by deleting a carbon atom (Figure 2a). For fabricating the multivacancy (MV) defect shown in Figure 2d, more than two carbon atoms are removed from the graphene layer. The Stone–Wales (SW) defect does not involve any addition or removal of atoms. One of the C–C bonds is rotated by 90° about the center point of the bond to form the SW defect, which is also known as the 5-7-7-5 defect.

Two types of orientations are considered for the SW defect in graphene. In the first case only vertical C–C bonds are rotated by 90°, which is called SW1 (Figure 2b). In the second case only inclined C–C bonds are rotated by 90°, and this is known as SW2 (Figure 2c). All defects are at a particular angle in the SW2 case. Note that all defects are randomly distributed in the graphene sheet. The concentrations of SV and MV defects are defined as²⁸

$$\phi = 1 - \frac{N_{\text{defect}}}{N_{\text{pristine}}} \quad (1)$$

where N_{defect} and N_{pristine} are the numbers of carbon atoms in the defective and pristine graphene, respectively. The concentrations in the SW1 and SW2 cases are defined as

$$\phi = 1 - \frac{2N_{\text{SW-defect}}}{N_{\text{pristine}}} \quad (2)$$

where $N_{\text{SW-defect}}$ is the number of SW defects in graphene. The factor 2 in the numerator is to account for the fact that each SW defect involves two carbon atoms. The defect concentration is varied from 0 to 9.0% for all defects. Simulation systems are made up of a pristine or defective graphene sheet sandwiched between heneicosane nanofilms in the required phase as illustrated in Figure 1. Ideal crystal systems are constructed by positioning heneicosane molecules in an orthorhombic crystal with lattice parameters given by Jouti et al. from X-ray diffraction.⁴⁸ As a first step, the systems are simulated in the NPT ensemble for 2 ns with the Nosé–Hoover barostat (1 atm) and thermostat (259 K) with coupling times of 5.0 and 1.0 ps, respectively. After that, systems are equilibrated in the NVE ensemble for 2 ns. The temperature of the parallel-aligned system at 250 K and 1 atm is raised slowly from 250 to 400 K with a rate of 10 K/ns. Then, for equilibration, the system is simulated in the NPT ensemble for 2 ns and later in the NVE ensemble for 2 ns. To construct the graphene-disordered solid heneicosane systems, the liquid system, which is fabricated by heating the parallel-aligned system, is cooled from 400 K and 1 atm to the desired temperature (250 K) and pressure (1 atm) in the NPT ensemble with a rate of 2 K/ns. After that, the system is simulated in the NVT ensemble for 15–20 ns. Finally, the system is simulated for 2 ns in the NVE ensemble for equilibration. Note that the structure of heneicosane in the disordered systems is different between runs and is sensitive to the cooling rate and the initial equilibrium configuration utilized for the preparation of the system. So, three disordered systems have been fabricated from different starting configurations. Then, the conductance values obtained from three systems are averaged to obtain the final value at the target temperature. Note that, first, systems with lower percentage of defects are prepared from pristine systems and equilibrated. After that systems with higher percentage defects are constructed based on the obtained lower percentage equilibrated systems to maintain the stability of the defected graphene. Subsequently, they are equilibrated in the NPT ensemble.

We perform nonequilibrium molecular dynamics (NEMD) simulations on the equilibrated systems to evaluate the interfacial thermal conductance. Liu et al.²⁸ suggested that heat transfer occurs in two modes in graphene-based nanocomposites (Figure S1 in the Supporting Information). In the first mode, the energy is flowing from the side of heated heneicosane molecules to the cooled ones on the other side across the defective graphene. In the second mode, thermal

energy migrates into or out of the graphene sheet at the same time from both sides of its basal plane. Hence, we perform NEMD simulations in two ways by following our previous work²³ (details are given in the Supporting Information part III). The systems are simulated in the NVE ensemble. The velocity rescaling method is used to maintain the heat source and heat sink regions at the desired temperature. In the NEMD simulations an integration time step of 0.2 fs is utilized. After an initial transient time (6 ns), a constant heat flux is achieved, and a steady-state temperature profile is established. Afterward, the data are accumulated for 18 ns to evaluate the thermal conductance. The collected data are subdivided into three blocks, and from each a conductance value is calculated. From these three values a standard deviation is calculated, which is shown as an error bar.

3. SPECTRAL ANALYSIS OF INTERFACIAL THERMAL ENERGY TRANSFER

We have performed two types of spectral analysis to gain an insight into the mechanisms associated with heat transfer at the heneicosane–graphene interfaces. As a part of the spectral analysis, the vibrational density of states (VDOS) $D(\omega)$ is evaluated. The VDOS is the Fourier transform of the ensemble average of the atomic velocity autocorrelation function $\langle v_i(\tau) \cdot v_i(0) \rangle$.⁴⁹ It is calculated as follows

$$D(\omega) = \frac{1}{k_B T} \sum_i m_i \int_{-\infty}^{+\infty} d\tau e^{i\omega\tau} \langle v_i(\tau) \cdot v_i(0) \rangle \quad (3)$$

where v_i and m_i are the velocity vector and mass of atom i , respectively. ω is the frequency, and τ is time. A Gaussian convolution with a width of 1.6 THz is applied to smooth the spikes in the VDOS. The modulus of $D(\omega)$ is investigated below. The VDOS of carbon atoms in the graphene sheet and heneicosane united atoms in the first adsorption layer (this is recognized as the first peak near graphene in the heneicosane density profile) are used for the analysis of interfacial heat transfer. To obtain the vibrational spectra, the velocities of the designated heneicosane and graphene atoms are sampled every 20 fs for 0.8 ps blocks. The data are collected after the system reaches equilibrium in the NVE ensemble. The production run of 1 ns is utilized in the VDOS calculations. Furthermore, to quantify the overlap of the VDOS of the two materials at the interface an overlap factor (S) is evaluated⁵⁰

$$S = \frac{\int_0^\infty D_g(\omega) D_h(\omega) d\omega}{\int_0^\infty D_g(\omega) d\omega \cdot \int_0^\infty D_h(\omega) d\omega} \quad (4)$$

where $D_g(\omega)$ and $D_h(\omega)$ indicate the VDOS of graphene and of the first adsorption layer of heneicosane molecules, respectively. The decomposition of the interfacial heat flux in the spectral domain is the second spectral analysis, which is defined as⁵¹

$$q(\omega) = \frac{2}{A} \mathcal{R} \sum_{j \in h, i \in g} \int_{-\infty}^{+\infty} d\tau e^{i\omega\tau} \langle F_{ij}(\tau) \cdot v_i(0) \rangle \quad (5)$$

where F_{ij} is the total force exerted on a carbon atom i in the graphene (g) due to the all united atoms of heneicosane (h) in the first adsorption layer and v_i is the velocity vector of carbon atom i in graphene. \mathcal{R} indicates only the real part of the Fourier transform of the force–velocity cross-correlation function $\langle F_{ij}(\tau) \cdot v_i(0) \rangle$ is used, and A is the cross section of the system. To

calculate $q(\omega)$ the data were sampled every 20 fs for 0.8 ps in the NEMD simulation with a production run of 6 ns.

4. RESULTS AND DISCUSSION

4.1. Interfacial Thermal Conductance. The interfacial thermal conductance, G , is utilized to characterize the interfacial heat transfer between two unlike substances

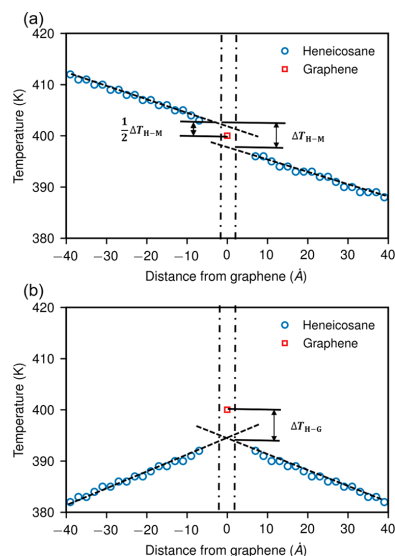


Figure 3. Temperature profiles along the z -axis in the 9.0% SV defective graphene–liquid heneicosane system at 400 K and 1 atm under (a) heat-matrix mode and (b) heat-graphene mode. The interface position between graphene and heneicosane is indicated by vertical dash-dotted lines. The temperature drops at the interface under heat-matrix and heat-graphene mode are shown as $\frac{\Delta T_{H-M}}{2}$ and ΔT_{H-G} , respectively.

$$G = \frac{q}{\Delta T} \quad (6)$$

where q is the amount of heat flux flowing through the interface and ΔT is the temperature drop at the interface. To calculate the temperature drop at the interface, the steady-state temperature profile along the z -axis (heat flux direction) was evaluated during the production run of the NEMD simulations. To describe the temperature drop calculation procedure in detail, as an example, steady-state temperature profiles along the heat-transport direction (z) in the liquid heneicosane–monolayer graphene with 9% SV defects at 400 K and 1 atm under both heating modes are shown in Figure 3. The temperature distribution is evaluated in bins of 0.2 nm thickness based on previous works.^{52,53} Note that past works suggest that fine bins are not recommended for calculating the temperature drop, and the bin size should be selected in such way that a large enough number of particles are presented in each bin so that the fluctuations in the temperature profile in the interface region are not significant. As expected, the temperature decreases toward the sink region from the source region, and a temperature drop is noticeable at the interface which is a characteristic of interfacial resistance to the heat transfer. Masuduzzaman and Kim⁵⁴ showed that the temperature jump across the interface is sensitive to the

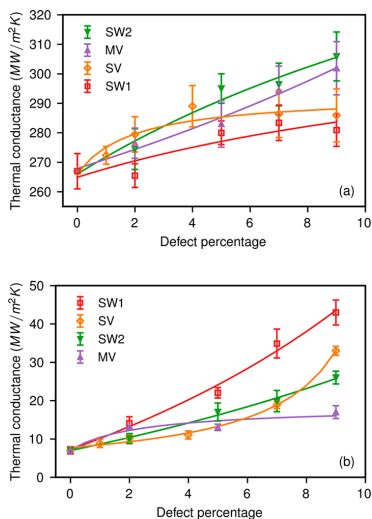


Figure 4. Variation of the interfacial thermal conductance between parallel-aligned heneicosane crystal and monolayer graphene with SV, SW1, SW2, and MV defects as a function of defect percentage under (a) heat-matrix mode and (b) heat-graphene mode. Solid lines are a guide to the eye.

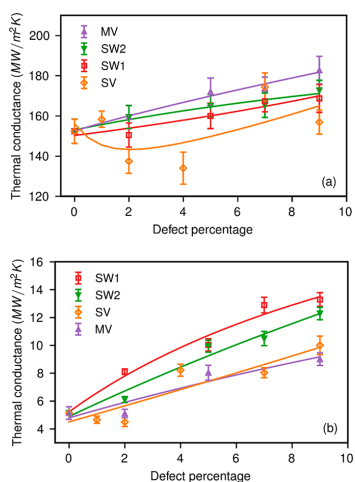


Figure 5. Variation of the interfacial thermal conductance between perpendicular-aligned heneicosane crystal and monolayer graphene with SV, SW1, SW2, and MV defects as a function of defect percentage under (a) heat-matrix mode and (b) heat-graphene mode. Solid lines are a guide to the eye.

boundary position and the film thickness (channel width). They observed that for large enough films, the interface position closer to the solid surface gives results which are in good agreement with the experimental values in comparison to the results obtained by considering the boundary position far away from the solid surface atoms. Therefore, for evaluating the temperature drop the interface location is taken as the center point between the average position of graphene atoms and the first peak

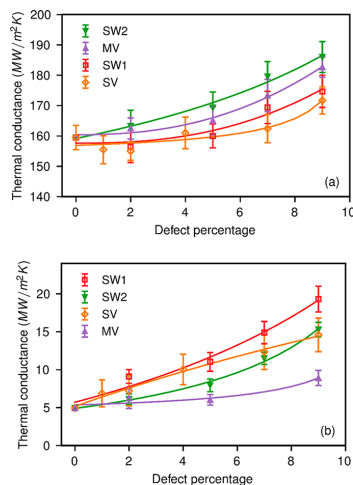


Figure 6. Variation of the interfacial thermal conductance between liquid heneicosane and monolayer graphene with SV, SW1, SW2, and MV defects as a function of defect percentage under (a) heat-matrix mode and (b) heat-graphene mode. Solid lines are a guide to the eye.

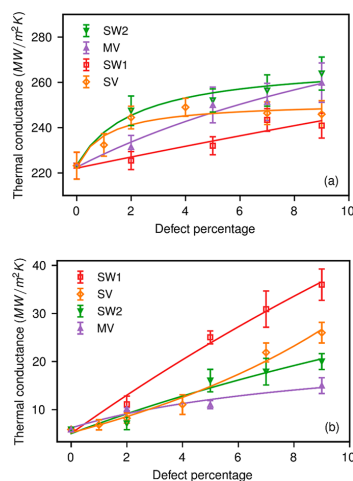


Figure 7. Variation of the interfacial thermal conductance between disordered solid heneicosane and monolayer graphene with SV, SW1, SW2, and MV defects as a function of defect percentage under (a) heat-matrix mode and (b) heat-graphene mode. Solid lines are a guide to the eye.

position in the atomic heneicosane density profile. A straight line is fitted to the temperature profile in the bulk region, and the fit line is extrapolated to the position of the interface to determine the temperature of heneicosane at the interface. Additionally, the temperature of the graphene is used as shown in Figure 3 for evaluating the temperature drop.

4.2. Interfacial Thermal Conductance as a Function of Defect Percentage. Variation of the thermal conductance at the interface between a graphene sheet with four types of defects (SV, MV, SW1, and SW2) and heneicosane in the liquid state

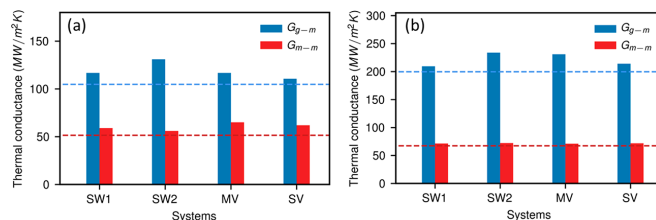


Figure 8. Values of interfacial thermal conductance G_{g-m} and G_{m-m} under heat-matrix mode (a) between liquid heneicosane and monolayer graphene with SV, SW1, SW2, and MV defects at 9.0% and (b) between parallel-aligned heneicosane and monolayer graphene with SV, SW1, SW2, and MV defects at 9.0%. Dashed lines represent values of G_{g-m} and G_{m-m} for a system with a pristine graphene monolayer.

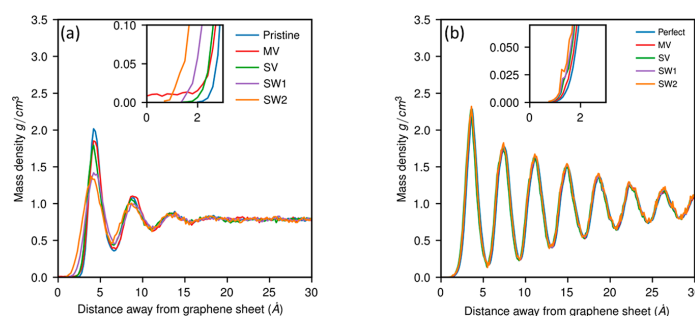


Figure 9. Density profiles of (a) liquid heneicosane at 400 K and 1 atm in contact with monolayer graphene with no defects (pristine), SV, SW1, SW2, and MV defects at 9% and (b) parallel-aligned heneicosane at 250 K and 1 atm in contact with graphene with no defects (pristine), SV, SW1, SW2, and MV defects.

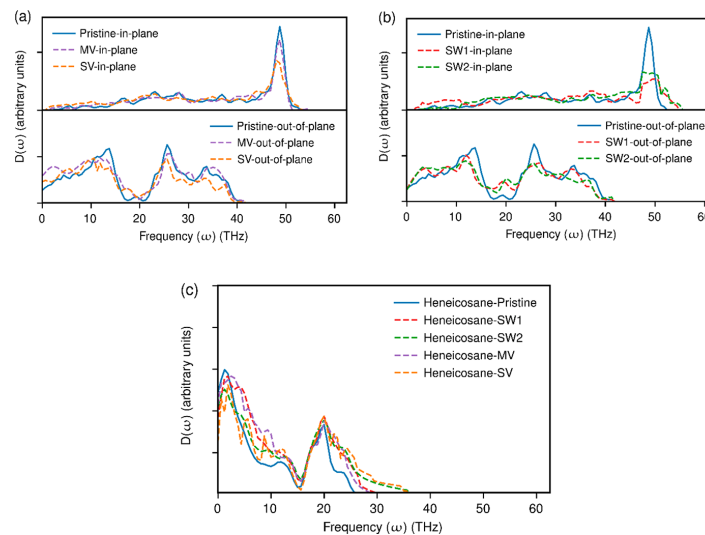


Figure 10. For the liquid heneicosane system at 400 K and 1 atm: (a) vibrational densities of states in arbitrary units along in-plane and out-of-plane directions for pristine graphene and graphene with 9.0% MV and SV defects, (b) vibrational densities of states along in-plane and out-of-plane directions for graphene with 9.0% SW1 and SW2 defects, and (c) overall vibrational densities of states for heneicosane molecules in the first adsorption layer.

and in both solid states (perfect crystal and disordered solid state) at various defect percentages under both heating modes (heat-matrix and heat-graphene) is examined (Figures 4, 5, 6,

and 7). First, as expected, the thermal conductance under the heat-matrix mode is observed to be 2 orders of magnitude higher than under the heat-graphene mode regardless of the phase and

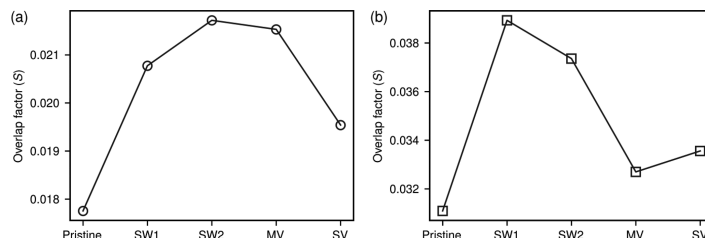


Figure 11. Overlap factor for liquid heneicosane systems under the heat-matrix mode at 400 K and 1 atm (a) between the total vibrational densities of states of heneicosane and out-of-plane vibrational densities of states of pristine and 9.0% defective graphene and (b) between the in-plane and out-of-plane vibrational densities of states of pristine and 9.0% defective graphene.

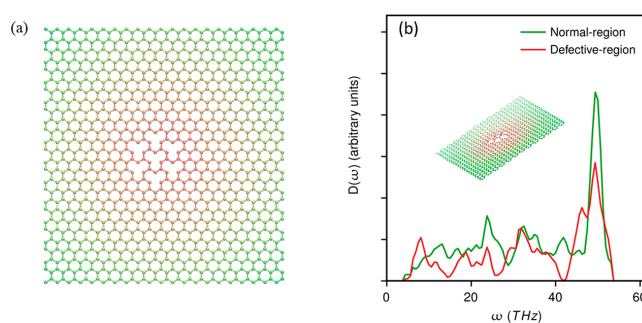


Figure 12. (a) Schematic illustration of monolayer graphene with seven SV defects concentrated in the central region. (b) In-plane VDOS of a graphene with seven SV defects embedded in liquid heneicosane at 400 K and 1 atm.

structure of heneicosane for pristine graphene systems. Lower values under the heat-graphene mode are due to the resistance to “internal” heat transfer between the vibrational modes (primarily between low-frequency vibrational modes and medium- and high-frequency vibrational modes) within the monolayer graphene.²³ This has been discussed extensively in previous works, which have examined the mode of heating effect on the thermal conductance at graphene–liquid octane and graphene–polymer interfaces.^{28,55} With an increase in the defect percentage, the conductance under the heat matrix mode is only 1 order of magnitude higher than that under the heat-graphene mode for all types of defects. More details about this will be given below. Second, among the interfaces of graphene with the solid heneicosane the thermal conductance ordering is parallel-aligned crystal > disordered > perpendicular-aligned. Moreover, the conductance for the graphene–liquid interface is close to that for the perpendicular-aligned system under the heat-matrix mode. This has been qualitatively explained by the structure of heneicosane in the interface region. The parallel-aligned crystal system has the most number of heneicosane atoms in contact with the graphene sheet, which results in the highest conductance. On the other hand, the smallest number of atoms is in contact with the graphene in the perpendicular-aligned crystal system. This results in the lowest conductance. The disordered solid state is crystalline with small domains. This structure allows a sufficient number of atoms to be in contact with graphene so as to have a thermal conductance higher than that of the perpendicular-aligned system or the liquid. Third, for each type of defect, the thermal conductance exhibits a tendency to increase with the defect percentage in the examined range (up to 9.0%) irrespective of the phase and structure of heneicosane

and the heating mode. Similar increasing tendencies have been observed for graphene with SV defects and liquid octane interfaces.⁵⁶ Among the four types of defects, for heneicosane in the liquid state and in all solid states, SW2 and MV defects most enhance the thermal conductance under the heat-matrix mode at high defect percentage. On the other hand, under the heat-graphene mode, the SW1 defect shows the largest improvement in conductance as compared to the three other defects at high defect percentage. The highest improvement in the conductance for parallel-aligned, perpendicular-aligned, disordered, and liquid systems with 9.0% defects is 14.2, 19.9, 19.9, and 18.2% in comparison with pristine graphene systems under the heat-matrix mode whereas under the heat-graphene mode the major enhancement is 512, 158, 275, and 513%, respectively. In the absolute term, under the heat-matrix mode, for parallel-aligned and disordered systems with defects the maximum improvement in thermal conductance is ~ 40 MW/m² K over the pristine systems whereas the highest enhancement of ~ 30 MW/m² K is noticed for perpendicular-aligned and liquid systems. However, the lowest increment in conductance is noticed for perpendicular-aligned system with SV defects. The maximum increase in the conductance for defective graphene over defect-free graphene under the heat-graphene mode is close to 30, 36, 8, and 14 MW/m² K for parallel-aligned, disordered, perpendicular-aligned, and liquid systems, respectively.

In total, it can be concluded that all defects in graphene enhance the interfacial thermal energy transfer, and the amount of increment in conductance with defects depends on the type of defect, heating mode, and phase and orientation of heneicosane.

The intermolecular interaction between graphene and heneicosane as well as between different heneicosane molecules

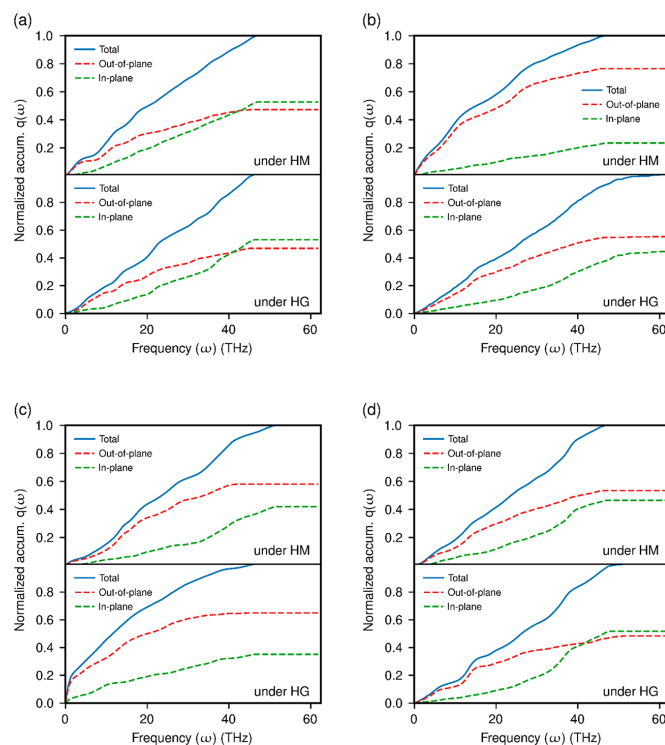


Figure 13. Directionally resolved normalized cumulative spectral heat flux ($q(\omega)$) at the interface between parallel-aligned heneicosane crystal and 9.0% defective graphene under heat-matrix and heat-graphene modes when the graphene has defect type (a) SW1, (b) SW2, (c) MV, and (d) SV. Here, the $q(\omega)$ is calculated from graphene to heneicosane. The heat-matrix mode and heat-graphene mode are abbreviated as HM and HG in the figures, respectively.

is treated using the LJ potential in our molecular model. This means that the heat is transferred across the interface by means of LJ interactions. As discussed in our previous paper,²³ when the distance between heneicosane molecules that are separated by the monolayer graphene is less than the LJ cutoff radius, heat flows across the interface via two channels under the heat-matrix mode. In first channel, the heat enters the graphene from the matrix and then exits the graphene to the other side matrix. In second channel, the heat is directly transferred from matrix to matrix without first entering the graphene between heneicosane molecules on both sides. We have adopted the same approach as in our previous paper²³ to quantify the matrix-to-matrix energy transfer, and the thermal conductance calculated in this way is referred to as G_{m-m} . Then G_{g-m} is obtained as $G_{g-m} = G - G_{m-m}$, where G is the thermal conductance obtained under normal heat-matrix mode simulations. The values of G_{g-m} and G_{m-m} for systems with four types of defects (SV, MV, SW1, and SW2) at 9.0% in graphene and heneicosane in the liquid (Figure 8a) and parallel-aligned solid state (Figure 8b) are examined. We observe that G_{g-m} and G_{m-m} are higher for liquid heneicosane systems with defective graphene as compared to a system with no defects. This implies that the introduction of defects improves both matrix-to-matrix and graphene-to-matrix pathways. The enhancement in G_{m-m} is more noticeable for the MV defect. However, for the solid system, the magnitude of G_{m-m} is similar for all systems (Perpendicular-aligned and disordered

systems results are not shown here). This indicates that the enhancement in interfacial conductance mainly stems from an increase in graphene-to-matrix transfer.

Density distributions of heneicosane atoms in liquid (Figure 9a) and parallel-aligned (Figure 9b) systems are calculated by dividing the simulation system into slabs with a thickness of 0.02 Å along the z -direction. For liquid heneicosane (Figure 9a), density curves situate closer to the graphene in systems with defects, especially for the MV defect. This is because the MV defect is large enough for heneicosane to go through the graphene over the simulation time (Figure S3, Supporting Information). This is attributed to be the cause for the highest G_{m-m} for a liquid system with a MV defect (Figure 8a) because it reduces the distance between liquid heneicosane molecules separated by the defective graphene layer.²³ As for the solid heneicosane systems (Figure 9b), atoms vibrate around their mean positions, density distributions look similar irrespective of the defect type, and the distance between heneicosane molecules, which are located on both sides of the defective graphene layer, is changed insignificantly, which is believed to be reason for the minimal variation in G_{m-m} (Figure 8b).

4.3. Vibrational Density of States Analysis. The vibrational spectral analysis is done to gain an insight into the mechanism of thermal energy transfer at defective graphene–heneicosane interfaces. The profiles of in-plane and out-of-plane vibrational densities of states (VDOS) for pristine graphene,

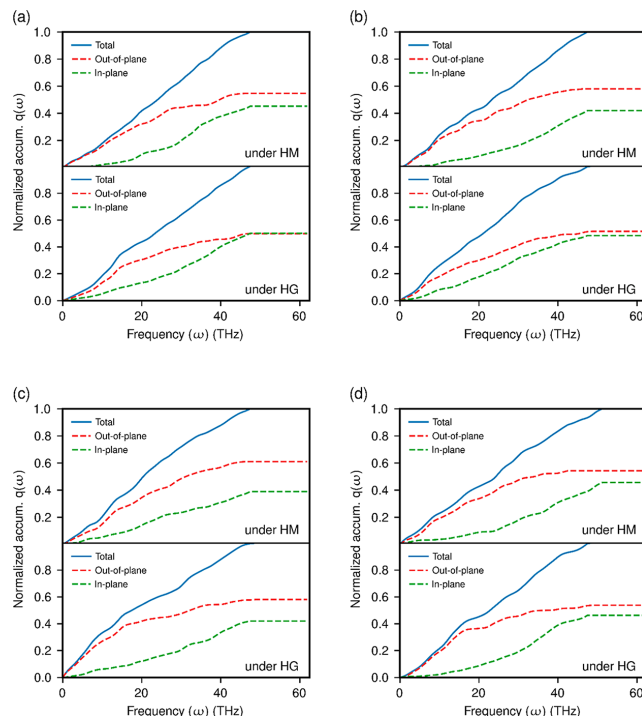


Figure 14. Directionally resolved normalized cumulative spectral heat flux ($q(\omega)$) at the interface between perpendicular-aligned heneicosane crystal and 9.0% defective graphene under heat-matrix and heat-graphene modes when the graphene has defect type (a) SW1, (b) SW2, (c) MV, and (d) SV. Here, the $q(\omega)$ is calculated from graphene to heneicosane. The heat-matrix mode and heat-graphene mode are abbreviated as HM and HG in the figures, respectively.

graphene with four types of defects at 9%, and overall VDOS of the first adsorption layer heneicosane atoms in the liquid heneicosane–graphene systems are shown in Figure 10. As expected, the pristine graphene VDOS is dominated by the middle- (15–40 THz) and high-frequency ranges (>40 THz). On the contrary, the vibrational spectra of heneicosane in the vicinity of the pristine graphene occupy the low- and middle-frequency ranges. The overlap between the VDOS of two different materials has been examined to qualitatively understand which vibrational modes are important for the interfacial heat transfer.^{14,16,28,30,42,57–59} The overlap between the vibrational spectra of graphene and liquid heneicosane happens predominantly in the low- and middle-frequency ranges. This indicates that heat transfer at the interface is mainly carried by the coupling between the low-frequency vibrations of graphene and heneicosane, which is in line with past works.^{16,42,55} The VDOS of heneicosane in crystal and disordered solid states also exhibit similar characteristics and frequency ranges (Figures S4–S6, Supporting Information). The VDOS of liquid heneicosane in the vicinity of defective graphene show new vibrational modes with higher frequencies than formed heneicosane in contact with pristine graphene VDOS for all types of defects. At the same time the graphene out-of-plane vibrations in the low-frequency region are enhanced, and the in-plane vibrations in the high-frequency range are suppressed considerably for SV, SW1, and SW2 defects as compared to the neat graphene. In contrast, for the MV defect the decrement in

the in-plane vibrations is not significant in the high-frequency region. For the SV defect, this is attributed to the structurally less rigid graphene in the in-plane direction due to the deletion of atoms.²⁸ Thus, both graphene and heneicosane VDOS change with the introduction of defects. In order to quantify the overlap between two VDOS, the overlap factor (S) is evaluated, which indicates the phonon–phonon coupling at the interface. The overlap factor between the VDOS of heneicosane and defective graphene can be used to explain the thermal conductance results under the heat-matrix mode. As illustrated in Figure 11a, the SW2 defective graphene system shows the highest overlap in comparison to other defective systems. This indicates a better thermal coupling between low-frequency vibrations of heneicosane and SW2 defective graphene which results in higher heat transfer across the interface and a larger thermal conductance value. Namsani and Singh⁴² have also noticed similar observations for defective graphene/liquid gold systems under the heat-matrix mode. Note that for the other three systems, the overlap factor characteristics also suggest the same conclusion (Figures S7–S9, Supporting Information).

The thermal energy is injected into the graphene sheet under the heat-graphene mode. This means energy is added into all vibrational modes simultaneously. In agreement with past studies,^{14,16,28,30,60} a pristine graphene sheet exhibits considerably more high- and medium-frequency vibrations than low-frequency vibrations (Figure 10). In addition, the VDOS of graphene in the plane is dominated by high-frequency

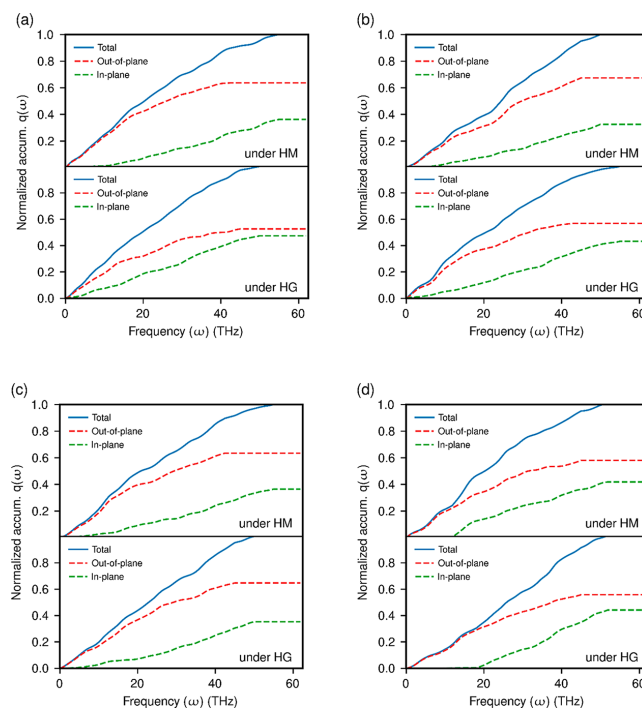


Figure 15. Directionally resolved normalized cumulative spectral heat flux ($q(\omega)$) at the interface between liquid heneicosane and 9.0% defective graphene under heat-matrix and heat-graphene modes when the graphene has defect type (a) SW1, (b) SW2, (c) MV, and (d) SV. Here, the $q(\omega)$ is calculated from graphene to heneicosane. The heat-matrix mode and heat-graphene mode are abbreviated as HM and HG in the figures, respectively.

vibrational modes whereas the out-of-plane vibrational modes occupy the low- and middle-frequency regions. Therefore, most of the injected energy will be added to the middle- and high-frequency vibrations. Earlier works^{28,55} have indicated that the energy associated with middle- and high-frequency vibrations of the graphene should first be converted into lower-frequency vibrations before it can be transferred to the heneicosane molecules under the heat-graphene mode. It is believed that this process of “internal” resistance to the transfer of heat within graphene between the high-frequency vibrations and the low-frequency vibrations is the cause for the low interfacial thermal conductance under the heat-graphene mode in comparison with the heat-matrix mode.^{28,55} Furthermore, the overlap factor between the in-plane and out-of-plane VDOS of defective graphene can be used to discuss conductance results under the heat-graphene mode. It is observed that the overlap factor for systems with defects is higher than that for pristine graphene systems (Figure 11b). This implies better thermal coupling between the in-plane and out-of-plane vibrational modes and less resistance to internal heat transfer. We believe this is the reason for the enhancement of thermal conductance with defects under the heat-graphene mode. The largest improvement in the conductance is for the SW defective liquid system under the heat-graphene mode (Figure. 6b) which can be attributed to the larger overlap factor. Hong et al.⁶¹ also suggested that the defects in graphene can improve the coupling between the in-plane and out-of-plane vibrations inside the graphene and observed higher thermal conductance at the

graphene/phosphorene interface with defects under the heat-graphene mode.

However, it is still unclear how changes in the VDOS of graphene are locally related to the defects. Are the vibrations of graphene atoms far away from the defects influenced by the defects? In order to clarify this issue, we simulated a liquid heneicosane-defective graphene system, where all SV defects (seven defects are considered as an example) are concentrated in the middle part of the sheet as illustrated in Figure 12a. We defined the region within a radius of 14.0 Å from the center as a defective region (shown in red in Figure 12a) and the rest of the region as a normal region (green in Figure 12a). It is observed that the in-plane VDOS of atoms in the defective region shows lower magnitude than for atoms in the normal region in the high-frequency region (Figure 12b). This trend is similar to the VDOS of all atoms (Figure 10). It can be inferred that the introduction of defects locally influences the vibrations of atoms in the vicinity of defects. Similar observations have been noticed for graphene with SW1, SW2, and MV defects (Figure S10, Supporting Information).

4.4. Spectral Heat Flux Analysis. The spectral heat flux $q(\omega)$ is calculated using eq 5 to gain further insight into which frequency type and range of vibrations are crucial for heat transfer at the interface. The frequency-dependent heat flux $q(\omega)$ is normalized with respect to the highest value of $q(\omega)$, and a running average of $q(\omega)$ versus frequency is analyzed to quantitatively understand which frequency vibrations make dominant contributions to the interfacial heat transfer

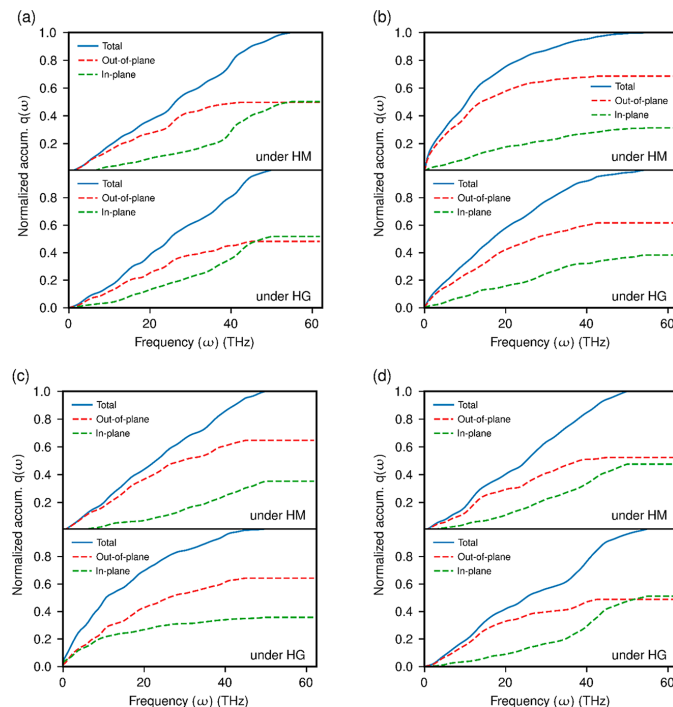


Figure 16. Directionally resolved normalized cumulative spectral heat flux ($q(\omega)$) at the interface between disordered solid heneicosane and 9.0% defective graphene under heat-matrix and heat-graphene modes when the graphene has defect type (a) SW1, (b) SW2, (c) MV, and (d) SV. Here, the $q(\omega)$ is calculated from graphene to heneicosane. The heat-matrix mode and heat-graphene mode are abbreviated as HM and HG in the figures, respectively.

(calculation details are given in the [Supporting Information part V](#)). [Figures 13, 14, 15, and 16](#) show spectrally mapped heat flux that is resolved along in-plane and out-of-plane directions for all states of heneicosane and graphene with four types of defects at 9.0%. Among the four types of defects, systems with larger contribution from out-of-plane vibrational modes to the total spectral heat flux exhibit larger thermal conductance values under the heat-matrix mode for heneicosane in the liquid state and in all solid states. This seems to be related to the enhanced overlap between the vibrations of heneicosane and the out-of-plane vibrations of defective graphene in the low- and midfrequency regions. We, therefore, anticipate that the augmentation of out-of-plane vibrations in graphene by means of defects could facilitate enhanced heat transfer across the interfaces under the heat-matrix mode. Note that our previous study also suggested that pristine graphene systems, in which the out-of-plane vibrations make dominant contribution, exhibited large thermal conductance under the heat-matrix mode. In liquid systems the out-of-plane vibrational modes always contribute more to the interfacial heat transfer than the in-plane vibrational modes under both heating modes regardless of the defect type ([Figure 15](#)). In contrast, a few systems with SW1 and SV defects and heneicosane in the solid state ([Figures 13a, 13d, 14a, 16a, and 16d](#)) show that the in-plane vibrations make more contribution to the total heat transfer over the out-of-plane vibrations. This could be attributed to the improved thermal coupling between the in-plane and out-of-plane vibrations inside

the graphene with the introduction of a particular type of defect. Moreover, the advantage of the in-plane cumulative $q(\omega)$ under the heat-graphene mode is much higher than under the heat-matrix mode for heneicosane in both liquid and solid states and graphene with SW1, SW2, and SV defects ([Figures 13–15a, b, and d](#)). This indicates that the in-plane vibrational modes contribute more to the total heat flux under the heat-graphene mode than the under the heat-matrix mode. Therefore, it can be implied that the energy added into the in-plane vibrations is less unfavorably transferred to the heneicosane in these systems. The profiles of in-plane VDOS of graphene with SW1, SW2, and SV defects show that the high-frequency range vibrations are significantly suppressed for heneicosane in the liquid state and in all solid states ([Figures 10 and Figures S4–S6](#)). This causes more heat to be injected into the low- and middle-frequency vibrations. This is believed to be the reason for in-plane vibrations making more contribution to the total heat flux than the out-of-plane vibrations. On the other hand, for MV defective graphene the in-plane VDOS has similar characteristics to pristine graphene with a noticeable peak in the high-frequency range. Therefore, more energy is injected into the high-frequency vibrations, and it first must be transferred to slow and out-of-plane vibrations internally inside the graphene before passing through the interface. This results in a reduced contribution to the interfacial heat transfer by the in-plane vibrations. Finally, from VDOS profiles it is well understood that the overlap between the VDOS of graphene and heneicosane

does not exist beyond the maximum frequency of heneicosane $\omega_{\max,H}$. Nevertheless, it is evident from the normalized cumulative $q(\omega)$ that interfacial heat transfer still occurs in the high-frequency range. This shows that other passages, namely surface modes, could enable the flow of heat at the interface.^{51,62}

In summary, we notice that, in contrast to pristine graphene systems, for some type of defects the in-plane vibrational modes make greater contribution (up to 55% for the parallel-aligned system with SW1 defect under the heat-graphene mode) than the out-of-plane vibrational modes to the total heat transfer at the interfaces under both heating modes.

5. CONCLUSIONS

Nonequilibrium molecular dynamic simulations have been performed to examine the thermal energy transfer across the interface between monolayer graphene with three types of defects and heneicosane in solid and liquid states. The thermal conductance at the interface between defective graphene and heneicosane in both solid and liquid phases is found to be increasing with an increase in the defect percent in the tested range (up to 9%) for all types of defects. The enhancement in the thermal conductance is found to be sensitive to the type of defect, heneicosane phase and structure, and heating mode. The maximum improvement of ~ 41 MW/m² K is noticed for the 9% SW1 defective parallel-aligned heneicosane crystal system. Furthermore, we have clearly demonstrated that the changes in the VDOS of graphene with defects can be traced to the defective region. Our previous work illustrates that in pristine graphene systems the advantage of out-of-plane vibrations contribution to the interfacial heat transfer is obvious for heneicosane in the liquid and in all solids under both heating modes. In contrast to this, a considerable amount of the heat (up to 55%) is transferred by graphene in-plane vibrational modes for a few cases, which can be attributed to the defects in graphene. Our work suggests a potential way, that is, by introducing defects, to improve the interfacial heat transfer in nanocomposites. Note that the interfacial thermal conductance obtained under the heat-matrix mode, which is 1 or 2 orders of magnitude larger than the value evaluated under the heat graphene-mode, is to be utilized for calculating the effective thermal conductivity of the graphene-based alkane nanocomposites from the effective medium theory.⁵⁵ Moreover, we anticipate that the study of heat transfer in systems where the heat is injected into the solid nanoparticles finds application in thermal therapy methods.^{63,64}

■ ASSOCIATED CONTENT

Supporting Information

The Supporting Information is available free of charge at <https://pubs.acs.org/doi/10.1021/acs.jpcc.1c04676>.

Force field parameters for *n*-heneicosane and graphene (Tables S1 and S2); size and energy parameters for CH₂ and CH₃ units in the heneicosane molecule and carbon atoms in the graphene monolayer; additional information on system and simulation procedures; illustration of heating modes (Figure S1); NEMD simulation setups (Figure S2); illustration of a single liquid heneicosane molecule going through the MV defective single-layer graphene (Figure S3); VDOS profiles and overlap factors for perpendicular-aligned, parallel-aligned, and disordered solid systems (Figures S4–S9), in-plane and out-of-plane spectrally resolved heat flux and VDOS formulas;

illustration of monolayer graphene with different types of concentrated defects and the in-plane VDOS of a graphene with defects embedded in liquid heneicosane (Figure S10); directionally resolved normalized cumulative spectral heat flux at the interface between pristine graphene and heneicosane (Figures S11–S14) (PDF)

■ AUTHOR INFORMATION

Corresponding Authors

Hari Krishna Chilukoti – Technische Universität Darmstadt, Eduard-Zintl-Institut für Anorganische und Physikalische Chemie, 64287 Darmstadt, Germany; Department of Mechanical Engineering, National Institute of Technology Warangal, 506004 Warangal, Telangana, India; orcid.org/0000-0002-7882-0805; Email: chk@nitw.ac.in
Tianhang Zhou – Technische Universität Darmstadt, Eduard-Zintl-Institut für Anorganische und Physikalische Chemie, 64287 Darmstadt, Germany; Email: t.zhou@theo.chemie.tu-darmstadt.de

Authors

Zhenghao Wu – Technische Universität Darmstadt, Eduard-Zintl-Institut für Anorganische und Physikalische Chemie, 64287 Darmstadt, Germany; orcid.org/0000-0003-2862-4432
Florian Müller-Plathe – Technische Universität Darmstadt, Eduard-Zintl-Institut für Anorganische und Physikalische Chemie, 64287 Darmstadt, Germany; orcid.org/0000-0002-9111-7786

Complete contact information is available at: <https://pubs.acs.org/10.1021/acs.jpcc.1c04676>

Notes

The authors declare no competing financial interest.

■ ACKNOWLEDGMENTS

We kindly acknowledge the financial support by the Deutsche Forschungsgemeinschaft (DFG, German Research Foundation)—Project SFB-TRR 75, Project number 84292822. H.K.C. also grateful for financial support from the NIT Warangal, India through the research seed grant (P1086-RSM).

■ REFERENCES

- (1) Wang, Y.; Tang, B.; Zhang, S. Single-Walled Carbon Nanotube/Phase Change Material Composites: Sunlight-Driven, Reversible, Form-Stable Phase Transitions for Solar Thermal Energy Storage. *Adv. Funct. Mater.* **2013**, *23* (35), 4354–4360.
- (2) Kandasamy, R.; Wang, X. Q.; Mujumdar, A. S. Transient Cooling of Electronics Using Phase Change Material (PCM)-Based Heat Sinks. *Appl. Therm. Eng.* **2008**, *28* (8–9), 1047–1057.
- (3) Shon, J.; Kim, H.; Lee, K. Improved Heat Storage Rate for an Automobile Coolant Waste Heat Recovery System Using Phase-Change Material in a Fin-Tube Heat Exchanger. *Appl. Energy* **2014**, *113*, 680–689.
- (4) Yuan, Y.; Zhang, N.; Tao, W.; Cao, X.; He, Y. Fatty Acids as Phase Change Materials: A Review. *Renewable Sustainable Energy Rev.* **2014**, *29*, 482–498.
- (5) Harish, S.; Orejon, D.; Takata, Y.; Kohno, M. Thermal Conductivity Enhancement of Lauric Acid Phase Change Nanocomposite with Graphene Nanoplatelets. *Appl. Therm. Eng.* **2015**, *80*, 205–211.
- (6) Liang, Q.; Yao, X.; Wang, W.; Liu, Y.; Wong, C. P. A Three-Dimensional Vertically Aligned Functionalized Multilayer Graphene

Architecture: An Approach for Graphene-Based Thermal Interfacial Materials. *ACS Nano* **2011**, *5* (3), 2392–2401.

(7) Veca, L. M.; Mezziani, M. J.; Wang, W.; Wang, X.; Lu, F.; Zhang, P.; Lin, Y.; Fee, R.; Connell, J. W.; Sun, Y.-P. Carbon Nanosheets for Polymeric Nanocomposites with High Thermal Conductivity. *Adv. Mater.* **2009**, *21* (20), 2088–2092.

(8) Sun, X.; Ramesh, P.; Itkis, M. E.; Bekyarova, E.; Haddon, R. C. Dependence of the Thermal Conductivity of Two-Dimensional Graphite Nanoplatelet-Based Composites on the Nanoparticle Size Distribution. *J. Phys.: Condens. Matter* **2010**, *22* (33), 334216.

(9) Shahil, K. M. F.; Balandin, A. A. Graphene-Multilayer Graphene Nanocomposites as Highly Efficient Thermal Interface Materials. *Nano Lett.* **2012**, *12* (2), 861–867.

(10) Yu, W.; Xie, H.; Wang, X.; Wang, X. Significant Thermal Conductivity Enhancement for Nanofluids Containing Graphene Nanosheets. *Phys. Lett. A* **2011**, *375* (10), 1323–1328.

(11) Nan, C. W.; Birringer, R.; Clarke, D. R.; Gleiter, H. Effective Thermal Conductivity of Particulate Composites with Interfacial Thermal Resistance. *J. Appl. Phys.* **1997**, *81* (10), 6692–6699.

(12) Hasan, M. R.; Vo, T. Q.; Kim, B. Manipulating Thermal Resistance at the Solid-Fluid Interface through Monolayer Deposition. *RSC Adv.* **2019**, *9* (9), 4948–4956.

(13) Liang, Z.; Tsai, H.-L. Reduction of Solid-Solid Thermal Boundary Resistance by Inserting an Interlayer. *Int. J. Heat Mass Transfer* **2012**, *55* (11), 2999–3007.

(14) Li, M.; Zhou, H.; Zhang, Y.; Liao, Y.; Zhou, H. Effect of Defects on Thermal Conductivity of Graphene/Epoxy Nanocomposites. *Carbon* **2018**, *130*, 295–303.

(15) Clancy, T. C.; Frankland, S. J.V.; Hinkley, J. A.; Gates, T. S. Multiscale Modeling of Thermal Conductivity of Polymer/Carbon Nanocomposites. *Int. J. Therm. Sci.* **2010**, *49* (9), 1555–1560.

(16) Wang, Y.; Zhan, H. F.; Xiang, Y.; Yang, C.; Wang, C. M.; Zhang, Y. Y. Effect of Covalent Functionalization on Thermal Transport across Graphene-Polymer Interfaces. *J. Phys. Chem. C* **2015**, *119* (22), 12731–12738.

(17) Gao, Y.; Müller-Plathe, F. Increasing the Thermal Conductivity of Graphene-Polyamide-6,6 Nanocomposites by Surface-Grafted Polymer Chains: Calculation with Molecular Dynamics and Effective-Medium Approximation. *J. Phys. Chem. B* **2016**, *120* (7), 1336–1346.

(18) Gao, Y.; Müller-Plathe, F. Effect of Grafted Chains on the Heat Transfer between Carbon Nanotubes in a Polyamide-6.6 Matrix: A Molecular Dynamics Study. *Polymer* **2017**, *129*, 228–234.

(19) Wang, M.; Hu, N.; Zhou, L.; Yan, C. Enhanced Interfacial Thermal Transport across Graphene-Polymer Interfaces by Grafting Polymer Chains. *Carbon* **2015**, *85*, 414–421.

(20) Wang, Y.; Keblinski, P. Effect of Interfacial Interactions and Nanoscale Confinement on Octane Melting. *J. Appl. Phys.* **2012**, *111* (6), 064321.

(21) Rastgarkafshgarkolaei, R.; Zeng, Y.; Khodadadi, J. M. A Molecular Dynamics Study of the Effect of Thermal Boundary Conductance on Thermal Transport of Ideal Crystal of N-Alkanes with Different Number of Carbon Atoms. *J. Appl. Phys.* **2016**, *119* (20), 205107.

(22) Babaei, H.; Keblinski, P.; Khodadadi, J. M. Thermal Conductivity Enhancement of Paraffins by Increasing the Alignment of Molecules through Adding CNT/Graphene. *Int. J. Heat Mass Transfer* **2013**, *58* (1–2), 209–216.

(23) Chilukoti, H. K.; Zhou, T.; Ardham, V. R.; Böhm, M. C.; Müller-Plathe, F. Thermal Energy Transport across the Interface between Phase Change Material N-Heneicosane in Solid and Liquid Phases and Few-Layer Graphene. *J. Phys. Chem. C* **2019**, *123* (48), 29192–29202.

(24) Chilukoti, H. K.; Kikugawa, G.; Shibahara, M.; Ohara, T. Local Thermal Transport of Liquid Alkanes in the Vicinity of α -Quartz Solid Surfaces and Thermal Resistance over the Interfaces: A Molecular Dynamics Study. *Phys. Rev. E* **2015**, *91* (5), 52404.

(25) Giri, A.; Braun, J. L.; Hopkins, P. E. Implications of Interfacial Bond Strength on the Spectral Contributions to Thermal Boundary

Conductance across Solid, Liquid, and Gas Interfaces: A Molecular Dynamics Study. *J. Phys. Chem. C* **2016**, *120* (43), 24847–24856.

(26) Ramos-Alvarado, B.; Kumar, S.; Peterson, G. P. Solid-Liquid Thermal Transport and Its Relationship with Wettability and the Interfacial Liquid Structure. *J. Phys. Chem. Lett.* **2016**, *7* (17), 3497–3501.

(27) Ardham, V. R.; Leroy, F. Communication: Is a Coarse-Grained Model for Water Sufficient to Compute Kapitza Conductance on Non-Polar Surfaces? *J. Chem. Phys.* **2017**, *147* (15), 151102.

(28) Liu, Y.; Hu, C.; Huang, J.; Sumpster, B. G.; Qiao, R. Tuning Interfacial Thermal Conductance of Graphene Embedded in Soft Materials by Vacancy Defects. *J. Chem. Phys.* **2015**, *142* (24), 244703.

(29) Gonzalez-Valle, C. U.; Paniagua-Guerra, L. E.; Ramos-Alvarado, B. Implications of the Interface Modeling Approach on the Heat Transfer across Graphite-Water Interfaces. *J. Phys. Chem. C* **2019**, *123* (36), 22311–22323.

(30) Wang, Y.; Yang, C.; Cheng, Y.; Zhang, Y. A Molecular Dynamics Study on Thermal and Mechanical Properties of Graphene-Paraffin Nanocomposites. *RSC Adv.* **2015**, *5* (101), 82638–82644.

(31) Verma, A.; Kumar, R.; Parashar, A. Enhanced Thermal Transport across a Bi-Crystalline Graphene-Polymer Interface: An Atomistic Approach. *Phys. Chem. Chem. Phys.* **2019**, *21* (11), 6229–6237.

(32) Rajasekaran, G.; Narayanan, P.; Parashar, A. Effect of Point and Line Defects on Mechanical and Thermal Properties of Graphene: A Review. *Crit. Rev. Solid State Mater. Sci.* **2016**, *41* (1), 47–71.

(33) Novoselov, K. S.; Geim, A. K.; Morozov, S. V.; Jiang, D.; Zhang, Y.; Dubonos, S. V.; Grigorieva, I. V.; Firsov, A. A. Electric Field Effect in Atomically Thin Carbon Films. *Science* **2004**, *306* (5696), 666–669.

(34) Stone, A. J.; Wales, D. J. Theoretical Studies of Icosahedral C₆₀ and Some Related Species. *Chem. Phys. Lett.* **1986**, *128* (5), 501–503.

(35) Banhart, F.; Kotakoski, J.; Krasheninnikov, A. V. Structural Defects in Graphene. *ACS Nano* **2011**, *5* (1), 26–41.

(36) Ci, L.; Song, L.; Jin, C.; Jariwala, D.; Wu, D.; Li, Y.; Srivastava, A.; Wang, Z. F.; Storr, K.; Balicas, L.; Liu, F.; Ajayan, P. M. Atomic Layers of Hybridized Boron Nitride and Graphene Domains. *Nat. Mater.* **2010**, *9* (5), 430–435.

(37) Cretu, O.; Krasheninnikov, A. V.; Rodríguez-Manzo, J. A.; Sun, L.; Nieminen, R. M.; Banhart, F. Migration and Localization of Metal Atoms on Strained Graphene. *Phys. Rev. Lett.* **2010**, *105* (19), 196102.

(38) Chen, S.; Wu, Q.; Mishra, C.; Kang, J.; Zhang, H.; Cho, K.; Cai, W.; Balandin, A. A.; Ruoff, R. S. Thermal Conductivity of Isotopically Modified Graphene. *Nat. Mater.* **2012**, *11* (3), 203–207.

(39) Loh, G. C.; Teo, E. H. T.; Tay, B. K. Compounded Effect of Vacancy on Interfacial Thermal Transport in Diamond-Graphene Nanostructures. *Diamond Relat. Mater.* **2011**, *20* (8), 1137–1142.

(40) Fthenakis, Z. G.; Zhu, Z.; Tománek, D. Effect of Structural Defects on the Thermal Conductivity of Graphene: From Point to Line Defects to Haekelites. *Phys. Rev. B: Condens. Matter Mater. Phys.* **2014**, *89* (12), 125421.

(41) Li, M.; Zhou, H.; Zhang, Y.; Liao, Y.; Zhou, H. Effect of Defects on Thermal Conductivity of Graphene/Epoxy Nanocomposites. *Carbon* **2018**, *130*, 295–303.

(42) Namsani, S.; Singh, J. K. Enhancement of Thermal Energy Transport across the Gold-Graphene Interface Using Nanoscale Defects: A Molecular Dynamics Study. *J. Phys. Chem. C* **2018**, *122* (4), 2113–2121.

(43) Haynes, W. M., Ed. *CRC Handbook of Chemistry and Physics: A Ready-Reference Book of Chemical and Physical Data*; CRC Press: Boca Raton, FL, 2016.

(44) Chilukoti, H. K.; Müller-Plathe, F.; Yang, H. Application of Reverse Nonequilibrium Molecular Dynamics to the Calculation of the Mutual Diffusion Coefficient of Alkane Mixtures. *J. Phys. Chem. B* **2018**, *122* (39), 9210–9217.

(45) Nath, S. K.; Escobedo, F. A.; De Pablo, J. J. On the Simulation of Vapor-Liquid Equilibria for Alkanes. *J. Chem. Phys.* **1998**, *108* (23), 9905–9911.

(46) Lindsay, L.; Broido, D. A. Optimized Tersoff and Brenner Empirical Potential Parameters for Lattice Dynamics and Phonon

Thermal Transport in Carbon Nanotubes and Graphene. *Phys. Rev. B: Condens. Matter Mater. Phys.* **2010**, *81* (20), 205441.

(47) Plimpton, S. Fast Parallel Algorithms for Short-Range Molecular Dynamics. *J. Comput. Phys.* **1995**, *117* (1), 1–19.

(48) Jouti, B.; Petitjean, D.; Provost, E.; Bouroukba, M.; Dirand, M. Structural Evolutions of the N-Heneicosane and n-Tricosane Molecular Alloys at 293 K. *J. Mol. Struct.* **1995**, *356* (3), 191–199.

(49) Brooks, C. L. Computer Simulation of Liquids. *J. Solution Chem.* **1989**, *18* (1), 99.

(50) Lan, J.; Li, B. Thermal Rectifying Effect in Two-Dimensional Anharmonic Lattices. *Phys. Rev. B: Condens. Matter Mater. Phys.* **2006**, *74* (21), 214305.

(51) Säskilähti, K.; Oksanen, J.; Tulkki, J.; Volz, S. Spectral Mapping of Heat Transfer Mechanisms at Liquid-Solid Interfaces. *Phys. Rev. E: Stat. Phys., Plasmas, Fluids, Relat. Interdiscip. Top.* **2016**, *93* (5), 1–8.

(52) Pham, A. T.; Barisik, M.; Kim, B. Interfacial Thermal Resistance between the Graphene-Coated Copper and Liquid Water. *Int. J. Heat Mass Transfer* **2016**, *97*, 422–431.

(53) Pham, A.; Barisik, M.; Kim, B. Pressure Dependence of Kapitza Resistance at Gold/Water and Silicon/Water Interfaces. *J. Chem. Phys.* **2013**, *139* (24), 244702.

(54) Masduzzaman, M.; Kim, B. Scale Effects in Nanoscale Heat Transfer for Fourier's Law in a Dissimilar Molecular Interface. *ACS Omega* **2020**, *5* (41), 26527–26536.

(55) Hu, L.; Desai, T.; Keblinski, P. Determination of Interfacial Thermal Resistance at the Nanoscale. *Phys. Rev. B: Condens. Matter Mater. Phys.* **2011**, *83* (19), 1–5.

(56) Liu, Y.; Huang, J.; Yang, B.; Sumpster, B. G.; Qiao, R. Duality of the Interfacial Thermal Conductance in Graphene-Based Nanocomposites. *Carbon* **2014**, *75*, 169–177.

(57) Gonzalez-Valle, C. U.; Ramos-Alvarado, B. Spectral Mapping of Thermal Transport across SiC-Water Interfaces. *Int. J. Heat Mass Transfer* **2019**, *131*, 645–653.

(58) Kim, B. H.; Beskok, A.; Cagin, T. Molecular Dynamics Simulations of Thermal Resistance at the Liquid-Solid Interface. *J. Chem. Phys.* **2008**, *129* (17), 174701.

(59) Konatham, D.; Striolo, A. Thermal Boundary Resistance at the Graphene-Oil Interface. *Appl. Phys. Lett.* **2009**, *95* (16), 163105.

(60) Wang, X.; Zhang, J.; Chen, Y.; Chan, P. K. L. Investigation of Interfacial Thermal Transport across Graphene and an Organic Semiconductor Using Molecular Dynamics Simulations. *Phys. Chem. Chem. Phys.* **2017**, *19* (24), 15933–15941.

(61) Hong, Y.; Zhang, J.; Zeng, X. C. Interlayer Thermal Conductance within a Phosphorene and Graphene Bilayer. *Nanoscale* **2016**, *8* (46), 19211–19218.

(62) Han, H.; Mérabia, S.; Müller-Plathe, F. Thermal Transport at Solid-Liquid Interfaces: High Pressure Facilitates Heat Flow through Nonlocal Liquid Structuring. *J. Phys. Chem. Lett.* **2017**, *8* (9), 1946–1951.

(63) Tascini, A. S.; Armstrong, J.; Chiavazzo, E.; Fasano, M.; Asinari, P.; Bresme, F. Thermal Transport across Nanoparticle-Fluid Interfaces: The Interplay of Interfacial Curvature and Nanoparticle-Fluid Interactions. *Phys. Chem. Chem. Phys.* **2017**, *19* (4), 3244–3253.

(64) Ho, D., Ed. *Nanodiamonds: Applications in Biology and Nanoscale Medicine*; Springer: New York, 2010; pp 1–286.

Supporting information

Effect of Defects on the Interfacial Thermal Conductance between *n*-Heneicosane in Solid and Liquid Phases and a Graphene Monolayer

Tianhang Zhou^{1,*}, *Hari Krishna Chilukoti*^{1,2,*}, *Zhenghao Wu*¹ and *Florian Müller-Plathe*¹

¹ Technische Universität Darmstadt, Eduard-Zintl-Institut für Anorganische und Physikalische Chemie, 64287 Darmstadt, Germany.

² Department of Mechanical Engineering, National Institute of Technology Warangal, 506004, Warangal, Telangana, India

*All correspondence should be addressed to

E-mail: chk@nitw.ac.in (H.K. Chilukoti), t.zhou@theo.chemie.tu-darmstadt.de (T. Zhou)

I. Force field parameters

Table S1. The NERD potential parameters for *n*-heneicosane⁴⁸.

	Potential form	Parameters
Bond stretching potential	$\frac{V(r)}{k_B} = \frac{k_r}{2}(r - b_{eq})^2$	$k_r = 96500 \text{ K/\AA}^2$ $b_{eq} = 1.54 \text{ \AA}$
Bond bending potential	$\frac{V(\theta)}{k_B} = \frac{k_\theta}{2}(\theta - \theta_{eq})^2$	$k_\theta = 62500 \text{ K/rad}^2$ $\theta_{eq} = 114.0^\circ$
Torsion potential	$\frac{V(\phi)}{k_B} = V_0 + V_1(1 + \cos \phi) + V_2(1 - \cos 2\phi) + V_3(1 + \cos 3\phi)$	$V_0 = 0 \text{ K}, V_1 = 355.04 \text{ K}, V_2 = -68.19 \text{ K}, V_3 = 701.32 \text{ K}$

Table S2. Optimized Tersoff potential parameters for graphene⁴⁹

$A = 1393.6 \text{ eV}$	$B = 430.0 \text{ eV}$
$\lambda_1 = 3.4879 \text{ \AA}^{-1}$	$\lambda_2 = 2.2119 \text{ \AA}^{-1}$
$\lambda_3 = 0.0000 \text{ \AA}^{-1}$	$n = 0.72751$
$c = 38049.0$	$\beta = 1.5724 \times 10^{-7}$
$d = 4.3484$	$h = -0.930$
$R = 1.95 \text{ \AA}$	$D = 0.15 \text{ \AA}$

The potential considers bond stretching, bond bending and torsional motion for intramolecular interactions. The Lennard-Jones (LJ) potential is used to treat the intermolecular interaction between united atoms

$$V(r) = 4\epsilon \left[\left(\frac{r}{\sigma} \right)^{12} - \left(\frac{r}{\sigma} \right)^6 \right] \quad (\text{S1})$$

where the distance between two united atoms is given by r . The size and energy parameters for CH₂ and CH₃ units are $\sigma_{\text{CH}_2} = 0.393$ and $\sigma_{\text{CH}_3} = 0.391$ nm and $\epsilon_{\text{CH}_2}/k_B = 45.8$ K and $\epsilon_{\text{CH}_3}/k_B = 104$ K, respectively. An all-atom model is used to represent graphene and the interactions among carbon atoms is considered using the optimized Tersoff potential⁴⁷ (Table S2, Supporting information). The LJ potential is utilized to treat the interaction between graphene and heneicosane atoms. The energy and size parameters for carbon atoms are $\epsilon_C/k_B = 27.7$ K and $\sigma_C = 0.383$ nm.⁴⁸ The LJ parameters between unlike atoms is obtained by using the Lorentz-Berthelot mixing rules

$$\epsilon_{ij} = \sqrt{\epsilon_{ii}\epsilon_{jj}} \quad \text{and} \quad \sigma_{ij} = \frac{\sigma_{ii} + \sigma_{jj}}{2} \quad (\text{S2})$$

II. Detail information of systems

The parallel-aligned systems have a cross section of $L_x \times L_y = 5.27 \times 5.62$ nm² and the non-defective graphene layer has 1092 carbon atoms. The cross section of perpendicular-aligned systems is $L_x \times L_y = 5.22 \times 5.87$ nm² and the non-defective graphene is composed of 1176 carbons. The lengths of systems along x -axis are in the range of 5.19 to 5.31 nm and along y -axis are in the range 5.58 to 5.90 nm for disordered solid and liquid systems. These lengths are sensitive to the original sizes of the parent system, which they are fabricated. The lengths of crystal systems along the x - and y - axis are chosen in such a manner that the lowest lattice mismatch occurs between graphene and the perfect heneicosane crystal. The lengths of systems along the z axis are in the range of 15.1 to 22.1 nm depending on the phase

and structure of heneicosane.

III. Simulations

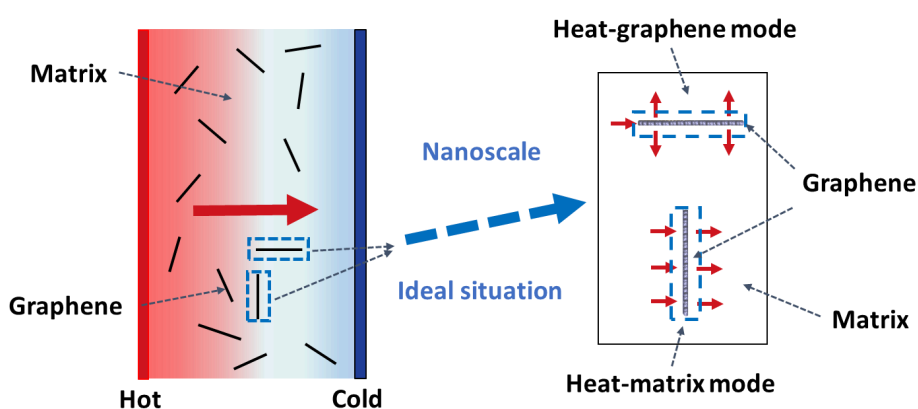


Figure S1. Schematic illustration of two modes of heat transport in nanocomposites dispersed with graphene viz., heat-matrix mode and heat-graphene mode. The heat transfer direction is indicated by red arrows.

To simulate the heat-matrix mode, a constant amount of energy per time is added into the source region and subtracted from the sink region, which are positioned in side heneicosane at the end of the system (Figure. 3). In this manner a heat flux with constant magnitude is introduced in the system along z-direction. The simulations conducted in this way are referred to as “heat-matrix mode”. To mimic the heat-graphene mode, a constant amount of energy per time is added to the graphene and a half of that magnitude is subtracted from each of two sink regions, which are situated at the two ends of the simulation system in heneicosane. This case is hereafter named as “heat-graphene mode”. The width of the source and sink regions in the matrix is 5 Å.

Additionally, the heneicosane atoms in two regions, which are beyond the heat source and sink regions, having a width of 7 Å on two ends of the system are frozen (Figure. 3). This procedure guarantees that all heat had to pass through the graphene. Furthermore, the simulation system length along z -axis has been elongated by 10 nm of vacuum, which efficiently isolates periodic images of the particles from each of them. In NEMD simulations, under the heat-matrix mode, a temperature gradient is introduced in the system by keeping the source region at $T + \Delta T$ and the sink region at $T - \Delta T$, where T is the system equilibrium temperature. The temperature of the graphene is maintained at T and both heat sink regions are kept at $T - \Delta T$ under the heat-graphene mode. A ΔT of 50 and 25 K is used in all heat-matrix and heat-graphene simulations, respectively.

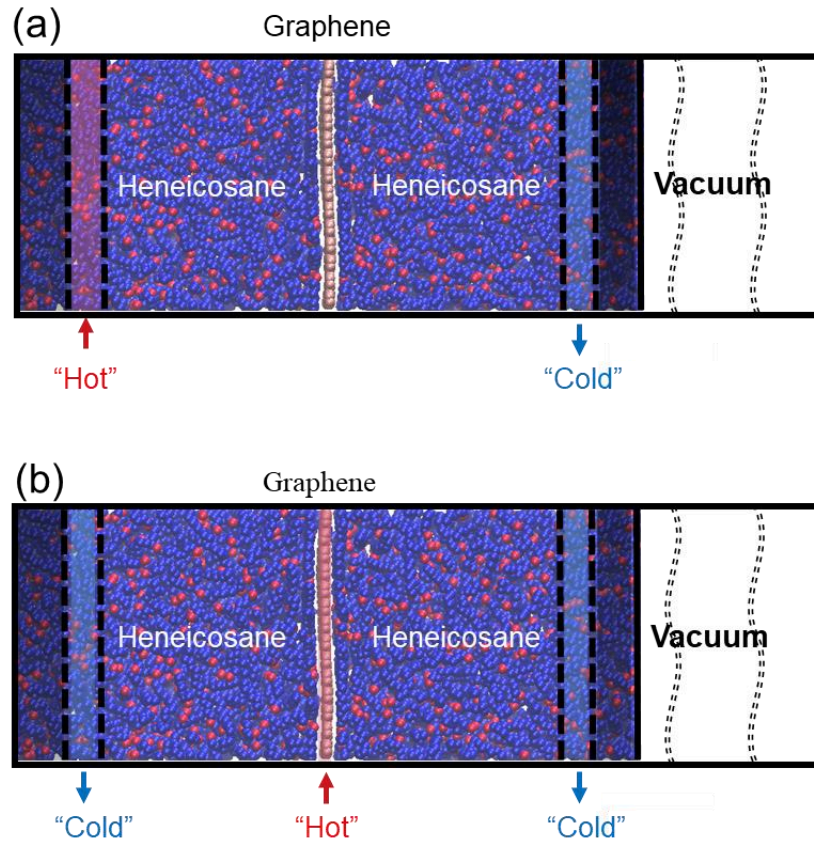


Figure S2. Snapshots of 9.0 % SV defective monolayer graphene-liquid heneicosane system under (a) heat-matrix mode and (b) heat-graphene mode. Heat source and heat sink region are labeled as "hot" and "cold", respectively. The NEMD simulations have been performed for both modes.

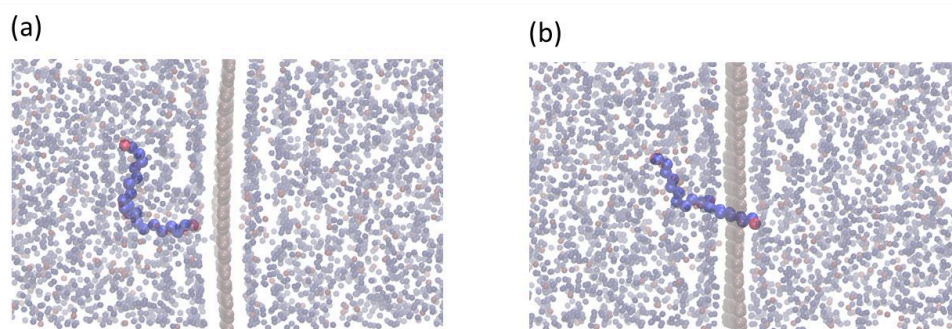


Figure S3. Snapshots illustrating the process of a single liquid heneicosane molecule moving through a MV defective in the monolayer graphene: (a) before crossing and (b) during crossing. The crossing heneicosane molecule is shown with larger beads for clarity. The CH_3 and CH_2 units of heneicosane molecules are shown in the red and blue color, respectively.

IV. VDOS profiles and overlap factor

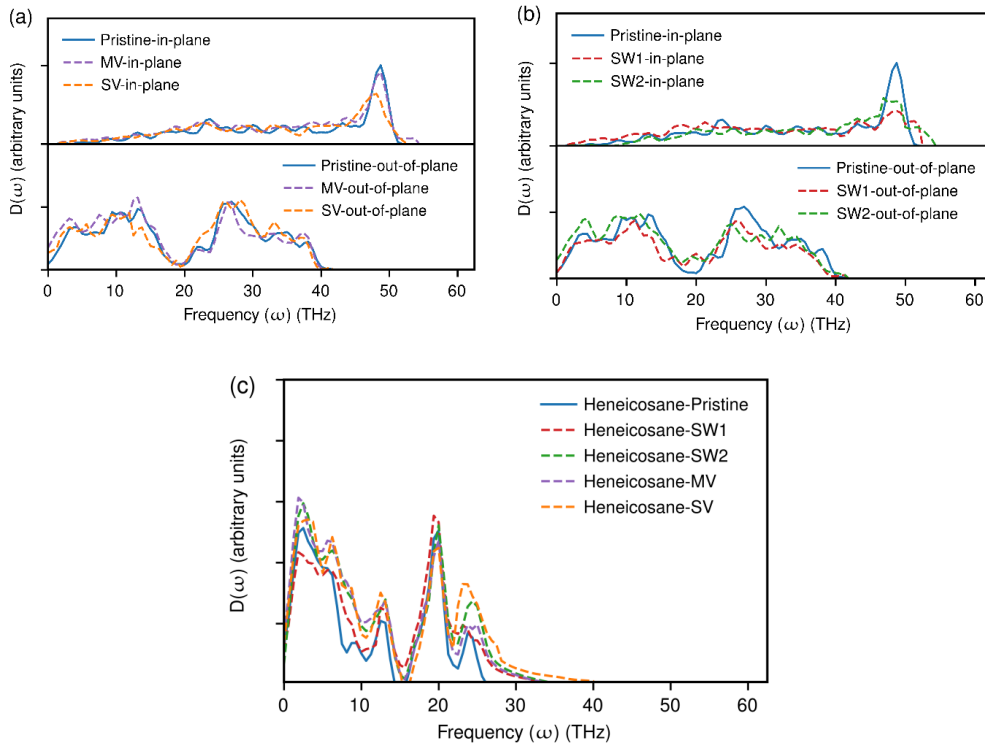


Figure S4. For parallel-aligned heneicosane crystal system at 250 K and 1 atm (a) VDOS profiles in arbitrary units along in-plane and out-of-plane directions for pristine graphene and graphene with 9.0 % SV and MV defects (b) VDOS profiles along in-plane and out-of-plane direction for graphene with 9.0 % SW1 and SW2 defects (c) overall VDOS for heneicosane molecules in the first adsorption layer

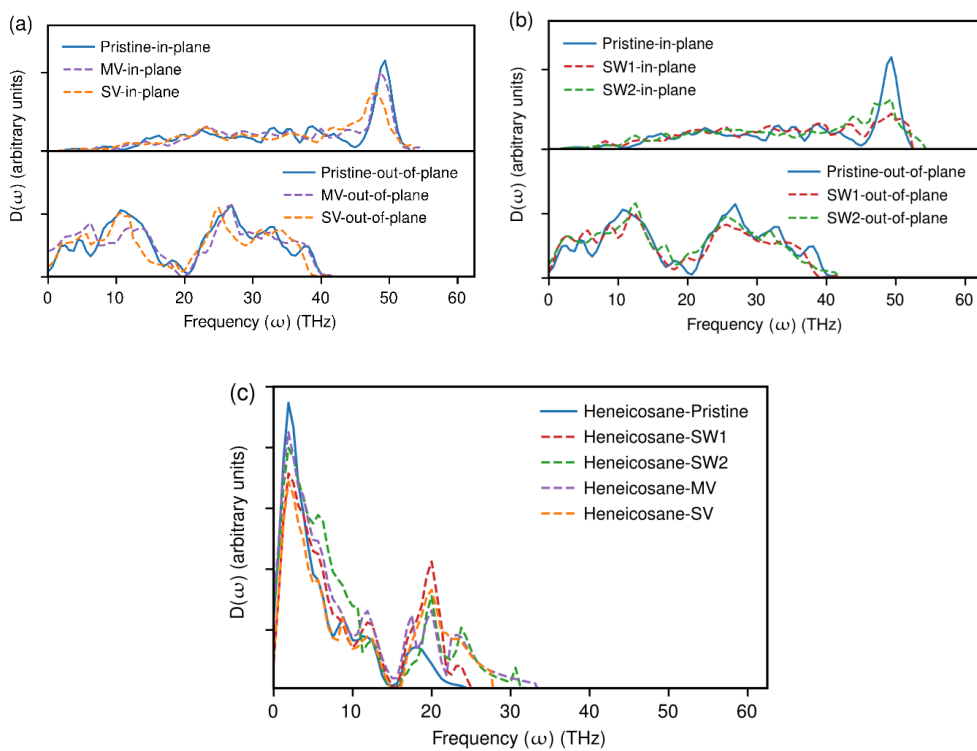


Figure S5. For perpendicular-aligned heneicosane crystal system at 250 K and 1 atm (a) VDOS profiles in arbitrary units along in-plane and out-of-plane directions for pristine graphene and graphene with 9.0 % SV and MV defects (b) VDOS profiles along in-plane and out-of-plane direction for graphene with 9.0 % SW1 and SW2 defects (c) overall VDOS for heneicosane molecules in the first adsorption layer

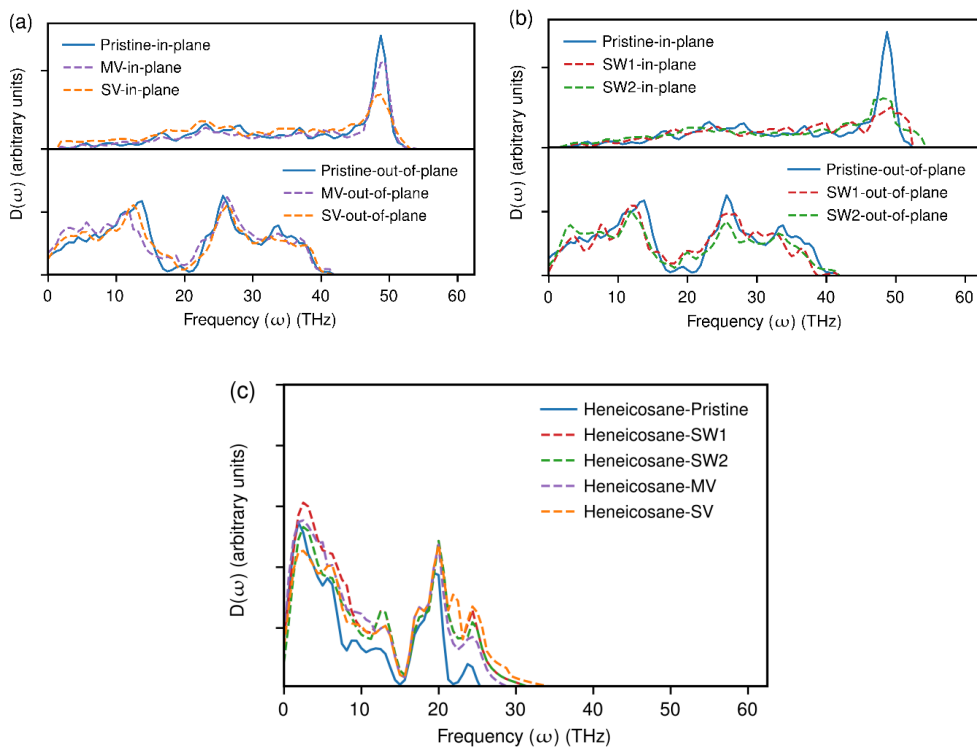


Figure S6. For disordered solid heneicosane system at 250 K and 1 atm (a) VDOS profiles in arbitrary units along in-plane and out-of-plane directions for pristine graphene and graphene with 9.0 % SV and MV defects (b) VDOS profiles along in-plane and out-of-plane direction for graphene with 9.0 % SW1 and SW2 defects (c) overall VDOS for heneicosane molecules in the first adsorption layer

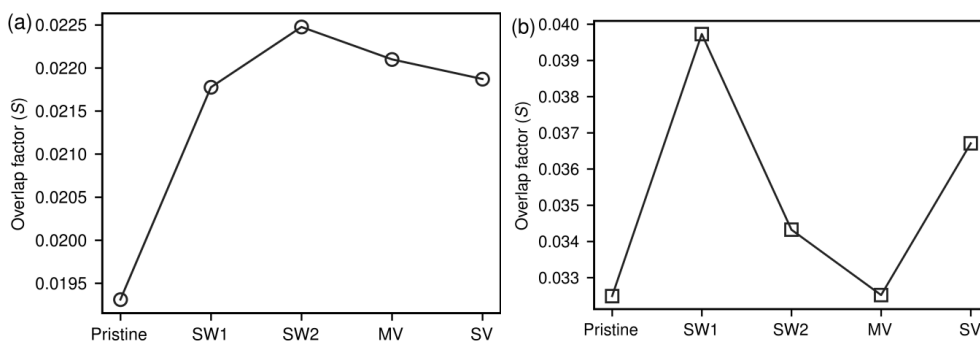


Figure S7. The overlap factor for parallel-aligned heneicosane crystal systems under heat-matrix mode at 250 K and 1 atm (a) between the total VDOS of heneicosane and out-of-plane VDOS of pristine and 9.0 % defective graphene (b) between the in-plane and out-of-plane VDOS of pristine and 9.0 % defective graphene.

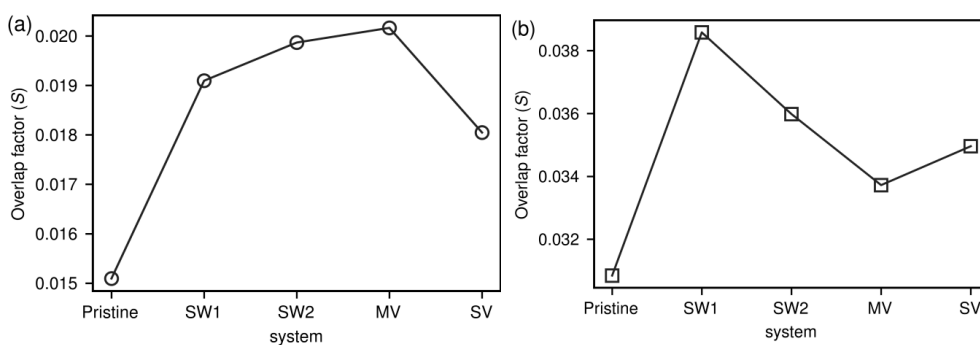


Figure S8. The overlap factor for perpendicular-aligned heneicosane crystal systems under heat-matrix mode at 250 K and 1 atm (a) between the total VDOS of heneicosane and out-of-plane VDOS of pristine and 9.0 % defective graphene (b) between the in-plane and out-of-plane VDOS of pristine and 9.0 % defective graphene.

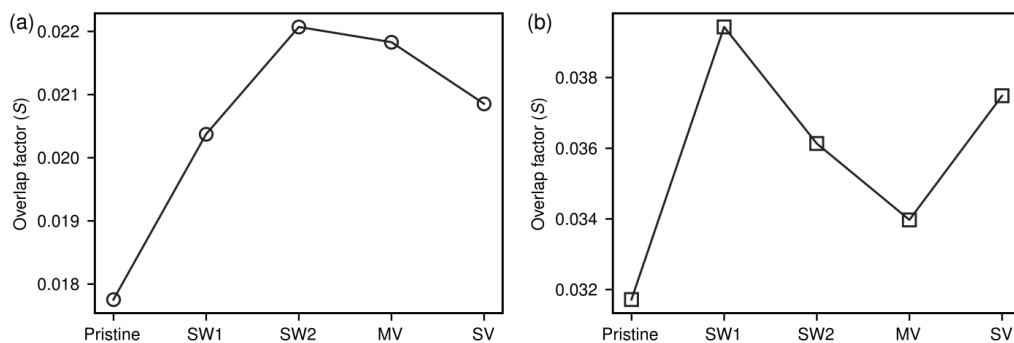


Figure S9. The overlap factor for disordered solid heneicosane systems under heat-matrix mode at 250 K and 1 atm (a) between the total VDOS of heneicosane and out-of-plane VDOS of pristine and 9.0 % defective graphene (b) between the in-plane and out-of-plane VDOS of pristine and 9.0 % defective graphene.

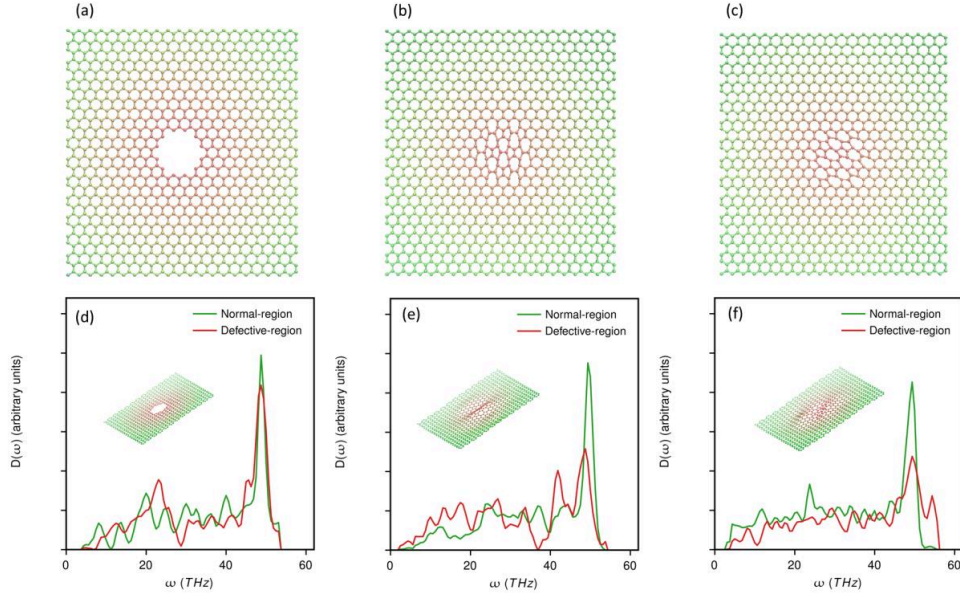


Figure S10. Schematic illustration of monolayer graphene with different types of accumulative defects in the central region at the initial condition (a) MV, (b) SW1, (c) SW2. In-plane VDOS of a graphene with (d) MV, (e) SW1, (f) SW2 defects embedded in liquid heneicosane at 400 K and 1 atm. The inset shows the defective graphene where heneicosane molecules are not shown for clarity.

V. Spectral heat flux and VDOS

It should be noted that the output forces and velocities has three components along Cartesian coordinates. The components along x - and y -axis describe transverse or in-plane mode contributions to total VDOS and total spectral heat flux. The in-plane VDOS and in-plane spectral heat flux are calculated as follows

$$D(\omega)_{\text{in-plane}} = \frac{1}{k_B T} \sum_i m_i \int_{-\infty}^{+\infty} d\tau e^{i\omega\tau} \langle v_{xy,i}(\tau) \cdot v_{xy,i}(0) \rangle \quad (\text{S3})$$

$$q(\omega)_{\text{in-plane}} = \frac{2}{A} \mathbb{R} \sum_{j \in h, i \in g} \int_{-\infty}^{+\infty} d\tau e^{i\omega\tau} \langle F_{xy,ij}(\tau) \cdot v_{xy,i}(0) \rangle \quad (\text{S4})$$

Similarly, the components along z-axis describe longitudinal or out-of-plane mode contributions to total VDOS and total spectral heat flux. The out-of-plane VDOS and out-of-plane spectral heat flux are calculated as follows

$$D(\omega)_{\text{out-of-plane}} = \frac{1}{k_B T} \sum_i m_i \int_{-\infty}^{+\infty} d\tau e^{i\omega\tau} \langle v_{z,i}(\tau) \cdot v_{z,i}(0) \rangle \quad (\text{S5})$$

$$q(\omega)_{\text{out-of-plane}} = \frac{2}{A} \mathbb{R} \sum_{j \in h, i \in g} \int_{-\infty}^{+\infty} d\tau e^{i\omega\tau} \langle F_{z,ij}(\tau) \cdot v_{z,i}(0) \rangle \quad (\text{S6})$$

As expected, the summation of in-plane and out-of-plane spectrally resolved heat flux gives the total spectral heat flux. $q(\omega)_{\text{total}} = q(\omega)_{\text{in-plane}} + q(\omega)_{\text{out-of-plane}}$. Normalized cumulative heat flux is calculated as follows

$$\text{Normalized cumulative } q_i(\omega) = \int_0^\omega \frac{q_i(\omega)}{\int_0^\infty q_{\text{total}}(\omega)} d\omega \quad (\text{S7})$$

where $i = \text{in-plane, out-of-plane, total}$

V. Spectral heat flux plots for pristine graphene

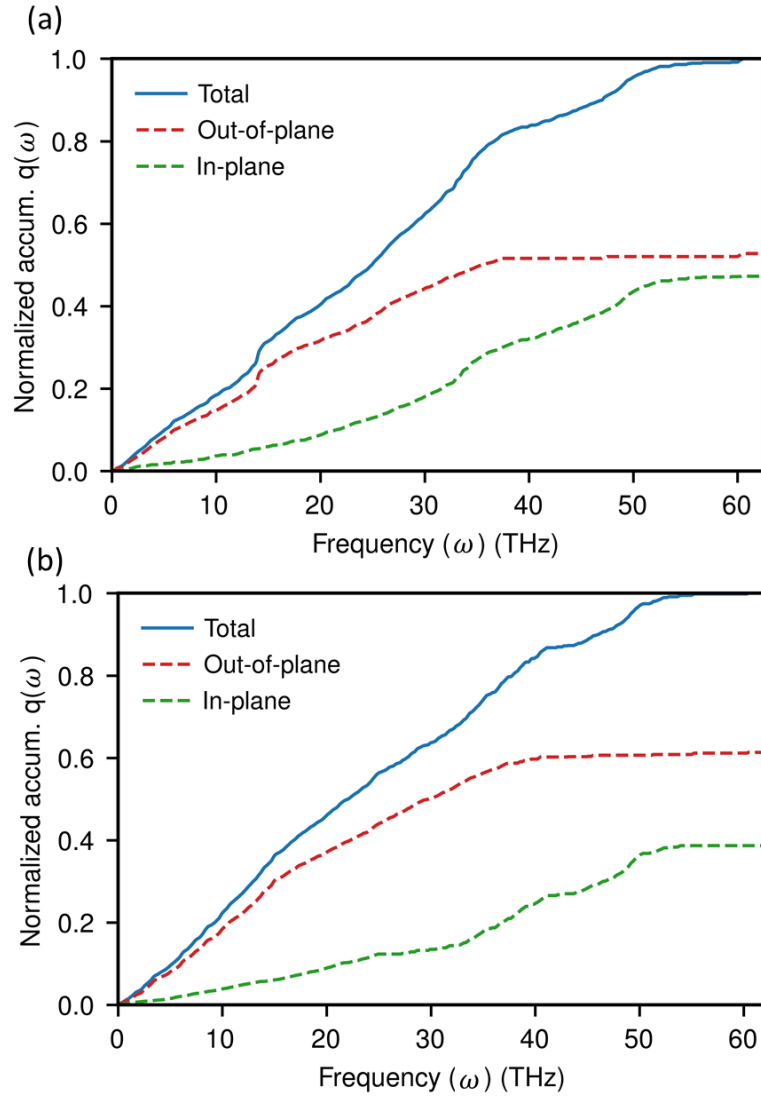


Figure S11. Directional decomposition of the normalized cumulative spectral heat flux at the interface between pristine graphene and parallel-aligned heneicosane crystal when the system is under (a) heat-matrix mode and (b) heat-graphene mode. Here, $q(\omega)$ is calculated from graphene to heneicosane.

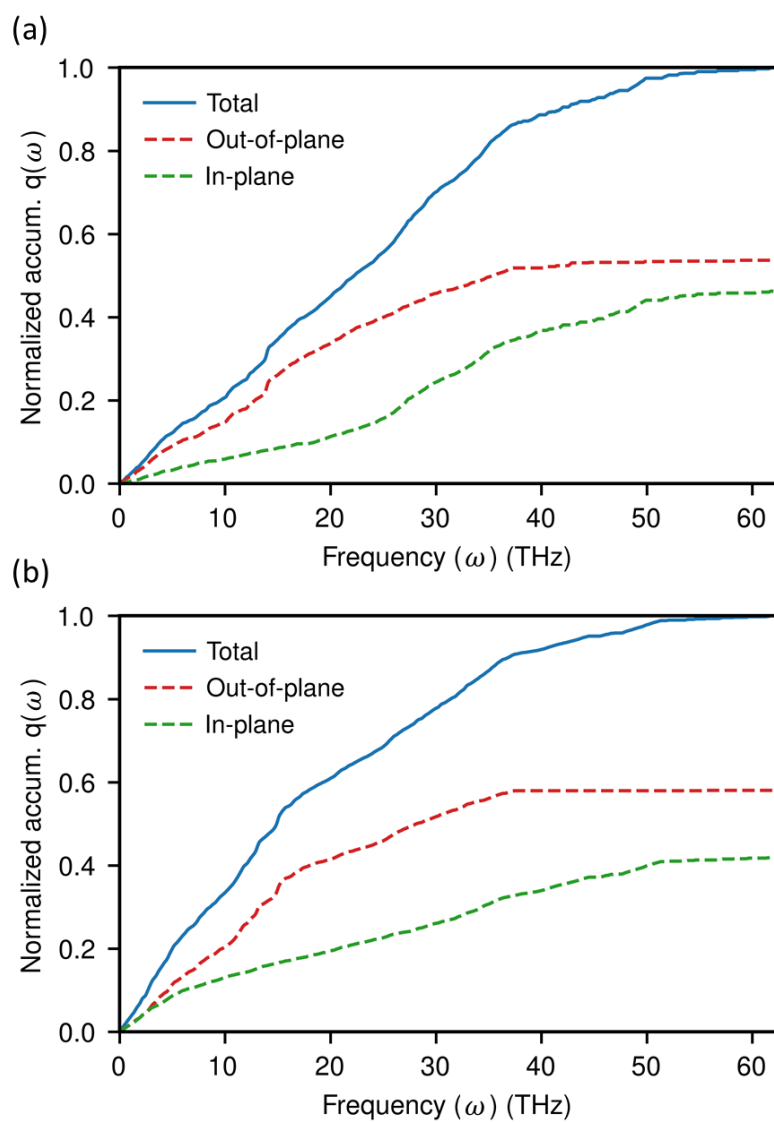


Figure S12. Directional decomposition of the normalized cumulative spectral heat flux at the interface between pristine graphene and disordered solid heneicosane when the the system is under (a) heat-matrix mode and (b) heat-graphene mode. Here, $q(\omega)$ is calculated from graphene to heneicosane.

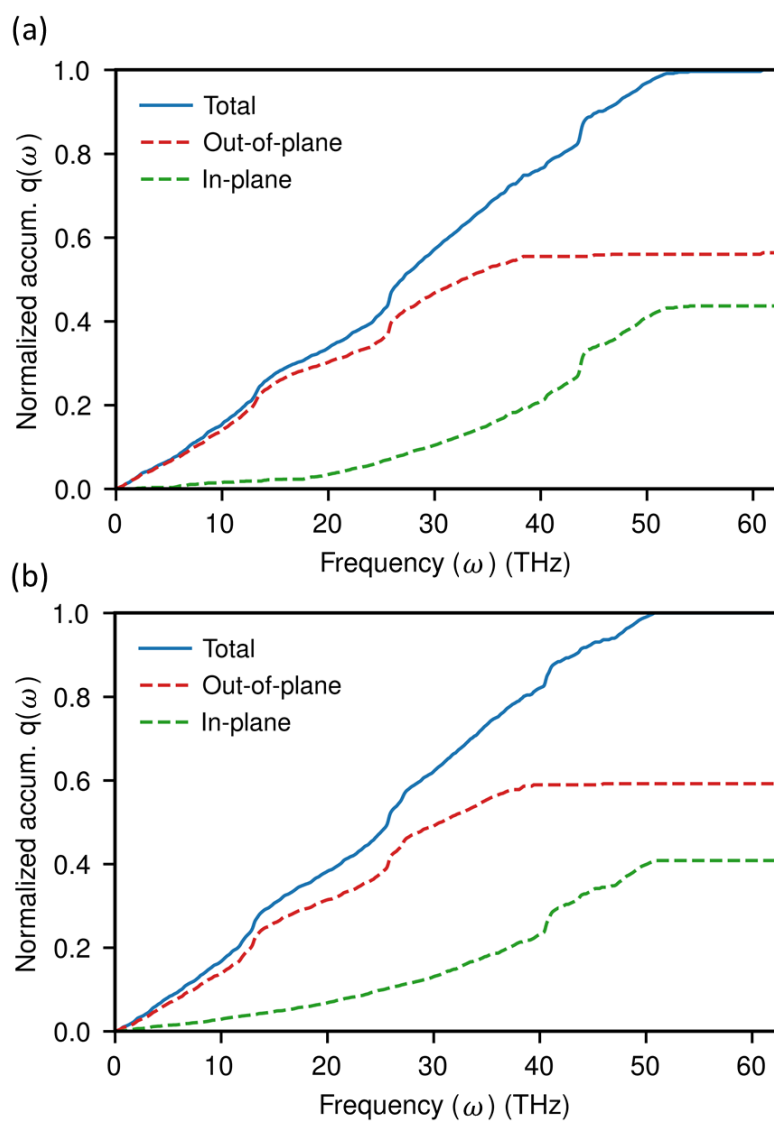


Figure S13. Directional decomposition of the normalized cumulative spectral heat flux at the interface between pristine graphene and perpendicular-aligned heneicosane crystal when the system is under (a) heat-matrix mode and (b) heat-graphene mode. Here, $q(\omega)$ is calculated from graphene to heneicosane.

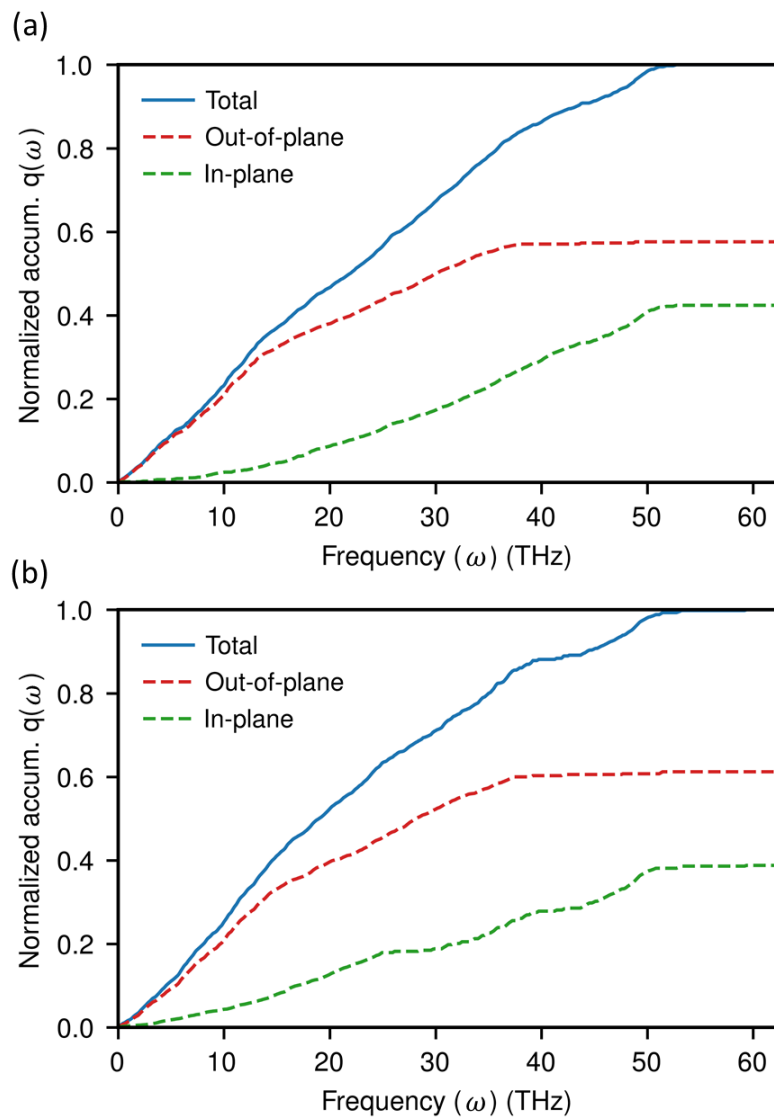


Figure S14. Directional decomposition of the normalized cumulative spectral heat flux at the interface between pristine graphene and liquid heneicosane when the system is under (a) heat-matrix mode and (b) heat-graphene mode. Here, $q(\omega)$ is calculated from graphene to heneicosane.

Erklärung zum Eigenanteil an den Veröffentlichungen

Im Folgenden ist aufgelistet, mit welchem Anteil ich an den Veröffentlichungen beteiligt war.

Mein Anteil an der folgenden Veröffentlichung beträgt 85%

[1] Zhou, T.; Schneider, J.; Wu. Z.; Müller-Plathe, F., The Compatibilization Efficiency of Additives in Homopolymer Blends: a Dissipative Particle Dynamics Study. *Macromolecules*. 2021, 54 (20), 9551-9564.

Mein Anteil an der folgenden Veröffentlichung beträgt 75%
(Eingereicht zur Begutachtung am 13/01/2022).

[2] Zhou, T.; Qiu. D.; Wu. Z.; Albert. S.; Bag S.; Schneider. J.; Müller-Plathe, F., The Compatibilization Efficiency of Graft Copolymers in Incompatible Polymer Blends: Dissipative Particle Dynamics Simulations Combined with Machine Learning, in revision by industry cooperators.

Mein Anteil an der folgenden Veröffentlichung beträgt 80%
(Eingereicht zur Begutachtung am 06/11/2021).

[3] Zhou, T.; Wu. Z.; Das, S.; Eslami, H.; Müller-Plathe, F., How Ethanol Disinfectants Disintegrate Coronavirus Model Membranes: A Dissipative-Particle-Dynamics Simulation Study. *Journal of Chemical Theory and Computation*, in revision.

Mein Anteil an der folgenden Veröffentlichung beträgt 65%

[4] Zhou, T.; Wu. Z.; Chilukoti, H. K.; Müller-Plathe, F., Sequence-Engineering Polyethylene-Polypropylene Copolymers with High Thermal Conductivity Using a Molecular-Dynamics-Based Genetic Algorithm. *Journal of Chemical Theory and Computation*. 2021, 17 (6), 3772–3782.

Mein Anteil an der folgenden Veröffentlichung beträgt 85%

[5] Zhou, T.; Chilukoti, H. K.; Wu. Z.; Müller-plathe, F., Effect of Defects on the Interfacial Thermal Conductance between n-Heneicosane in Solid and Liquid Phases and a Graphene Monolayer. *Journal of Physical Chemistry C*. 2021, 125 (25), 14149–14162.

Datum: 18.02.2022

Tianhang Zhou

Unterschrift Antragsteller

Erklärung zur Begutachtung der Veröffentlichungen

Prof. Dr. Florian Müller-Plathe
Referent

Prof. Dr. Nico van der Vegt

18.02.2022

Korreferent

Datum:

Weder Referent (Prof. Dr. Florian Müller-Plathe) noch Koreferent (Prof. Dr. Nico van der Vegt) der vorliegenden kumulativen Doktorarbeit waren an der Begutachtung nachstehender Veröffentlichungen beteiligt:

- [1] The Compatibilization Efficiency of Additives in Homopolymer Blends: a Dissipative Particle Dynamics Study
- [2] The Compatibilization Efficiency of Graft Copolymers in Incompatible Polymer Blends: Dissipative Particle Dynamics Simulations Combined with Machine Learning
- [3] How Ethanolic Disinfectants Disintegrate Coronavirus Model Membranes: A Dissipative-Particle-Dynamics Simulation Study
- [4] Sequence-Engineering Polyethylene-Polypropylene Copolymers with High Thermal Conductivity Using a Molecular-Dynamics-Based Genetic Algorithm
- [5] Effect of Defects on the Interfacial Thermal Conductance between n-Heneicosane in Solid and Liquid Phases and a Graphene Monolayer

Datum: 18.2.22



Referent
Prof. Dr. Florian Müller-Plathe

Korreferent
Prof. Dr. Nico van der Vegt

